PENINSULA TECHNIKON

FACULTY OF ENGINEERING

DEPARTMENT OF MECHANICAL ENGINEERING

The metallurgical phase transformations in ROQ-tuf AD690 due to the MMA welding process

By

Sherwyn M Daames

Submitted in part-fulfillment of the requirement for

Masters Degree of Technology (MTech): Mechanical Engineering

Under the supervision of
Dr. Graeme J Oliver

DECEMBER 2002

Certificate of Originality

I, Sherwyn Daames, the undersigned, hereby declare that the work contained in this thesis is my own and has never previously been submitted for the awarding of a degree. All information taken from other sources have been clearly referenced.

Signature: 

Date: .....

Acknowledgements

I would like to extend my heartfelt thanks to my wife Renee' for her encouragement and assistance in the writing of the manuscript.

Thanks also to Kevin Douglas of K.D. Engineering for valuable input and assistance in the design and manufacture of the quench tank.

I would also like to thank the head of department, Mr. Jacobs, for making it possible for me to study in the Mechanical Engineering department and for all assistance rendered.

I would also like to extend my heartfelt thanks to the NRF. for funding my research.

I would also like to thank my supervisor Dr. Graeme Oliver for constructive criticism and guidance during the research phase and the writing of the manuscript, without whom, this work would not have been possible.

SUMMARY

Phase transformations in steel are of profound commercial importance due to the fact that they influence the physical and mechanical properties of the end product. During the casting process, which occurs at temperatures in excess of 1500°C, the microstructure of the steel is austenitic. During slow cooling the austenite will decompose into lower temperature microstructures such as ferrite, pearlite or hard, brittle cementite, the latter becoming increasingly present the higher the carbon content of the steel. Steel manufacturers, however, make use of additional forming processes such as rolling, quenching and reheat or tempering to impart specific mechanical or metallurgical properties to a particular steel. If the cooling rate is increased, as would be the case during a quenching process, the austenite will decompose forming a needle like microstructure called bainite in addition to the other microstructures. A further increase in the cooling rate will result in the diffusionless transformation of part of the austenite to form martensite, a hard brittle microstructure. If heat was now to be applied to the steel, as in a tempering process, some of the martensite formed during the quenching process will again transform into a softer microstructure such as pearlite or ferrite.

INTRODUCTION

During the fusion welding process a weldment is locally heated by the welding heat source or arc. The temperatures generated by the arc are usually well in excess of 1500°C, creating a localised molten weld pool. The weld pool and adjacent material, or Heat Affected Zone, (HAZ.) will experience grain growth and the associated metallurgical phase transformations as the weld metal cools down. The rate of cooling will determine the metallurgical microstructures present and hence the mechanical properties of the weld and surrounding material. The purpose of this research is to determine the phase transformations taking place in ROQ-tuff AD690, a low carbon, tempered martensitic steel, when subjected to the Manual

Metal Arc (M.M.A.) welding process. Due to the unavailability of both Time Temperature Transformation (TTT) and Continuous Cooling Transformation (CCT) data for ROQ-tuff AD690, an attempt was made to generate our own data. A TTT curve graphically depicts the percentage of austenite transformed as a function of temperature and time. The Johnson-Mehl-Avrami-Kolmogorov (JMAK) Equation can be used to predict the fraction of austenite transformed into pearlite as a function of time. The JMAK equation represents the transformation kinetics at a particular temperature. From a series of S-shaped JMAK curves a TTT diagram can be generated. The TTT diagram relates metallurgical phase transformation as a function of time and temperature, which is ideal for curve fitting the linear equations required in a Finite Element Analysis. Plates of ROQ-tuff AD690 having dimensions 100x100mm and thicknesses of 10 and 16mm were single butt-welded using two low carbon steel electrodes, namely, Oerlikon Armcord LH and Afrox Transarc 118. Thermocouples were embedded in the plates from which the heat input to the weld body per pass could be determined. Using the Armcord LH electrode, the heat inputs per pass was calculated at 3.51kJ and 8.42kJ for the 10 and 16mm plates respectively. The Transarc 118 electrode generated heat inputs per pass of 4.08kJ and 8.15kJ for the 10 and 16mm plates. The maximum temperature attained by the weld body was 248.7°C, measured during the 8^{th} pass on a 16mm plate using a Transarc 118 electrode. The specific heat capacity of ROQ-tuff AD690 was calculated at 11.45kJ/kgK. Although the Transarc 118 electrode had a higher energy consumption than the Armcord LH electrode, it had a 17% higher material deposition rate, meaning less runs were required to weld a similar thickness of material. Prior to welding some of the plates were stress relieved, whilst others were welded in the as supplied condition. Pre and post weld stress levels in the plates were determined utilizing the Debro-30 Ultrasonic Stress Meter. As would be expected, the plates that were not stress relieved had the highest post weld stresses. Also, the stresses were highly tensile on the bottom of the plate

and compressive on the top, as would be expected. The post-welded plates were machined to form tensile test specimens and these were then subjected to a uni-axial tensile test. The tensile test for plate 6, which was welded with a Armcord LH electrode resulted in a ultimate tensile strength (UTS.) of 877.69MPa., whilst plate 8, which was welded with a Transarc 118 electrode, yielded a UTS. of 815.33MPa. This compared favourably with data supplied by ISCOR, which gave a UTS of between 760-895MPa for ROQ-tuff. Young's Modulus of Elasticity (E) computed from the Stress versus Strain curve was 230.15GPa and 257.9GPa for plates 6 and 8 respectively. This would indicate that the welds obtained were mechanically sound and ductile. Samples were also taken at various positions along the weld from which metallurgical specimens were prepared. Micrographs were then taken and yielded the following microstructures. The centre of the weld contained primarily ferrite and sorbitic pearlite. The centre of the Transarc 118 weld is dominated by austenitic ferrite and pearlitic sorbite, which is ductile, giving the weld excellent mechanical properties. The left hand side of the same weld contained martensite pearlite and ferrite, whilst the right contained ferrite and pearlite. A similar analysis was carried out on the twelve-pass Armcord LH weld yielding the following results. The centre portion of the weld contained martensite and ferritic sorbite. The left hand side contained lamellar pearlite, ferrite, cementite and fine martensite. The right hand side of the weld contained cementite and fine martensite. As was highlighted previously, phase transformations are dependent on cooling rate. To determine the cooling rates necessary to create these microstructures a quench tank was designed and built. The following quenching media were used, namely, brine, cold water, oil and still air cooling or normalising. Jominy bars were machined and thermocouples were once again embedded in them. The readings from the thermocouples were used to used to create cooling rate curves As would be expected, the brine produced the most severe quench, resulting in a cooling rate of 33.8°C/s at the end in contact with the brine. The end of the Jominy bar furthest from the

brine experienced a cooling rate of 0.47°C/s. The cold water quench produced cooling rates of 10.7°C/s and 0.23°C/s at the emersed and furthest ends of the bar respectively, whilst the oil quench produced cooling rates of 3.5°C/s and 0.47°C/s at similar positions. The normalised bar experienced a maximum cooling rate of 0.71°C/s at the ends. The post-quenched Jominy bars were subjected to a hardness test, with readings taken within close proximity of the couple positions. Hardness is defined as the measure of the resistance of a material to an applied force and involves the use of an indenter of fixed geometry under static load. Using a pyramidal diamond indenter under a 150kg load the following hardness values were obtained. The brine quenched bar produced hardness values ranging from 50.6 Rockwell C (Rc) to 45.4 Rc at the emersed and furthest ends of the bar respectively. The hardness values for the water-quenched bar ranged from 40.1 Rc to 28.6 Rc. The oil quenched bar produced hardness values ranging from 31.6 Rc to 28.2 Rc. The bars were then sectioned within close proximity of where the couples were embedded and metallurgical samples were prepared yielding martensite having a hardness value of 514 Brinel at the quench end. Midway along the length of the bar the microstructure was troosto-martensite having a hardness of 478 Brinel. The furthest end of the bar contained pearlite and ferrite and had a hardness value of 429 Brinel. As would be expected the water-quenched bar portrays the same phenomena, yielding the harder microstructure at the quenched end and progressively softer microstructures the further you move away from the quenched end. Previously, the welds were analysed and microstructures identified. Post-quenched Jominy bars have now been analysed and microstructures identified. The cooling rates and associated hardness values are known. It would be safe then to conclude that the microstructure found in the welded plate, which is similar to the microstructure in the Jominy bar must have experienced a similar cooling rate and therefore have almost identical hardness values. It has long been established that there is a relationship between metallurgical microstructure and

mechanical properties. The finer the austenite grain size, the greater the ductility and yield strength of the steel. Conversely, the larger the austenite grain size, the more hardenable the steel due to the reduction in pearlite nucleation sites. The critical cooling rate is defined as the quench rate just sufficient to prevent the transformation of austenite to ferrite and pearlite, producing martensite. The critical cooling rate for martensite formation was calculated and found to be 1.892°C/s. Subjecting ROQ-tuff AD690 to a cooling rate of higher than 1.892°C/s will result in the formation of martensite, which compares well with results found from the quenched bars. Finally, a coupled Thermo-Mechano-Metallurgical (TMM.) Finite Element analysis was carried out to verify the metallurgical phases found in actual welds. The results obtained correlates well with physical evidence.

CONCLUSIONS

ROQ-tuff AD690 welds exceptionally well producing structural quality joints. The low hydrogen electrodes, namely Transarc 118 and Armcord LH produce welds of similar metallurgical composition, although the Armcord welds are slightly more brittle and produce more weld spatter. The mechanical properties are sound and compares well with ISCOR data. The correlation of phases identified in actual welds and those obtained from Jominy quench specimens is good. It would, however, have been a good exercise to carry out a micro-hardness analysis of the weld microstructure as an additional mechanism for phase identification, since surface hardness values obtained from the Jominy bars are not a precise indication of microstructural hardness. This would, however, have been a time consuming exercise, the fact that the facilities are not available apart. The TMM model works well as a mechanism for predicting weld microstructure. It will not however replace physical sampling and microscopy.

TABLE OF CONTENTS

CHAPTER 3 – TENSILE TESTING

CHAPTER 4 – HEAT TREATMENT OF STEEL

CHAPTER 5 – ULTRASONIC STRESS MEASUREMENT

CHAPTER 6 – METALLOGRAPHIC SPECIMEN PREPARATION

CHAPTER 7 - MICROSTRUCTURE

CHAPTER 8 – THE FINITE ELEMENT METHOD

PART B - EXPERIMENTAL

CHAPTER 9 – EXPERIMENTAL PROCEDURE

CHAPTER 10 – FINITE ELEMENT ANALYSIS

CHAPTER 11 - CONCLUSIONS

LIST OF FIGURES

LIST OF TABLES

CHAPTER 1 – MANUAL METAL ARC WELDING.

1.1 Introduction to the MMA. Welding Method

The Manual Metal Arc (MMA) welding process was first devised in Russia at the end of the nineteenth century [8] and involves the conversion of electrical energy to thermal energy by means of a counter current transfer of electrons by means of an arc. The Manual Metal Arc (MMA) welding process can be used for welding all thicknesses of material above 5mm, and is the principal method for making butt and fillet welds. The method is simple, fast and introduces little distortion in the work-piece, provided it is securely clamped during the welding process. The striking of an arc between the tip of an electrode and the base metal forming a weld pool facilitates welding. The intense heat melts the tip of the electrode and the electromagnetic field set up between the electrode and the base metal causes droplets of molten electrode to be deposited in the welding pool forming a weld. On cooling, the weld usually has metallurgical properties similar to that of the parent metal and mechanical properties equal to or better than the parent metal, provided the correct electrode and welding procedures are used.

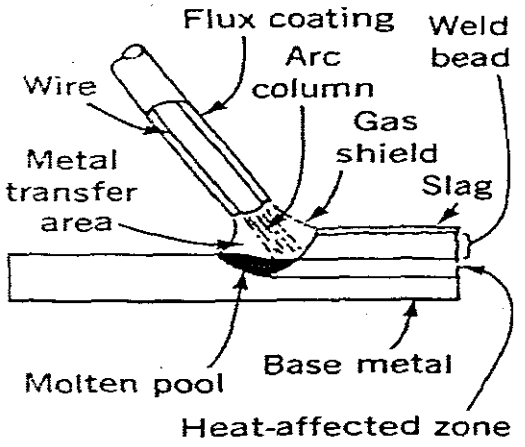

Figure 1.1. Depicting the MMA process (from Welding and Welding Technology)

Welding in the flat position, depicted in figure 1.1, is the most common welding position requiring the least skill to produce a sound bead. The angle of the electrode, usually 10 to 25° in the direction of travel, is largely determined on the voltage and amperage settings of the machine and the thickness of the metal being welded.

1.2 The Electrode

Usually, consists of a steel core covered with a coating containing several elements, as is depicted in figure 1.2, some of which combust under the intense heat generated by the arc. This gas shield protects the molten weld pool from ingress by the oxygen and nitrogen in the atmosphere. The other constituents of the coating melt to form a protective slag, which promotes slower cooling of the weld bead, thereby reducing the occurrence of hot cracking and the formation of undesireable metallurgical microstructures such as martensite. MMA. electrodes are distinguished from each other by their coating composition. The coating may be rutile, basic or semi-basic. Even though the rutile electrode coatings "exhibit acidic chemical reactions, they are still referred to as rutile electrodes due to the large amount of rutile sand used in the flux composition."[2]

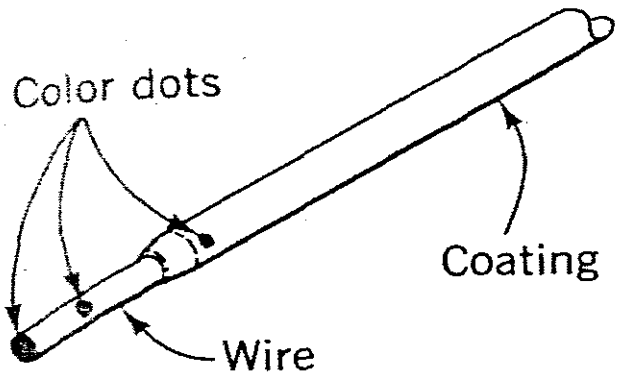

Figure 1.2. Depicting MMA. electrode constituents and markings (from Welding and Welding Technology)

The basic coated hydrogen-controlled electrodes such as Oerlikon Armcord LH, or the Afrox Transarc 118 "contain calcite ($CaCO_3$) and fluospar (CaF_2) as the main coating constituents and exhibit a basic chemical reaction." [2] The acidity or basicity of the chemical reaction may be calculated from the following simplified formula:

$$B = \frac{CaO + CaF_2 + MgO + K_2O + \frac{1}{2}(MnO + FeO)}{SiO_2 + \frac{1}{2}(Al_2O_3 + TiO_2)} \qquad (1.1)$$

If the flux composition gives a value of :

B<1 $\Rightarrow$ composition acid or rutile

B=1 $\Rightarrow$ neutral reaction

1>B<2.5 $\Rightarrow$ composition semi-basic

B>2.5 $\Rightarrow$ composition basic

Another major constituent of all electrode coatings is silica, which acts as both a viscocity inhibitor and binding medium. The functions of the major mineral constituents of the flux are indicated in the table 1.1 below.

Mineral	Chemical Symbol	Function
Rutile Sand	TiO_2	Arc Stabiliser; Slag Former
Calcite	CaC_{O3}	CO2 Shielding gas emmiter; Increasing basicity
Fluospar	CaF_2	H2 inhibitor; Slag former and conditioner.
Silica	SiO_2	Slag former giving increased weld metal viscocity and increasing the acid reaction of the slag

Table 1.1. Indicating the functions of major flux constituents (from Transarc Welding Consumables Catologue)

The presence of moisture in the weld coating of hydrogen controlled electrodes, may induce the adverse effect of hot cracking in hardenable steels. To reduce the possibility of moisture ingress, specific storage conditions must be adhered to. The electrodes must be "stored at an ambient temperature of ±25°C with a relative humidity of 50%."[2] If these conditions cannot be maintained, moisture will enter the electrode coating, which will require baking in an oven at elevated temperatures of between 300 and 350°C for periods of around 2hrs prior to use.

1.3 Electrode Classification

A committee of the American Welding Society (AWS) prepared a specification whereby arc welding electrodes are classified by means of filler metal. The specification covers all filler metals ranging from mild steel to corrosion–resisting chromium and chromium nickel steel covered welding electrodes. The AWS. A5.5 specification covers the electrodes used in the MMA. operation, having a minimum tensile strength of 760Mpa. Electrodes are classified by a six digit code, preceded by the letter E, denoting welding electrode. The first two digits following E denotes the tensile strength in pounds per square inch (psi) (×1000). The relationship between Psi and Mpa can be determined by the following conversion factor:

$$1\text{Mpa} \approx 130\text{Psi}$$

The third digit indicates the position of welding in which the electrode may be used, whilst a combination of three and four gives data on the electrode polarity as well as coating constituents.

The AWS. 5.18 specification covers filler metals used for gas shielded arc welding such as the TIG. process. Filler metals are "classified on the basis of their chemical composition and mechanical properties of their weld metal in the as-welded condition, using the gas metal arc welding (GMAW) procedure." [2] The designation is ER70S-X where X has a value of between 2 and 7 or the letter G. For the wire used in the Tig. welding experiments, the last digit is 7. The filler metal has "substantially more manganese when compared to the others which provides better wetting and weld appearance with slightly higher tensile and yield strengths." [2] The recommended shielding gas is Corgon-2, a mixture of CO_2 and Argon.

1.4 MMA. Welding Variables

It has been found [1] that "four variables influence the quality of the weld obtained", namely:-

1.4.1 the current setting or amperage
1.4.2 the length of the arc or arc voltage
1.4.3 the rate of travel
1.4.4 the angle of the electrode

Each of the above will now be analysed in more detail

1.4.1 The current setting

The current, which the welding machine supplies to the arc, must change with the size of the electrode being used. The larger the electrode diameter, the higher the current setting. An empirical rule has been devised for the current setting, which states that "the current setting should be equal to the diameter of the electrode in inches" [2]. The following example will demonstrate this:

¼" = 0.25" ⇒ ±250A current setting

It should be noted that the electrode diameter is denoted by the diameter of the steel or alloy core only.

1.4.2 The length of the arc

Variations in the arc length will produce welds of varying quality. As a general rule, the arc length increases as the arc voltage increases. It has been determined [2] "that the arc length is slightly less than the diameter of the electrode being used", and since it is virtually impossible to physically measure this gap during welding, guidance is obtained from the sound produced by the arc. At the correct arc length, the arc produces a sharp energetic crackle. It should be noted, however, that this distinction is gained by experience.

1.4.3 The rate of travel

The rate of travel changes with the thickness of the metal being welded. It follows that the thicker the plate, the higher the current setting and the slower the rate of travel. This results in a higher material deposition per unit travel, resulting in a more concave weld. I t should be stated, however, that the slower the rate of travel, the higher the heat input per unit run. This could be detrimental on the inter-pass temperature, which may have to be limited to a certain value.

1.4.4 The angle of electrodes

When welding on plates in the flat position, the electrode should make an angle of 90° with the work-piece. In other than flat welding, good results are obtained if the welding rod bisects the included angle is in half.

1.5 The Preparation of Butt Welds – flat position

A butt weld joins two plates end to end with the plates lying on the same plane. The plates are usually beveled to form a V to facilitate welding at the bottom of the joint. The angle of the V (60° included angle in our case) should be sufficient to allow easy welding at the bottom of the joint. Intuitively, one would see that the larger the included angle, the more weld metal would be required to fill the V. A compromise between economy and accessibility has been found in an included angle of 60°.

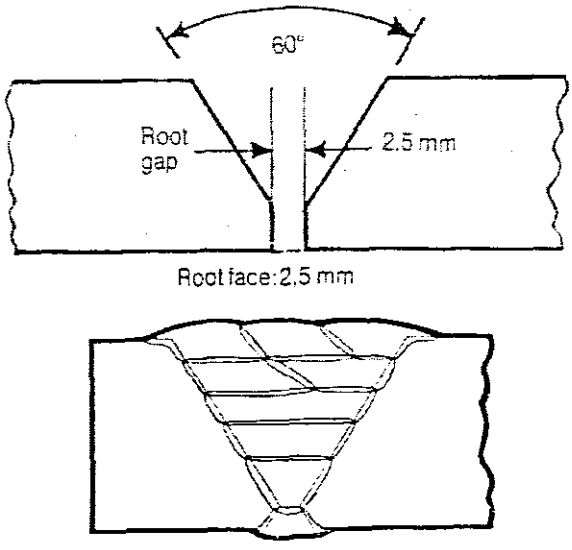

Figure 1.3. Depicting Single Butt weld geometry (from Afrox Welding Consumables Catologue.)

With reference to figure 2, the plates have to be prepared taking care to ensure a constant root gap, since the root run is sensitive to any excessive changes in root gap. The plates are tacked onto the workbench taking precautions to ensure that the tacks are strong enough to withstand the stresses that will be generated by the cooling of the weld metal. Since low hydrogen electrodes such as Armcord LH and Transarc 118 have a tendency to stick, runner plates are welded on either side of the parent metal to ensure that a weld of consistent quality is obtained. The root run is carried out with the amperage slightly lower than for the other runs to accommodate the root gap and prevent burn through. The following runs are carried out after de-slagging to ensure good penetration has been obtained and to prevent slag inclusions or porosity. Finally, depositing a small sealing run completes the back of a butt weld. "If the penetration of the first run is inadequate or uneven, the back must first be gouged out before carrying out the sealing run." [4]

1.6 The Welding Bead

The weld bead is without a doubt the most important part of the welding operation. For this reason some of the most common causes of weld bead defects will be briefly analysed.

1.6.1 Porous Weld Beads

"Porosity is impurity in the bead caused by incorrect preparation of the plates, i.e. jagged edges providing areas for slag inclusions, insufficient puddling time, the use of old or wet electrodes, or too small an arc gap." [4] The arc gap must be short when welding with low hydrogen electrodes such as Armcord LH or Transarc 118. To correct the situation, the source of the impurity must be determined. This is usually facilitated by first analyzing the base metal under a microscope to determine if the microstructure is sound. The more obvious causes are then eliminated afterwards.

1.6.2 Poor Penetration

"Poor penetration or fusion is usually the result of too fast a travel by the electrode, although it can also result if the electrode diameter versus current setting is too low for the thickness of material being welded." [4] Poor penetration occurs commonly on the backside of a butt weld when the two pieces being joined do not have sufficient root clearance and the electrode has been allowed to burn through. To eliminate these errors, adequate root spacing should be allowed to facilitate proper penetration, whilst the electrode travel is just fast enough to fill the crater whilst maintaining the correct arc length. A smaller diameter electrode may be used to facilitate the root run.

1.6.3 Undercutting

"Is caused primarily by the incorrect manipulation of the electrode, and may be compounded by current settings that are too high."[4] The main concern with undercutting is that although the weld bead may be sound, the decrease in load bearing area along the side of the weld may result in failure of the component. Moving the electrode away from the base metal before the transfer of sufficient metal to the welding pool has occurred as well as to large a diameter electrode and too high a current setting are the main contributors to this phenomenon. The most obvious remedies to this problem would be to shorten the arc gap, decrease the speed of travel and or decrease the current setting.

1.6.4 Warping

Is largely caused by uneven heating and cooling of the base metal and can be minimised by limiting the amount of heat input to the base metal and the use of jigs and fixtures.

1.6.5 Weld Appearance

"Although the appearance of a weld does not indicate its inherent strength, it does give some indication as to whether correct electrode manipulation was followed." [4] Incorrect arc length and voltage and current settings can also be detected by this visual inspection. An arc length that is too high will produce weld splatter, whilst a varying speed of travel will produce a bead of varying width and depth of penetration. A sound weld bead usually has a consistent material deposition rate.

1.7 Critical Post – Weld Criteria

1.7.1 Material Composition

Roqtuf AD690 is a low-alloy carbon manganese steel having a chemical composition as indicated in table 2 below.

Chemical composition % (ladle analysis)										
Grade	Max thickness	C	Mn	Si	S (max)	P (max)	Mo	Ni	Cr	B
ROQ-tuf AD690	32mm	0.12/ 0.21	0.45/ 0.70	0.20/ 0.35	0.040	0.035	0.50/ 0.65	-	-	0.001/ 0.005

Table 1.2. Depicting chemical composition of ROQ-tuf AD690 (courtesy ISCOR product manuals)

The welding operation produces very rapid heating and cooling rates in the base metal adjacent to the weld known as the Heat Affected Zone (HAZ). "For materials low in carbon no appreciable hardening takes place, but above 0.15% carbon hardening becomes increasingly more significant depending on the cooling rate." [2] Carbon manganese steels having a hardness value of around 350HV in the HAZ will be susceptible to cracking. Cracks may appear immediately after welding or up to 72hrs after welding, as is the case with hydrogen induced cracking. Since the susceptibility to cracking depends largely on the carbon content and other elements, which have varying effects on the tendency of the material to harden, it is important that we know exactly what their effect would be. This quantification can be obtained by applying the carbon equivalent (CE) formula, which is given below.

$$CE = C + \frac{\%Mn}{6} + \frac{(\%Ni + \%Cu)}{15} + \frac{(\%Cr + \%Mo + \%V)}{5} \qquad (1.2)$$

The calculation of CE for ROQ-tuf AD690 would therefore be as follows:

$$CE_{ROQ} = 0.165 + \frac{0.575}{6} + \frac{(0+0)}{15} + \frac{(0+0.575+0)}{5}$$
$$= 0.3758$$

From this result we can deduce, that ROQ-tuf AD690 is susceptible to cracking.

1.7.2 Cooling Rate

The hardness of the microstructure in the HAZ depends on the cooling rate of the material. The faster the cooling rate, the harder the microstructures produced and the more susceptible they are to cracking. "The cooling rate is governed by the mass of the material, temperature of the base material and the heat input to the base material." [2] Other factors such as the ambient temperature of the surrounding air and whether there is a draught would also impact on the cooling rate albeit to a lesser extent since their influence can largely be controlled in a laboratory situation. Each of the three major factors influencing the cooling rate will now be analysed in more detail.

1.7.2.1 Volume of material

Most of the heat generated during the welding process will dissipate into the base metal through the process of conduction heat transfer. The joint type i.e. whether butt, double butt or T-joint, governs the number of paths through which heat can be conducted away from the weld. A combined thickness factor, "ct", in mm, which takes into consideration the thickness of both materials to be welded, gives a good indication of how high the cooling rate is for a particular joint, and hence how susceptible the joint is to cracking. The determination of "ct" for a single butt weld is explained in figure 3 below.

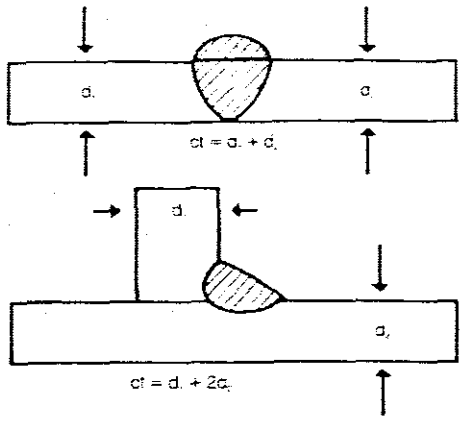

Figure 1.4. Depicting a Single Butt Joint and a T-Joint (from Afrox Welding Consumables Catologue)

1.7.2.2 Temperature of base material

It follows, that the lower the temperature of the base material, the greater the effect of quenching on the deposited weld metal and the HAZ. Apart from preventing hardening by reducing the cooling rate, preheating of the base material facilitates the diffusion of hydrogen from the weld metal and surrounding HAZ before solidification. "Practical preheating temperatures range from 150^0C for structural steels to 300^0C for high carbon low alloy steels. Preheating is applied locally to the joint and it is important that a width of no less than three times the material thickness is uniform in temperature, and the temperature is maintained throughout the welding operation." [2] The International Institute of Welding (IIW) has established a formula whereby the preheat temperature, (T_o), of a material of known thickness can be determined.

$$T_o = 1440Pc - 392 \qquad (1.3)$$

Where Pc is termed the cracking factor and is obtained by the following expression:

$$Pc = C + \frac{Si}{30} + \frac{Mn}{20} + \frac{Cu}{20} + \frac{Ni}{60} + \frac{Cr}{20} + \frac{Mo}{15} + \frac{V}{10} + 5B + \frac{t}{600} + \frac{H}{60} \qquad (1.4)$$

where:

C denotes Carbon
Si denotes Silicon
Mn denotes Manganese
Cu denotes Copper
Ni denotes Nickel
Cr denotes Chromium
Mo denotes Molybdenum
V denotes Vanadium
B denotes Boron
t denotes Plate Thickness
H denotes Diffusable Hydrogen in mls/100g weld metal

Although the manufacturers literature suggests that preheat is unnecessary for thicknesses below 25mm, the calculation has been carried out and appears as Appendix A.

1.7.2.3 Heat input

The larger the heat input, the slower the cooling rate and the less the tendency to form an undesireable microstructure. There is, however, a limit to the amount of heat that can be imparted to a body, without detrimentally influencing the mechanical properties of the weld metal. It has been found "that increasing the heat input has the following effects" [2]

1. A decrease in the weld metal manganese and silicon contents, which implies that the strengthening effect of the manganese is lost.
2. A decrease in the yield and ultimate tensile strengths.
3. A decrease in the hardness of the as deposited weld material.
4. An increase in the grain size of the equiaxed fine grain regions.

Manganese has the effect of moving the knee of the TTT diagram to the left, resulting in the formation of softer more ductile microstructures. If the manganese is lost from the weld pool the resulting weld will be brittle and hence have a lower yield and UTS. Excessive heat inputs, especially in multi-pass welds will have a tempering effect on previously deposited material. A weld consists of two primary regions, namely, the Fusion Zone and the Heat Affected Zone (HAZ.) The fusion zone will become completely austenitic and transform to ferrite and pearlite on cooling. The material in the HAZ will experience microstructural changes without melting and will have a fine grain size upon cooling. If the heat input were to be increased above the level necessary for sound welding to take place, the fusion zone will be increased resulting in a larger HAZ. The material closest to the fusion zone will thus experience grain growth.

The total heat input for the two plate thicknesses of ROQ-tuf AD690, using the Armcord LH and Transarc 118 electrodes, was determined and appears below.
The heat input per pass, in kilojoules per millimetre (kJ/mm), to the plates was determined by the following expression:

$$Heat\ Input(Q) = \frac{Arc\ voltage(V) \times current(I) \times time(s) \times Efficiency(\eta)}{distance\ travelled(mm) \times 1000} \qquad (1.5)$$

The BDH-400 welding machine has a function, which enables the user to recall the average voltage at the end of a particular welding pass. Based on these figures and the times obtained from the thermal couples, the heat input per pass was determined. The total heat input to the plate was then the summation of all the consecutive heat inputs.

Calculation for the 10mm plate, using the Armcord LH electrode:

- Current setting: 120A
- Voltage: 20.9V
- Time per run: 40s
- Distance traveled: 100mm
- Ambient temperature: 22.2^0C
- Efficiency: 70%
- number of passes: 5

$$Q/pass = \frac{(20.9 \times 120 \times 40 \times 0.7)}{(100 \times 1000)}$$
$$= 0.702kJ \rightarrow$$
$$Q_{Tot} = 0.823 \times 5$$
$$= 3.51kJ \rightarrow$$

Calculation for the 16mm plate, using the Armcord LH electrode:

- Current setting: 120A
- Voltage: 20.9V
- Time per run: 40s
- Distance traveled: 100mm
- Ambient temperature: 22.2^0C
- Efficiency: 70%
- Number of passes: 12

$$Q/pass = \frac{(20.9 \times 120 \times 40 \times 0.7)}{(100 \times 1000)}$$
$$= 0.702kJ \rightarrow$$
$$Q_{Tot} = 0.702 \times 12$$
$$= 8.42kJ \rightarrow$$

Calculation for the 10mm plate using the Transarc 118 electrode:
This electrode performed best at 130A

- Current setting: 130A
- Voltage: 22.4V
- Time per run: 40s
- Distance traveled: 100mm
- Ambient temperature: 22.2^{0}C
- Efficiency: 70%
- Number of passes: 10

$$Q/pass = \frac{(22.4 \times 130 \times 40 \times 0.7)}{(100 \times 1000)}$$
$$= 0.815kJ \rightarrow$$
$$Q_{Tot} = 0.815 \times 5$$
$$= 4.08kJ \rightarrow$$

Calculation for the 16mm plate using the Transarc 118 electrode:
This electrode performed best at 130A

- Current setting: 130A
- Voltage: 22.4V
- Time per run: 40s
- Distance traveled: 100mm
- Ambient temperature: 22.2^{0}C
- Efficiency: 70%
- Number of passes: 10

$$Q/pass = \frac{(22.4 \times 130 \times 40 \times 0.7)}{(100 \times 1000)}$$
$$= 0.815kJ \rightarrow$$
$$Q_{Tot} = 0.815 \times 10$$
$$= 8.15kJ \rightarrow$$

From the above calculations, one can deduce that the heat input into the 10mm plate by the Transarc 118 electrode is approximately 15% more than that by the Armcord LH electrode. In the case of the 16mm plate, however, the number of passes required by the Transarc 118 electrode is 10 as opposed to the 12 for the Armcord LH electrode. This results in a 3% higher heat input in the instance of the Armcord LH electrode. From the above, the deduction can also be made that the Transarc 118 electrode has a 20% higher material deposition rate than the Armcord LH electrode.

- Determination of the specific heat capacity (cp) for ROQ-tuf AD690

The specific heat capacity for the steel can be determined using the data obtained from the thermo-couples and the readings from the welding machine. The approach is as follows:

1. The heat input to the weld is given by:

$$Q = V \times I \times \eta \tag{1.6}$$

where: Q is the heat input in kJ
V is the voltage, obtained from BDH-400
I is the current setting on BDH-400
η is an efficiency factor

There will however be losses in the form of radiation and surface conduction, hence the need for an efficiency factor. The heat imparted to the body via the welding process, given by equation 1.6, will cause an increase in the temperature of the body. This temperature rise is obtained from the thermo-couples.

$$\begin{aligned} Q &= mcp\Delta T \\ &= mcp(T_2 - T_1) \end{aligned} \tag{1.7}$$

$$cp = \frac{V \times I \times \eta}{(T_2 - T_1)} \quad (kJ/kgK) \tag{1.8}$$

CHAPTER 2 – HARDNESS TESTING.

2.1 Introduction

Hardness testing is one of the oldest mechanical testing methods. It's simplicity and speed has made it suitable for applications in the field of quality control. The test is often non-destructive to the components tested, as opposed to the tensile test, previously dealt with. Each of the above mentioned tests, however, have their particular application.

2.2 Hardness

This is the ability of a material to resist surface indentation or scratching. It is therefore a good indication of resistance to abrasion or wear. One of the main uses of the hardness test is the determination of the quality of a heat treatment process. Since, hardness is not a fundamental property of material, it implies that the value of the material hardness will vary, depending on the test method being applied. It is for this reason that it is essential that the test method be specified at all times, when quoting hardness numbers.
The most common test in use today are:

- Brinel test (BS 240:1986)
- Vickers test (BS 427:1982)
- Rockwell test (BS 891:1989)

2.3 The Brinel test

An indentor, consisting of hardened steel or tungsten carbide ball, is pressed onto the surface of the test specimen for a standard time, usually 10 to 15 seconds, under a standard load. An indentation is made on the surface of the specimen, which is then measured in two mutually perpendicular directions and the average calculated.

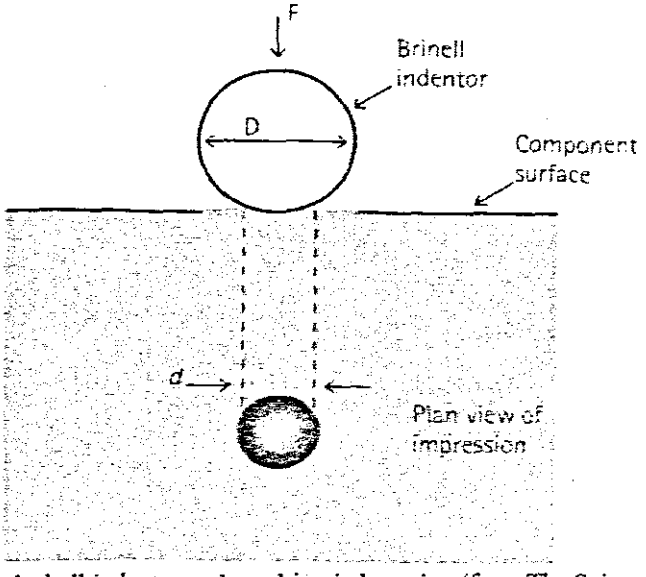

Figure 2.1. Depicting the ball indentor and resulting indentation (from The Science & Engineering of Materials.)

The Brinel Hardness Number (BHN.) is the calculated from the following expression:

$$HB = \frac{Applied\ load\ (kg)}{surface\ area\ of\ impression\ made\ (mm^2)}$$

$$= \frac{2F}{\pi D\left\{D - \sqrt{D^2 - d^2}\right\}} \qquad (2.1)$$

where 'F' is the load in kilograms

'D' is the ball diameter in mm

'd' is the diameter of the impression in mm

To ensure that the ball is not pushed to deep into the surface of the specimen under test, as would be the case for very soft materials, the relationship d=0.25D to 0.50D must be maintained at all times. This implies that the ball diameter and load applied is specified for the material under test at all times. BS 240 contains tables indicating values for F/D^2 for most materials.

Some common values are as follows:

$$Steel, \quad \frac{F}{D^2} = 30$$

$$Copper\ Alloys, \quad \frac{F}{D^2} = 10$$

This implies, that if the indentor size is known, the size of the load may quite simply be determined.

2.3.1 Disadvantages of the Brinel test

2.3.1.1 The indentor causes a large impression in the specimen, usually, 2 – 4mm in diameter. This could act as a region of stress concentration in a component.

2.3.1.2 The large depth of the impression precludes its use on plated or surface hardened components, as the impression would also measure the hardness of the underlying structures.

2.3.1.3 The use of the Brinel test is limited to materials of hardness up to 450HB for the steel ball and 600HB for the tungsten carbide ball.

2.4 The Vickers test

The Vickers indentor consisting of a square based pyramid having an included angle of 136° is a distinct improvement over the spherical indentor of the Brinel test. The Vickers hardness (HV), is again a function of the applied load and the size of the resulting indentation, as is indicated in figure below.

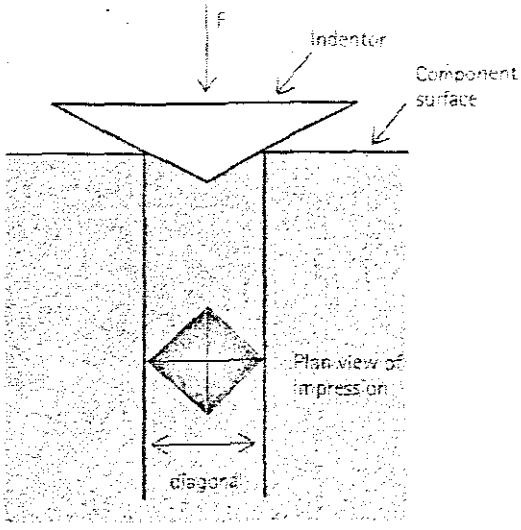

Figure 2.2. Depicting the diamond indentor and resulting indentation (from The Science & Engineering of Materials.)

The advantages of θ=136° is that HB ≈ HV, up to a value of 300.

2.4.1 Advantages of the Vickers test

2.4.1.1 It is suitable for testing both hard and soft material
2.4.1.2 Since all impressions are geometrically similar, the only variable is the load selection, which should be sufficient to produce an indentation large enough to facilitate accurate measurement.
2.4.1.3 The results obtained are extremely accurate making it the preferred test method for R&D work.

2.4.2 Disadvantages of the Vickers test

2.4.2.1 Since the size of the impression formed is small, surface of the component under test must be highly polished and secured perpendicular to the indentor.
2.4.2.2 A considerable amount of time is required to perform this test.

2.5 Microhardness testing

Microhardness test may be performed with the Vickers indentor, which is incorporated into a microscope. This facilitates the accurate measurement of impressions made under loads of 1 - 1000 grams. This type of testing is used to determine the hardness of microconstituents e.g. the phases present in the heat affected zone (HAZ) of a welded component.

2.6 The Rockwell test

This test differs from those previously dealt with, in that it measures the depth of indentation as opposed to the size (diameter or cross-section), and relates this to the hardness of the material, as is indicated in the figure below. This results in a considerable saving in time to perform the test, since the hardness value can be directly read from a scale on the machine.

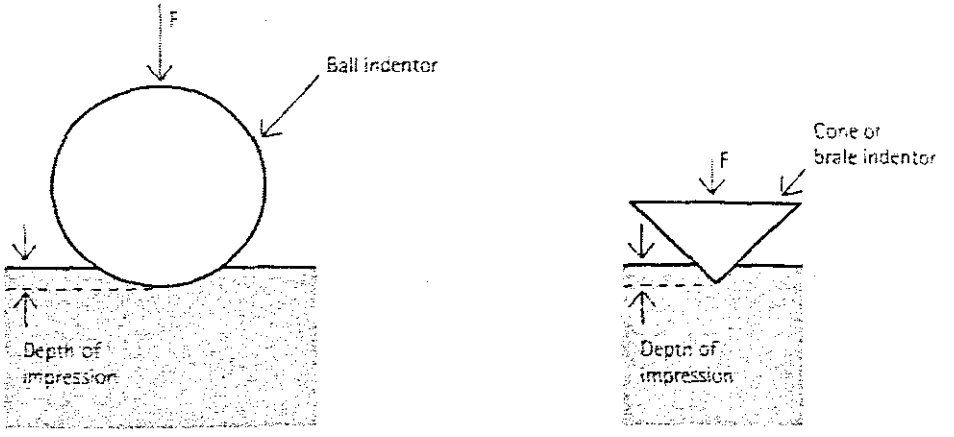

Figure 2.3. Depicting the ball and diamond indentors of the Rockwell Test (from The Science & Engineering of Materials.)

There are numerous Rockwell scales, but the most common are the following:

- B –scale uses a 1/16" diameter steel ball indentor under a 100kg load. It is used to measure the hardness of non-ferrous metals such as brass, bronze and copper and it's alloys.

- C –scale uses a 120^0 diamond indentor, termed a BRALE, under a 150kg load. It is primarily used to measure the hardness of steel.

2.6.1 Advantages of the Rockwell test

2.6.1.1 The speed at which a test may be carried out makes it ideal for use in a production environment, where speed of results is essential for controlling process quality.

2.6.1.2 The size of the indentation formed falls mid-way between that obtained from the Brinel and Vickers tests.

2.6.1.3 The specimen surface does not have to accurately, since the machine can accommodate some misalignment.

CHAPTER 3 – TENSILE TESTING.

3.1 Introduction

Uni-axial tensile testing is one of the most frequently performed mechanical tests. The test usually involves the gripping of a specimen at both ends and subjecting it to increasing axial load until it breaks. The data gleaned from the tensile test may be used to determine amongst others, Young's modulus, which is a good indication of the ductility of the material.

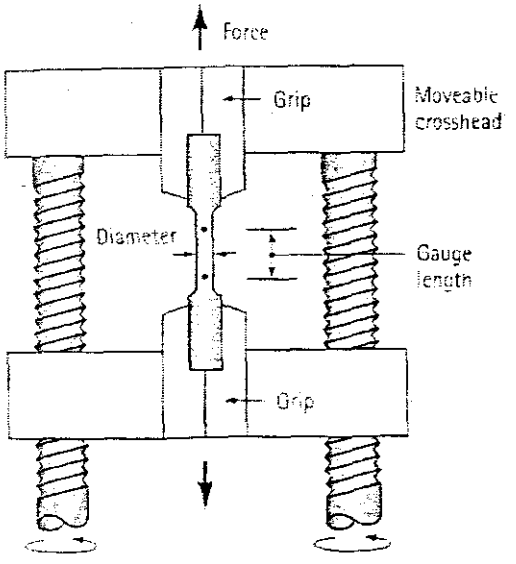

Figure 3.1. Depicting a uni-axial tensile testing device. (from The Science and Engineering of Materials, 1996.)

3.2 Elastic versus Plastic Deformation

When a solid material is subjected to stress within the limits of proportionality, the bonds between the atoms are stretched. When the stress is removed, the bonds relax and the material returns to its original shape. This reversible deformation is termed elastic deformation. At stress values above the limits of proportionality, planes of atoms slide over one another. Material subjected to this type of deformation will not return to its original state and is said to have undergone plastic deformation. For most materials the initial portion of the curve is approximately linear and is represented by the following equation:

$$E = \frac{\delta}{\varepsilon} \qquad (3.1)$$

where E is Young's modulus
δ is the stress
ε is the strain

Within the limits of proportionality, the ratio, ν, of the magnitude of the lateral contraction strain to the axial strain termed Poisson's ratio is represented by the following

$$\nu = \frac{\varepsilon_y}{-\varepsilon_x} \tag{3.2}$$

equation:

where ν is termed Poisson's ratio
ε is the strain in the in the x and y directions respectively.
(for a y-direction tensile test)

Plastic strain or permanent set occurs when the stress level exceeds the limits of proportionality and usually corresponds to the first deviation from linearity. Since the determination of the onset of plasticity depends on the accuracy of the equipment being used, it was decided to instead use the 0.2% offset strain as the determining factor for the value of the yield strength of the material.

3.3 Yield Points

The stress strain curve for steel has an initial maxima followed by lower stresses. The initial maximum is the yield point after which all the deformation at any instant is occurring within a relatively small region of the specimen. Continued elongation of the specimen occurs by propagation of the deforming region, termed the Lüders band, along the gauge section rather than by increased strain within the deforming region. When the Lüders band has traversed the entire gauge section, the values of the stress on the curve will again show an increase. For most engineering purposes the lower yield strength is quoted as the onset of yielding. The ultimate or tensile strength is the highest value of the engineering stress. In ductile materials, the tensile strength corresponds to the point at which necking occurs.

3.4 Ductility

The two most commonly used measures of material ductility are percent elongation and percent reduction in area and are given by the following equations:

$$\%El = \left[\left(L_f - L_0\right)/ L_0\right] \times 100 \tag{3.3}$$

where El is the elongation percentage
L0 is the initial gage length
Lf is the final gage length

$$\%RA = \left[\left(A_0 - A_f\right)/ A_0\right] \times 100 \tag{3.4}$$

where RA is the percentage reduction in cross-sectional area
A_0 is the initial cross-sectional area
A_f is the final cross-sectional area

When carrying out a tensile test on sheet specimens, a portion of the elongation occurs during diffuse necking. Maintaining the same ratio of width to gauge length for all specimens can standardize this. To avoid end defects from the shoulders, the length of the transition region should at least be as large as the diameter. The total length of the reduced section should be at least 4×d. It should be borne in mind, however, that some elongation, which is a function of sheet thickness, also occurs during localized necking.

3.5 True Stress and Strain

If the tensile testing results are to be used to predict the behaviour of a particular metal, when subjected to other forms of loading, it is desirable to plot the data in terms of true stress and strain as depicted in the following formulae:

$$True\ Stress: \quad \sigma = \frac{F}{A} \tag{3.5}$$

where F is the tensile force

$$True\ Strain: \quad \varepsilon = \ln\left(\frac{L}{L_0}\right) \tag{3.6}$$

A is the cross-sectional area

where L is the length of the specimen at the onset of necking
L0 is the original length of the specimen

It should be stressed, however, that equation (3.6) only applies up to the point at which necking starts.
Provided the deformation is uniform along the gauge section, the true stress and strain, may be computed from the engineering stress and strain and is given by the following equations:

$$\sigma = S(1+e) \tag{3.7}$$
$$= \left|\frac{F}{A_0}\right|\left(1+\left\{\frac{\Delta L}{L_0}\right\}\right)$$

$$\varepsilon = \ln(1+e) \tag{3.8}$$
$$= \ln\left(1+\left\{\frac{\Delta L}{L}\right\}\right)$$

At very low strain levels, the differences between true and engineering stress is very small. In such instances it does not matter which was used for the computation of Young's modulus.
The figure below gives a clear depiction of the differences between true and engineering stress and strain.

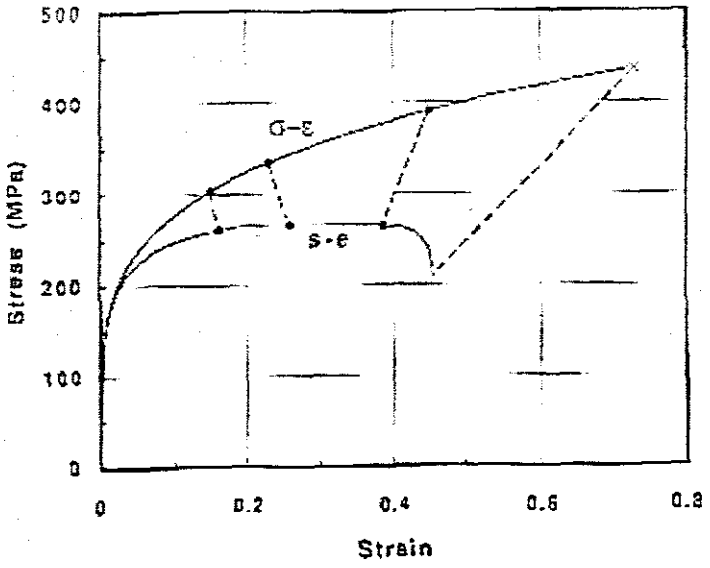

Figure 3.2. Depicting the difference between true and engineering stress and strain (from Tensile Testing 2nd Edition, 1993.)

3.6 Bridgman Correction

When the neck becomes sharp, the stress state at the center of the neck is no longer uni-axial tension. As the material is stretched in the axial direction, it is subjected to contraction in the lateral directions. This contraction is resisted by the adjacent regions, which have larger cross-sections than at the neck, and are therefore no longer deforming. This scenario gives rise to tri-axial tension in the central region, with lateral stresses as well as axial tension, as is indicated in figure 4, below. It has previously been established [4] that only the portion of the axial stress that exceeds the lateral stress, contributes to plastic flow. The Bridgman formula, given below, takes into account this phenomena to determine the corrected true stress from the measured true stress.

$$\bar{\sigma}/\sigma_z(av) = \left\{(1+2R/a)\ln[1+a/2R]\right\}^{-1} \qquad (3.9)$$

where a=(D/2), the radius of the specimen at the base of the neck
R is the radius of curvature of the neck

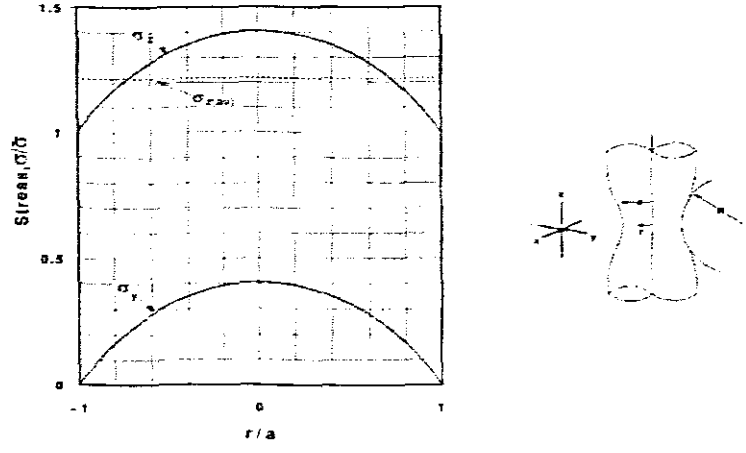

Figure 3.3. Depicting the stress distribution across the neck of a tensile test specimen (from Tensile Testing 2nd Edition, 1993.)

3.7 Temperature Rise

A tensile test specimen can undergo an appreciable increase in temperature during testing, since the mechanical energy provided by the tensile testing machine is dissipated as heat energy. The temperature rise is proportional to the amount of energy provided, and to the amount of heat retained by the specimen. It follows, that if the test were carried out rapidly, the increase in temperature of the specimen would be large, since there would be very little time for the heat energy to dissipate. Since the temperature rise can have a significant impact on the properties being measured, it is advisable to carry out the test at as slow a rate as possible.

3.8 Sheet Anisotropy

Variation in the stress versus strain curve can often be attributed to the fact that the specimens were cut from materials at different orientations to the prior rolling direction. The parameter commonly used to characterize sheet anisotropy of a metal bar is the strain ratio, or R-value, which is defined as the ratio of the contractile strains measured in a tensile test before necking occurs, and is given by the following expression:

$$R = \varepsilon_w / \varepsilon_t \tag{3.10}$$

where ε_w is the width strain given by $\ln(w/w_0)$
ε_t is the thickness strain given by $\ln(t/t_0)$

The value of R would be equal to 1 for an isotropic material although values greater or less than 1 is also common.

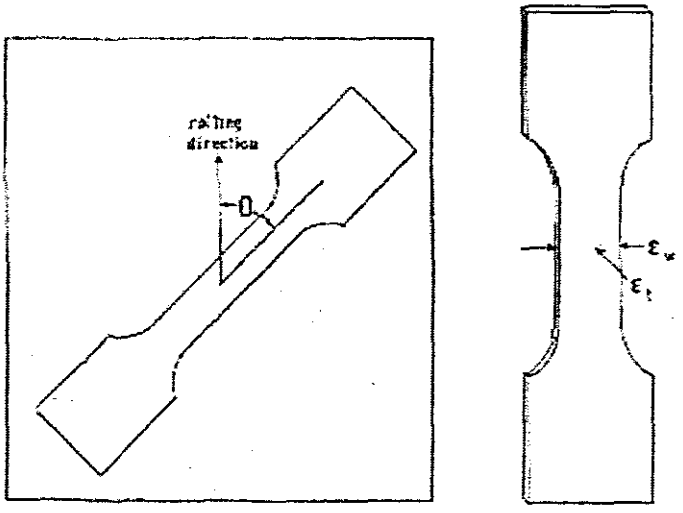

Figure 3.4. Depicting the effect of prior rolling direction on material properties (from Tensile Testing)

CHAPTER 4 – HEAT TREATMENT OF STEEL.

4.1 Introduction

Heat Treatment, covers a host of procedures of controlled heating and cooling, used by engineers and metallurgists to alter the microstructure of a material, thereby giving it properties capable of withstanding the conditions it will be subjected to during its service life. The heat treatment process that will be discussed in detail is quenching, in particular, the Jominy End Quench. The quenching process may be summarized by the following schematic equation:

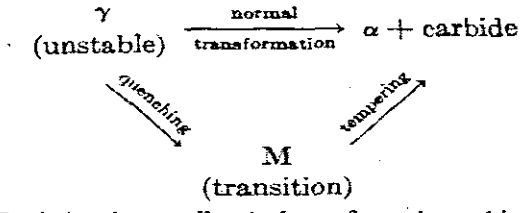

Figure 4.1. Depicting the metallurgical transformations taking place in steel

The equation may be explained as follows:

- Heating the steel to above A_{C1} ($\approx 720^0$C) results in the formation of unstable austenite.
- If the steel is allowed to cool to ambient temperature slowly, the austenite transforms to pearlite, (combination of ferrite and cementite).
- If the steel is subjected to rapid cooling, such as a brine quench, the austenite does not have time to transform to ferrite and cementite, and remains locked in the carbon saturated transition phase termed martensite.
- Subsequent reheating of the steel to a temperature below the transformation temperature will result in the excess carbon diffusing out, again resulting in the pearlite microstructure.

The quenching process will now be analysed in more detail.

4.2 Quench Hardening

If the steel that is heated to a temperature above A_{C1} (723^0C) is suddenly subjected to rapid cooling, such as would be obtained in a quench bath, the rapidity at which the heat is absorbed by the cooling medium in the bath will determine the hardness of the steel. The hardness obtainable in a particular quench bath depends on the following variables[13], namely:

4.2.1 the composition of the quench

4.2.2 the temperature of the quench

4.2.3 the volume of the quench bath (physical size)

There are numerous quench mediums, each having there particular application, namely, quench salts, oils and water. Quench salts are composed primarily of nitrite/nitrate salts.

They are completely water-soluble and provide high heat transfer rates and specific heat capacity. Table 4.1, below, gives an indication of the various commercially available quench salts and there application.

PRODUCT IDENTITY	MELTING POINT	WORKING RANGE
GROUP I		
Low Temperature Draw Salt	275 deg F (135 deg C)	300-1100 deg F (149-593 deg C)
Thermo-Quench	288 deg F (142 deg C)	300-1100 deg F (149-593 deg C)
Marquench	305 deg F (152 deg C)	350-1100 deg F (177-593 deg C)
Aus-Quench	354 deg F (179 deg C)	375-1100 deg F (191-593 deg C)
High Temp Draw Salt	430 deg F (221 deg C)	480-1100 deg F (249-593 deg C)
AL-2	500 deg F (260 deg C)	550-1100 deg F (288-593 deg C)
GROUP II		
Econo-Temp 300	300-325 deg F (150-163 deg C)	375-1100 deg F (191-593 deg C)
GROUP III		
#800	850 deg F (454 deg C)	925-1250 deg F(496-677 deg C)
#900	920 deg F(493 deg C)	1000-1300 deg F (538-704 deg C)
Uni-Hard® NF	1020 deg F(549 deg C)	1100-1700 deg F (593-927 deg C)
Cartecsal	810 deg F(432 deg C)	850-1750 deg F (454-954 deg C)
Wire Annealing	1050 deg F(565 deg C)	850-1750 deg F (454-954 deg C)

Table 4.1. Depicting various quench solutions and their operating characteristics (from Machinery's Handbook, 23rd Revised Edition, 1989.)

A greater degree of hardness is obtainable by quenching in salt or brine than in water or oil. It has been established [11], that the higher the temperature of the quench medium, the lower the hardness obtainable, due to the reduction in heat transfer rate between the specimen and the quenchant. The bath should be large enough to dissipate heat rapidly, whilst the temperature is maintained by regulating the flow rate, thus ensuring that successive specimens are quenched at the same rate.

4.3 Quenching Baths

As was stated earlier, the main aim for ensuring uniform temperature in the bath is for the purpose of repeatability of results. Subjecting the bath to agitation by passing air through an oil bath will ensure uniform temperature distribution through the oil, resulting in a higher heat transfer rate. Indicated below, is the quenching arrangement used by myself to perform either water, brine or oil quenching.

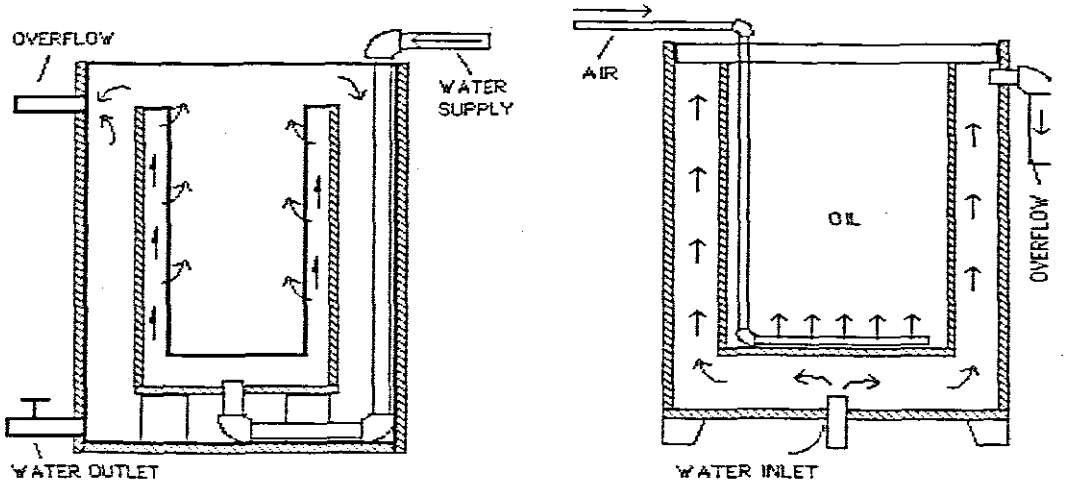

Figure 4.2. Depicting the quench tank used in experiments (from Machinery's Handbook, 23rd Revised Edition, 1998.)

Detail drawings of the design may be found as Appendix D.

4.4 The Jominy End-Quench Test

This is a standardised test used to determine the hardenability of steel. It has been primarily applied to round bar, due to uniformity of aspect ratio. The procedure, will however, be applied to flat bar, by myself, which apart from differences in geometry, is manufactured by an entirely different process, namely, rolling as opposed to extruding. The test is performed by subjecting the one end of the specimen to a quenching medium after it has been heated to the A_{C3} temperature. The end immersed in the quenchant will experience the most rapid cooling and will therefore have the hardest microstructure, namely, martensite. The further one moves from the quenched end, the less severe the heat transfer resulting in a softer microstructure. By embedding thermocouples in the specimen at various positions along its length, it possible to plot curves depicting the various cooling rates. The different microstructures and hardness's may then be superimposed on these continuous cooling transformation (CCT.) curves as is depicted in figure 4.3. Additional information, such as the grain size may also be added. Using the statistical formulae introduced in chapter 7, the mechanical properties of a tensile test piece will be approximated before performing the actual tensile test, and the results compared for conformance and accuracy.

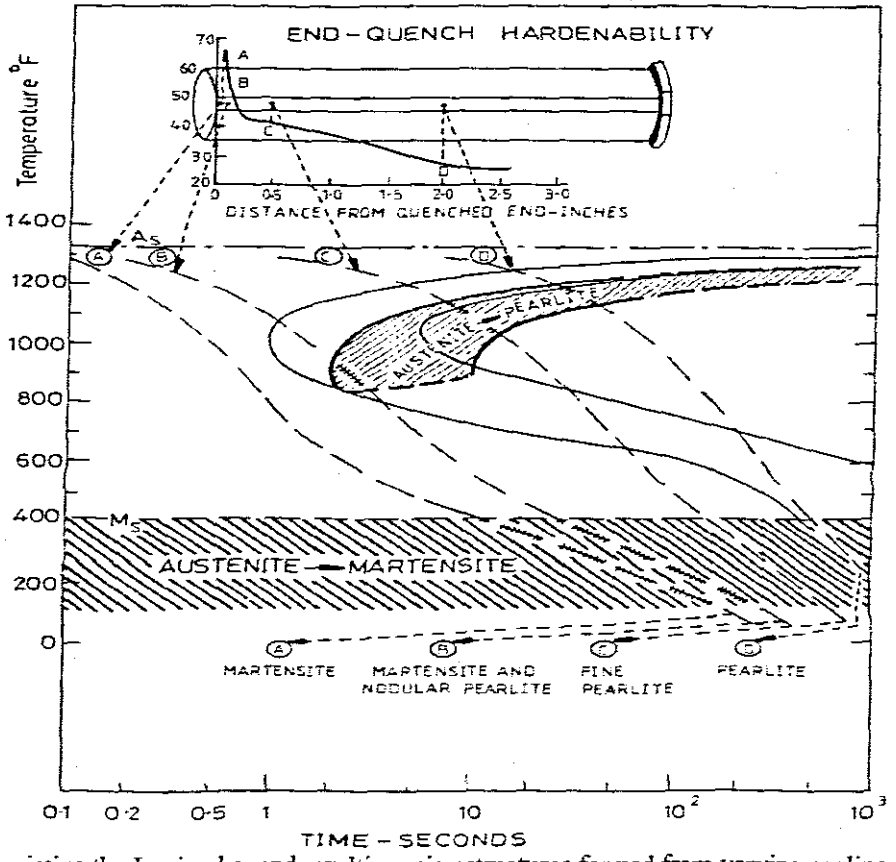

Figure 4.3. Depicting the Jominy bar and resulting microstructures formed from varying cooling regimes (from Phase Transformations in Metals and Alloys, 1992.)

End quench hardenability curves for various steels are extremely useful, since provided the cooling rate is known, the hardness may be directly read from the curve.

4.5 The Effects of Alloying Elements on Hardenability

The primary purpose for the addition of alloying elements is to increase the hardenability by delaying the time required for the decomposition from austenite into ferrite and pearlite [11]. This results in slower cooling rates, allowing for the production of fully martensitic steels. Alloying elements reduce the rate of austenite decomposition, by either reducing the growth or nucleation rate of ferrite, pearlite or bainite. The rate of pearlite formation at the nose of the C-curve in the Time Temperature Transformation (T.T.T.) diagram is the main factor limiting hardenability.

4.6 Quenched in Vacancies

The amount of vacancies present in steel increases exponentially with temperature [11]. This would imply that the amount of vacancies present in the steel when it is austenised would be high. Subjecting the steel to rapid cooling from this temperature would provide insufficient time for the vacancies to diffuse out, until a new equilibrium condition is reached, resulting in quenched in vacancies. With the elapse of time, some of the vacancies in excess of the equilibrium concentration will anneal out. Others will cluster together forming dislocation loops, which may increase in size by absorbing other vacancies.

Another method in which existing vacancies absorb others is by climbing, resulting in the formation of helical edge dislocations. Quenched vacancies also have the tendency to increase the rate at which atoms diffuse at the ageing temperature, thereby speeding up the nucleation and growth process. The approximate diffusion time is given approximately by the following equation [11]:

$$t \approx \frac{x^2}{4D} \qquad (4.1)$$

where: λ is the distance between two particular zones.
D is the diffusion coefficient

It has also been established, [5] that a specimen that was subjected to a more severe quench rate and then allowed to age at the same temperature as other differently quenched specimens, will have the highest initial level of Guinier Preston (GP) zone formation. The GP zones are tiny clusters of atoms that break away from the matrix in the early stages of the age hardening process. If the quench were to be interrupted at an intermediate temperature, a new equilibrium concentration will be established, resulting in a reduced rate of transformation. This is the procedure employed when generating T.T.T. diagrams. A reduction in the quench rate therefore provides more time for vacancies to diffuse out of the material. This factor plays a very important role when quenching large structures, since the cooling rate will vary considerably from the surface of the material to its center.

Vacancies have a tendency to diffuse into grain boundaries and dislocations, thereby influencing the distribution of precipitates. It was found [5] that the vacancy concentration

close to a boundary will be the equilibrium condition for the ageing temperature, whilst further away, it will be that for the quenching solution, as is depicted in figure 4.4, below.

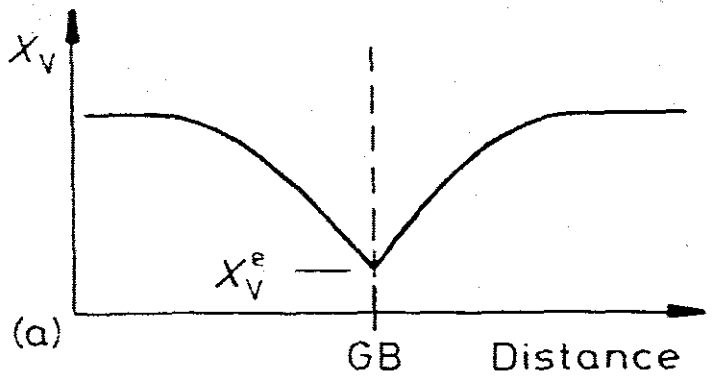

Figure 4.4. Depicting the vacancy concentration profile around the grain boundary (GB). (from Phase Transformations in Metals and Alloys, 1992.)

CHAPTER 5 – ULTRASONIC STRESS MEASUREMENT.

5.1 Introduction

Ultrasonic stress measurements are based on the acousto-elastic effect, which states that the ultrasonic wave velocity generated is dependent on the stress present in the material. This dependence of wave velocity on stress is given by the nonlinear theory of elasticity, which takes into account the fact that "real" material acts differently under elastic strain than is predicted by Hooke's linear theory. The velocity of small amplitude elastic waves propagating in a structure is dependent on the stress in the structure. This elastic wave velocity is related to stress by elastic constants of the second and third order. Therefore for an isotropic medium, the function that relates longitudinal and shear waves propagating parallel or perpendicular to the stress is given by [14]:

$$V^2_{111} = (V^0_{111})^2 - \frac{\sigma}{3\rho_0 K_0}\left[\frac{\lambda+\mu}{\mu}(4\lambda+10\mu+4m)+\lambda+2l\right] \qquad (5.1)$$

where:
V is the ultrasonic velocity in the stressed material
V^0 is the ultrasonic velocity in the unstressed material
σ is the uni-axial stress
ρ_0 and K_0 are the mass density and bulk modulus for zero stress
μ and λ are the Lame' constants (second order elastic constants)
m, l, n, are third order elastic constants

Consecutive indices (i, j, k = 1, 2, 3) represent the directions of the wave propagation, polarization and stress respectively. The stress value in a material, however, is not the only factor influencing the wave velocity. A sound wave propagating through a material may lose some of its energy due to scattering. This effect could be related to grain size, grain orientation in relation to that of the wave, and the anisotropy of the material under test. This loss of energy is termed attenuation and occurs along the entire travel path of the wave [14]. Another factor, which influences the ultrasonic wave velocity, is temperature. The higher the temperature of the body and its surroundings, the smaller the wave velocity. It has been established [15] that a temperature change of just 1^0C in the body may result in an increase in stress measurement of 10Mpa.

5.2 The Debro-30

The Debro-30 is a device that uses the principle of the acousto-elastic effect and the generation of ultrasonic waves to measure stress values in a material. The device consists of a cathode-ray oscilloscope and interchangeable probe-heads, which may be used for various applications. The oscilloscope is used to navigate the menus of the device as well as for the visualization of received ultrasonic pulses accepted by the receiving transducers.

5.3 The Probe-heads

As stated earlier, the device is supplied with numerous interchangeable probe-heads, namely:

- the 12LSV probe-head for the generation of subsurface longitudinal and shear (SV) waves;
- the 6L150 probe-head for the generation of subsurface longitudinal waves;
- the 6SH150 probe-head for the generation of subsurface shear (SH) waves, and
- the 1T probe-head for the generation of shear (SH) waves in mutually perpendicular planes

5.3.1 The 1T Probe-head

The 1T probe-head was chosen to determine the residual stress levels in the post-welded plates. This probe-head, consisting of one transducer capable of swiveling through 90^0, measures acoustic birefringence in steel plates. This rotation enables the probe to generate shear (SH) waves in two mutually perpendicular directions. The recording of two vastly different mutually perpendicular stress readings for the same plate could point to sheet anisotropy. The probe-head is also equipped with a temperature sensor for displaying the temperature of the specimen under test.

Acoustic birefringence, also termed acoustic anisotropy, is proportional to the difference in shear wave velocities polarised in two perpendicular directions. The polarized waves must coincide with the acoustical axis of the sample as well as with the principle stress planes. Acoustic birefringence is both stress and texture induced anisotropy dependent, and is calculated from the following expression:

$$B = B_S + B_T = 2 \times \frac{(T_1 - T_2)}{(T_1 + T_2)} \qquad (5.2)$$

where: B is the total anisotropy of the material
B_S is the stress-induced anisotropy
B_T is the texture-induced anisotropy
T_1 is the time of flight for the shear wave polarised in direction 1
T_2 is the time of flight for the shear wave polarised in direction 2

5.4 Stress Calculations

Prior to evaluating the stress, it is necessary to eliminate the influence of the texture induced (zero stress) anisotropy. This is accomplished by first measuring the acoustic birefringence on a stress free sample. Texture induced anisotropy is expressed as [15]:

$$B_0 = 2 \times \frac{(T_1^0 - T_2^0)}{[(T_1^0 + T_2^0) \times \beta_B]} \qquad (5.3)$$

where: B_0 is the stress-induced anisotropy
T_1^0 and T_2^0 are the times of flight in nanoseconds [ns] measured on a zero stress sample for polarisation directions 1 and 2 respectively.

β_B is the acousto-elastic constant for acoustic birefringence in [Mpa^{-1}]

The value of the stress only, can now be calculated from the following expression:

$$\sigma = 2 \times \frac{(T_1^0 - T_2^0)}{[(T_1^0 + T_2^0) \times (\beta_B - B_0)]} \qquad (5.4)$$

where: B_0 is the texture-induced anisotropy
β_B is the acousto elastic constant for acoustic birefringence in [Mpa^{-1}]

In the expressions mentioned previously, it is assumed that the acoustic axis and the sample geometrical axis coincide and are parallel to the polarization directions. If, however, this is not the case, reliable stress measurements are not possible.

5.5 Measuring Cycle of the 1T probe-head

The 1T probe-head utilizes a cycle of four steps to compute the value of the residual stress in a material. The correct constants have to be entered prior to commencing a measuring cycle. Times of flight for polarisation directions 1 and 2 can be measured for different bottom echoes. The chosen echoes, however, depend on the sample geometry and attenuation. In a sample having a small cross-sectional area, reflection from the samples edges may interfere with back wall reflections. To counter this, it is advisable to decrease the number of echoes. Four expected arrival times may be calculated when choosing bottom echoes **n** and **m**, where **n** is always the greater of the two values. The times of flight for the different echoes may be computed from the following expression:

(for ranges 1 and 3)

$$T_F = \frac{(2ng)}{V_T} \qquad (5.5)$$

(for ranges 2 and 4)

$$T_C = \frac{(2mg)}{V_T} \qquad (5.6)$$

where: T_F is the time for echo number **n**
T_C is the time for echo number **m**
V_T is the velocity of the shear wave

Materials having a very high value of anisotropy will show marked differences in the times of flight in polarisation directions 1 and 2. Should this be the case, the polarisation directions may be programmed for various times of flight. After selecting the number of echoes and determining the time of flight from the above expressions, the computed values should be entered and stored in the memory of the device. Figure 5.1 below shows the values of the calculated constants being displayed by the Debro-30.

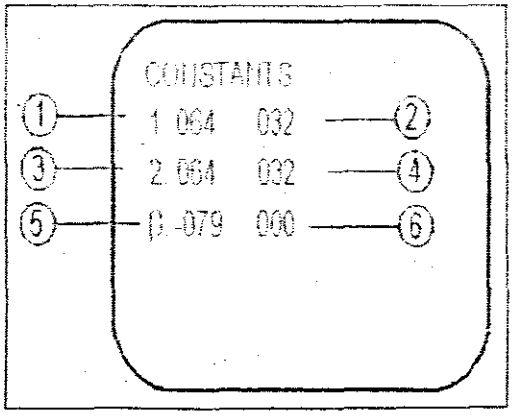

1. *Time of flight for further echo, for polarization in the direction 1[μs]*
2. *Time of flight for closer echo, for polarization in the direction 2 [μs].*
3. *Time of flight for further echo, for polarization in the direction 2[μs].*
4. *Time of flight for closer echo, for polarization in the direction 2[μs].*
5. *Acoustoelastic constant for birefringence measurement β_R [-10^{-7} Mpa^{-1}]*
6. *Texture induced (zero stress) anisotropy.*

Figure 5.1. Depicting constant setting menu on the Debro-30 (from Debro-30 Technical Manual)

Figure 5.2 depicts the display during the measuring cycle. The important aspect here is the positioning of the V-marker. The marker has to be positioned onto the first amplitude such that it cancels it out by adjusting both arms until they are at the same level.

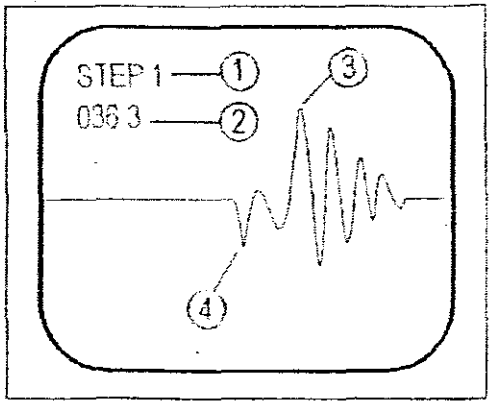

1. *Number of consecutive measuring steps.*
2. *Approximate time between transmitting pulse and marker [ns].*
3. *Ultrasonic pulse of longitudinal subsurface wave detected by first receiver.*
4. *V-Shape marker*

Figure 5.2. Depicting the screen during a measuring cycle

Figure 5.3 depicts the stress results at the end of the measuring cycle.

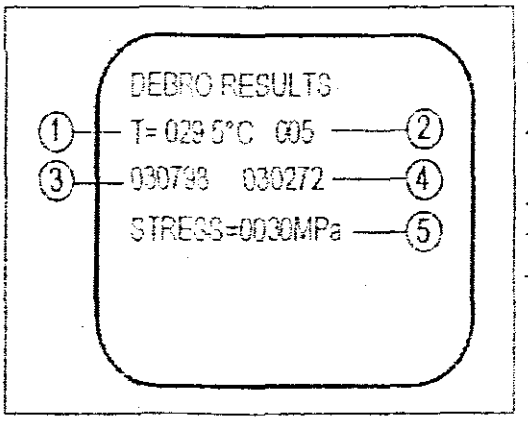

1. *Temperature of the object during measuring cycles.*
2. *Number of results stored in memory (if BUFFER is switched on).*
3. *Time of flight for longitudinal polarization.*
4. *Time of flight for perpendicular polarization.*
5. *Stress Value*

Figure 5.3. Depicting the stress results produced by the Debro-30

The measuring cycle of the 1T probe-head is comprised of four steps, with the probe-head set in direction 1, prior to commencement of the measuring cycle. The probe-head is then rotated through 90^0 between steps 2 and 3 of the measuring cycle. This rotation changes the

polarisation of the ultrasonic pulse from stress direction 1 to stress direction 2. The probe-head should be returned to direction 1 prior to the commencement a new cycle [15].

5.6 The Transducer of the 1T probe-head

The probe-head utilizes one transducer for the generation and receival of ultrasonic wave pulses. It is made from ceramic material named Lead Zirconate Titanate (PZT) and vibrates at a frequency of 4MHz in shear (see figure). A damping material of epoxy and quartz forms the backing for the transducer. The 1T probe-head does not have a protective cover, which implies that it comes into direct cover with the coupling media.

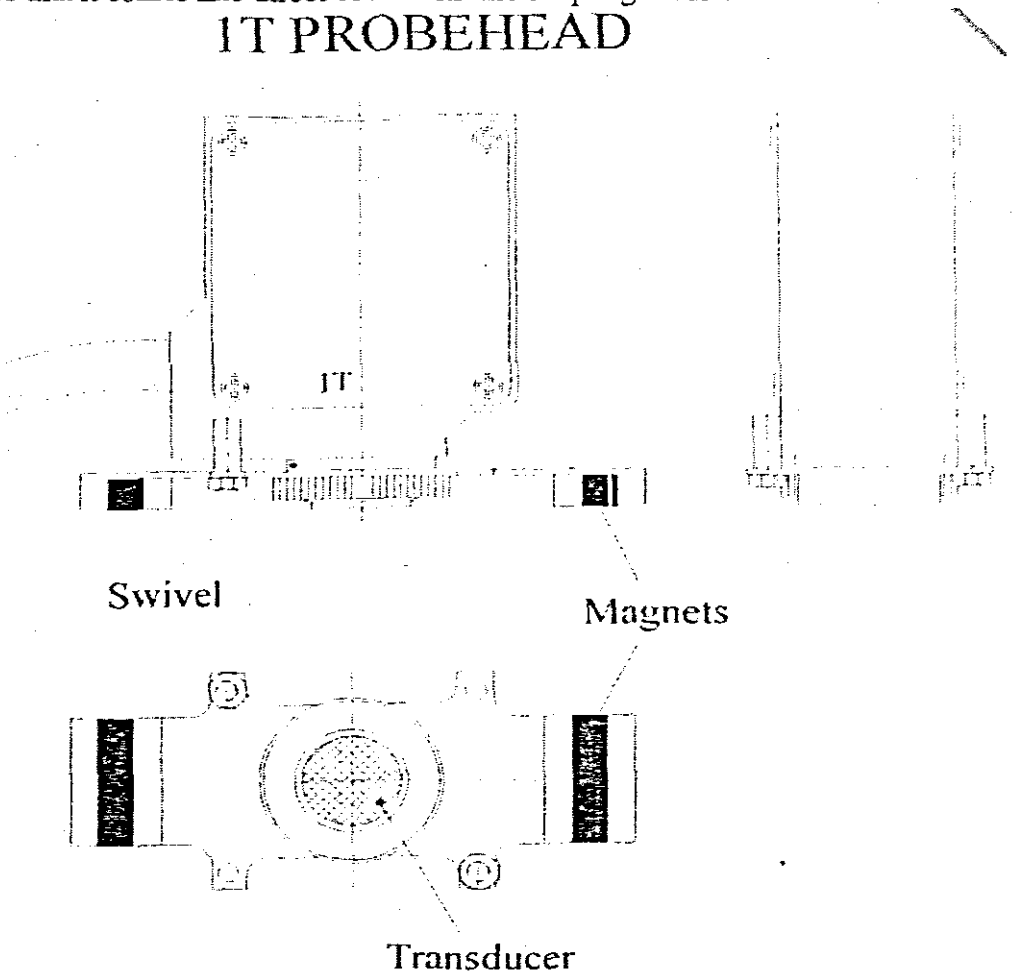

Figure 5.4. Depicting the T1 probe

5.7 Coupling Media

The surface contour and texture of the material to be tested by the ultrasonic stress measuring device are of extreme importance to the accuracy of the results since they may influence the times of flight. It is therefore necessary to prepare the surface of the sample to facilitate proper contact with the probe-head. A coupling media assures a constant coupling between the probe-head and the specimen under test. Failure to use a couplant might result in the deflection of the ultrasonic pulses between the boundaries of the two media.

CHAPTER 6 – METALLOGRAPHIC SPECIMEN PREPARATION.

6.1 Introduction

There are numerous methods for preparing metallographic specimens for macroscopic and microscopic examination. This can largely be attributed to the large diversity of materials, leading to the need to experiment to obtain the best preparation procedure. With this in mind, it would be safe to say that there is no universal technique for metallographic specimen preparation. The subsequent sections will outline the procedures to follow to ensure satisfactory specimen preparation, failure of which will result in erroneous interpretation and results.

6.2 Specimen Sectioning

Specimen preparation always involves the selection and separation from the bulk of a piece of material. This step is of special importance, since the sample must be representative of the feature to be analyzed. If mechanical cutting is to be used to prepare the sample, care should be taken to impart as little heat to the body as possible, thereby eliminating any subsequent material property changes. A means of countering this effect is to use large amounts of coolant during the cutting process. The main aim of this procedure is to immediately produce a surface suitable for fine grinding without spending undue time on correcting damage inflicted on the surface during the cutting process, since the longer the specimen preparation procedure, the more costly the sample. The method that has proven to be most economical is abrasive cutting [9]. A thin rapidly rotating consumable wheel, as is indicated in figure below, is used to produce high quality, low distortion cuts, in times ranging from 15 seconds to several minutes.

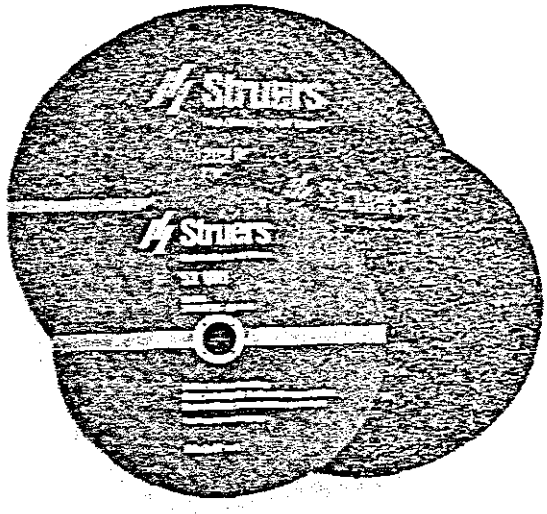

Figure 6.1. Depicting various cut-off disks (from Struers consumable catalogue)

Parameters of importance in abrasive cutting are wheel composition, coolant condition, and technique applied. Abrasive wheels are made of alumina or silicon carbide grains bonded together by a resin [9]. By varying the manufacturing process, either 'soft', or low wear resistance, or 'hard', high wear resistance wheels may be produced. The low wear resistance type wheels are typically used for cutting hard materials, whereas the high wear resistance wheels are used to cut soft materials.

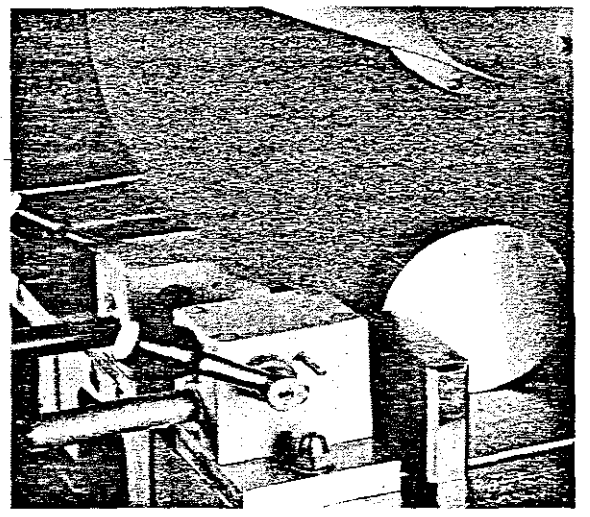

Figure 6.2. Depicting the first stage in specimen preparation, namely, the cutting of the specimen from the bulk. (from Struers Product Manual.)

6.3 Specimen Mounting

When working with irregularly shaped specimens, mounting in a resin facilitates ease of handling. This becomes extremely important when good sample edge retention is a prerequisite. Embedding is extremely useful, since multiple samples may be ground and polished at the same time. Figure 6.3 below depicts some previously mounted samples.

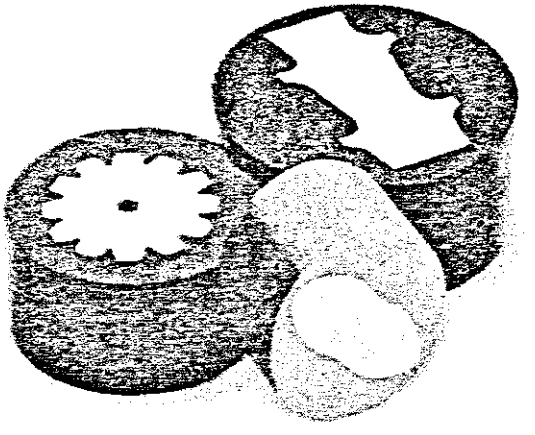

Figure 6.3. Depicting various mounted specimens

6.3.1 Plastic Embedding

Currently, this is the most popular method of mounting metallographic specimens. There are two types of embedding, namely, hot and cold mounting. The first type only will be dealt with, since this is the method currently in use in the welding laboratory. Hot mounting usually accomplished by the following reaction, namely:

$$Hot: \quad \text{Resin} + \text{Pressure} + Heat = Polymer$$

The procedure requires a press exerting a pressure in the region of 29Mpa on a specimen mould heated to approximately 150^0C. Under these conditions, the powdered resin fuses into a solid mass around the specimen. Thermosetting resins, such as phenolics, cure and harden irreversibly, whilst thermoplastics can be remelted again.

The granulated thermosetting plastic must satisfy the following criteria to ensure satisfactory mounting, namely [9]:

6.3.1.1 they must not react with the sample material, etchant, mould or any other reagent used during the preparation of the specimen

6.3.1.2 they should have moderate viscosity in the liquid state and be free from bubbles when solidified

6.3.1.3 they should have low linear shrinkage to ensure that the sample will remain bonded with the resin

6.3.1.4 they should have good adhesion properties

6.3.1.5 they should have a wear resistance and hardness similar to those of the specimen

Adding abrasive filler such as alumina may increase the hardness and wear resistance of thermosetting plastics.

6.4 Sample Identification

Since specimens are useful only if there origin is known, it stands to reason that they should be clearly marked so that there identity is not lost at any time during the preparation sequence. It is however, of paramount importance, that the marking operation does not cause any blemish to the surface of the specimen. Identification markings should be placed on the surface opposite the critical face to avoid damage to the specimen.

6.5 Grinding and Polishing

The process of producing a satisfactory polished metallurgical specimen involves in sequential order, coarse and fine grinding, followed by polishing. This process serves to smooth the sample surface, whilst at the same time removing surface material damaged during the cutting process to reveal the true specimen macro-structure. Coarse grinding is employed to remove severe surface damage until a flat surface is obtained. The surface texture of approximately 10 to 100μa at this stage is comparable to that obtained by a filing operation. The fine grinding process then increases the surface texture to 1μm, which is suitable for macroscopic examination and etching only.

6.5.1 Mechanical Grinding and Polishing

This procedure, which is very common, is usually accomplished by means of rotating wheels or continuous belts. Scratches, deformation and smearing are characteristic consequences of this process. The course grinding process is usually associated with surface deformation, whilst polishing produces smearing due to plastic flow. During the grinding process, large amounts of surface material are removed. At the end of this process, however, the surface still appears to be scratched. The polishing process is assumed to produce a flat scratch free surface. This is, however, not the case. What has occurred is the scratch troughs have been filled with polish and loose surface material, resulting in the smeared black layer indicated in figure 6.4 below.

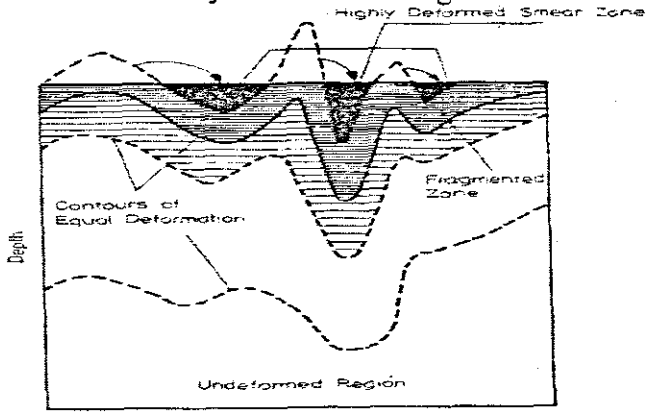

Figure 6.4. Depicting a cross-section through a specimen's surface. (from Metallographic Etching, 1978.)

The adjacent deeper layers contain material having decreasing severity of deformation. Since the most deformed areas have the greatest reaction to etching solutions, this would explain why scratches seem to reappear after etching. It has been established [9] that the depth of roughness (scratches), plus the depth of deformation equals the total depth of disturbed material. The depth of roughness has been found to be directly proportional to the particle size of the abrasive being used, whilst the depth of deformation approaches a constant value.

From this it can be concluded that the removal of all deformation is the key to successful optical measurements and microhardness testing. It can also be said that to limit the depth of deformed material, coarse grinding should be kept to a minimum, whilst more time is spent on the finer grinding and polishing stages, ensuring meticulous cleaning between all steps to prevent cross contamination of abrasive particles.

6.5.2 Factors influencing mechanical grinding and polishing

6.5.2.1 Grinding and Polishing compounds

Metallographic grinding and polishing is facilitated by the use of inorganic powders, some of which are listed in the table below.

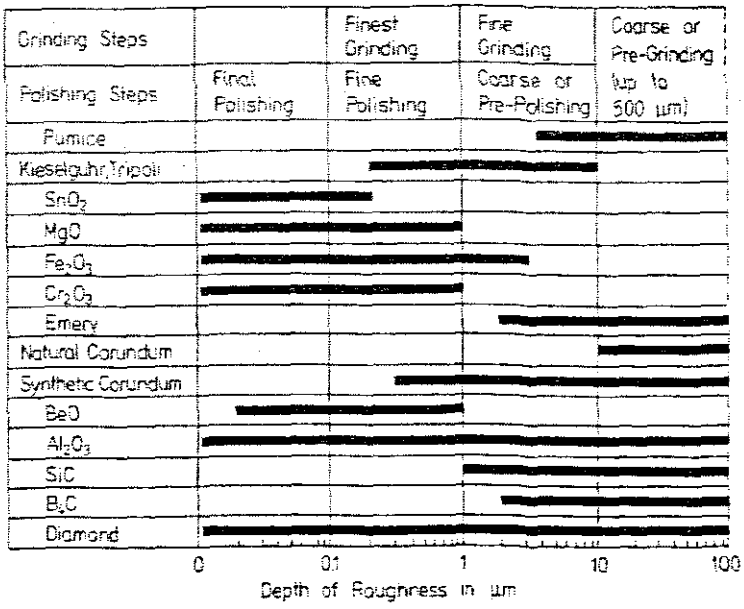

Table 6.1. Depicting various Grinding and Polishing Compounds. (from Metallographic Etching, 1978.)

6.5.2.2 Grinding and Polishing fluids

As a norm, all metallographic specimen preparation steps require a liquid coolant, the advantages of which are:

- the control of heat at the specimen abrasive
- the control of harmful dust generated during grinding/polishing
- the extension of the lifespan of fixed abrasives, since material removed continuously flushed away

6.5.2.3 Pressure, Time and Velocity

Although increased pressure, time and velocity of the abrasive disc will result in faster material removal, they may also result in other detrimental effects, such as:

- the excessive pressure may cause heating at the abrasive specimen interface, which may alter the microstructure of the specimen being prepared. The pressure should not be too high during the polishing stage.
- the use of cloth polishing with abrasives other than diamond should be as brief as possible, since severe surface deformation may result due to differing material removal rates for the individual microstructural constituents.

- it has been established [9], that the harder the material, the slower the grinding and polishing speeds

- since the higher grinding and polishing speeds will generate more heat, sensitive materials should be prepared at lower speeds to limit thermal effects.

6.5.2.4 Specimen Motion during grinding and polishing

Specimen motion is critical for edge retention. The best results are obtained when the specimen is held flat against the abrasive surface at all times. Most modern machines, such as the one depicted in figure 6.5, below, which is also available in the welding laboratory, have the built in feature of counter- rotation to the abrasive material.

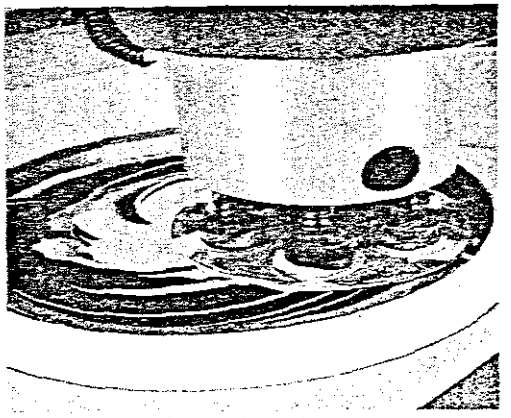

Figure 6.5. Depicting the polishing process

6.5.3 Grinding and polishing substrates

Here we are concerned with the material to which the abrasive is bonded, of which there are many different types, each having unique characteristics [9], namely:

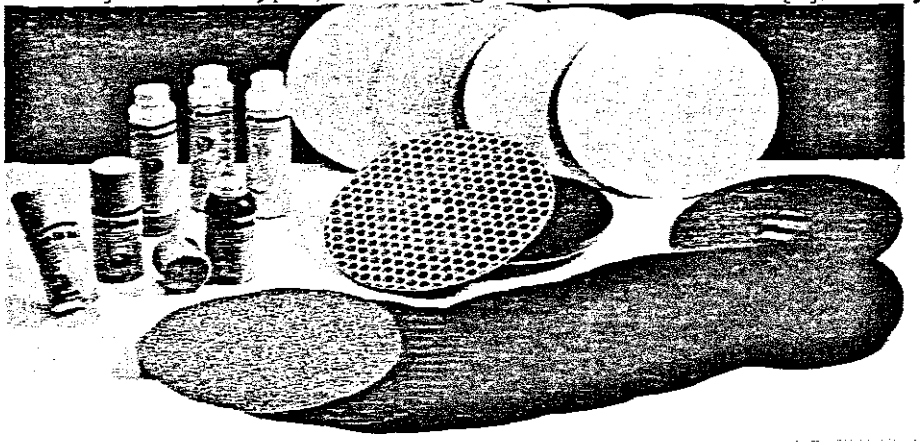

Figure 6.6. Depicting various grinding and polishing backing media and fluids. (from Struers Product Manual.)

6.5.3.1 hard and firm backing materials have the tendency to promote deeper surface deformation.

6.5.3.2 the more elastic backing materials produce less deformation, but have the negative effect of producing surface relief and edge rounding.

6.6 Cleaning

The success or failure of producing a satisfactory metallographic specimen may be decided by the cleaning operation, which should be meticulously carried out after every step, for reasons previously mentioned. Clean grease free surfaces are essential if etching is to be successful, since residues of fingerprints on a specimen surface will result in various areas being attacked at different rates. Rinsing is the most common form of cleaning. This is accomplished by holding the specimen under running water, whilst swabbing with a soft brush or cotton wool to remove any loose material. This is followed by rinsing the specimen in alcohol or benzene after which it may be placed in a hot box to ensure the vaporisation of all remaining liquid residing in pores and cracks.

6.7 Etching

The microstructure usually only becomes visible after etching due to the fact that a highly polished specimen will reflect incident light, the very principle on which most microscopes work.

6.7.1 Electrochemical (Chemical) Etching

During the etching of metallic specimens, reduction and oxidation reactions take place [9]. All metals in contact with the etchant become ionized by losing electrons. The rate at which the reaction proceeds is determined by the electrochemical potential of the constituent elements compared to that of a reference electrode, namely, hydrogen. Acids will attack all elements having a higher electro-affinity than hydrogen, whilst those having a lower affinity will be attacked by the addition of an oxidizing agent to the etchant. This results in the different microstructural constituents being attacked at differing rates, resulting in the contrast on the specimen surface, which can be observed by means of a microscope. This etching process produces subdivisions of very small anodic and cathodic regions termed crystals. Irregularities in the crystal structure at the grain boundaries are the main reason why these miniature cells are so distinct.

The time of etching could range from several seconds to hours, depending on the sample material and the contrast required. The application of an etchant usually results in the dulling of the specimen surface after which it is rinsed in water to prevent any further chemical activity. The application of an alcohol to the specimen surface helps to prevent the formation of water spots after which the specimen is placed in a stream of hot air to complete the drying process.

6.8 Specimen Storage

If specimens are to be kept for extended periods of time, precautionary steps should be taken to protect them from atmospheric corrosion. This can be accomplished by the use of one of the following:

- storage in a dessication cabinet
- the application of a plastic coating

- the application of cellophane tape

6.9 Microscopy

Microscopy is defined as the use of a microscope. Here, we are concerned with the identification of metallurgical phases and flaws, present on the underlying specimens surface. It is the norm to start at the lowest magnification and move to the highest magnification possible on the microscope. The addition of a digital camera, further enhances the capability of the microscope, since the image may then be fed, via a frame grabber, to a computer monitor. This also aids in the storage and retrieval and printing of images, since they may be stored on the hard drive of the computer.

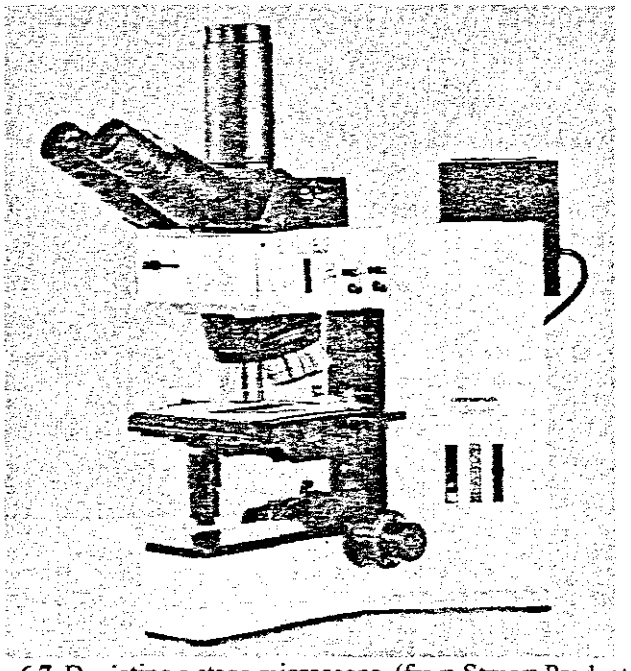

Figure 6.7. Depicting a stage microscope. (from Struers Product Manual.)

The computer in the welding laboratory is equipped with a frame grabber from Soft Imaging Systems, which together with the Sony digital camera has greatly increased the capabilities of the Olympus microscope.

CHAPTER 7 – MICROSTRUCTURE.

7.1 Introduction

All materials are comprised of atoms arranged in a sometimes-complex lattice structure. Steel, irrespective of the grade, is comprised primarily of carbon and iron. The steel may also contain, in varying proportions, additional alloying constituents, such as manganese, nickel, chromium, etc each making a unique contribution to the final properties of the steel. However, since the major constituents are always carbon and iron, they have the greatest influence on the way in which the lattice structure changes when the alloy is either heated or cooled. At room temperature, iron has a body centred cubic (bcc.) lattice structure capable of dissolving only a small percentage of carbon [5]. As the iron is heated to a temperature beyond 910^0C, it undergoes a phase change from a bcc. to that of a face centred cubic (fcc.) structure capable of dissolving appreciably more carbon. If the steel were to be cooled gradually, the carbon will again diffuse out of the fcc. lattice structure until the final lattice structure is that of bcc. Subjecting the steel to more rapid cooling rates, however, greatly reduces the time for the carbon to diffuse out, resulting in it being trapped in solution. The product formed is not in equilibrium, and has significantly different properties of hardness, ductility and strength, which can be used advantageously by engineers. The phase transformations and differing microstructures, will now be analyzed in more detail.

7.2 The Iron-Carbon Diagram

The Fe-Fe_3C phase diagram provides the basis for understanding the treatment and properties of steels. The dividing point between steels and cast-irons is 2.11%C, where the eutectic reaction becomes possible, as is indicated in the figure below. The eutectoid may be defined as a solid state reaction in which one solid phase transforms to two other solid phases. Steels can also again be subdivided into hypoeutectoid and hypereutectoid. The difference between the two again being the carbon content, with the former applying to all steels containing less than 0.77%C, and the latter to all steels containing more than 0.77%C. Iron goes through two allotropic transformations during heating or cooling. Immediately after solidification, iron forms a bcc structure termed δ-ferrite. On further cooling, the iron transforms to a fcc structure termed γ or austenite. Further cooling results in iron again transforming to the bcc structure termed α or ferrite. Both δ and α-ferrite and γ are solid solutions of interstitial carbon atoms in iron. Due to the differences in the lattice structure of bcc and fcc crystals, a greater number of carbon atoms can be accommodated in austenite. The maximum solubility of carbon in austenite is 2.11%C, whereas the value is 0.0218%C for α-ferrite and 0.09%C for δ-ferrite.

The stoichiometric compound Fe_3C, or cementite, is formed when the solubility of carbon in solid iron is exceeded. Stoichiometric compounds are compounds having a fixed composition. Cementite has a fixed ratio of three iron atoms to one carbon atom. Fe_3C contains 6.67%C, is extremely hard and brittle and is present in all commercial steels. In being able to control the amount size and shape of cementite, one is able to control the properties of the steel.

7.3 The Eutectoid Reaction

Heating a steel above the Ac_1 temperature of 727°C results in the formation of a structure containing only austenite grains. The cooling of the steel will result in the eutectoid reaction, which is given by the following expression:

$$\gamma_{x\%C} \rightarrow \alpha_{y\%C} + Fe_3C_{6.67\%C} \qquad (7.1)$$

During the eutectic reaction, the two phases that are formed have different compositions, which mean that atoms must diffuse between the phases whilst the reaction is in process. Most of the carbon in the austenite diffuses into the cementite, whilst the iron atoms diffuse into the ferrite.

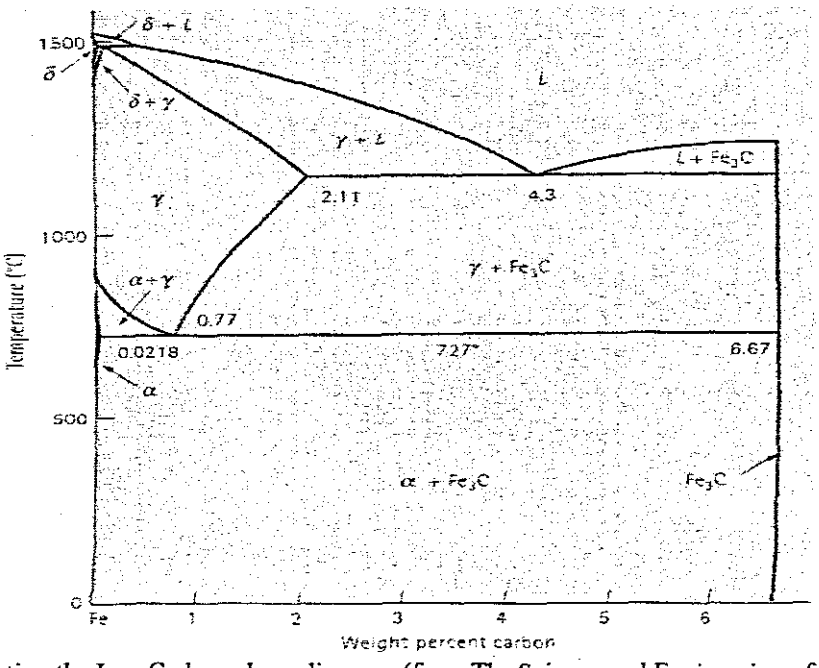

Figure 7.1. Depicting the Iron-Carbon phase diagram. (from The Science and Engineering of Materials, 1996.)

We are primarily concerned with weldable steels, i.e. those with a carbon content of less than 0.5%. At elevated temperature Austenite is formed having a Face Centered Cubic (FCC.) structure, which is capable of dissolving 2%C in its interstitial zones. Under equilibrium cooling conditions the austenite will transform to Pearlite and Ferrite, which has a Body Centered Cubic (BCC.) structure capable of dissolving 0.025%C in its interstices.

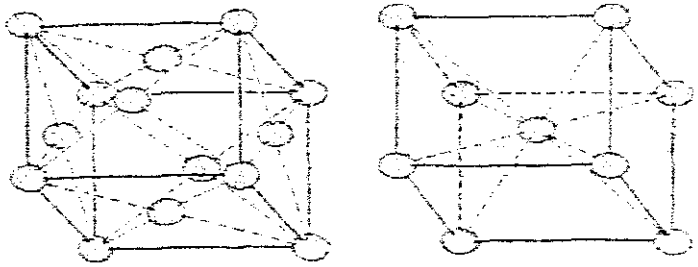

Figure 7.2 (a) and (b). Depicting a face centred cubic structure (left) and a body centred cubic structure (right) (from Elements of Material Science, 1970.)

Cementite, or iron-carbide (Fe_3C) is a hard brittle microstructure that is formed when the excess carbon in the austenite diffuses into the Pearlite. The Pearlite microstructure therefore is comprised of platelet lathes of ferrite and Cementite and has properties resembling both constituents.

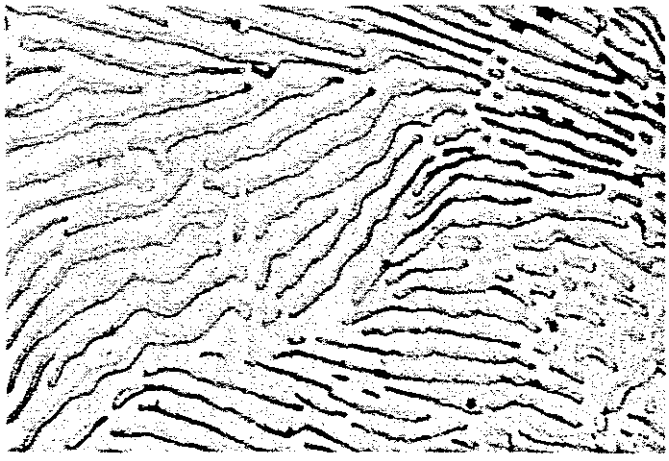

Figure 7.3. Depicting Pearlite microstructure (white strands). Cementite microstructure (black nodules) ×2500 (from Elements of Material Science, 1970.)

The transformation from austenite to pearlite requires a considerable time in which to take place, since the crystal structure has to change from fcc. to bcc. and the excess carbon in the austenite has to diffuse to the cementite plates. This time dependency of the transformation has resulted in the formation of a number of other metallurgical structures, depending on the chemical composition of the weld and parent metal and the cooling rate. When austenite is subjected to extremely slow cooling, the microstructure produced is fine pearlite, which has a fine grain size and is much harder than ordinary pearlite.

An increase in the cooling rate will result in the formation of a microstructure such as martensite, which is formed when the transformation from austenite to pearlite is completely suppressed. The surplus carbon in the austenite does not have sufficient time to diffuse out and remains trapped in a saturated solution having a body-centred tetragonal structure. The martensite microstructure is hard, brittle, highly stressed internally and has a needle like (acicular) appearance when viewed through a microscope.

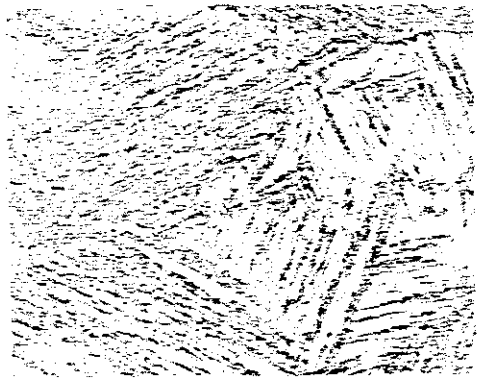

Figure 7.4. Depicting lathe type martensite, common in low carbon steel. (from Phase Transformations in Metals and Alloys, 1992.)

The bainite microstructure is formed in certain alloy steels if the cooling rate is fast enough to suppress the austenite-pearlite transformation, but the steel is not quenched to

below the martensite start (MS start) temperature of approximately 350^0C. The properties of bainite are intermediate between martensite and pearlite.

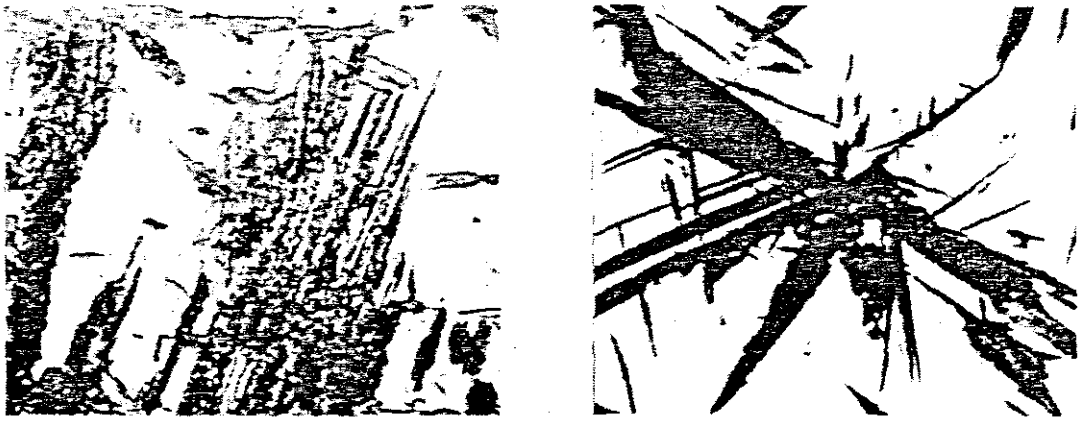

Figure 7.5. Depicting (a) Upper bainite (grey feathery plates) ×600. (b) Lower bainite (dark needles) ×400 (from The Science and Engineering of Materials, 1996.)

The microstructures depicted above are by no means the only ones that may occur in a particular alloy; in fact, there are atlases available that depict the various microstructures that may result in an alloy, when subjected to a welding process.

7.4 Time, Temperature, Transformation (TTT.) Curves

It was stated previously, that the phase transformations taking place in a steel are rate dependent. Similarly, microstructures formed in the heat affected zone (HAZ.) of a welded component are functions of time and temperature. A TTT. diagram, as is indicated in figure 7.6, below, indicates the time required for the transformation to various microstructures at constant temperature to take place. These diagrams therefore provide a useful guide to the transformations most likely to take place in the HAZ.

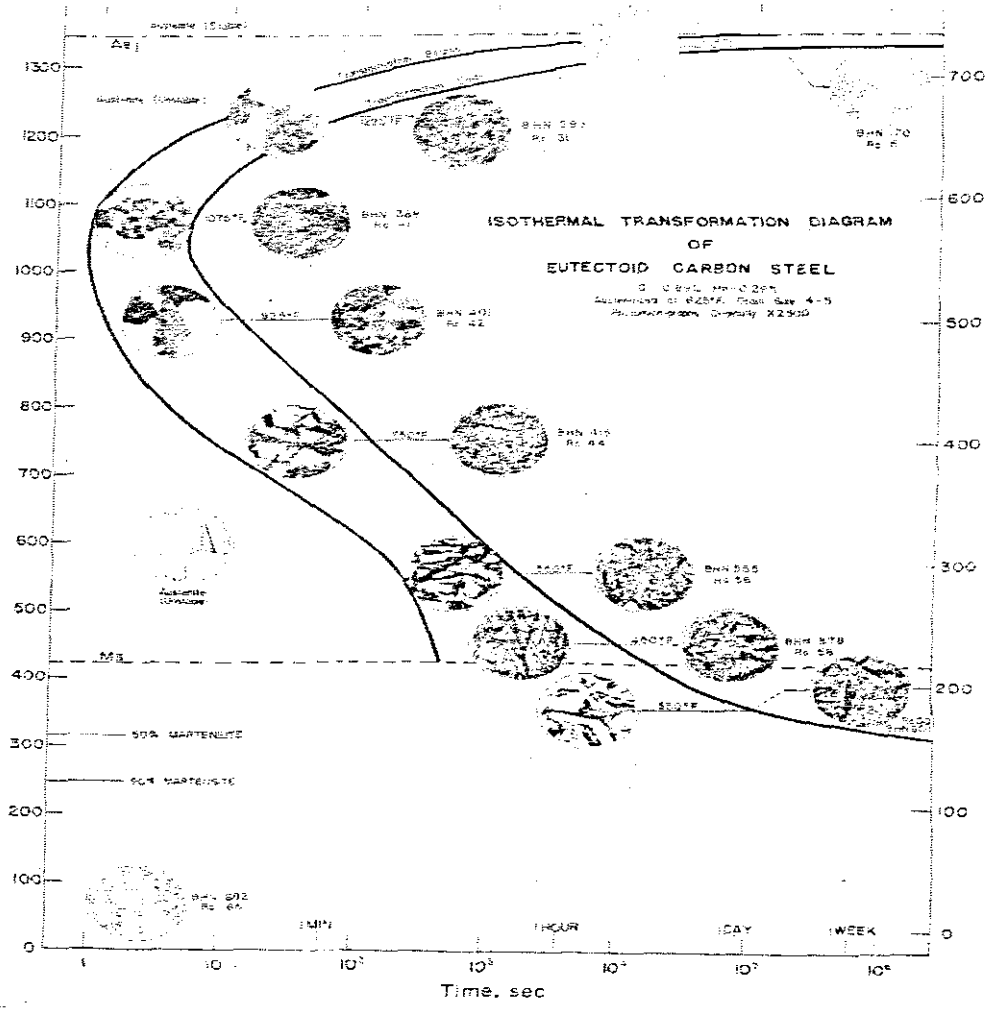

Figure 7.6. Depicting a TTT. curve for a 0.89% Carbon-Manganese steel (from Transformation in Metals, 1969.)

According to Gray et al [8], the following points of interest has arisen, with regards to TTT. diagrams, namely:

- The time for austenite transformation is shortest at the nose (knee) of the curve. If the cooling rate is fast enough to by-pass the nose, transformation takes place at a lower temperature, resulting in the formation of a harder microstructure.

- The final microstructure formed is a function of the transformation temperature.

- The shape of the curve and its position on the time axis depends on the carbon and alloy content of the steel. Carbon, manganese and nickel will produce a shift to the right on the time axis, whereas chromium and molybdenum alter the shape of the curve by shifting the

austenite-pearlite transformation more to the right on the time axis than the austenite-bainite transformation, resulting in a change in the shape of the curve.

- If the TTT. curve is right shifted, this could result in a situation where the transformation start curve is never reached, no matter how slow the cooling rate is, resulting in the formation of a hard brittle microstructure such as martensite.

These curves are generated by heating specimens, of similar geometric proportions, to a temperature well above the A_1 (720^0C), for a period long enough to dissolve all carbides present and homogenize the austenite. The samples are then transferred to either a salt or lead quench bath, having a temperature below the A_1, and held there for varying periods of time after which they are removed, and allowed to cool to ambient temperature. The specimens are then subjected to a metallurgical examination, to determine the time required for the decomposition to start and finish, at the temperature of the bath. The temperature of the furnace is decreased and the test repeated, until two curves indicating the start and finish of transformation at different temperatures are obtained. On their own, these curves are not very valuable to the welding engineer, but when combined with a Continuous Cooling Transformation (CCT.) diagram, it is possible to predict what the post-weld microstructure would be, and the necessary steps such as post-weld heat treatment and pre-heating may then be prescribed to remove an undesirable microstructure.

7.5 Continuous Cooling Transformation (CCT.) Diagrams

Since a welding process involves transient heat fluxes the TTT. diagram is not an accurate representation of this phenomenon. More relevant information can be gleaned from a CCT. diagram, in which phase changes are tracked for a number of cooling rates. These curves, as is depicted in the figure below, are obtained by subjecting specimens, of similar geometric proportions, to varying cooling rates, such as would be obtained by quenching in water, brine and oil, and plotting a temperature profile. The microstructure and associated hardness produced may also be plotted on the curve. The generation of CCT. diagrams will be discussed in more detail in the chapter on Quenching.

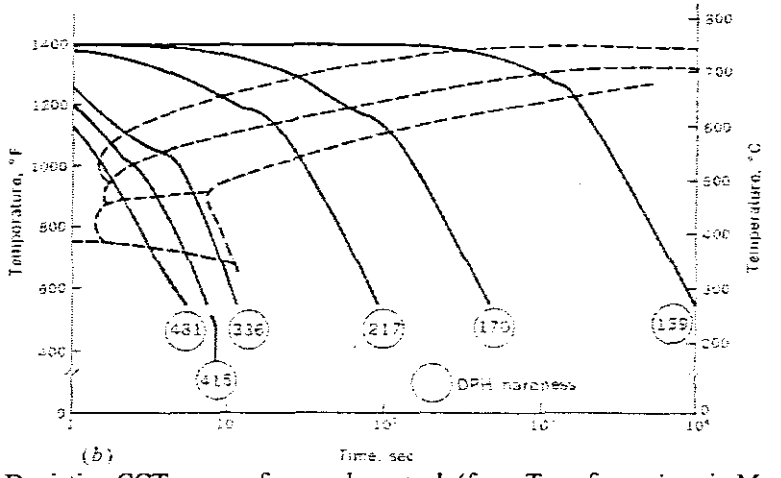

Figure 7.7. Depicting CCT. curves for a carbon steel. (from Transformations in Metals, 1969.)

7.6 Metallography

This is the science of characterizing the structure and properties of a metal. Specimens of the quenched and post-welded plates were prepared (see chapter on etching), and the images were analyzed using microscopy to supplement the interpretation of the quenching data. Optical microscopy can be successfully applied to reveal microstructural features, such as grain boundaries, which require a magnification of less than 2000. Using micrographs from atlases, the microstructures were identified and labeled. The transition from ferrite to pearlite and the onset of the bainite transformation could be determined. The difference in the structure between upper and lower bainite is more difficult to resolve, and an electron microscope is required.

7.7 Phase Transformations

In most materials, the atoms are arranged in regular patterns to form crystals. This crystal structure determines the properties of the material such as its strength, ductility conductivity, etc. The crystal structure can be changed as a function of the chemical composition, temperature, pressure and magnetic field, as is the case in a fusion welding process, and this change is termed a phase transformation. Phase transformations can however be controlled to manipulate the properties of materials and hence predict its final microstructure.

Phase transformations may also occur in the solid state through the processes of atomic rearrangement or diffusion-controlled reactions. An example of such a transformation is the transformation of austenite to pearlite.

7.8 Features of HAZ. Microstructures

7.8.1 Line Defects

The most common type of defect is the dislocation, which involves the edge of an extra plane of atoms in a crystal structure. This gives rise to zones of compression and tension, resulting in a net increase in energy along the dislocation. The displacement distance for atoms around the dislocation is termed the Burgers vector, and is usually at right angles to the edge or dislocation line. Another type of dislocation is the screw dislocation, which has its displacement parallel to the linear defect. Both dislocation types result from the crystallization process, where a slight misalignment of adjacent parts of a growing crystal, results in either the introduction or elimination of rows of atoms.

7.8.2 Boundaries

Atoms occurring on the surface of a body differ from those deeper in the lattice structure, in that they have neighbours on one side only. This results in surface atoms having higher energy levels than do internal ones.

7.8.2.1 Grain Boundaries

A Material is usually comprised of many crystals, or grains, the shape of which is controlled by the presence of surrounding grains. The atoms within a particular grain

structure are arranged in a particular orientation. The grain boundaries, however, are not, resulting in an increase in energy at the interface between grains. This would explain why the transition zone between grains dissolve more readily when subjected to chemical attack, such as etching [9].

7.8.2.2 Tilt Boundaries

This type of boundary may be considered as an array of dislocations that produce a small misorientation between adjoining lattice structures. Tilt boundaries are again comprised of low-angle tilt and low-angle twist boundaries, as is depicted in the figure below.

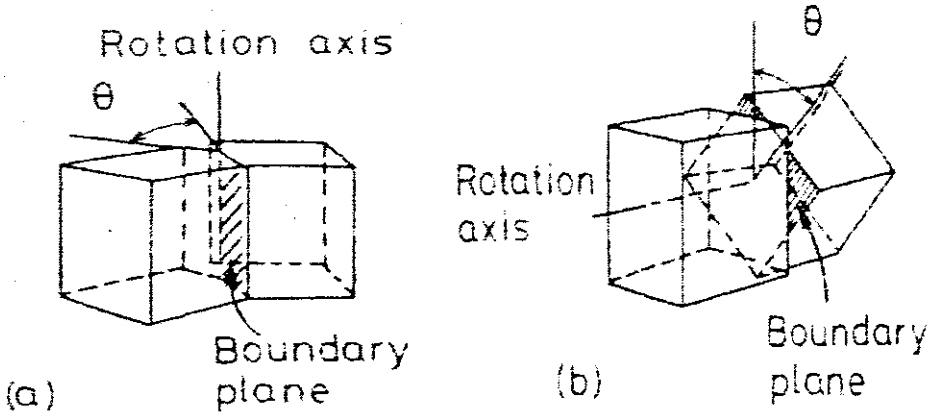

Figure 7.8. Depicting the relative orientations of the crystals and the boundary forming (a) a tilt boundary, (b) a twist boundary. (from Phase Transformation in Metals and Alloys, 1992.)

The low-angle tilt boundaries, originate from edge dislocations, whereas twist boundaries originate from screw dislocations. Although the atoms in the regions of these dislocations match perfectly, the cores are regions of poor fit, resulting in this boundary having a lower energy level than a regular boundary. Also, due to the fact that the boundary is unsymmetrical with respect to the two surrounding lattice structures, means that two Burgers vectors are required to accommodate the distortion [5].

7.9 Grain Growth

Grain growth is the systematic increase in the average size of grains at temperatures high enough to cause significant atomic movement. Steel subjected to the upper austenite temperature range for an extended period of time will experience an increase in grain size due to grain boundary migration and coalescence. This increase in grain size is detrimental in the sense that it results in decreased mechanical properties such as fracture toughness and ductility. It has previously been established [6], that a convex surface has more surface tension than does a concave one. The former will try to alleviate this tension by the movement of atoms across the boundaries of the two grain types, resulting in the grain boundary moving to the center of curvature of the lattice structure. Since small grains tend to have more convex surfaces than do larger grains, they disappear by fusing with the larger grains, resulting in grain growth. It would be expected, that since the elevated temperature produced grain growth, a subsequent reduction in temperature would reverse the process. This is, however, not the case, since a reduction in temperature slows down the process of atomic migration, but will not reverse the process.

The width of this coarse grained zone is a function of the welding process being employed as well as well as the heat input [10]. In instances where the specific energy input is high (25-75kJ/mm), wide HAZ's are produced and the grain structure tends to be coarse, both in the parent metal and the HAZ. It is for this reason that normalizing procedures are applied to the post-welded component, with the aim of grain refinement and hence improved mechanical properties. During normalizing, the specimen is heated to approximately 830^0C and allowed to cool to ambient temperature. Heating in the lower austenite range (T_1 to T_2), figure 2.8, produces fine-grained microstructures.

7.9.1 Specification of Grain Size

The grain size may be defined by an index, which is specified by both the American Society for Testing and Materials (ASTM.) and the British Standards (BS 4490: 1989) [11]. The ASTM. grain size number is determined from the following formula:

$$N = 2^{n-1} \tag{7.2}$$

where: N is the grains per square inch at a magnification ×100
n is the ASTM. grain size number from tables

$$m = 2^{G_E+3} \tag{7.3}$$

The British Standard grain size index $\mathbf{G_E}$ is determined from the following equation:

where: m is the number of grains per square millimeter at a magnification ×1
$\mathbf{G_E}$ is the grain size index from tables

For purposes of simplicity, the ASTM. grain size number $\boldsymbol{n}$ and the BS. Grain size index $\boldsymbol{G_E}$ are the same, as is evident from table 7.1, below.

Grain size index G_E or number n	Average grains per mm² at 1×	Average grains per inch² at 100×
0	8	0.5
1	16	1
2	32	2
3	64	4
4	128	8
5	256	16
6	512	32
7	1024	64
8	2048	128

From BS4490-1989.

Table 7.1. Depicting the numbers of grains for both the ASTM. and BS. (from The science and Engineering of Materials, 1996.)

It has been established [5], that the grain size is directly related to the strength of the material, hence, the finer the grains, the greater the resistance to slip at dislocation points.

7.10 Hardness Number

Hardness is the ability of a material to resist penetration of its surface, and has a strong correlation with the tensile strength of the material. After determination of the microstructure, the micro-hardness of the various constituents were determined, using the Vickers Knoop test, discussed in more detail in the chapter 5, on Testing.

7.11 Metallurgical changes and there consequences

Since fusion-welding processes subject material to extreme heating, cooling and straining, it is not uncommon for the chemical composition of the Heat Affected Zone (HAZ.) to be altered. There may also be the issue of the absorption of harmful gases, which will have detrimental effects on the weld HAZ, such as cracked, porous, brittle or weak zones. Some of these negative effects can be countered through the use of post-weld heat treatment, but most times this option is either too expensive or impracticable to apply.

The HAZ is a particularly complex region, since it forms the interface between the existing parent metal and the newly deposited molten material. The chemical composition of the weld pool can be controlled by the addition of desirable elements through the filler wire or electrode to produce a more tolerant microstructure. The adjacent parent material, however, remains unaltered. In the end all the constituent regions of the weld must function together as a unit.

7.12 Partial Transformation in the HAZ.

The pearlite in the parent metal directly adjacent to the HAZ will also experience a partial transformation to austenite (T_0 to T_1), as can be seen from figure 7.9, below. If the cooling rate is fast enough, this austenite will transform to martensite resulting in an extremely hard, brittle microstructure.

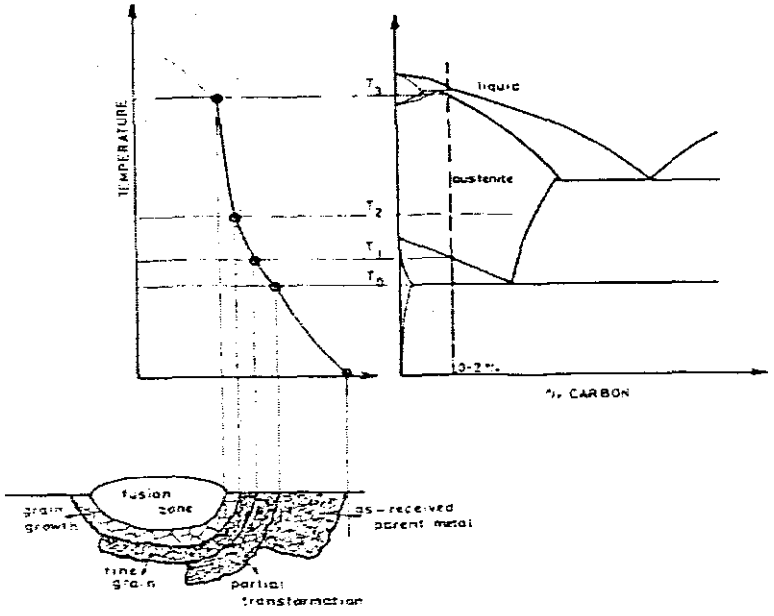

Figure 7.9. Depicting the microstructures present in a 0.2%C steel weld. (from Rational Welding Design, 1982.)

7.12.1 Tempered Microstructures in Multipass Welds

It has been established [12] that single pass welds produce the most significant deterioration in toughness, which occurs in the coarse grained heat affected zone (CGHAZ.). Here, the plate microstructure has been completely transformed, and the resultant toughness bears no correlation to that of the parent metal. During multi-pass welding, each bead is partially reheated and tempered by consecutive passes. This reheating greatly improves the toughness of the weld, since the carbon previously trapped in the martensite is allowed to diffuse out, resulting in a softer less brittle

microstructure, such as ferrite and spheroidised carbides. The effect of multi-pass reheating is two-fold, namely:

1. Studies have shown that the intercritically reheated CGHAZ. is responsible for the greatest degradation in toughness. The principal factors contributing to this degradation are:
   - Large prior austenite grain size and a course substructure, resulting in inferior properties
   - The presence of unfavourable microstructures such as upper bainite or a martensite/austenite/carbide constituent.
   - The dissolution and subsequent hardening of precipitates.
   - Excessive free nitrogen content.

The degree to which any of these factors influence the CGHAZ. toughness will be determined by the interaction between the welding thermal cycle, the actual welding procedure, and the plate chemical composition.

2. Successive passes affect the microstructure of the HAZ. by producing alternating layers of partially normalized material. This tempering effect is detected by variations in hardness and notch toughness at various positions in the HAZ. [12] as is indicated in the figure below.

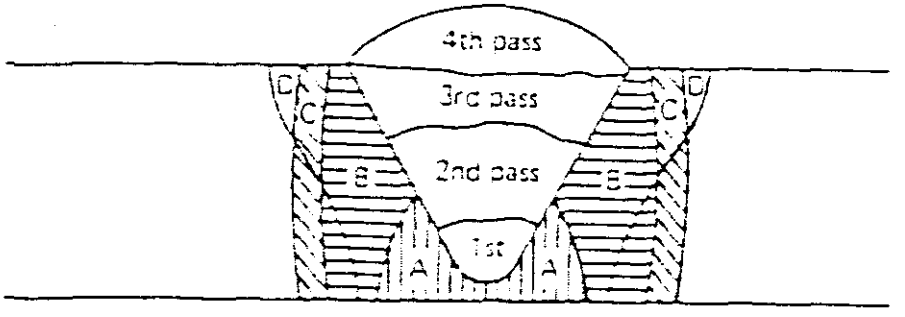

Figure 7.10. Depicting the effect of the deposition of successive passes on phase transformations in the base metal, (from Some Aspects of HAZ. and Weld Metal Toughness.)

In region **A.** the first pass produces a substantial increase in hardness, depending on the rate of cooling and carbon content of the base metal. This region will however, experience an increase in notch toughness when the higher interpass temperatures of subsequent passes temper it. It would however, not be possible to determine the exact variation of hardness in the HAZ., since the factors involved in the hardening and normalizing are much to complex. A similar effect will be experienced in regions **B**, **C** and **D**.

7.13 Heat Flow in Welding

Weld solidification involves both the parent or base metal and the newly deposited weld metal, which has approximately the same chemical composition. The variables involved in weld solidification are:

- the rate of the heat input, q (kJ/mm), is largely determined by the type of welding and the weld size.

- the speed of the arc movement along the joint, v (m/s)
- the thermal conductivity of the metal being welded, K_s (kJ/kgK)
- the thickness of the plate being welded, t (mm)
- the volumetric thermal capacity of the material, $c\rho$ (kJ/m^3 ^{0}C)

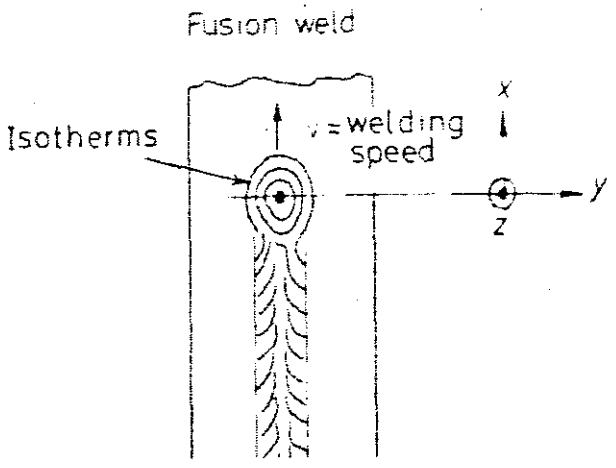

Figure 7.11. Depicting the distribution of isotherms about the heat source in fusion welding, (from Phase Transformations in Metals and Alloys, 1992.)

Assuming that the arc moves in the x-plane as indicated in figure 7.10, the resulting heat distribution in the three dimensional solid plate is given by the solution of the following differential equation [8]:

$$\frac{\partial^2 T}{\partial x^2}+\frac{\partial^2 T}{\partial y^2}+\frac{\partial^2 T}{\partial z^2}=2K_s v\frac{\partial T}{\partial(x-vt)} \qquad (7.4)$$

where: x, y and z are the co-ordinates as defined in figure
t is the time in seconds

The solution of equation 7.1 gives the temperature distribution about the moving heat source in the form of isotherms as is indicated in figure 7.12, below.

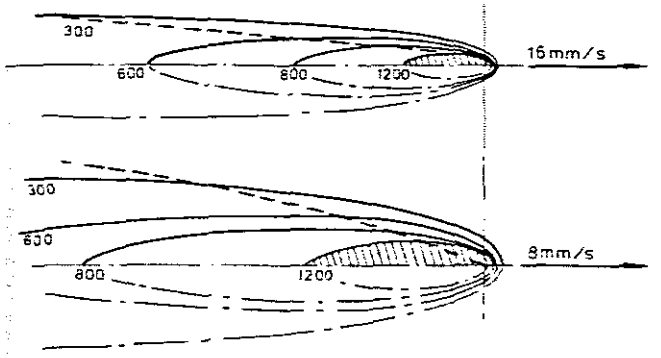

Figure 7.12. Depicting the effect of change in velocity on the shape of the thermal field distribution. (from Rational Welding Design, 1982.)

Gray et al [8] have established that the maximum width w of an isotherm at temperature T is given approximately by the following equation:

$$w = \frac{1}{2}\frac{q}{vt}\frac{1}{c\rho}\frac{1}{T} - \frac{4}{5}\frac{\lambda}{v} \qquad (7.5)$$

where: $\lambda = K_s/c\rho$ termed diffusivity, and is the measure of the temperature spreading rate (m^2/s)

It should become evident that the second term of equation 7.2 will become negligible for a rapidly moving, high heat input rate applied to a material of low diffusivity.

7.14 Solidification of Fusion Welds

The welding arc will initially cause melting back of the base metal (penetration) and this will result in dilution of the filler metal. The effect of dilution is significant, since it has been established [5] that the weld metal may contain 50 – 70% of the amount of Niobium (Nb), Titanium (Ti) or Vanadium (V) as is present in the base metal in micro-alloyed steels.

Dilution has the following adverse effects on the weld metal, namely:

- it changes the composition of the melt (deposition)
- surface layers of the base metal are dissolved in the weld pool
- the weld pool is cooled down appreciably by the foreign material

Depending on the material type and thickness, the base metal usually acts as a very efficient heat sink. It has been observed [5], that at the eutectic temperature, solidification nuclei begin to form at the oxide free surface of the melted-back base metal. Due to the near homogeneity of the weld pool and base metal, "wetting" of the base metal is very effective. This implies that there is virtually no nucleation barrier to solidification, resulting in very little undercooling. This produces weld and base metal nuclei having the same lattice structure and grain orientation at the solid liquid interface.

Due to the extremely high temperatures generated directly below the arc and the high heat absorption rate of the base metal, there is, initially, a steep temperature gradient in the weld pool, resulting in a low degree of constitutional supercooling. The actual thermal gradient present at a particular time is a function of the plate thickness and the welding process being utilized. The grain size of the post-weld microstructure, at this stage, is largely determined by the grain size of the base metal. Due to the severity of the thermal cycle at the interface between the weld pool and base metal, the microstructure in this region is predominantly coarse grained.

Due to the dynamic nature of the welding process, resulting in a constantly changing position of the maximum temperature gradient, the growing columnar crystals will

continuously have to change direction to keep pace with the moving arc, whilst at the same time maintaining their preferred growth direction, as is evident from figure 7.13.

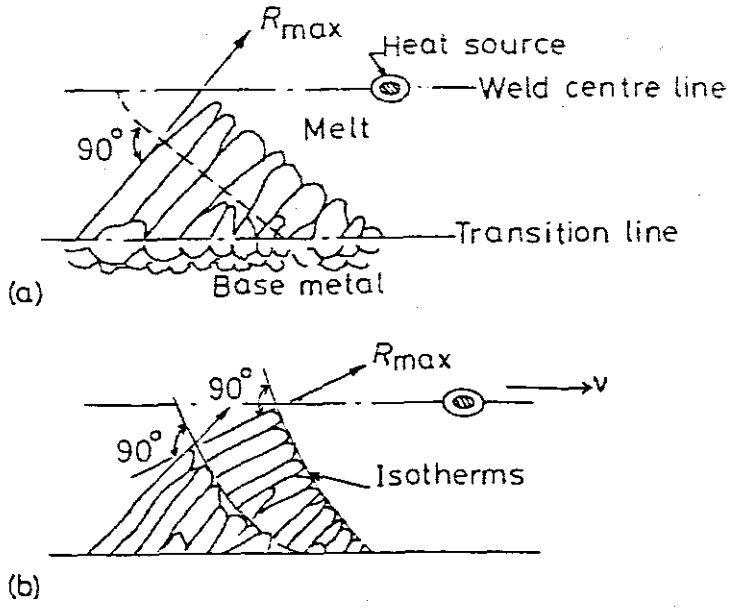

Figure 7.13. Depicting the growth of columnar crystals occurring always at approximately 90^0 to the isotherms. (from Phase Transformations in Metals and Alloys, 1992.)

7.14.1 Influence of Welding Speed

It has been established that varying the welding speed may alter the shape of the weld pool [8] as is evident from figure below. As was previously stated, growing crystals will tend to follow the steepest temperature gradient. Any subsequent change in the welding speed will alter the solidification behaviour of the material, due to the fact that the rate at which direction has to changed by any individual crystal will be either reduced or increased, resulting in either a wide convex weld or a narrow concave weld.

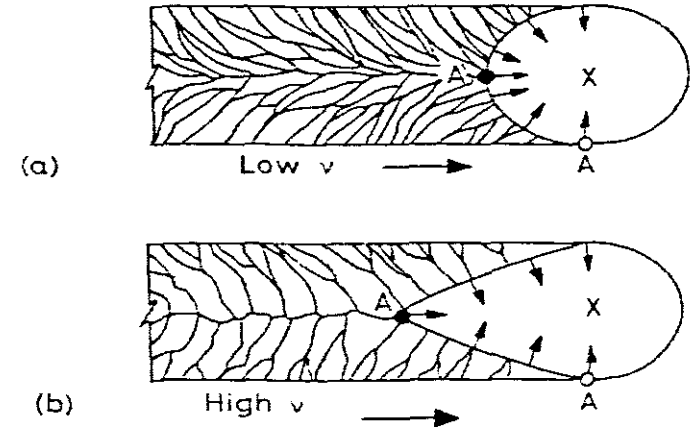

Figure 2.14. Depicting the effect of increased welding speed on the shape of the welding pool and crystal growth. (from Phase Transformation in Metals and Alloys, (1992.)

7.15 Statistical assessment of trends in transformation behaviour

Numerous attempts have been made to analyze statistically the data available and thereby extend the scientific knowledge of the behaviour of steel to assist in the production and heat treatment of the great variety of alloy steels. Multiple regression equations have been obtained during the study of the following:

- The determination of the critical range of heating
- The martensite transformation
- The bainite transformation
- The critical cooling conditions
- The effect on austenising conditions

These regression equations can be safely applied to hypoeutectoid steels with up to 0.6%C

7.15.1 The critical range on heating between Ac_1 and Ac_3

Many determinations of the critical temperatures for hypoeutectoid steels were derived resulting in the following:

$$A_{C1}\ (^0C) = 723 - 20.7Mn + 16.9Ni + 29.1Si + 16.9Cr = 290As + 6.38W \qquad (7.6)$$

Where the chemical symbols denote the weight % of the alloying element

$$A_{C3}\ (^0C) = 910 - 203\sqrt{C} - 15.2Ni + 44.7Si + 104V + 31.5Mo + 13.1W \qquad (7.7)$$

7.15.2 The Martensite transformation range

The temperature range for the formation of martensite depends on the composition of the austenite from which it is formed. The relationship between the start of the transformation, Ms, and steel composition has been investigated by many researchers [16], and may be determined from the following expression:

$$M_S\ (^0C) = 539 - 423C - 30.4Mn + 17.7Ni + 12.1Cr + 7.5Mo \qquad (7.8)$$

7.15.3 The Bainite transformation range

When austenite is subjected to rapid cooling to below the pearlite transformation curve, a new eutectoid product termed bainite is produced. Although bainite is also a mixture of ferrite and cementite, it is microstructurally quite different from pearlite and has its own C-curve on a TTT. diagram. The bainite that forms just below the nose of the curve is termed upper bainite, or feathery bainite, whilst that formed at lower temperatures is termed lower or acicular bainite, as is depicted in figure 2.5.

Steven and Haynes [16], studied the Bainite transformation range and provided the following quantitative formulae:

$$B_S(^0C) = 830 - 270C - 90Mn - 37Ni - 70Cr - 83Mo \qquad (7.9)$$

$$with \quad B_{50} = B_S - 60^0C \qquad (7.10)$$

$$and \quad B_f = B_S - 120^0C \qquad (7.11)$$

where B_S denotes the bainite start temperature in degrees Celsius
C, Mn, Ni, Cr and Mo are the weight percentages of the alloying constituents
B_{50} denotes 50% bainite
B_f denotes the end of the bainite transformation

7.15.4 The ferrite-pearlite transformation range

The temperature for the ferrite transformation on air cooling of CMn steels for 10mm round bar is given by the following expression:

$$10mm\ bar\ diameter\ F_S(^0C) = 878 - 295C - 78Mn \qquad (7.12)$$

$$P_S(^0C) = 700 - 60Mn \qquad (7.13)$$

The pearlite start of transformation on air-cooling is given by the following expression:
The above equation may successfully be applied to diameters 10 to 1000mm.

The above equations apply for transformations occurring above normal austenitisation i.e. 10 to 60° above Ac3.

7.16 The critical cooling velocity and other significant cooling rates

The knowledge of the cooling kinetics in the weld metal is a significant element in the prediction of the metallographic structures. The criterion used is the cooling rate at 700°C *(VR700)*. The essential features, which influence the cooling rate, are welding machine voltage, V, amperage, I, travel speed, v, preheating, To, or in the case of multi-pass welding, interpass temperatures, Ti, the calorific efficiency, η, of the welding process and the thickness of the plates to be assembled. As was indicated in a previous chapter, an equivalent thickness must be taken into consideration, depending on the joint type. The material physical constants are also necessary for estimating the cooling rate in the weld. After Adams [16l], the cooling rate for a metal is given by the following differential equation, taking into account the equivalent thickness, the corrected energy and the preheating temperature.

$$\frac{dT}{dt} = 2K\pi / \eta E(T - T_0)^2 h[(\rho Cpe^2 / \eta E(T - T_0)] \qquad (7.14)$$

where: K is the thermal conductivity for low alloy steel, equal to 0.06 cal $cm^{-1}K^{-1}$
ρCp is the product of the mass volume and the specific heat,

equal to 2 cal $cm^{-3}K^{-1}$

The critical cooling velocity (CCV.) is that cooling velocity which must be equaled or exceeded in order to obtain a martensitic transformation. The alloying constituents and the austenitising conditions have an effect on the CCV., the limited rate of cooling LRC., and the cooling rate, Cp. The CCV for bainite formation in seconds, is given by the following expression:

$$\log C_B = 3.274C - 0.046Si + 0.626Mn + 0.706Cr + 0.520Mo + 0.026Ni + 0.675Cu - 1.818 \quad (7.15)$$

The LRC is defined as that rate of cooling which just suppresses the transformation to ferrite-pearlite, resulting in bainite formation. The LRC cooling time is given by the following expression:

$$\log C_F = 3.288C - 0.168Si + 1.068Mn + 1.266Cr + 2.087Mo + 0.300Ni + 0.626Cu - 1.931 \quad (7.16)$$

CP is defined as the rate of cooling which just suppresses the formation of pearlite. This will result in the formation of ferrite-bainite or ferrite-martensite and is given by the following expression:

$$\log C_P = 0.597C - 0.100Si + 1.395Mn + 1.295Cr + 3.730Mo + 0.395Ni + 0.398Cu - 0.869 \quad (7.17)$$

7.17 The relationship between hardness and tensile properties

The knowledge of the tensile properties of a material is of extreme value to the welding engineer as was discussed in a previously. Regression equations relating hardness and tensile properties have been established and are given by the following expressions [16]: The determination of the hardness in the weld tempered zone may be determined from the following formulae:

7.17.1 Tempered Martensite Hardness

$$Hv_M = -75 - 434C - 368Si - 15Mn + 17Cr + 37Ni - 335Mo - 2235V + 1000/P_r(260 + 616C + 321Si - 21Mn - 35Ni - 11Cr + 352Mo + 2345V) \quad (7.18)$$

where: P_r is a temper parameter

7.17.2 Tempered Bainite Hardness

$$Hv_B = 262 + 163C - 349Si - 64Mn - 7Ni - 187Cr - 458Mo - 857V + {}^{10^3}\!/_{P_r}(-149 + 43C + 336Si + 79Mn + 16Ni + 196Cr + 352Mo + 1095V) \quad (7.19)$$

7.17.3 Pearlite Ferrite Hardness

$$Hv_F = 152 - 493C - 10Mn - 19Mo + {}^{10^3}\!/_{P_r}(-37 + 726C + 14Mn + 17Mo) \quad (7.20)$$

7.17.4 Ultimate Tensile Strength

$$U.T.S.(MPa) = 19.13.10^{-4} HV^2 + 1.89HV + 181.5 \quad (7.21)$$

7.17.5 0.2% Yield Strength

$$Y.S.0.2(MPa) = -266.8 + U.T.S. + 30.41\log VR + 51.01 \quad (7.22)$$

7.17.6 % Rigidity

$$EI\%(5d) = (-1.38 + 18.2 \times 10^3)/U.T.S. \quad (7.23)$$

These formulae will be applied in the experimental work on ROQ-tuf AD690.

CHAPTER 8 – THE FINITE ELEMENT METHOD

8.1 Introduction

The Finite Element Method (FEM.), is a numerical method for solving complex problems in engineering and mathematical physics, with the use of computer simulations. Many problems in engineering, such as the structural analysis of a beam where the geometry changes dramatically, cannot be solved by conventional means, and therefore a numerical solver has to be employed to obtain solutions to the stresses and displacements at various points in the beam. Problems, such as the one just described, is the realm of the FEM., of which there are many commercial packages available. The validity and interpretation of the results obtained from the simulation, still depends on the ability and knowledge of the individual carrying out the simulation, since they have to be analyzed.

The application of the FEM. and more in particular, the use of the commercial package SYSWELD® to the solution of heat conduction in a three-dimensional plate due to a moving heat source as well as the quenching process, will be carried out. In both instances, a coupled thermo-metallurgical-mechanical (TMM.) analysis will have to be carried out, which will yield approximations on the dissipation of heat in the plate in the form of thermal contours. This stage will also produce values of stress and strain induced in the plate due to the arc. The metallurgical analysis will approximate the phase proportions present in the heat affected zone (HAZ.) and surroundings, by taking into account the chemical composition, specific heats, conductivity and continuous cooling transformation (CCT.) data to approximate the phase transformations taking place in the material. This will be displayed symbolically and in percentile form as bainite, martensite and pearlite. The mechanical analysis will then use the results obtained from the previous two analyses to predict the mechanical properties, such as the yield strength and Young's modulus of the post welded or quenched material. The results obtained from the simulation will then be verified by comparing with those obtained from actual experiments.

8.2 Modelling the Thermo-Mechano-Metallurgical (TMM) Process

8.2.1 Introduction

The simulation of a welding process requires the solution of a fully coupled thermo-mechano-metallurgical model, which takes into account the simultaneous solution of displacement equilibrium in a mechanical analysis, temperature equilibrium in a thermal analysis, and volume phase fraction equilibrium in a metallurgical phase transformation analysis. Ronda and Oliver [21] have derived evolution equations from the algebraic metallurgical equations and successfully applied them to carry out a coupled incremental numerical analysis of welding. In this formulation, the coupled mathematically consistent thermo-mechano-metallurgical (CTMM) problem is formulated as a variational problem and solved by using a Galerkin type finite element technique. In the formulation, the real

microstructure of the material is not assigned to the elements in the finite element mesh, giving rise to the concept of hybrid isobaric finite elements, representing the theory of dispersed particles. In these hybrid elements, the phase composition of the welded material is represented at the nodes, or Gauss points, which is then integrated. Since austenite can transform into fractions of either ferrite, pearlite, cementite, bainite or martensite upon cooling, the complexity of the derivation is self evident.

8.2.2 The Finite Element equation for solving the TMM. problem

Ronda and Oliver [21] have derived finite element equations for virtual work and internal energy, as well as appropriate phase evolution laws. The combination of these gives us the global finite element equation for solving the coupled thermo-mechano-mettalurgical problem.

$$\begin{bmatrix} -1 & {}^{t}\hat{\beta}_i & {}^{t}A_i \\ 0 & 0 & 0 \\ 0 & 0 & {}^{t}_{0}C \end{bmatrix} \begin{bmatrix} {}^{t+\Delta t}\dot{y}_i \\ {}^{t+\Delta t}\dot{u} \\ {}^{t+\Delta t}\dot{\theta} \end{bmatrix}^{(i)} + \begin{bmatrix} 0 & 0 & 0 \\ {}^{t}_{0}K_{uy} & {}^{t}_{0}K_{uu} & {}^{t}_{0}K_{u\theta} \\ {}^{t}_{0}K_{\theta y} & {}^{t}_{0}K_{\theta u} & {}^{t}_{0}K_{\theta\theta} \end{bmatrix} \begin{bmatrix} \Delta y_i \\ \Delta u \\ \Delta\theta \end{bmatrix}^{(i)} = \begin{bmatrix} {}^{t+\Delta t}R_{yi} \\ {}^{t+\Delta t}R_u \\ {}^{t+\Delta t}R_\theta \end{bmatrix} - \begin{bmatrix} {}^{t+\Delta t}_{0}F_{yi} \\ {}^{t+\Delta t}_{0}F_u \\ {}^{t+\Delta t}_{0}F_\theta \end{bmatrix}^{(i-1)} \tag{8.1}$$

Utilising backward finite differences to approximate the fraction rate, velocity and temperature rate, equation (8.1) can be rewritten in the following form:

$$\begin{bmatrix} {}^{t}_{0}K_{yy} & {}^{t}_{0}K_{yu} & {}^{t}_{0}K_{y\theta} \\ {}^{t}_{0}K_{uy} & {}^{t}_{0}K_{uu} & {}^{t}_{0}K_{u\theta} \\ {}^{t}_{0}K_{\theta y} & {}^{t}_{0}K_{\theta u} & {}^{t}_{0}\hat{K}_{\theta\theta} \end{bmatrix} \begin{bmatrix} \Delta_{yi} \\ \Delta_u \\ \Delta_\theta \end{bmatrix}^{(i)} = \begin{bmatrix} {}^{t+\Delta t}R_{yi} \\ {}^{t+\Delta t}R_u \\ {}^{t+\Delta t}R_\theta \end{bmatrix} - \begin{bmatrix} {}^{t+\Delta t}_{0}F_{yi} \\ {}^{t+\Delta t}_{0}F_u \\ {}^{t+\Delta t}_{0}F_\theta \end{bmatrix}^{(i-1)} \tag{8.2}$$

where $\tau = 1/\Delta t$, and the stiffness matrices are given by:

$$\begin{aligned} {}^{t}_{0}K_{yy} &= -\tau 1, \\ {}^{t}_{0}K_{yu} &= \tau\, {}^{t}\hat{B}_i, \\ {}^{t}_{0}K_{y\theta} &= \tau\, {}^{t}A_i, \\ {}^{t}_{0}K_{uy} &= {}^{t}_{0}K_{A}, \\ {}^{t}_{0}K_{\theta y} &= {}^{t}_{0}K_{mix}, \\ {}^{t}_{0}K_{\theta\theta} &= \tau\, {}^{t}_{0}C + {}^{t}_{0}K_{\theta\theta}, \end{aligned} \tag{8.3}$$

where ${}^{t}_{0}K_{\Lambda}$ is related to the plastic function $\Lambda(S,E,\int\dot{E}dt,\Theta,y_i)$ and the FE displacement-strain matrices B_L, B_{nL}, the stiffness matrix ${}^{t}_{0}K_{mix}$ are functions of the mixture rule used to evaluate material parameters for a multiphase body.

This non-linear system of finite element equations is then solved by the use of an iterative solver, such as the Newton-Raphson method.

8.3 Modeling of the moving Welding Arc

The MMA welding arc can best be represented as a three dimensional Gaussian pulse. The arc is a function of the voltage and current supplied by the welding machine. Since not all the energy supplied to the electrode is transferred to the work piece, an efficiency factor is introduced has to account for this loss of energy. The physical disparity between a Gaussian pulse and the welding arc is accounted for by the introduction of a deviation factor. After Ronda and Oliver [21], the heat flux representing an electric arc is given by:

$$F_{\theta}^{arc} = \phi\eta VI / 2\pi\delta_{arc}^{2} \exp(-r^{2} / 2\delta_{arc}^{2}) \qquad (8.4)$$

where V is the voltage
I is the current intensity
δ_{arc} is the deviation from the standard distribution and represents the thermal impression made by the electrode
η is the efficiency of energy transmission via the electric arc
ϕ is the net fraction heat input
r is the horizontal radial distance from the weld center.

This function is incorporated into Fortran code, which enables the user to specify the velocity and height of the arc, especially for multi-pass welding.

CHAPTER 9 – EXPERIMENTAL PROCEDURE.

9.1 Introduction

The concise recording and documentation of an experimental procedure is important if results and conclusions reached are to stand up to public scrutiny. That is the precise purpose of this chapter. The foregoing chapters, or literature survey was the foundation for the procedures, which will be covered here. The schematic diagram is an attempt to more clearly convey the experimental procedures followed and results obtained.

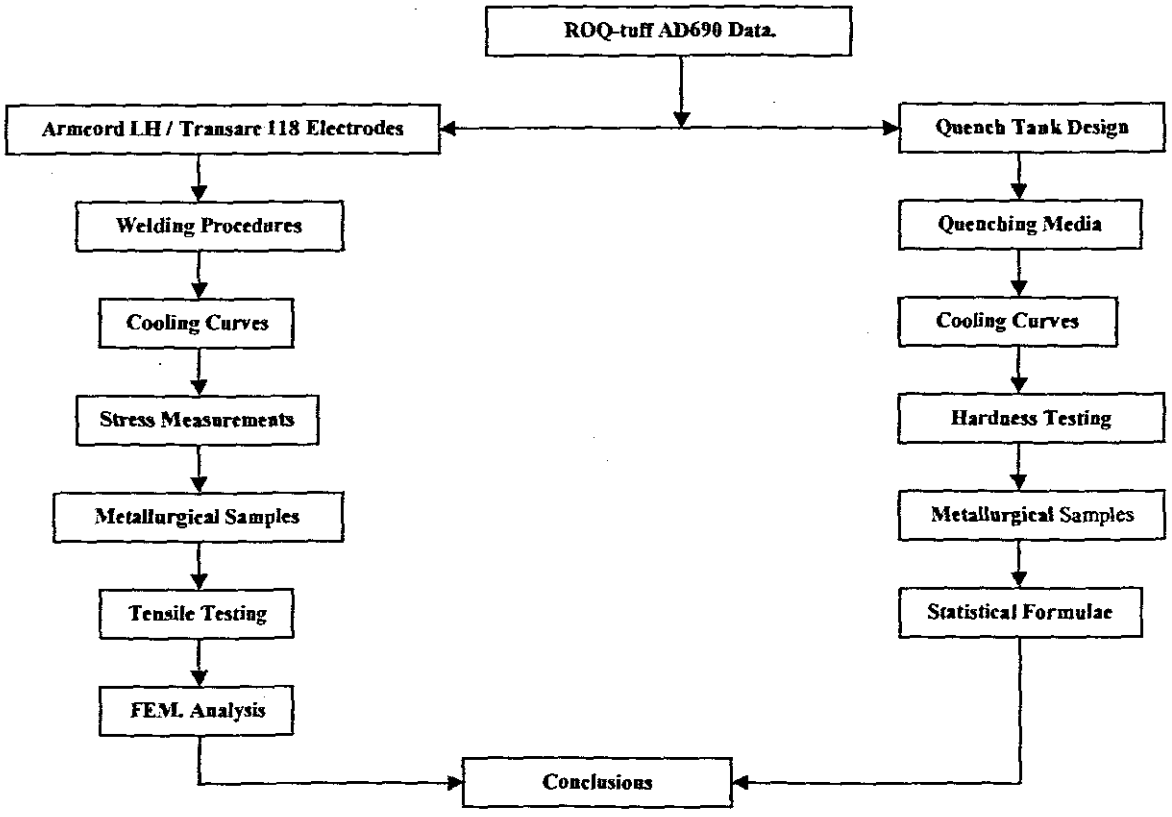

Figure 9.1. Depicting the experimental procedures followed

A brief introduction of ROQ-tuff AD690 will be given, including its chemical composition and mechanical properties. Since this is an analysis of the metallurgical changes that take place in the steel due to arc welding, it would be incomplete without data on the two electrodes used, namely Oerlikon Armcord LH and Afrox Transarc 118, both low hydrogen electrodes, suitable for high tensile strength welding. The welding procedure will then be covered, followed by the results of welding, namely the cooling curve data and ultrasonic stress measurements. Metallurgical microstructural results and the positions from which these samples were obtained will be discussed in detail. Tensile testing data and results will also be covered in detail, followed by input data and results from the finite element analysis. The second tier of my analysis was to ascertain all the phase transformations that can take place in the steel by first austenitising standard Jominy bars and then quenching them in either water, brine, oil or normalising. With the use of thermocouples, the cooling rate responsible for the ormation of a particular microstructure could be ascertained. Also, the mechanical properties of a particular phase could be determined by the use of hardness readings and statistical formulae. The correlation between these and the actual tensile test data for that particular microstructure

in the weld can then be veryfied for accuracy. The results obtained will then be discussed and conclusions drawn will be expounded upon.

9.2 Introduction to ROQ-tuf AD690

ROQ-tuf is a low alloy high tensile roller quenched and tempered steel used primarily in structural and pressure vessel applications. The steel is produced as a fully killed fine grain structure to which silicon and aluminium is added as deoxidising and grain grain refining agents respectively. The molten steel is vacuum-arc degassed to remove any impurities whilst at the same time reducing the sulphur content to below 0.010%. The shape of remaining sulphides is controlled by the addition of rare earth zirconium, which also has the additional advantage of improving the through thickness properties of the steel. The cast slab is then rolled to the required thickness after which it is subjected to a ultrasonic test to ascertain internal soundness. The steel is then subjected to a hardening process, which entails heating the plates to 900°C in an austenising furnace after which it is directly transferred to a roller quenching process. Distortion of the plates during quenching are limited due to the clamping action of the rollers. After quenching, the plates are tempered (620-690°C) to give them the desired mechanical properties. ISCOR, the manufacturer, has supplied the following chemical and mechanical data for the steel.

GRADE	MAX thickness	C	Mn	Si	S (max)	P (max)	Mo	Ni	Cr	B
ROQ-tuf AD690	32mm	0.12/ 0.21	0.45/ 0.70	0.20/ 0.35	0.040	0.035	0.50	-	-	0.001/ 0.005
ROQ-tuf AD690	50mm	0.12/ 0.21	0.45/ 0.70	0.20/ 0.35	0.040	0.035	0.45/ 0.60	1.20/ 1.50	-	0.001/ 0.005
ROQ-tuf AD690	150mm	0.12/ 0.21	0.45/ 0.70	0.20/ 0.35	0.040	0.035	0.45/ 0.60	1.20/ 1.50	0.85/ 1.20	0.001/ 0.005

Table 9.1. Chemical composition % (ladle analysis) (from ISCOR technical data sheets)

Mechanical Properties of ROQ-tuf alloy grade steels	ROQ-tuf AD690
	Up to 65mm thick
Tensile Strength (Mpa)	760-895
Yield strength (Mpa)	690
Elongation in 50mm (% min)	16
Reduction of area (% min)	
-rectangular specimens	40
-round specimens	50
Charpy impact test (J)	
-longitudinal at -50 degs celsius	27
-transverse at -50 degs celsius	20

Table 9.2. Mechanical properties of ROQ-tuf AD690 (from ISCOR data sheets)

9.3 The Welding Electrodes

ROQ-tuf was developed with weldability being a prime consideration. The low level of alloying elements in its chemical composition ensures good weldability. Sound crack-free, high strength welds are obtainable when welding ROQ-tuf, provided the necessary precautions are taken with regards to electrode selection, pre-heat, interpass temperature control and heat input to the material. ROQ-tuf is susceptible to hydrogen cracking in the heat affected zone (HAZ). It is with this fact in mind that it is recommended that low hydrogen processes and consumables be used when welding the material. The two electrodes selected for analysis are Afrox Transarc 118 and Oerlikon Armcord LH, both low hydrogen electrodes. The electrode chemical composition and mechanical properties are as follows:

Chemical Composition	
% Carbon	0.06/ 0.10
% Manganese	1.30/ 1.80
% Silicon	0.50 max
% Sulphur	0.025 max
% Phosphorus	0.025 max
% Nickel	1.70/ 2.50
% Molybdenum	0.30/ 0.50

Table 9.3. Chemical composition of Transarc 118 (from Afrox consumables catologue)

Mechanical Properties To AWS A5.5 in the as welded condition	
0.2% Proof stress	680-760 Mpa
Tensile strength	760 Mpa min
% Elongation on 50mm	20 min
Charpy V-notch at –51 degs celsius	45J min

Table 9.4. Mechanical properties of Transarc 118 (from Afrox consumables catologue)

Chemical Composition of Armcord LH.	
% Carbon	0.056
% Manganese	1.32
% Silicon	0.30
% Sulphur	0.027
% Phosphorus	0.017
% Nickel	2.07
% Molybdenum	0.36
% Chrome	0.32

Table 9.5 Depicting the chemical composition of the Armcord LH electrode (courtesy OESA Datasheets)

Mechanical Properties to AWS A5.5-92 in as welded condition	
Yield Strength	≥680 MPa
Tensile Strength	760-860 MPa
% Elongation on 50mm	≥16
Charpy V-notch at 51^{0}C	≥50J

Table 9.6 Depicting the Mechanical Properties of the Armcord LH electrode (courtesy OESA Datasheets)

9.4 The Welding Procedure

ROQ-tuf plates having dimensions of 100x100mm and thicknesses of 10 and 16mm were machined to have a 60° included butt angle. Equi-spaced holes were also drilled on either side of the 'V' along the top surface of the plates to accommodate thermo-couples, which would be used to determine inter-pass temperature increase, as is indicated in the figure below.

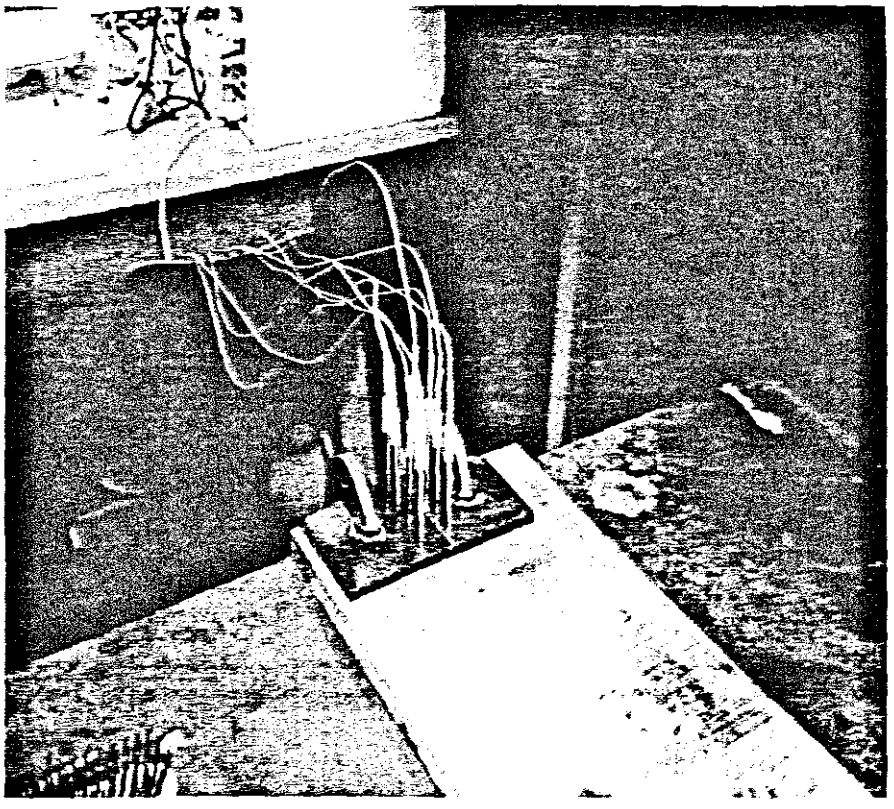

Figure 9.2. Depicting thermocouples embedded in plate prior to welding

Indicated above is an attempt to insulate the bottom surface of the plates from the worktable thereby limiting heat transfer to the surroundings. This, however, resulted in difficulties in creating an arc and was discarded as impractical. Prior to welding, the plates were subjected to an ultrasonic stress measurement to determine base stresses. The plates were then stress relieved in the welding laboratories furnace using the following procedure.

Heating			Cooling	
Temperature (°C)	Time		Temperature (°C)	Time
28-120 (heating)	20 minutes		610-480 (cooling)	2 hours 30 minutes
120 (hold time)	1 hour		480 (hold time)	1 hour
120-240 (heating)	20 minutes		480-360 (cooling)	2 hours 30 minutes
240 (hold time)	1 hour		360 (hold time)	1 hour
240-360 (heating)	20 minutes		360-280 (cooling)	2 hours 30 minutes
360 (hold time)	1 hour		280 (hold time)	1 hour
360-480 (heating)	20 minutes		280-150 (cooling)	2 hours 30 minutes
480 (hold time)	1 hour		150 (hold time)	1 hour
480-610 (heating)	20 minutes		Room temperature (cooling)	3 hours
610 (hold time)	1 hour			

Table 9.5. Depicting the Stress Relieving procedure followed

The pre and post-welded plates were again subjected to an ultrasonic stress measurement yielding the following results:

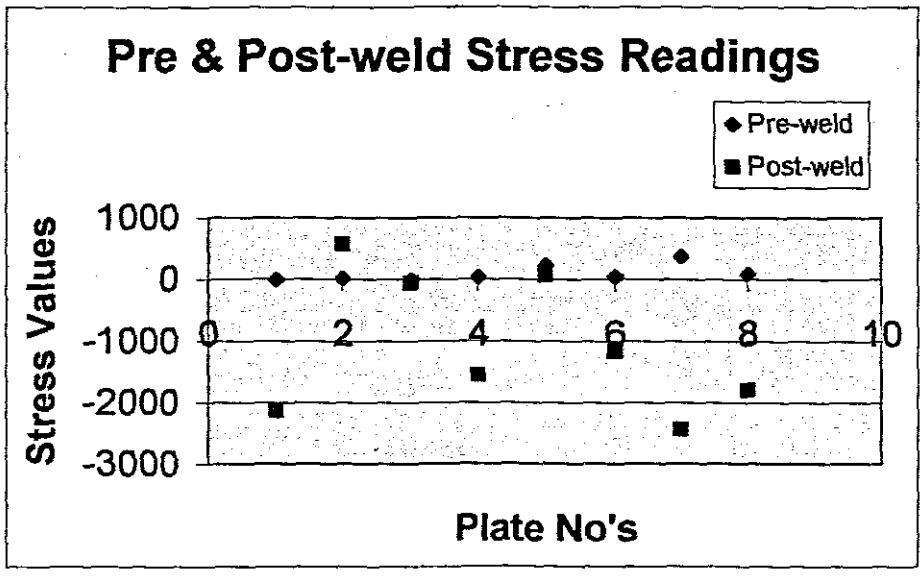

Graph 9.1. Depicting Pre and Post-weld Stresses in Mpa.

Plate No.	Thickness (mm)	Pre-weld	Post-weld	Electrode
2A+B	16	-9.3	-2140	Transarc
3A+B	10	18	566	Oerlikon
4A+B	10	-9	-60.5	Transarc
5A+B	16	33	-1565	Oerlikon
6A+B	16	223	70	Oerlikon
7A+B	16	39.5	-1175.5	Oerlikon
8A+B	10	370	-2444	Transarc
9A+B	10	89	-1799.5	Transarc

Table 9.6. Depicting stress readings (Mpa) used to create the figure above

From the data in table 9.6 it can be seen that the post-weld stresses measured on the top of the plates are predominantly compressive in nature. It should also be stated, that plates 6A & B, 7A & B, 8A & B and 9A & B was not heat-treated. This can be seen by the higher pre-weld stress values obtained from the Debro 30.

9.5 Heating and Cooling Curves

As was stated earlier, thermo-couples were embedded in the plates prior to the commencement of welding. The thermo-couples, which were numbered, as depicted in the figure below, produced a distinct temperature profile each time the welding arc passed by it.

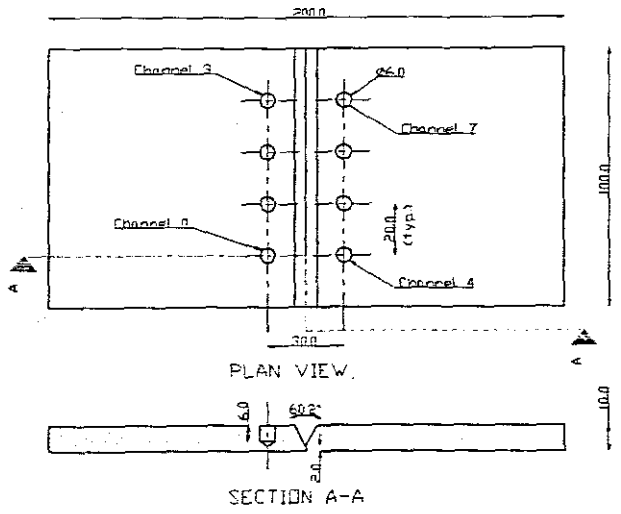

Figure 9.3. Depicting the layout of the butt-welded plates and thermo-couple numbers

From figure 9.2 it will be ascertained that couples 0 and 4 would experience an increase in temperature at approximately the same time followed by couples 1 and 5 until at the end of the welding run couples 3 and 7 will experience the effect of the welding arc. The temperature response obtained during the welding of the 10mm plates 3A & B using a 3.15mm Oerlikon electrode and plates 4A & B using a 3.15mm Transarc electrode will be discussed below.

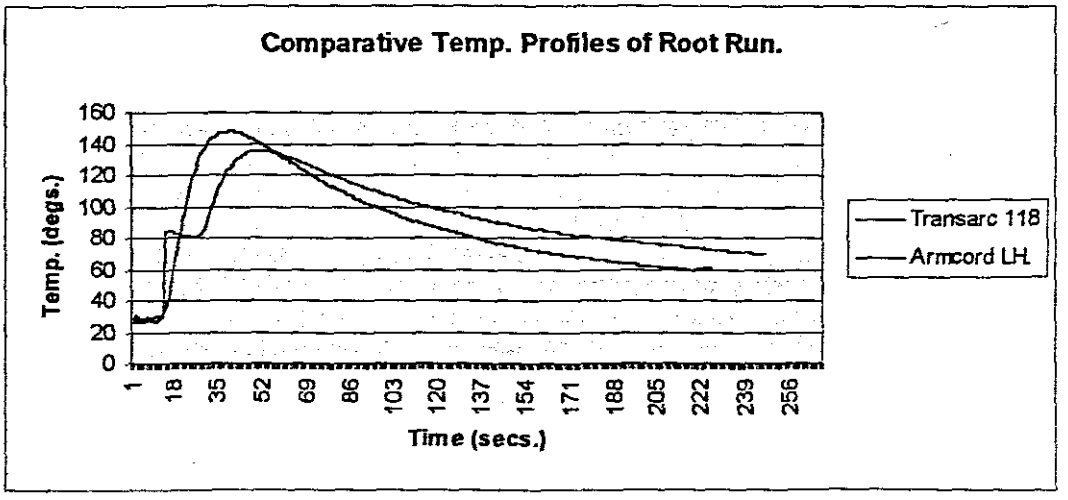

Graph 9.2. Depicting the comparative temperature profiles obtained on welding plates 3A & B and 4A & B

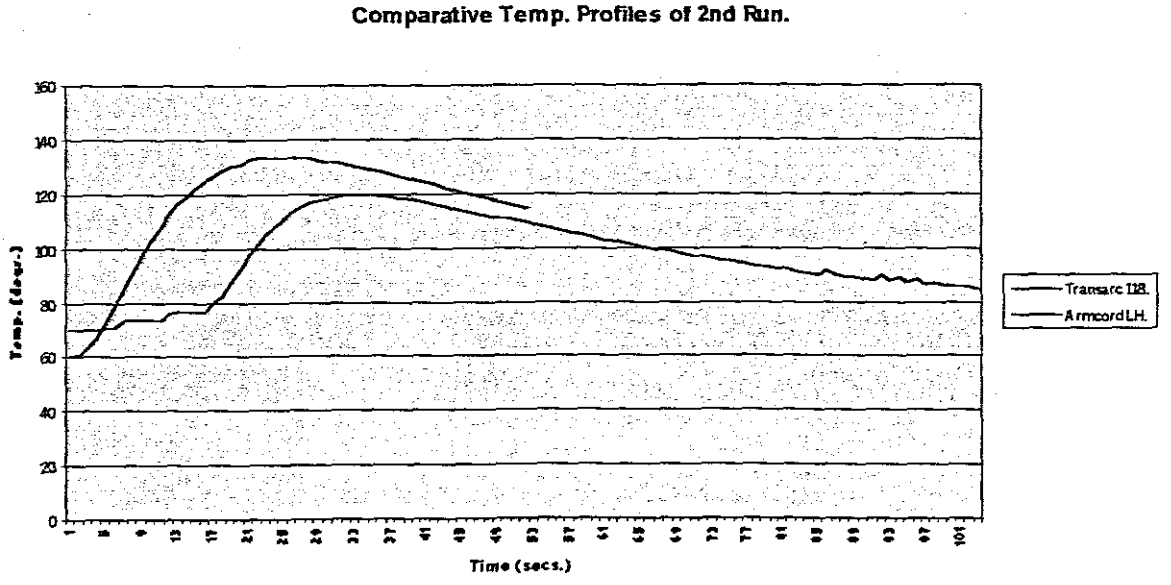

Graph 9.3. Depicting the comparative temperature profiles obtained on welding plates 3A & B and 4A & B

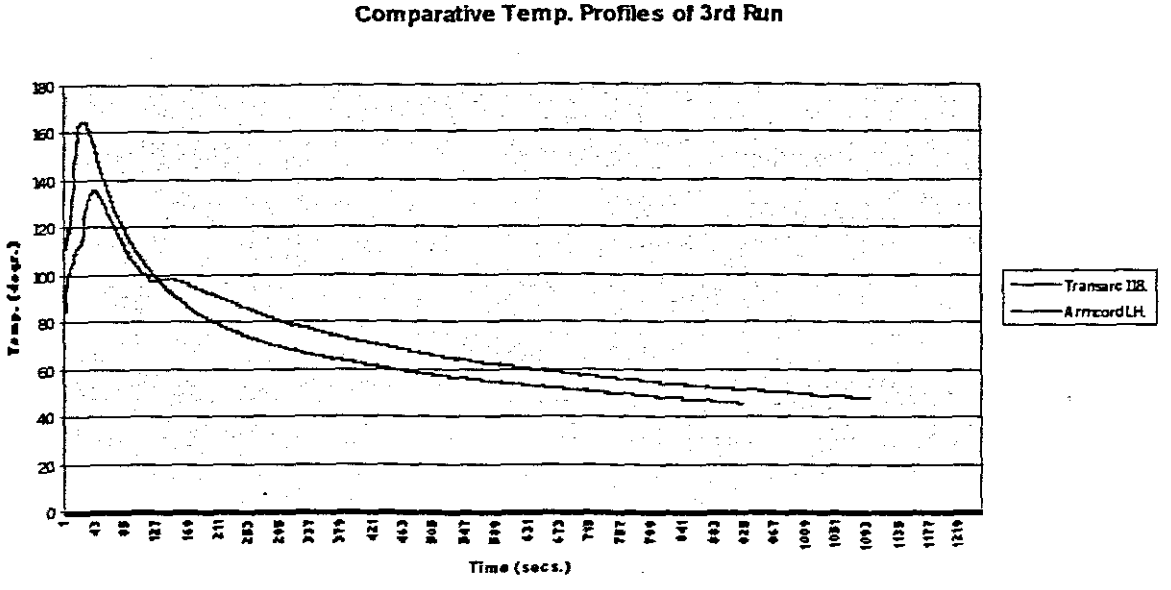

Graph 9.4. Depicting the comparative temperature profiles obtained on welding plates 3A & B and 4A & B

For the purpose of consistency, the graphs indicate the temperature profiles obtained from thermocouple number 3 only. The welding machine that was used is the Migatronic BDH-400, which is a microprocessor-controlled unit. The machine has a facility that enables the user to determine the optimal welding parameters for a particular electrode. For the both the 10mm and 16mm plates the parameters were as follows:

- Electrode – Oerlikon Armcord LH - 120Amps 20.9Volts
- Electrode – Afrox Transarc 118 - 130Amps 22.4Volts

Graph 9.2 depicts the Root Run. The higher energy input from the Transarc electrode is evident from the higher temperature registered by the thermocouple. The spike in the Armcord LH curve occurred when the thermocouple became briefly dislodged from its recess in the plate. The same temperature profiles are evident from graphs 9.3 and 9.4, with the Transarc electrode registering the higher temperature. Indicated in the figures below are the weld profiles and penetration obtained from the two electrodes.

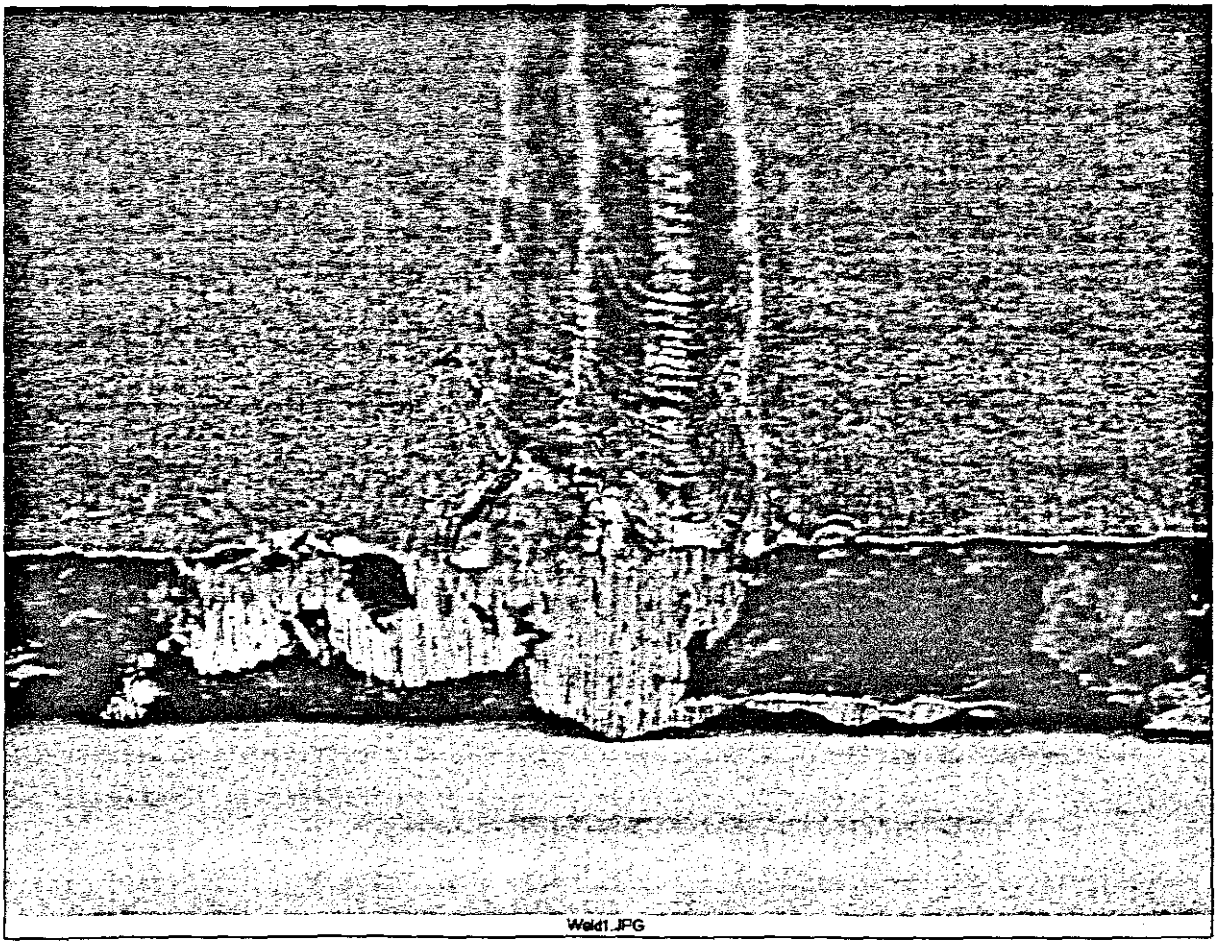

Figure 9.4. The spatter free welding profile and good penetration obtained from the Transarc 118 electrode

The Transarc 118 electrode produced a virtually spatter free weld having a good profile and penetration. The mechanical and metallurgical properties of the welds will be discussed in detail later on.

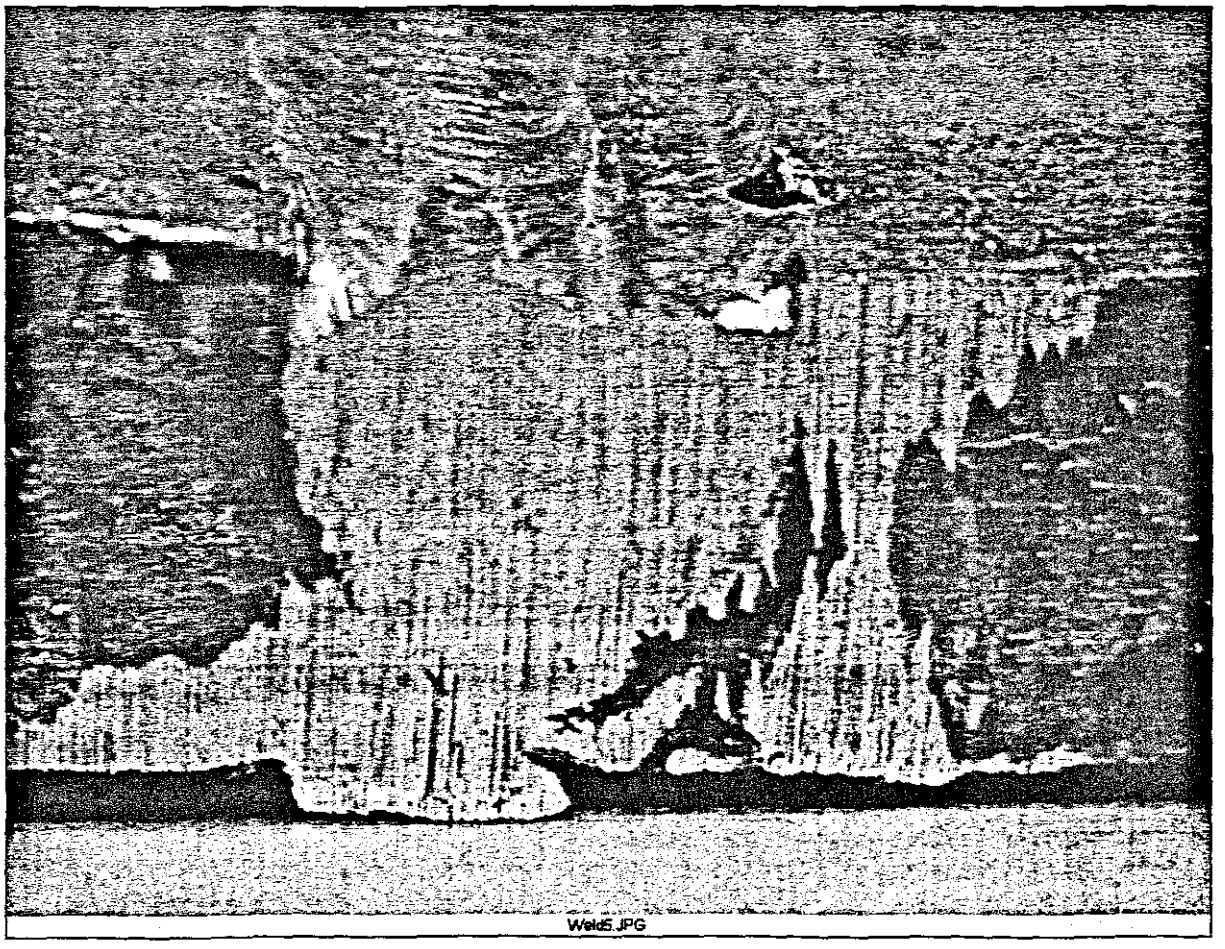

Figure 9.5. Depicting the weld produced using the Armcord LH electrode. Note the slag inclusion and increased spatter.

From the figure above, the increased spatter is quite clearly visible. A rather large slag inclusion due to poor de-slagging is visible. Some of the slag was however removed with a grinder, prior to applying the backing weld. The welding motion associated with the Transarc 118 electrode is much more smooth than that of the Armcord LH electrode. This is evident from the weld profile and the amount of weld spatter visible.

The temperature profiles produced by the two electrodes on welding the 16mm plates will now be discussed. Plates 2A & B were welded using the Transarc 118 electrode, whilst plates 3A & B were welded using the Armcord LH electrode. The temperature profiles were generated by the thermocouples as indicated in figure 9.2. The couples 3 and 7 are located opposite one another on the one end of the plate and as is evident from the graph, they detect the heat signature generated by the welding arc at approximately the same time. The slight difference in temperature between the two couples can be accounted for by the fact that the arc may be more biased to the couple reading the higher temperature. Close inspection of the following graphs will reveal this alternating of heat signature picked up the couples as the butt weld is being completed. The graphs also reveal the increase in parent metal temperature per completed run.

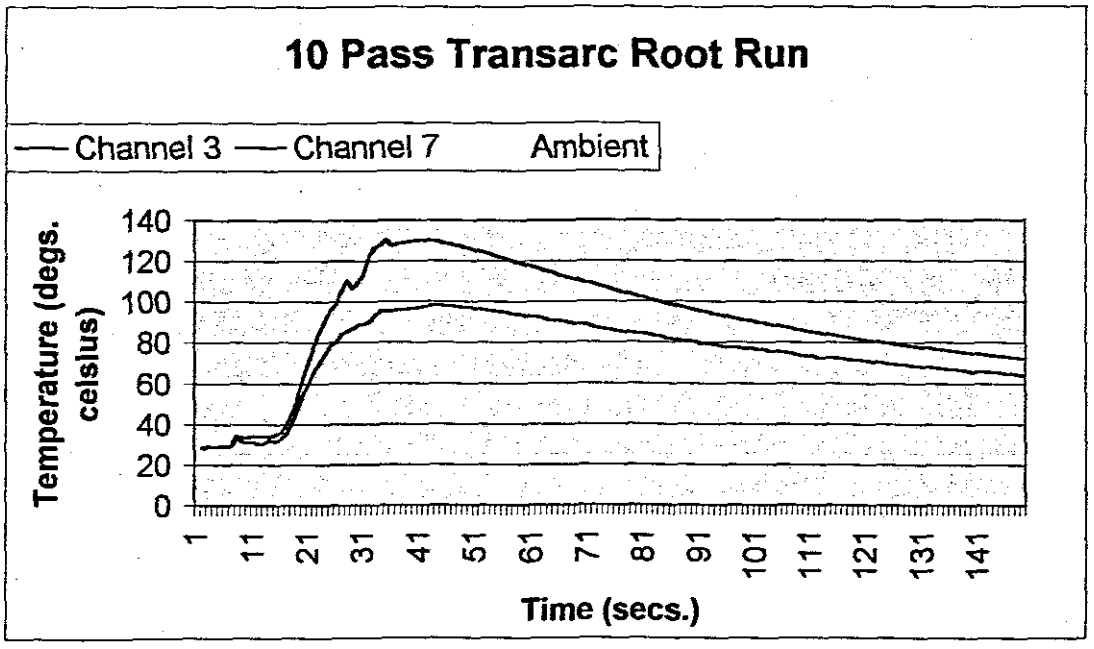

Graph 9.5 Depicting the root run for a 16mm plate

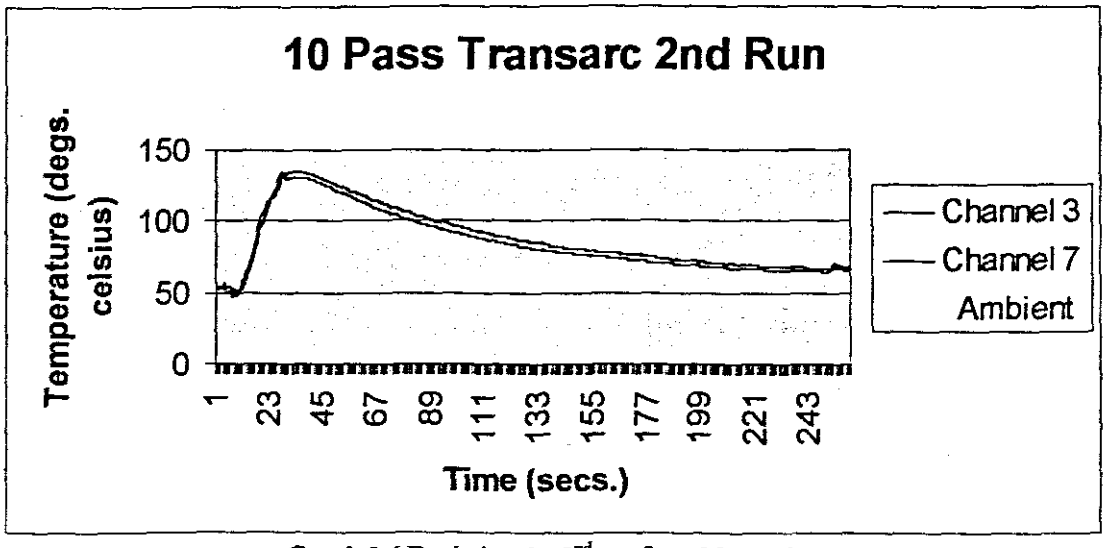

Graph 9.6 Depicting the 2nd run for a 16mm plate

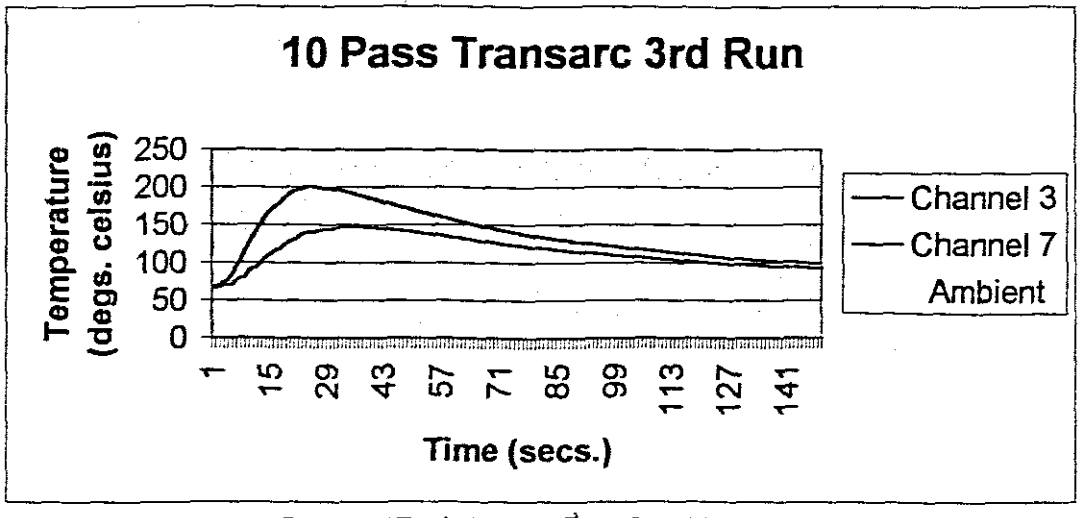

Graph 9.7 Depicting the 3rd run for a 16mm plate

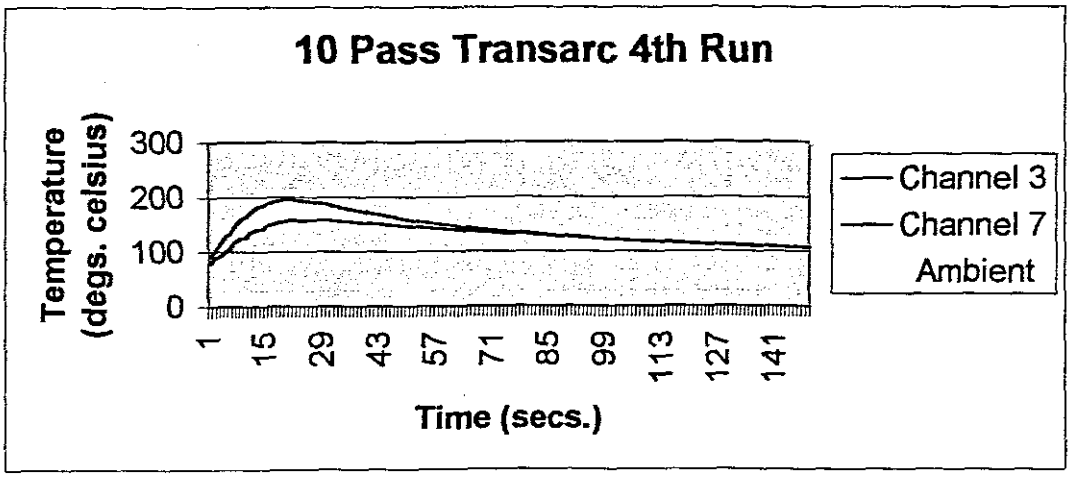

Graph 9.8 Depicting the 4th run for a 16mm plate

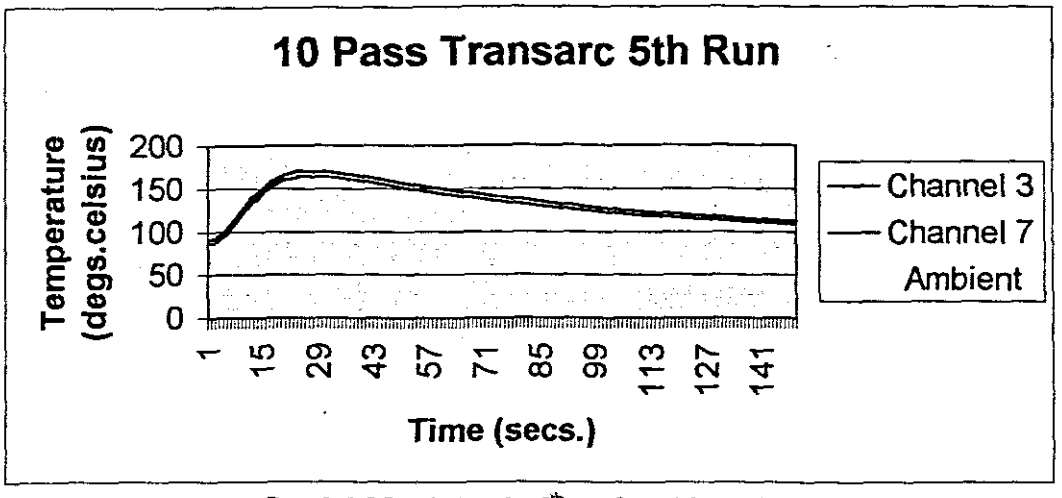

Graph 9.9 Depicting the 5th run for a 16mm plate

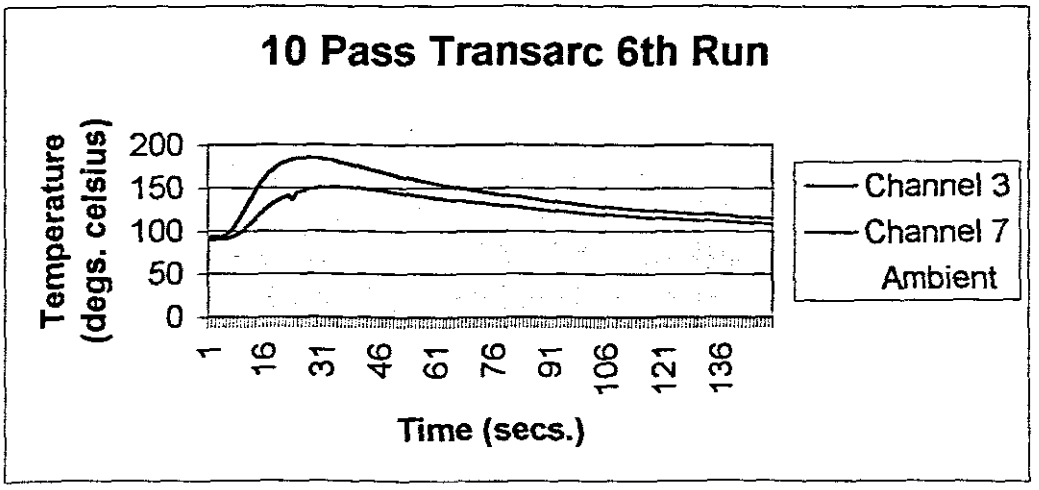

Graph 9.10 Depicting the 6th run for a 16mm plate

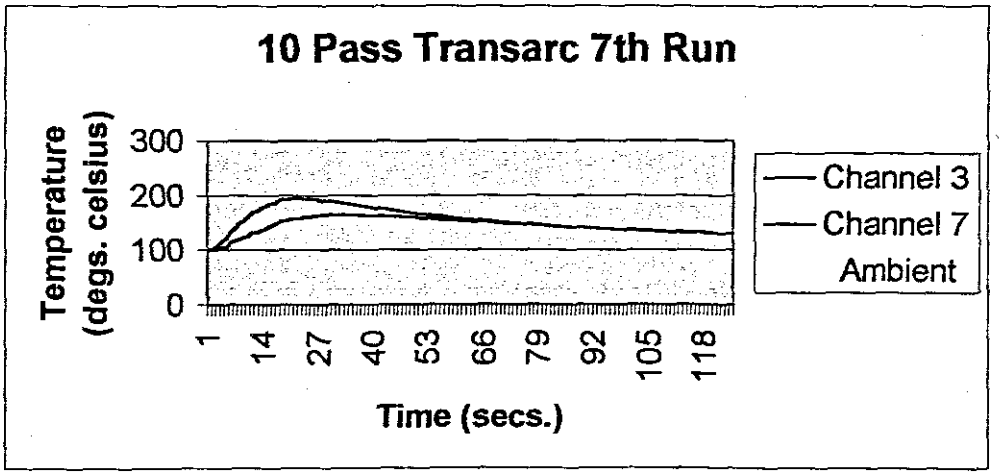

Graph 9.11 Depicting the 7th run for a 16mm plate

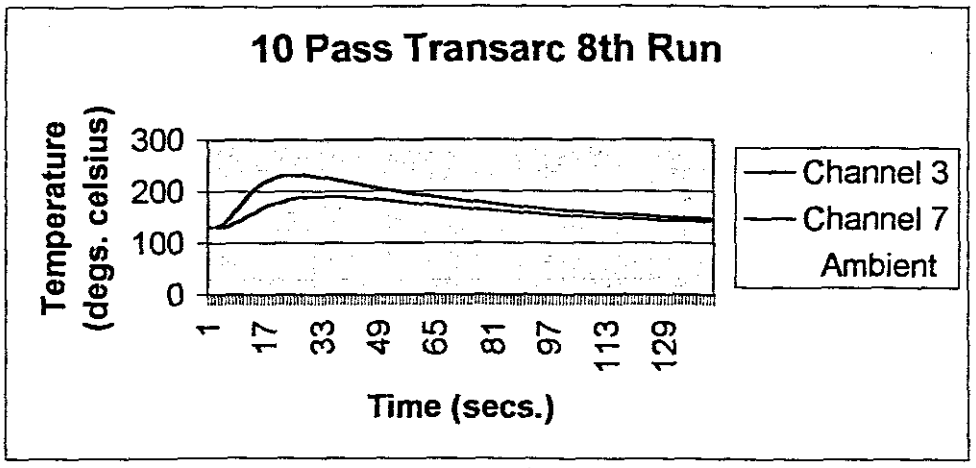

Graph 9.12 Depicting the 8th run for 16mm plate

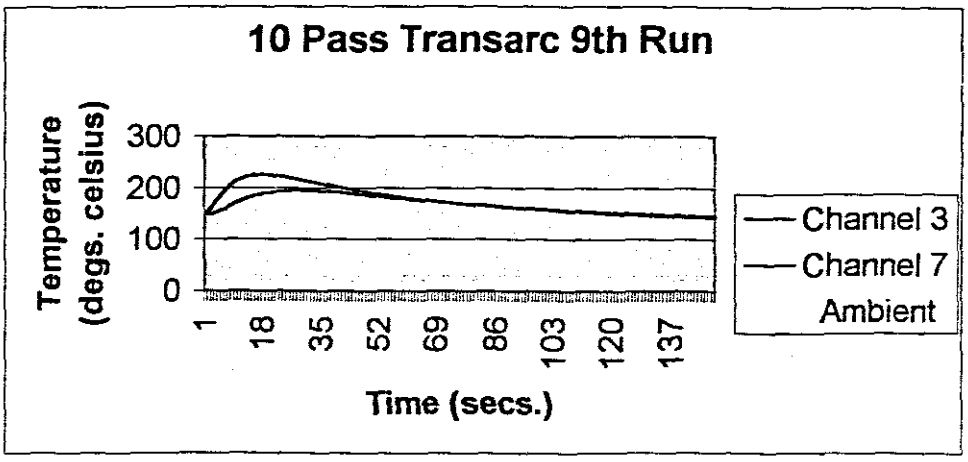

Graph 9.13 Depicting the 9th run for a 16mm plate

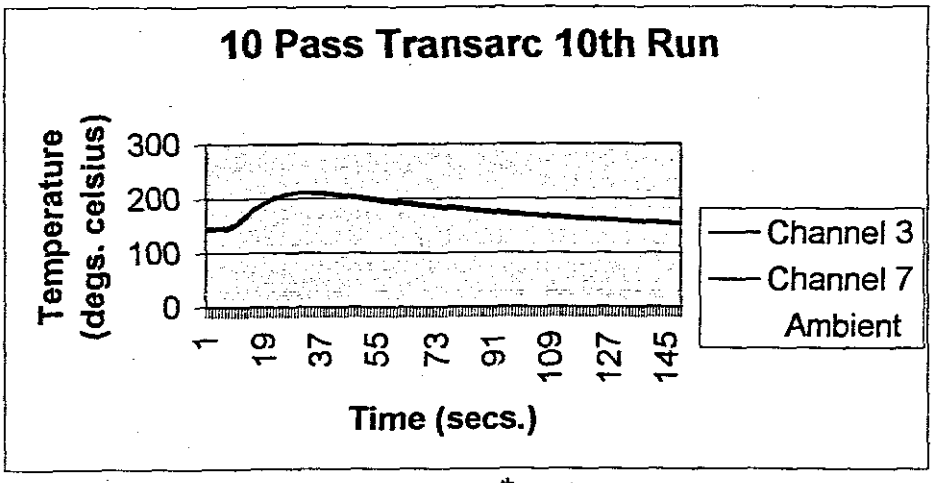

Graph 9.14 Depicting the 10th run for a 16mm plate

By inspection of the graphs above, it is evident that the base metal has experienced an increase in temperature from an ambient of 22°C to approximately 150°C during the course of a 12-pass weld. The following graphs depict the comparative heat signature produced by the welding arcs of the two electrodes. As would be expected, the Transarc 118 electrode produced a higher temperature spike than the Armcord LH electrode, due to its higher power consumption per run. It should, however, be mentioned that the Transarc 118 electrode has a 17% higher material deposition rate than the Armcord LH electrode, which will nullify its higher energy consumption per run.

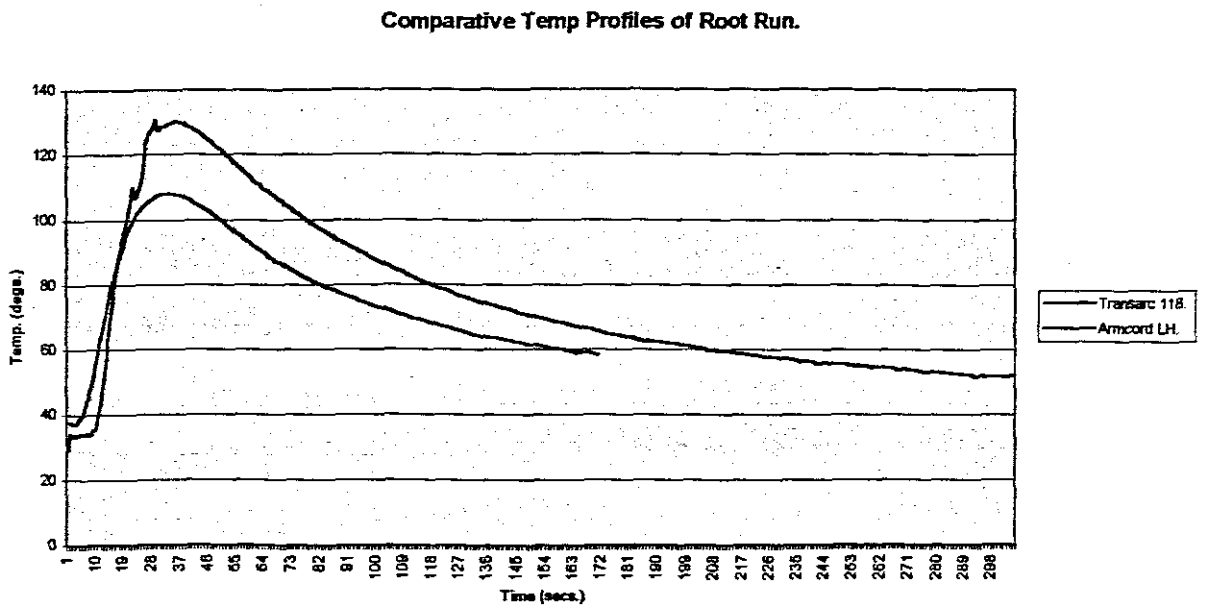

Graph 9.15 Depicting the comparative temperature profiles obtained for the two electrodes on a 10mm plate

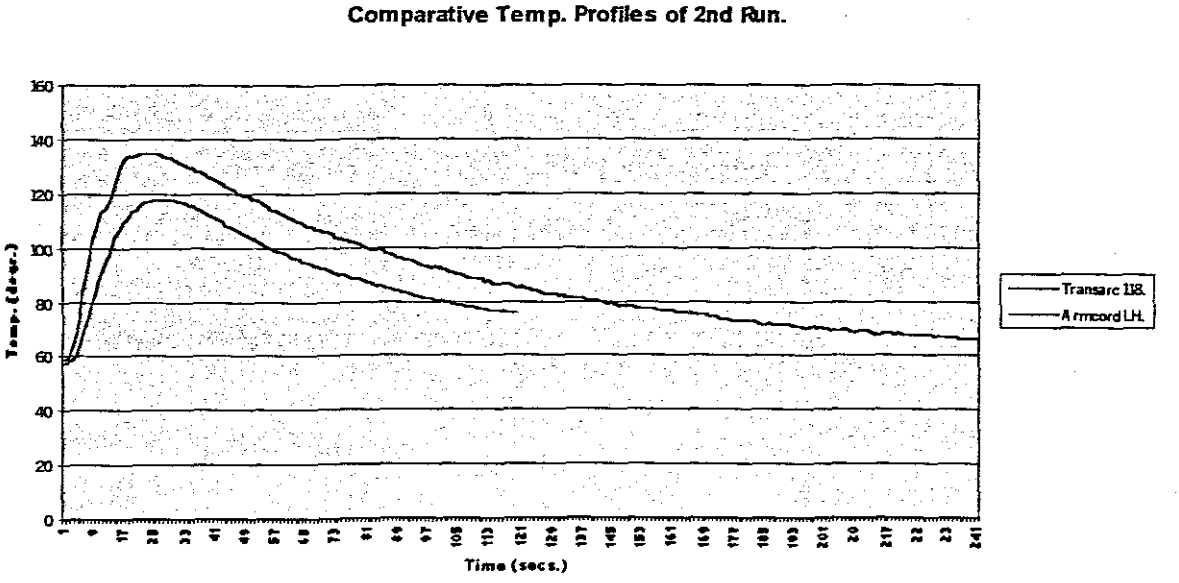

Graph 9.16 Depicting the comparative temperature profiles obtained for the two electrodes on a 10mm plate

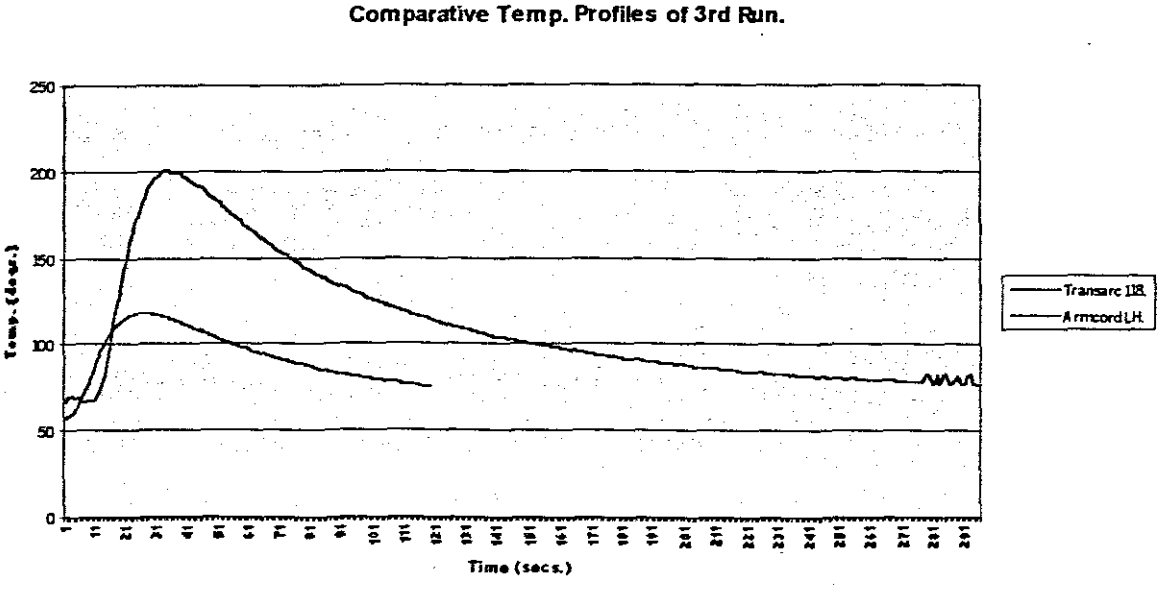

Graph 9.17 Depicting the comparative temperature profiles obtained for the two electrodes on a 10mm plate

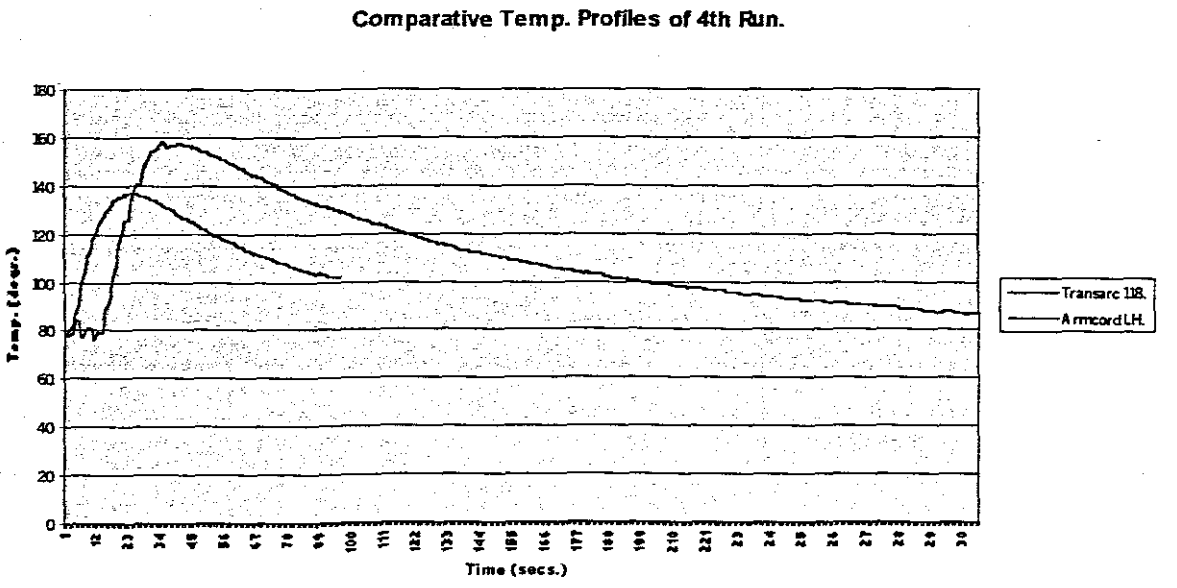

Graph 9.18 Depicting the comparative temperature profiles obtained for the two electrodes on a 10mm plate

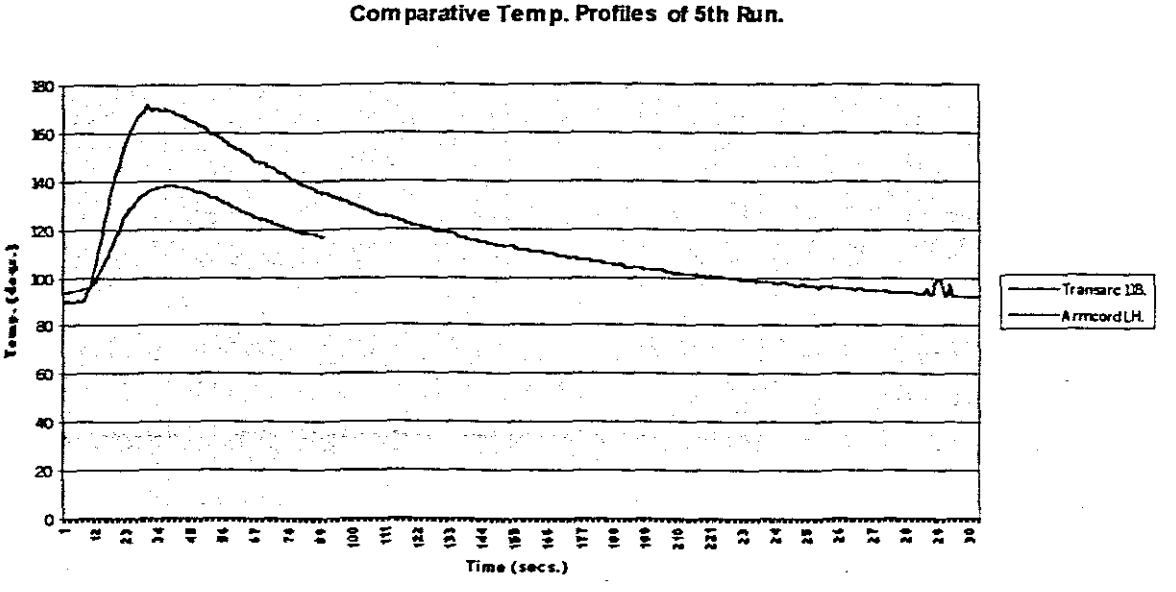

Graph 9.19 Depicting the comparative temperature profiles obtained for the two electrodes on a 10mm plate

9.6 Metallurgical Samples

The following metallurgical micrographs were produced by disecting the cross-section of the welds produced by both the Afrox Transarc 118 and Oerlikon Armcord LH. electrodes. Utilising the microscope and the digital camera with its software, the following micrographs were obtained from specimens exposed to a nital etchant for 10 seconds.

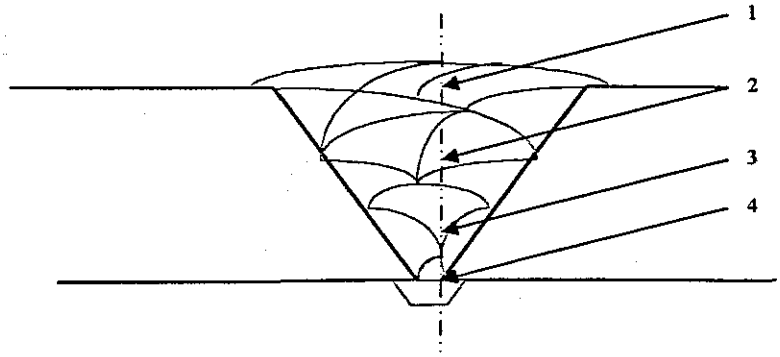

Figure 9.6. Depicting the cross-section of a 10-Pass Transarc Weld and the numbered positions from which micrographs were taken.

Micrograph 1.

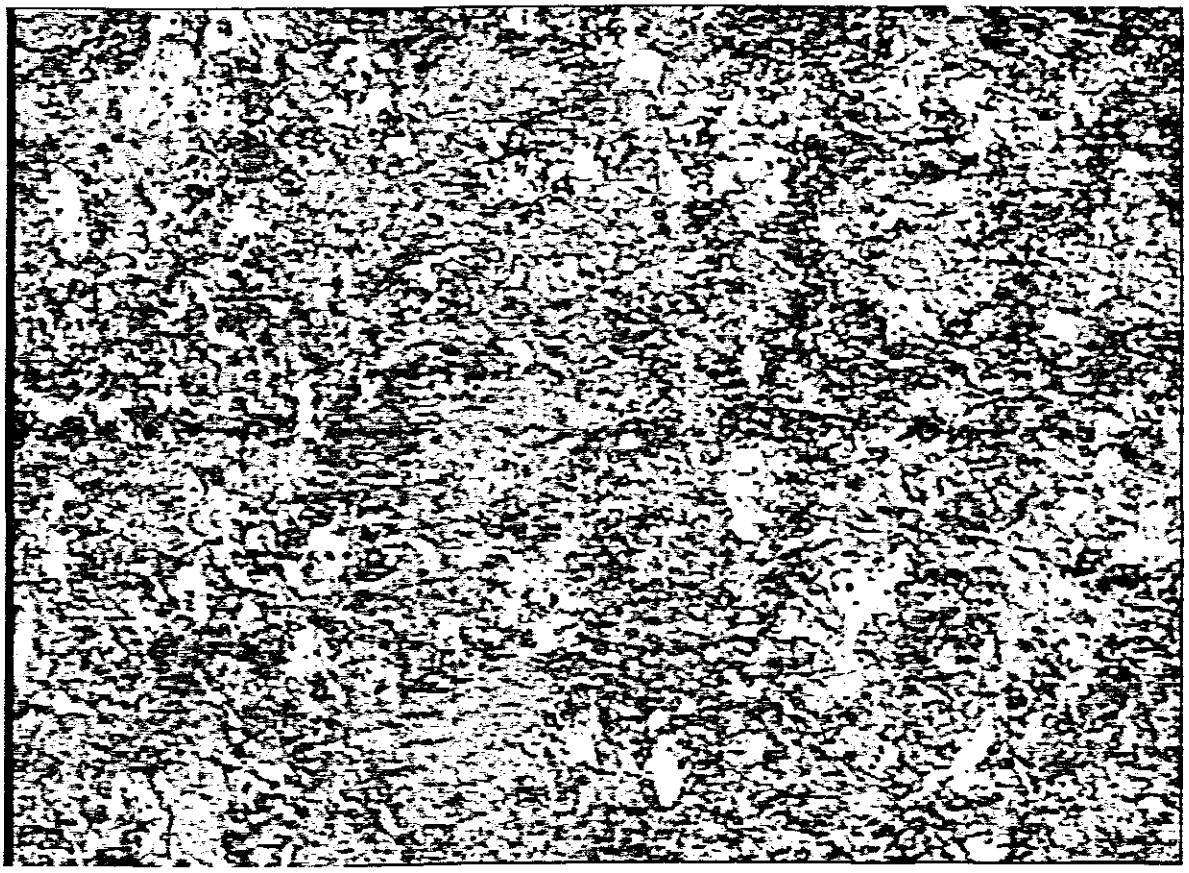

Figure 9.7. Cap of weld contains primary ferrite, α (white) and sorbitic pearlite.
All Micrographs Etched with 2% nitric acid in alcohol. Magnification 500x

Micrograph 2.

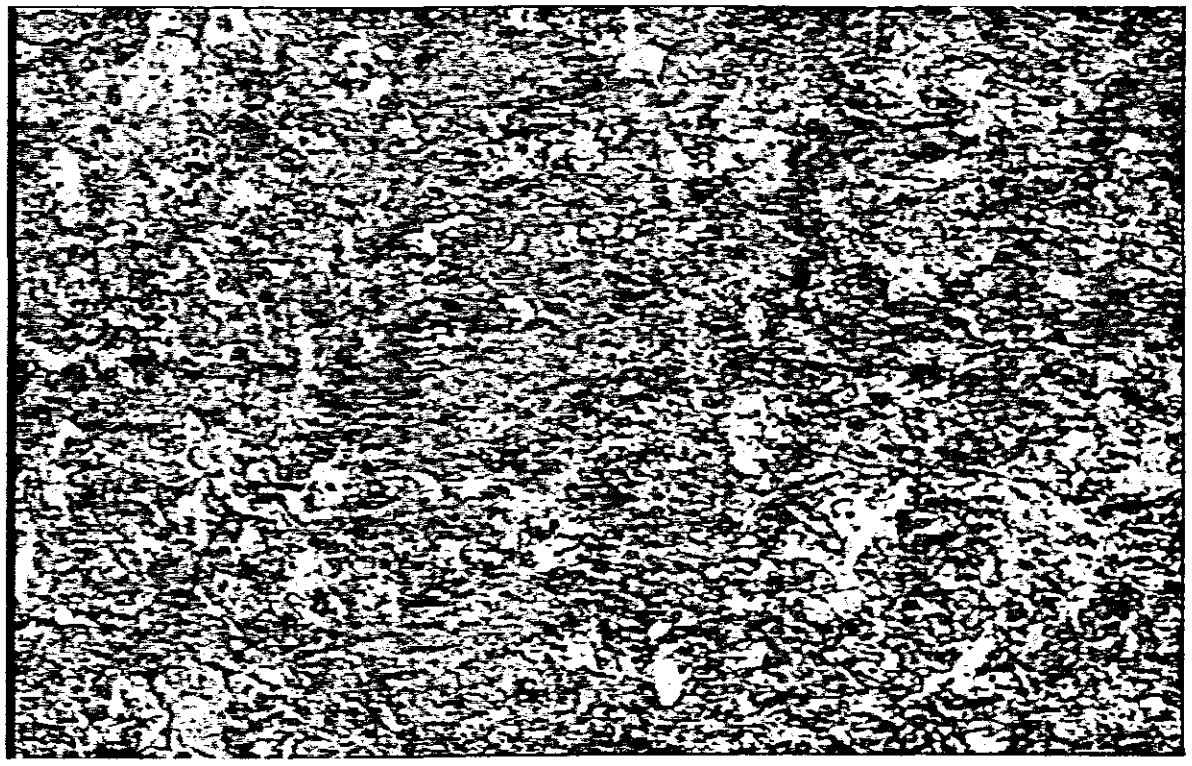

Figure 9.8. Middle of the weld maintains ferrite sorbite microstructure. Magnification 500x.

Micrograph 3.

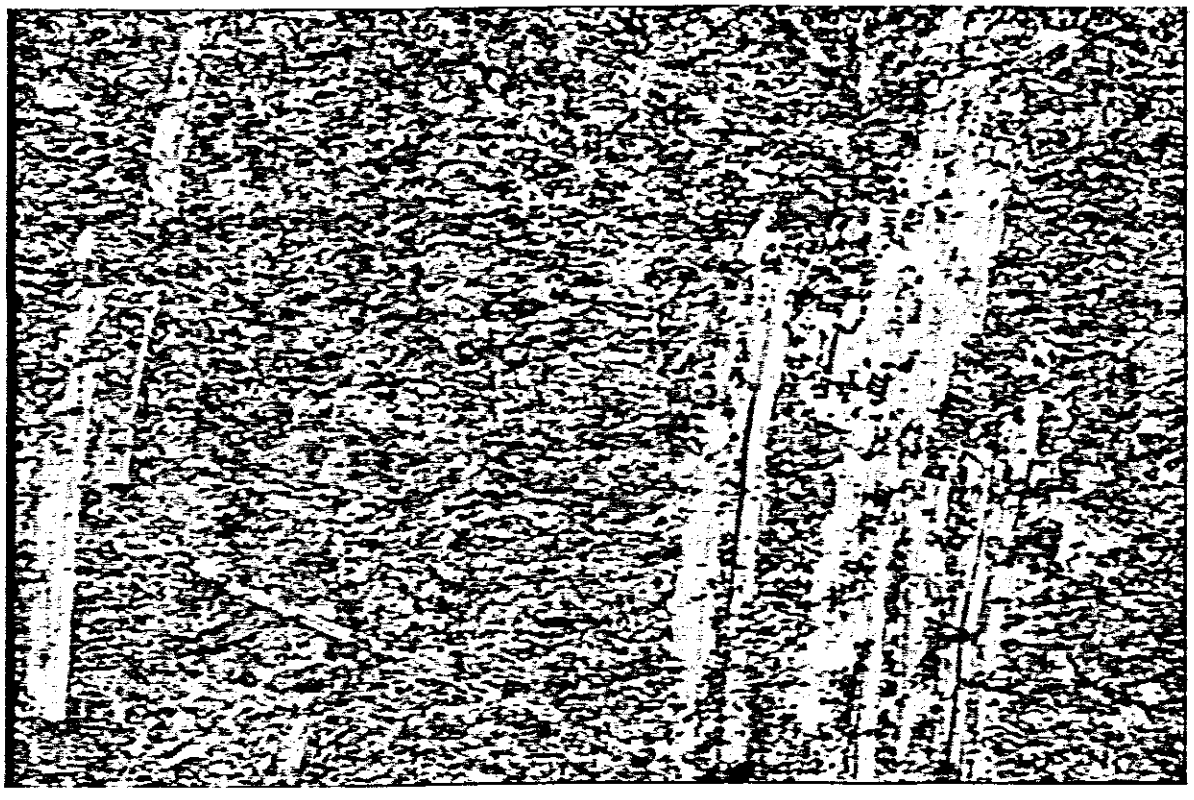

Figure 9.9. Ferrite lathes interspersed in an almost primarily sorbite microstructure. Magnification 500x.

Micrograph 4.

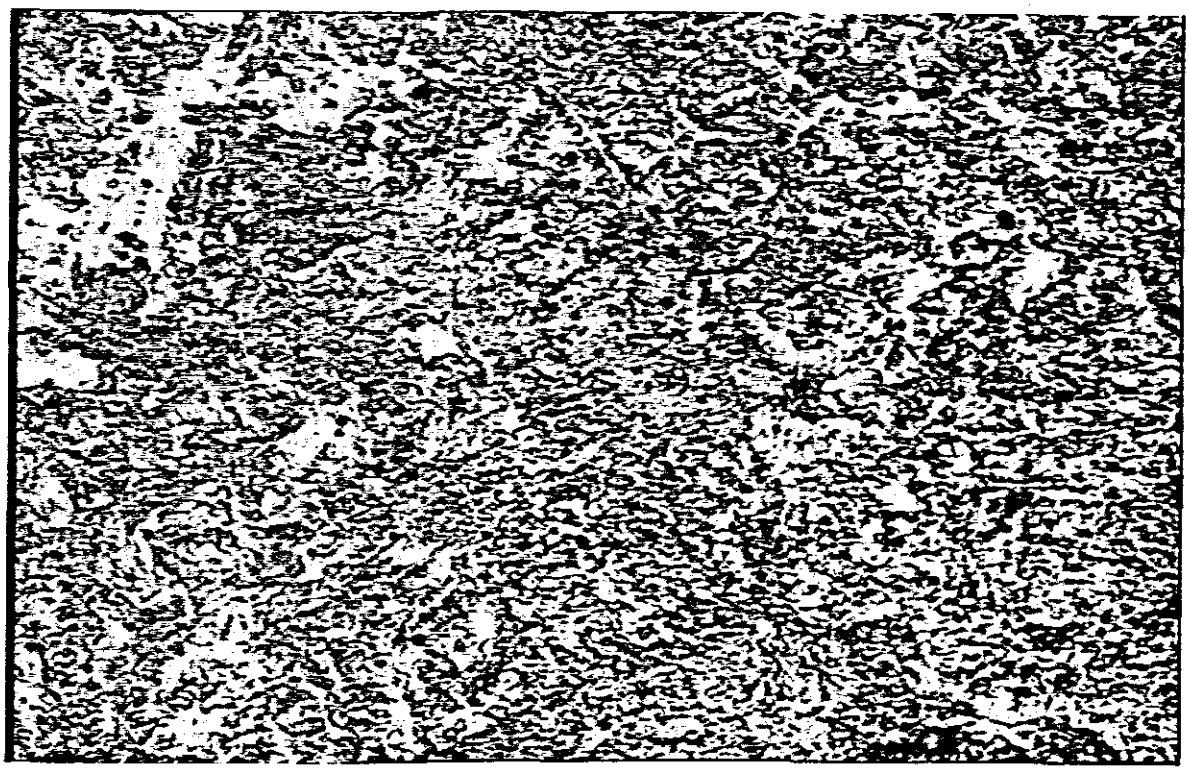

Figure 9.10. Here we find further dispersion of ferrite to leave almost 100% sorbite Magnification 500x.

From the preceding micrographs, it can be seen that the centre of the Transarc 118 weld is dominated by austenitic ferrite and pearlitic sorbite, which is ductile, giving the weld excellent mechanical properties. The left hand side of the same weld will now be analysed as is depicted in the figure 9.11 below.

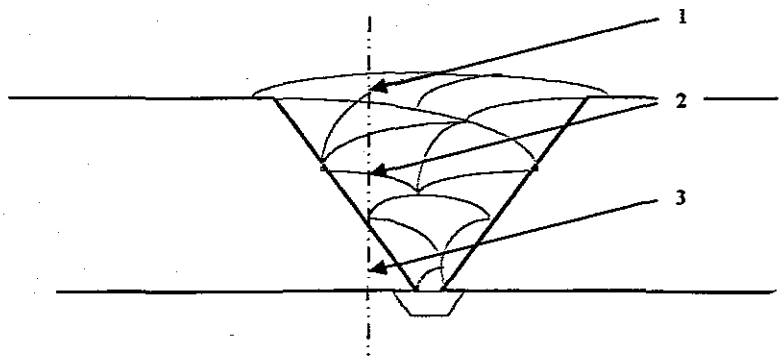

Figure 9.11. Depicting the cross-section of a 10-Pass Transarc Weld and the numbered positions from which micrographs were taken.

Micrograph 1.

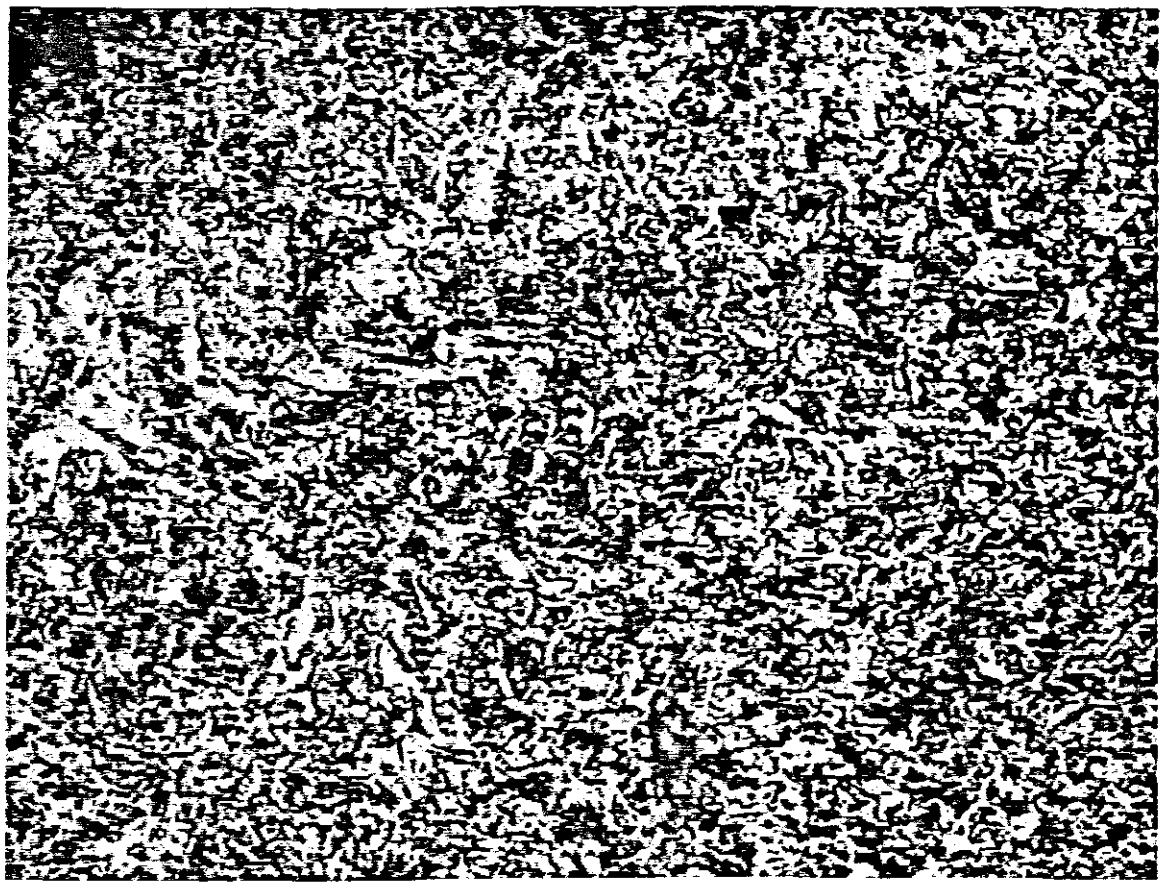

Figure 9.12. Austenite grains, showing the internal structure of martensite 500x

Micrograph 2.

Figure 9.13. Shows a ferrite network (white) enclosing grains of lamellar pearlite. 500x.

Micrograph 3.

Figure 9.14. Depicts a phase transformation. The left contains sorbitic pearlite, whilst the right contains ferrite (white) interspersed in grains of sorbitic pearlite. 500x.

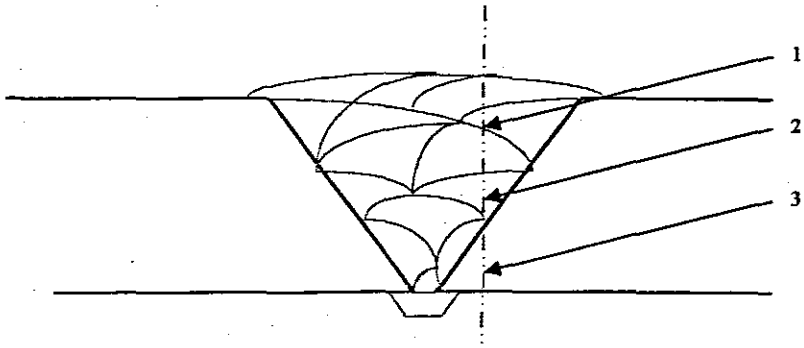

Figure 9.15. Depicting the cross-section of a 10-Pass Transarc Weld and the numbered positions from which micrographs were taken.

Micrograph 1.

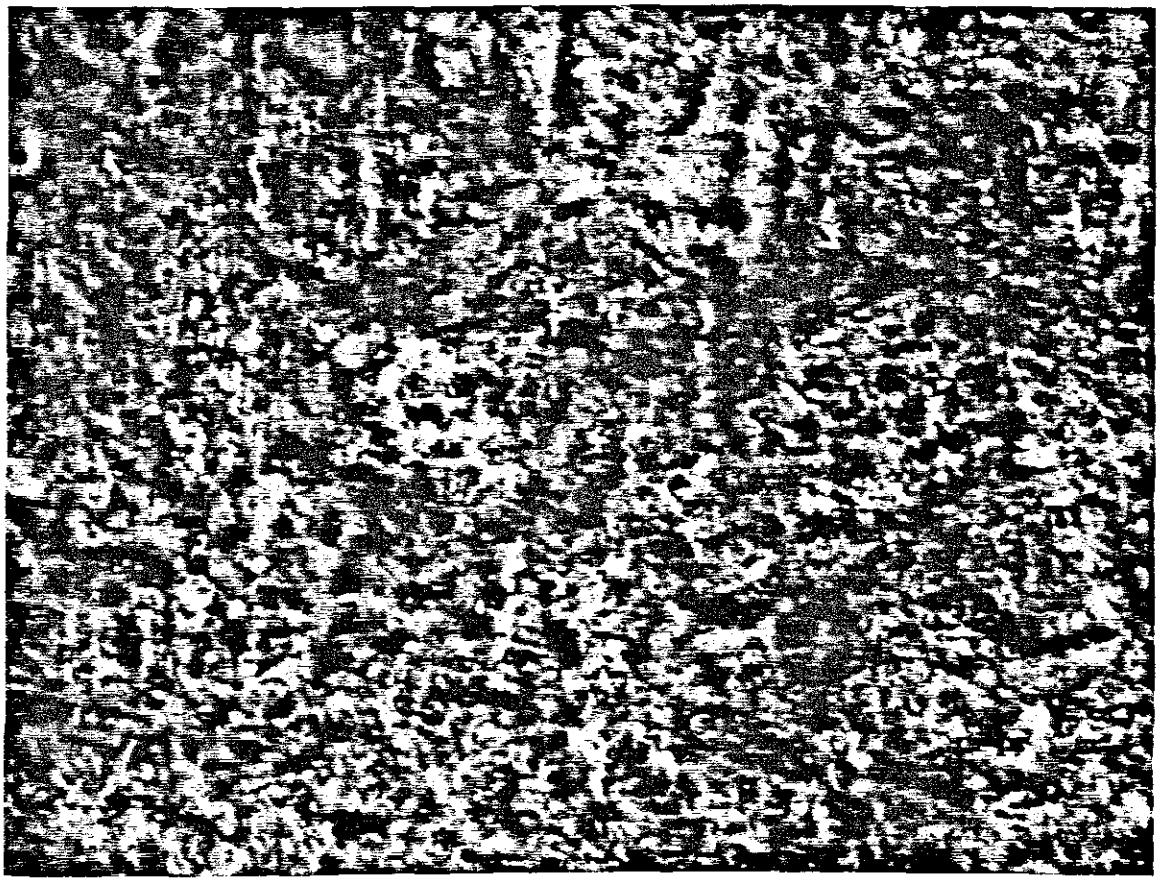

Figure 9.16. Depicts fine grained ferrite and sorbitic pearlite. 500x.

Micrograph 2.

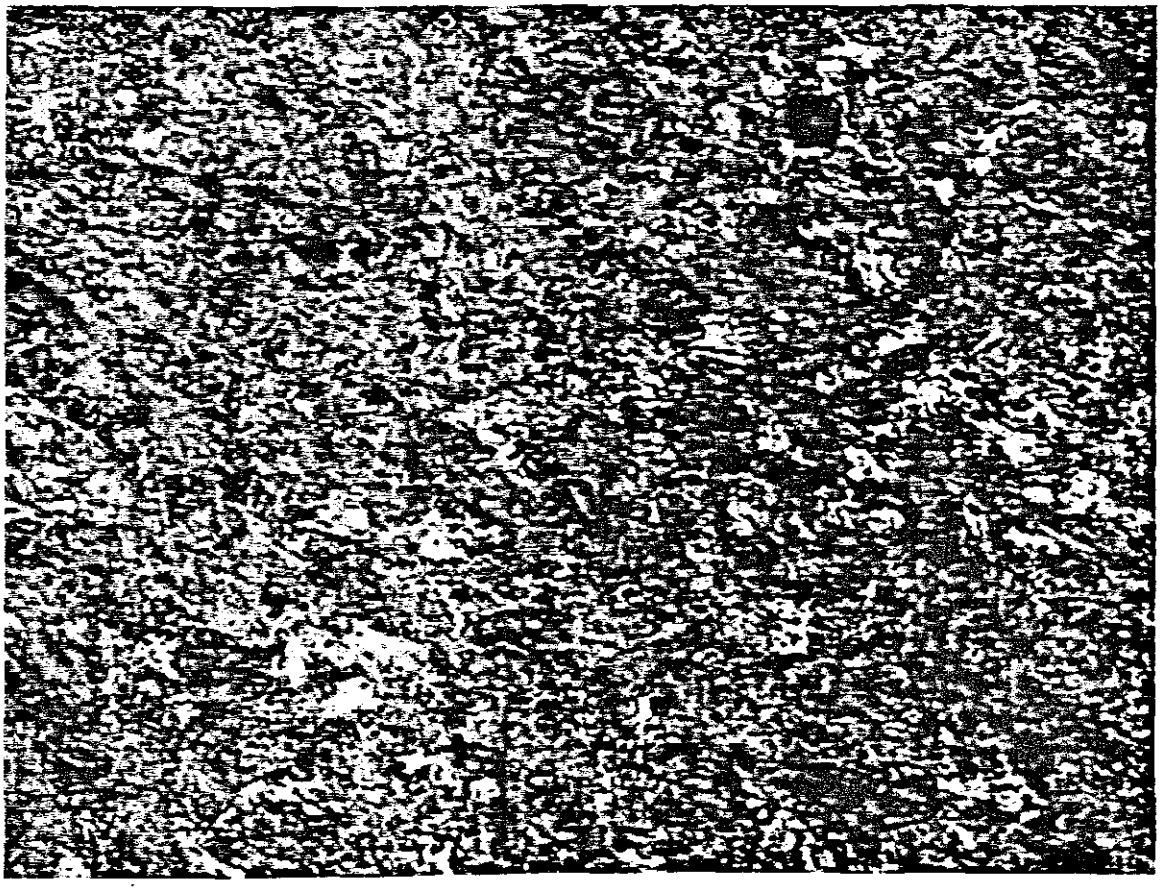

Figure 9.17. Depicting ferrite and fine lamellar and sorbitic pearlite. Also depicted is a slag inclusion, top right. 500x.

Micrograph 3.

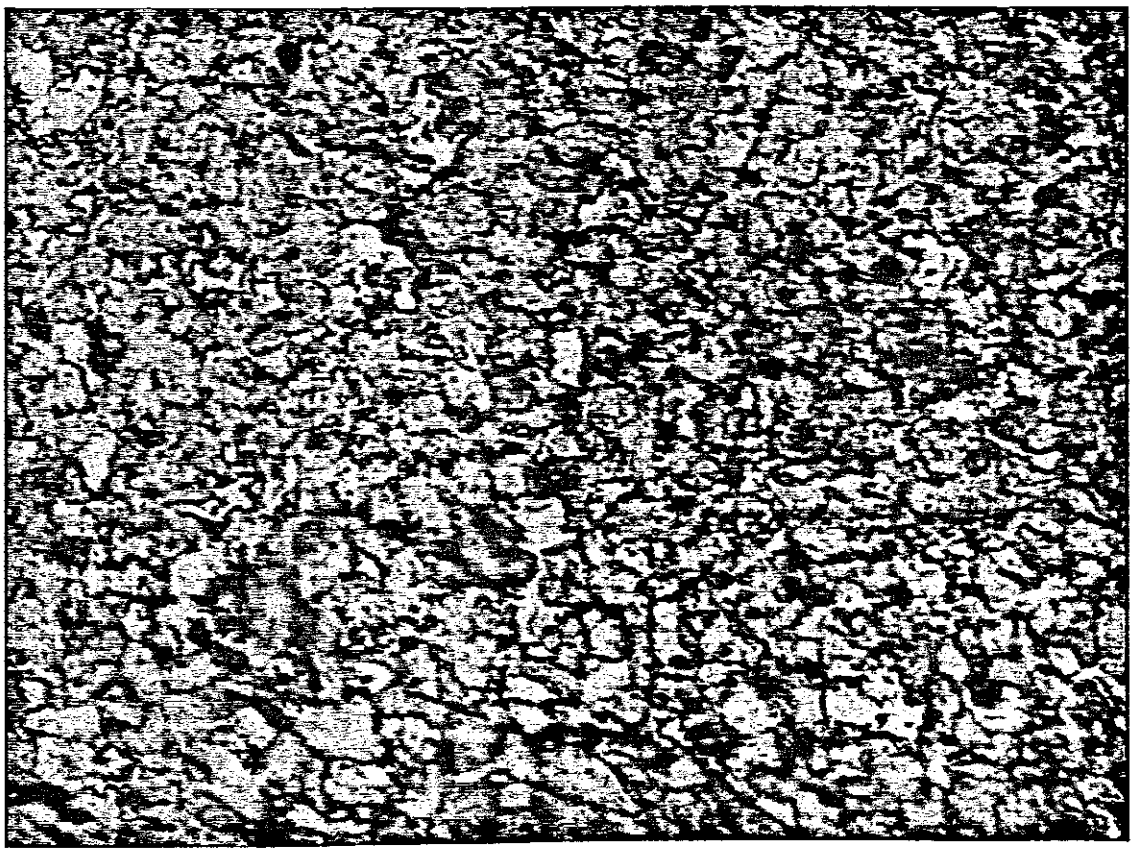

Figure 9.18. Depicting ferrite and fine lamellar pearlite. 500x.

9.7 Tensile Testing

To ascertain the effectiveness of the welding procedure and the quality of the welds produced, tensile testing was carried out. The specimens were machined from the post welded plates as is depicted in the figure below. The weld formed the centre of the tensile test specimens. Due to the thickness of the plates, (16mm) and the resulting difficulty in obtaining a tensile testing machine capable of pulling that thickness, it was decided to machine the specimens down to a thickness of 6mm, taking special care that the material is removed equally from both sides of the specimen whilst at the same time limiting heat input due to the machining process so as to limit any negative metallurgical effects on the welds.

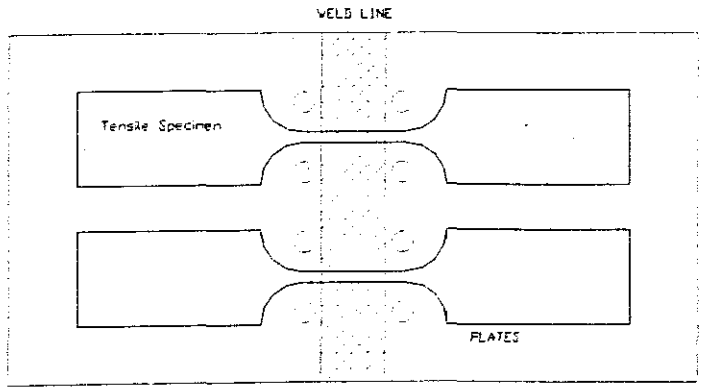

Figure 9.19. Depicting the layout of the tensile test specimens

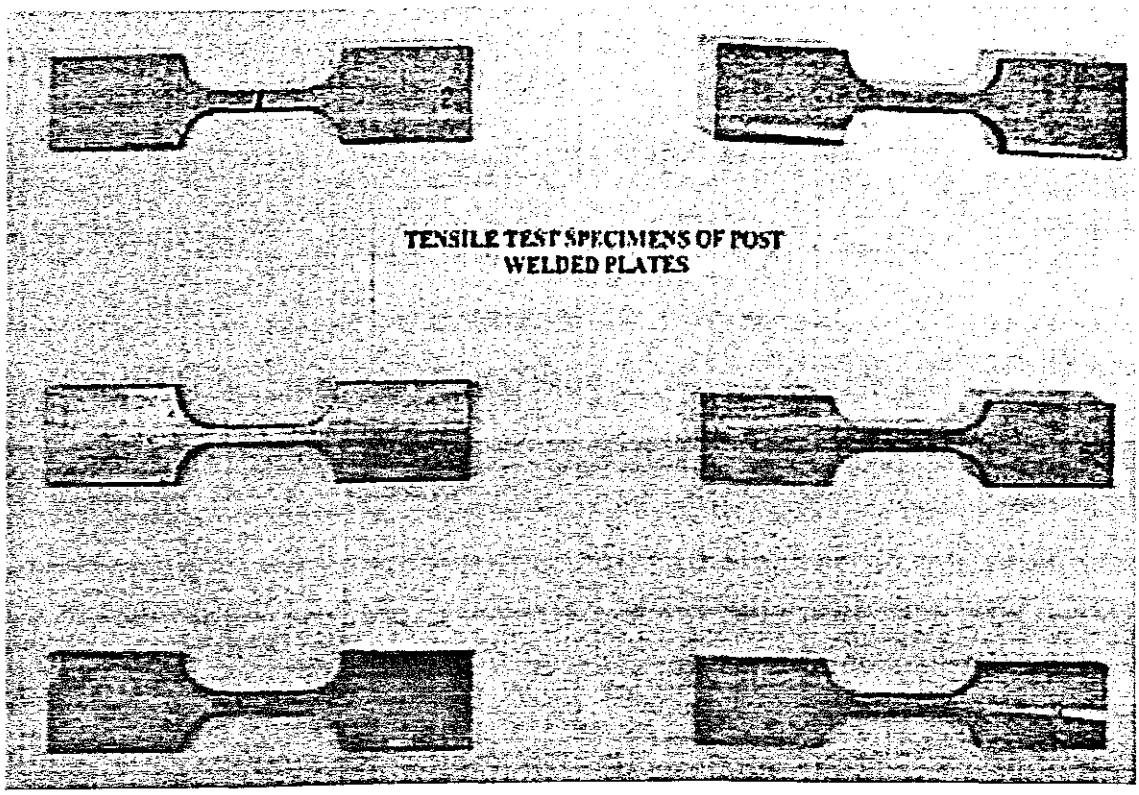

Figure 9.20. Depicting some of the post-machined tensile test specimens

The specimens were then subjected to an uni-axial tensile test using the electronically controlled tensile tester available in the Material Science Laboratory yielding the following results:

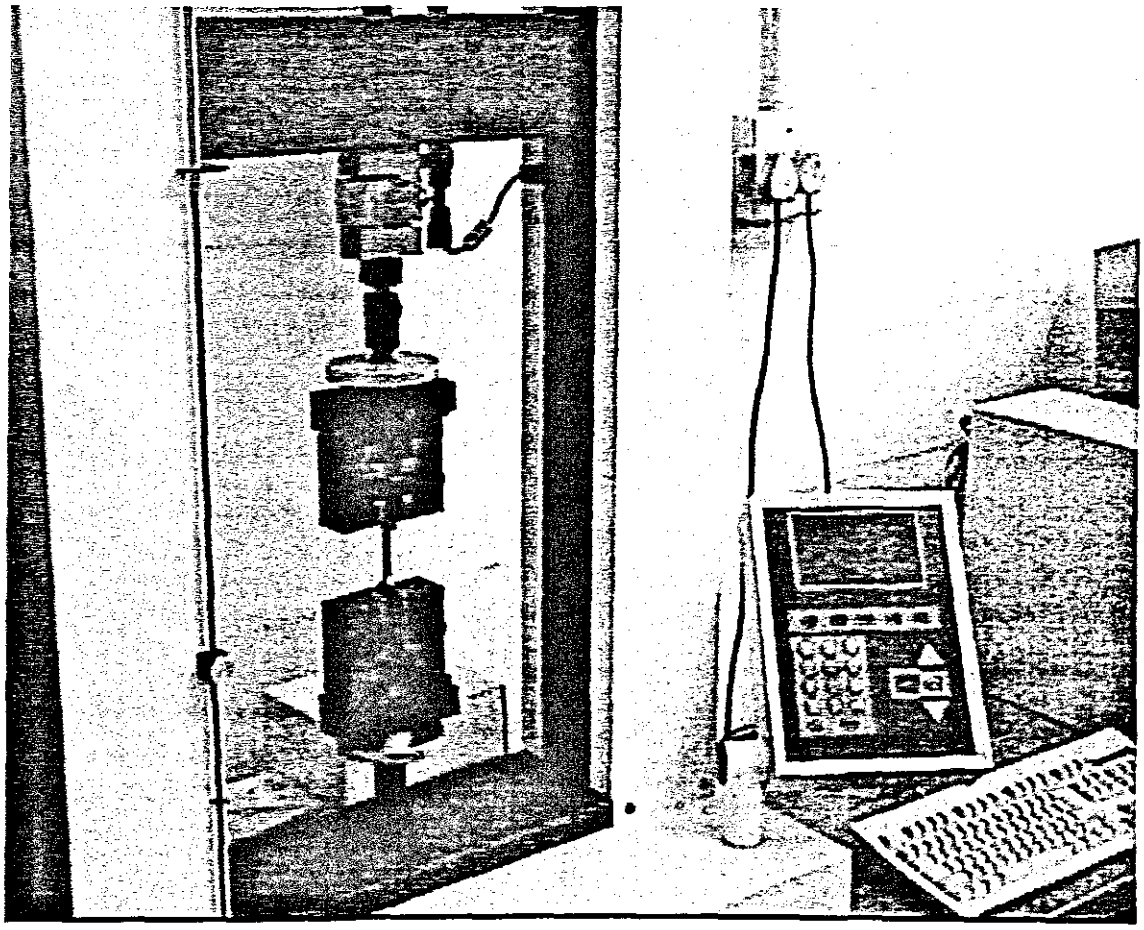

Figure 9.21. Depicting the computerized Houndsfield tensile tester

Visible in the figure is the PLC control panel on which all parameters for the test can be set. This unit interfaces with the hardware stored on the computer seen in the background on which all test data is stored. It is from here that the graphical results of the test can later be retrieved for further analysis. The tensile test specimen seen here is held in place by high strength anti-friction grips. In the discussion of results obtained later, it will be seen that on occasion, a fair amount of axial slip does take place. This is visible from the slow increase in the stress strain rate. The actual stress strain measurements are obtained from the load cell and transducer mounted on the top bridge. The rate of motion of the top bridge is controlled by means of hydraulically powered lead screws mounted in the two side pillars.

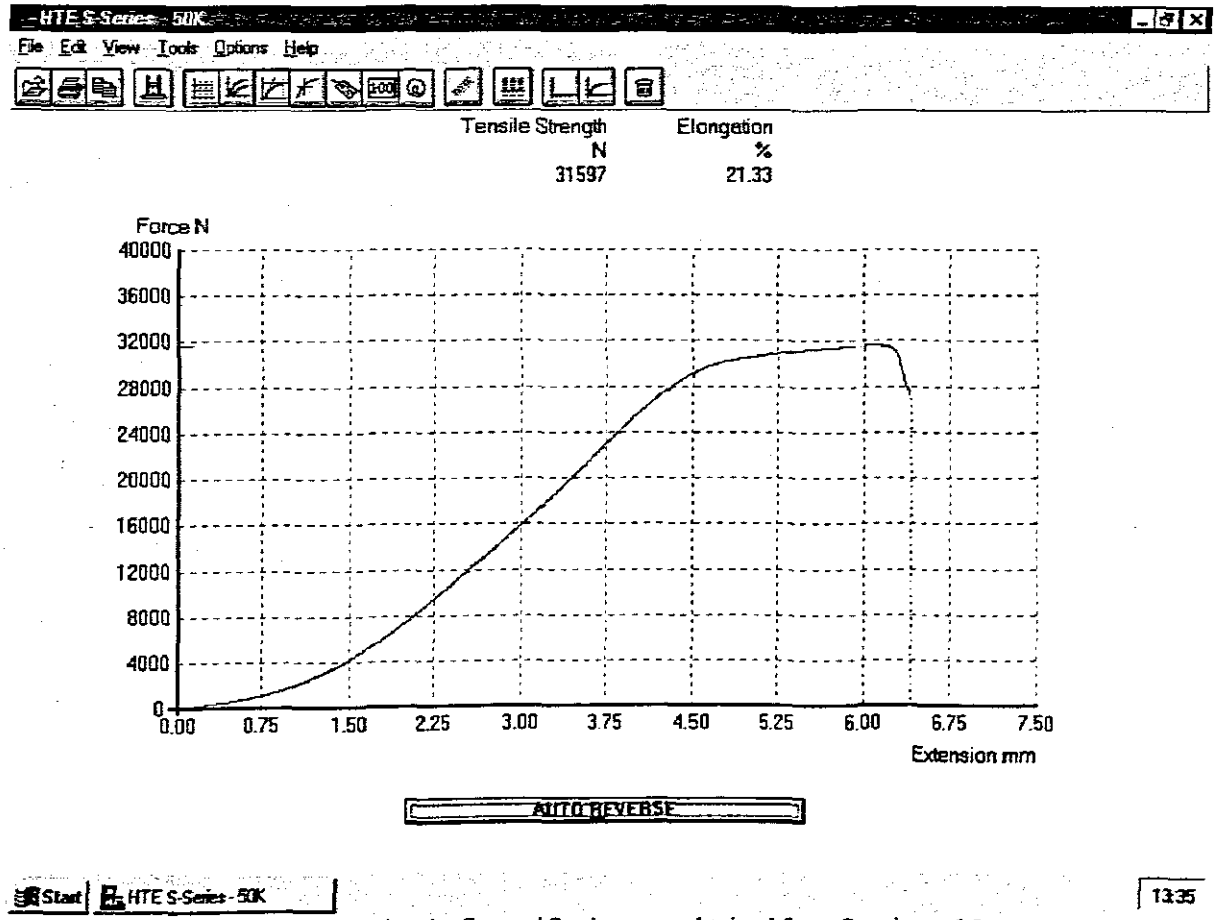

Figure 9.22. Depicting the Stress / Strain curve obtained from Specimen 6.2

The stress strain curve depicted above was obtained from tensile test specimen 2 machined from plate 6. The welding electrode used was Oerlikon Armcord LH. The UTS obtained from the test is 31.597kN. The cross-sectional area that was exposed to this load was 6 x 6 mm^2. From the following simple calculation the yield strength of the weld can be determined.

$$UTS. = \frac{F}{A}$$

$$UTS. = \frac{31.597 \times 10^3}{36 \times 10^{-6}}$$

$$UTS. = 877.69MPa$$

The data obtained from ISCOR gives ROQ-tuf AD690 a UTS. of 850 Mpa. This would imply that the weld was in fact stronger than the plate. A fair amount of slip at the grips took place, as is evident from the first portion of the curve. This would imply that the elongation percentage obtained is misleading and probably much too high. The parent material and the weld remained exceptionally ductile, however, as is evident from the rest of the stress / strain curve.

Young's Modulus was determined from the curve as follows:

$$E = \frac{\sigma}{\varepsilon}$$

$$E = \frac{\sigma_2 - \sigma_1}{\varepsilon_2 - \varepsilon_1}$$

$$E = \frac{805.55 \times 10^6 - 0}{4.5 \times 10^{-3} - 1 \times 10^{-3}}$$

$$E = 230.15GPa$$

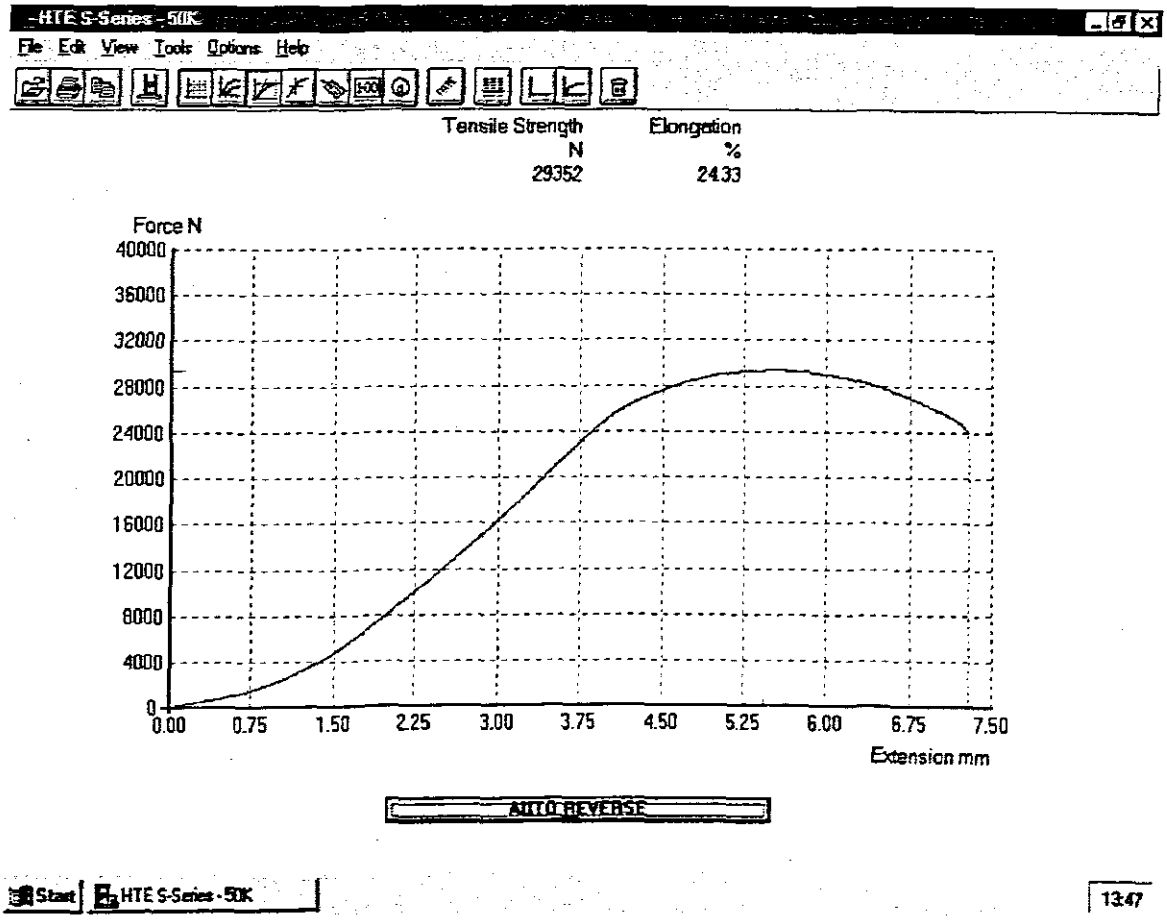

Figure 9.23. Depicting the Stress / Strain curve obtained from Specimen 8.2

The result above was obtained from specimen 2 machined from plate 8. The electrode utilised was the Transarc 118 electrode. It is evident once again from the start of the curve that a fair amount of slip has taken place prior to the generation of useful data. The specimen generated a UTS. of 29.352kN over a cross-sectional area of 36 mm^2. From the following simple calculation the yield strength of the weld was once again determined.

$$UTS. = \frac{F}{A}$$

$$UTS. = \frac{29.352 \times 10^3}{36 \times 10^{-6}}$$

$$UTS. = 815.33MPa$$

This result, although less than that obtained for Armcord LH., is still higher than the UTS. supplied by ISCOR for the steel. The percentage elongation for the specimen was determined at 24.33%. The Young's Modulus was once again determined for this specimen.

$$E = \frac{\sigma}{\varepsilon}$$

$$E = \frac{\sigma_2 - \sigma_1}{\varepsilon_2 - \varepsilon_1}$$

$$E = \frac{722.22 \times 10^6 - 0}{3.8 \times 10^{-3} - 1 \times 10^{-3}}$$

$$E = 257.9 GPa$$

From the results obtained from the tests, it may be safely concluded that the welding procedure employed is acceptable and that the welds produced by both electrodes are mechanically sound. Additional test results and pictures may be found in Appendix E.

9.8 Finite Element Analysis

As was stated earlier in the literature survey, a coupled thermo mechano metallurgical analysis was carried out using the commercially available finite element package Systus. Systus requires the continuos cooling transformation (CCT) data for the steel on whch the analysis is to be carried out. This information is entered as an input deck to facilitate the solver to produce meaningful results. Extreme difficulty was experienced in obtaining CCT and TTT data for ROQ-tuf AD690. An attempt was made to create our own TTT data by using the Johnson-Mehl-Avrami-Kolmogorov equation.

$$f(t) = 1 - \exp\left[-\frac{\pi}{3} N G^3 t^4\right] \qquad (1)$$

where: N is the nucleation rate and assumed constant. The nucleation rate is the number of nuclei that form in a unit volume (usually $1 mm^3$) per second.

G is the growth rate and assumed constant.

t is the time in seconds.

The JMAK equation represents the transformation kinetics at a particular temperature. From a series of S-shaped JMAK curves a TTT diagram can be generated. The TTT diagram relates metallurgical phase transformation as a function of time and temperature, which is ideal for curve fitting the linear equations required in a Finite Element Analysis. As with all finite element software, the procedure starts with the construction of the geometry, in this instance, only one half of the plate was modeled. This geometry is then transformed into an edge, which is meshed. The various material properties and boundary conditions are assigned to the nodes of the mesh. Utilising the Fortran code developed by Oliver et al, representing the moving welding arc, the finite element analysis was carried out for a 12-pass weld. The results obtained are as follows:

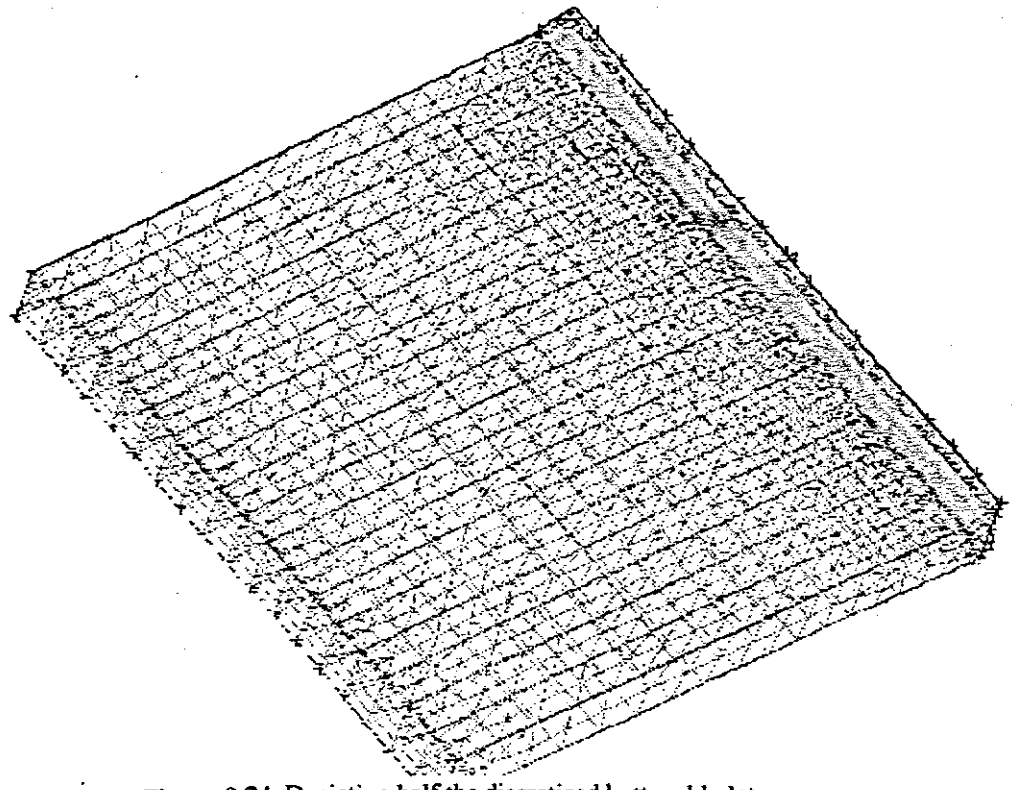

Figure 9.24. Depicting half the discretised butt-weld plate

The plate was made up of five thousand 3-D brick elements. Node refinement was employed in the regions closer to the weld to increase the accuracy of results obtained. The Fortran code representing the welding arc enabled the user to vary the velocity and depth at which the arc traversed the plate. The time required to carry out the actual welding operation was computed by the BDH100 welding machine at 10mm/s. This was the value of velocity used during the analysis. Inter-pass cooling was accounted for by running the analysis with the arc power set at zero.

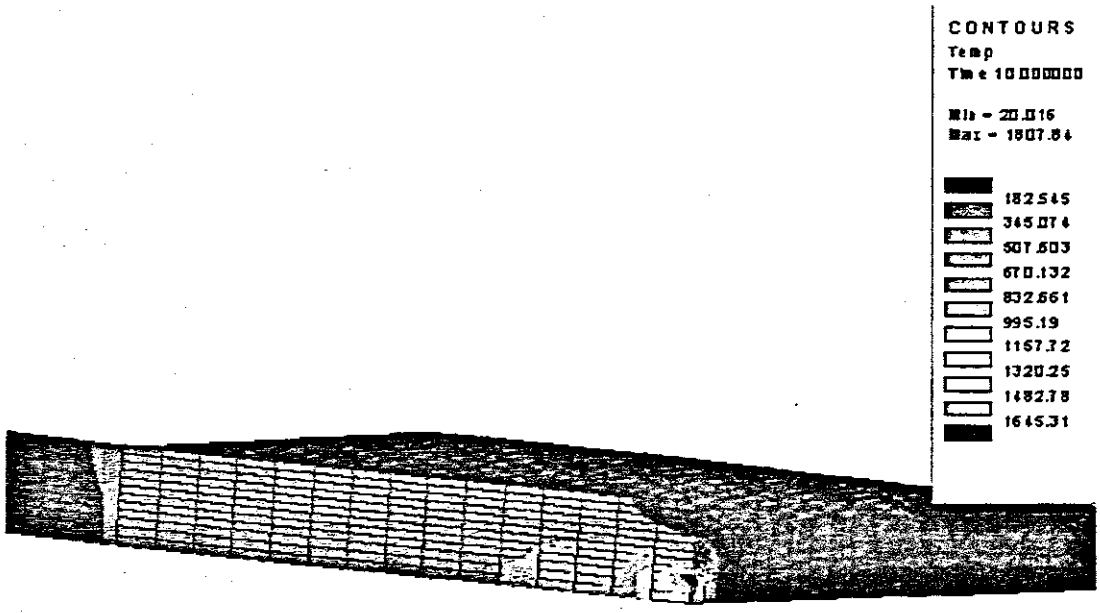

Figure 9.25. Depicting the temperature distribution profile for a 16mm plate at the end of root run

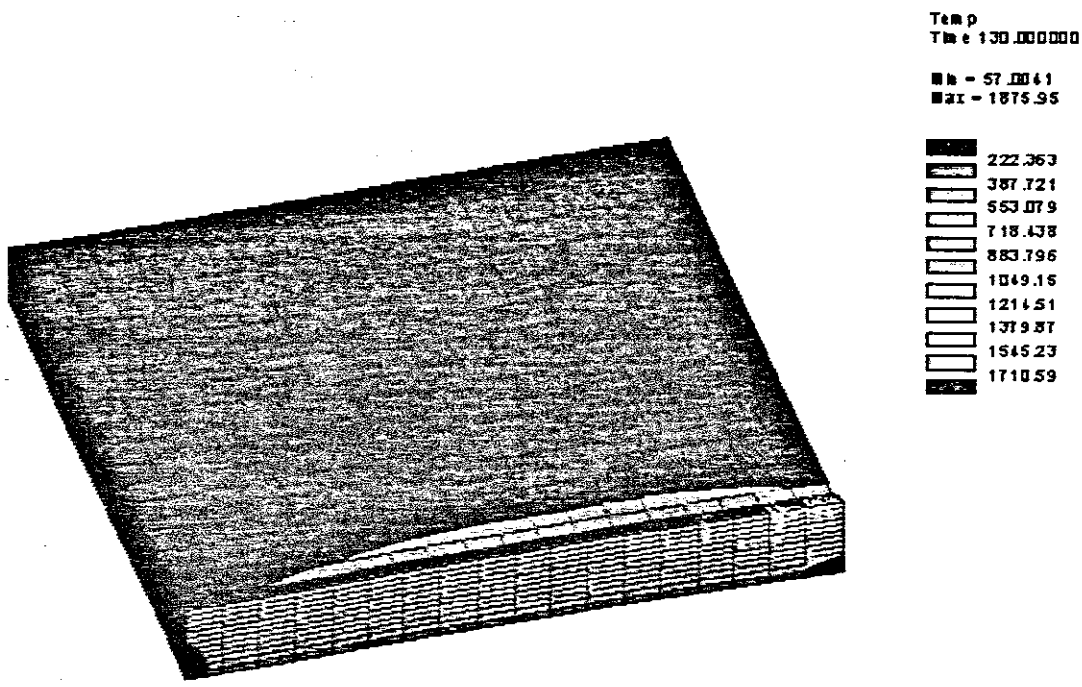

Figure 9.26. Depicting the temperature distribution profile for a 10mm plate at the end of the 4th run

9.9 Quench Tank Design

The first question that has to be answered here is why was quenching necessary? Since the purpose of this research was to determine the metallurgical phase transformations that take place in Roq-tuf AD690, it was imperative that all possible metallurgical phase transformations that may occur in the steel due to varying cooling rates, had to be determined. These varying cooling rates could be obtained by subjecting a standard bar of the aforementioned steel, heated to above the austenitising temperature, to different quench media and analyzing the results to determine the metallurgical phases produced. This was the primary and only reason for the design and construction of the quench tank. The tank similar to that depicted in figure 4.1 was constructed out of mild steel plate and treated with a rust inhibiting oxide. An insert to facilitate the use of the same tank for oil quenching as well was constructed. This quench tank differs from a Jominy quench tank in that the quenching medium is not directed onto the one end of the test bar by means of a nozzle. In our case the test bar has its one end immersed in a steadily flowing coolant stream. It is for this reason that the cooling rates obtained from the quench tank may not be as severe as those that may have been obtained from a Jominy quench. This quench tank, however, has the advantage of enabling the use of a number of quenching media, such as brine and oil, which would have been more difficult to obtain from a Jominy tank. The quench tank was equipped with a flow meter, which in turn was coupled to the municipal water supply. The test bars were machined to accommodate thermocouples at various positions along its length, from which the cooling rate data was obtained. Thermocouples also measure the temperature of the coolant entering and leaving the quench tank to determine the amount of heat absorbed by it.

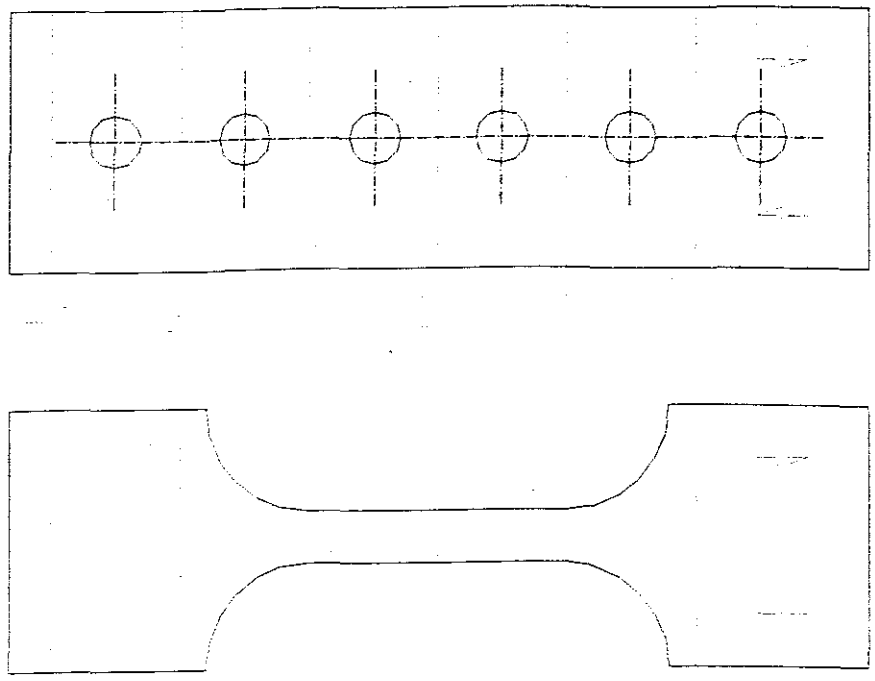

Figure 9.27. Depicting the test bars and the couple positions

The test bars were sectioned at regular intervals along its length and the metallurgical phase proportion present was determined through the use of microcopy. This phase was assigned to a particular cooling rate, obtained from the thermocouples. The end holes are

the points at which the specimens were held in the quench tank. Detailed drawings of the quench tank can be found in Appendix

9.10 Quenching Media

As was stated previously, the quench tank was designed to accommodate multiple cooling media, namely, brine, water and oil. In the instance of brine and oil quenching, a insert was installed to separate the oil or brine from the cooling water which acted as an additional heat transfer medium. The following pictures depict the the standard test bars that were subjected to either brine, water, oil quenching. A further normalising experiment was carried out, whereby the test bars were austenitised and allowed to cool in still air.

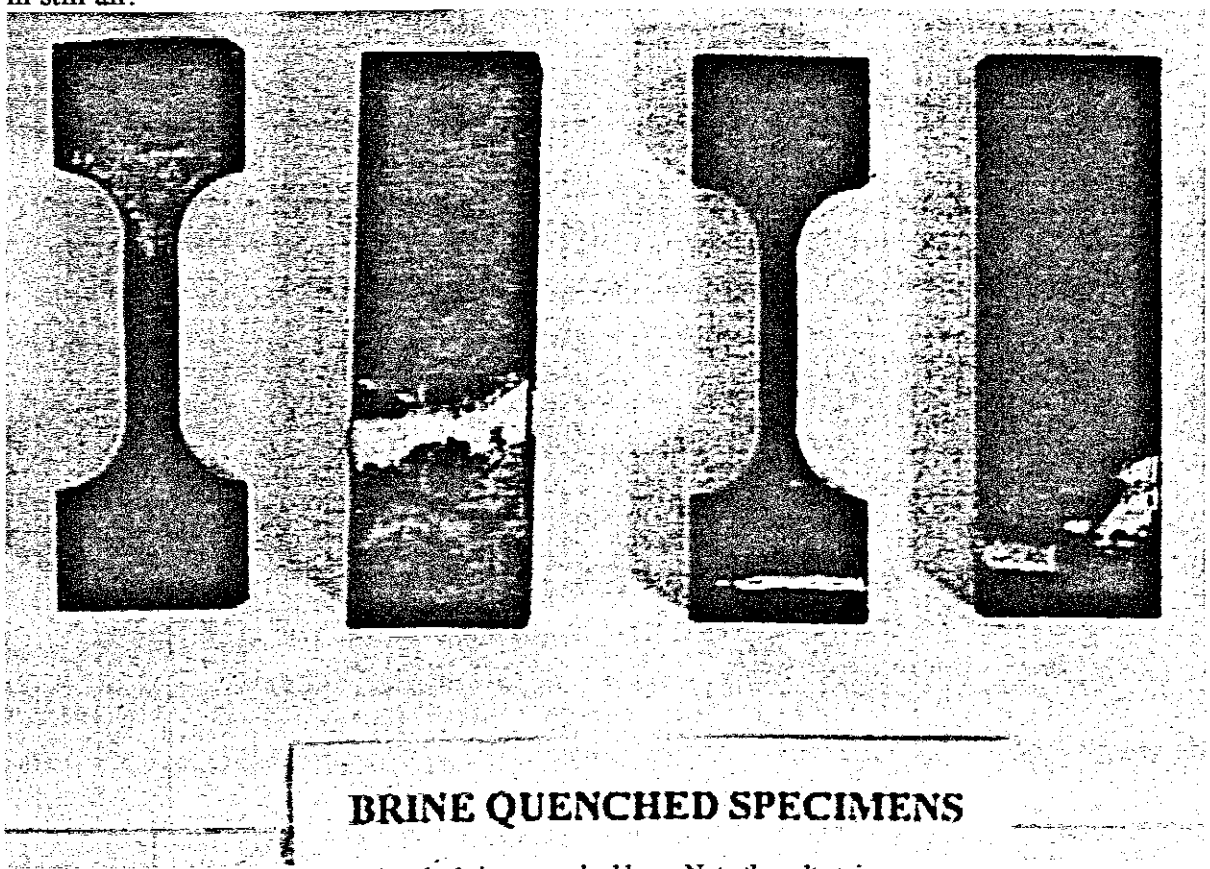

Figure 9.28. Depicting the brine quenched bars. Note the salt stains.

Extreme difficulty was experienced in obtaining any of the salts indicated in table 4.1. It was then decided to make a brine solution by using course salt. The brine solution should still provide the most rapid cooling rate. This assumption will be further evaluated in the sections on hardness testing and metallurgical analysis.

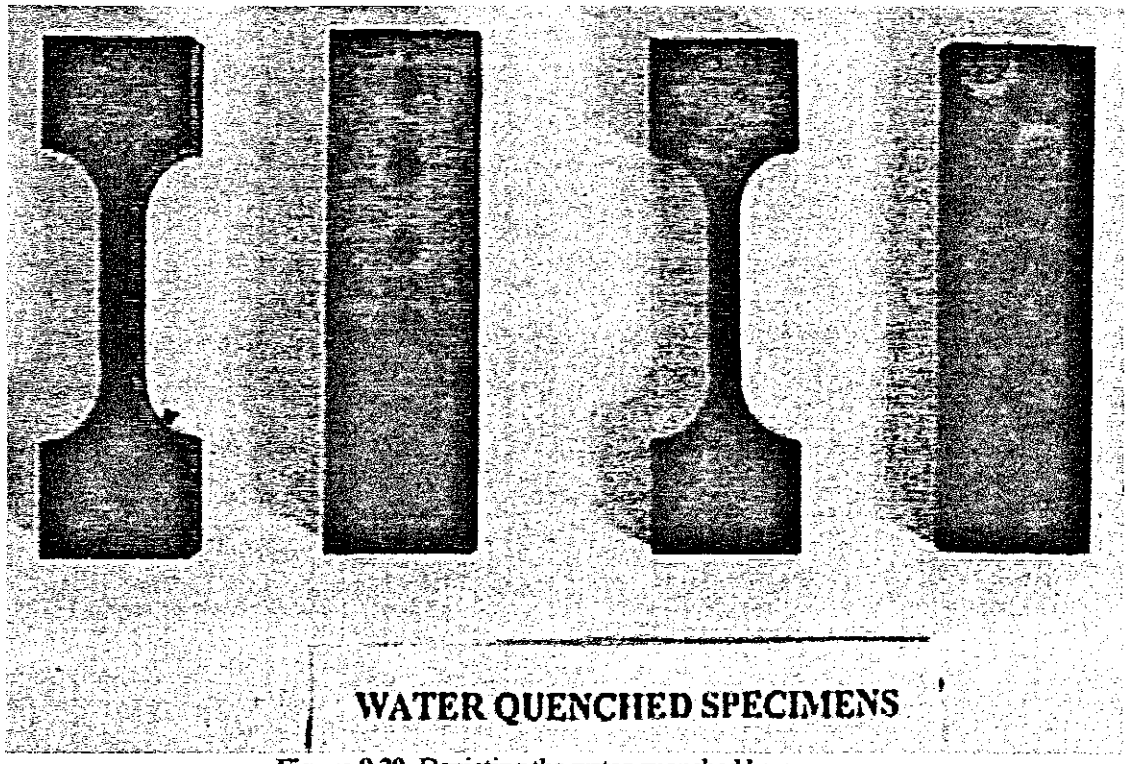

Figure 9.29. Depicting the water quenched bars

The water quench should provide the second most severe cooling rate, relative to the brine quench.

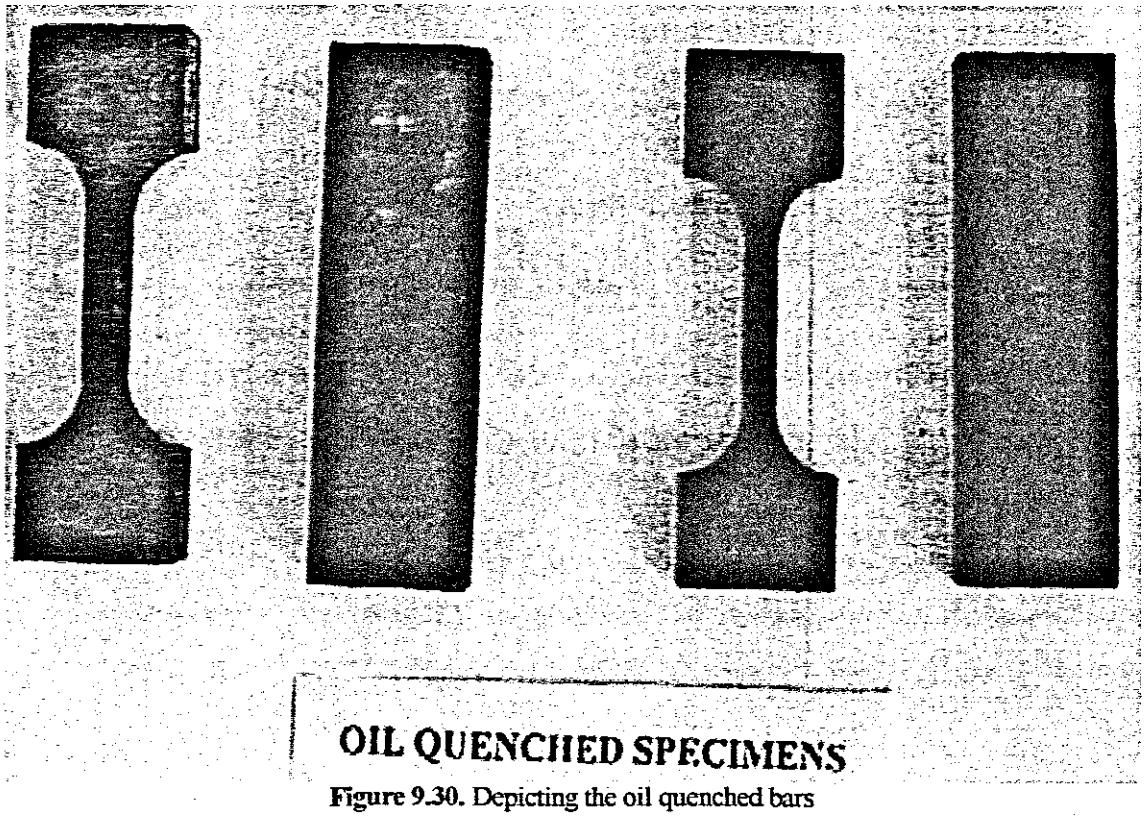

Figure 9.30. Depicting the oil quenched bars

The oil quenching medium used was BP. Quendila 19, an oil specifically developed for the quenching process. The oil produces minimal fumes during quenching and does not

denature when coming into contact with extremely hot surfaces. The viscosity of the oil is selected to ensure the oil drains readily from quenched components at normal operating temperature, thus saving time. Other advantages are high oxidation resistance, low carbon forming tendency and good hardening characteristics. The cooling rate produced is not as severe as that obtained by water, although higher than that which would be obtained by cooling in still air. The properties of BP Quendila 19 are given in table 9. below.

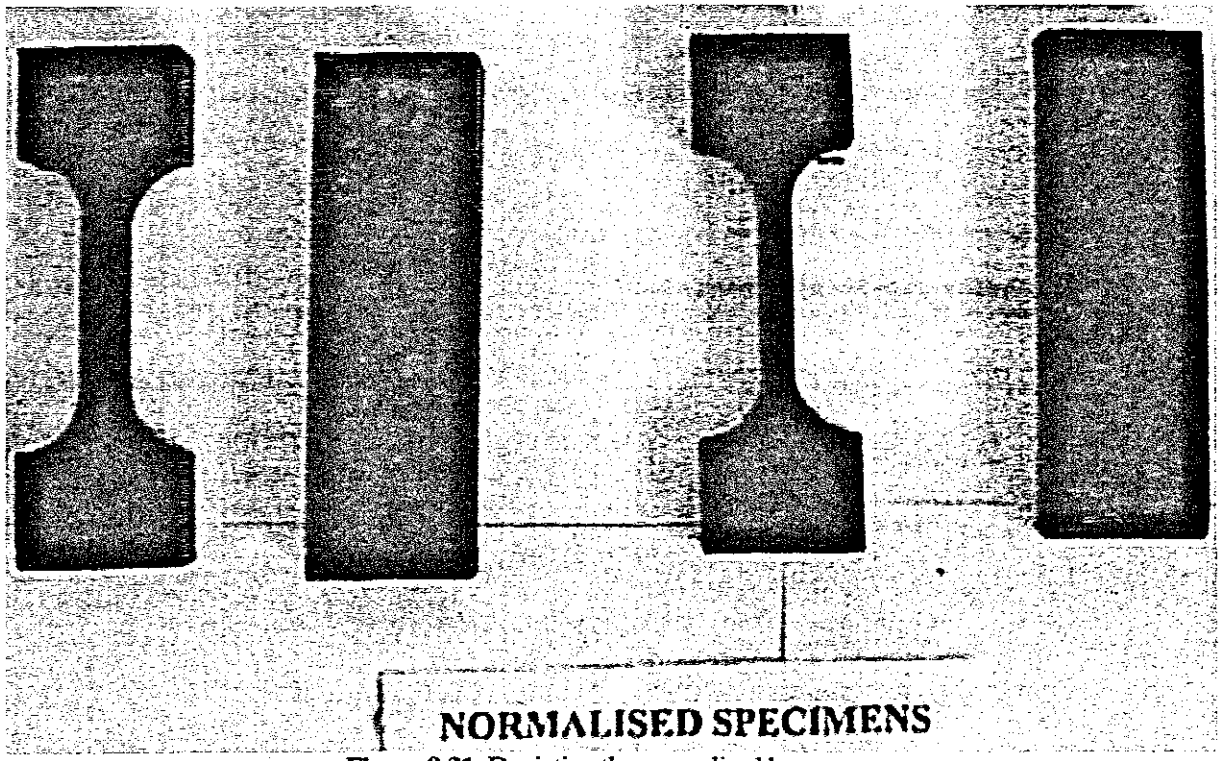

Figure 9.31. Depicting the normalised bars.

Viscosity (CSt)		Fire Point ^{0}C	Flash Point (PMCC) ^{0}C
40^{0}C	20	228	200
100^{0}C	4		

Table 9.7. Depicting the properties of BP. Quendila 19

9.11 Cooling Curves

Utilising the data obtained from the thermocouples and processing them by means of a C-Builder program developed by Oliver, the following cooling curves were obtained:

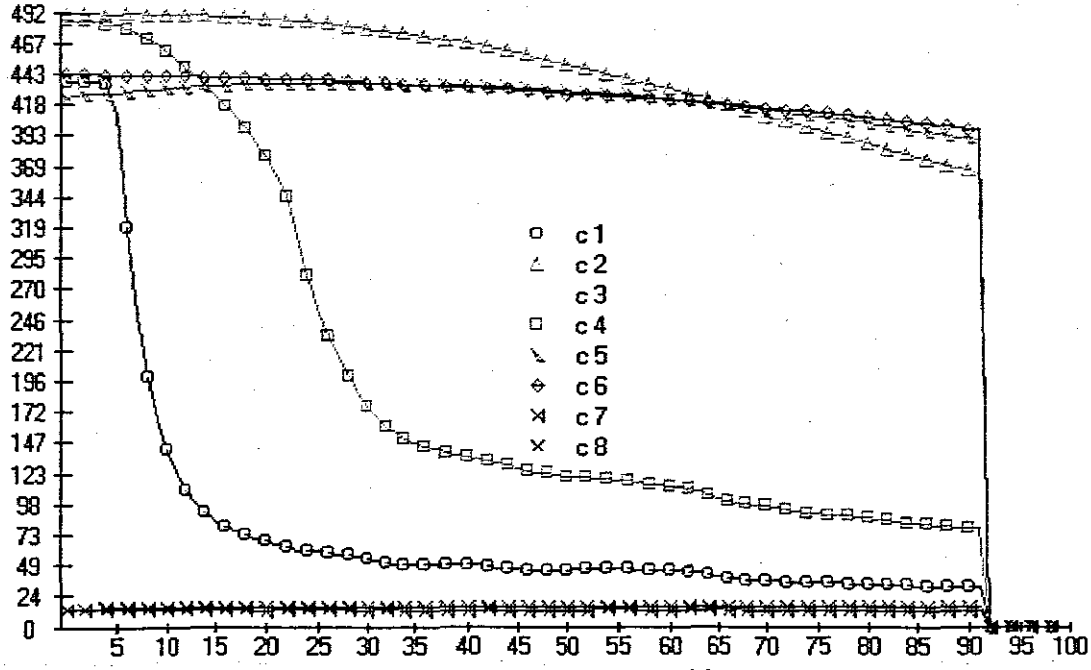

Graph 9.20. Depicting the cooling rates obtained from a brine quench

The graph indicated above was obtained on carrying out a brine quench on standard bar 5 of 16mm thickness. Thermocouples 1 to 6 were embedded in the bar, whilst couples 7 and 8 were recording the water inlet and outlet temperatures respectively. As would be expected, the couple closest to the end that was immersed in the brine mixture would experience the most rapid temperature decrease. This effect would decrease the further one moves away from the immersed end. The order in which the couples were embedded in the bar together with the cooling rate experienced is as follows:

Couple Number	Cooling Rate (^{0}C/s)
1	33.8
4	31.6
3	3.4
2	1.2
5	0.47
6	0.47

Table 9.8. The relative positional cooling rates recorded by the thermocouples for brine quench.

From the cooling rates above, one would expect to find a similar metallurgical microstructure in the regions where couples 1 and 4 were embedded, after which a considerable phase transformation will take place, due to the more mild cooling rate. This assumption will be further analysed in the section on metallurgical microstructures.

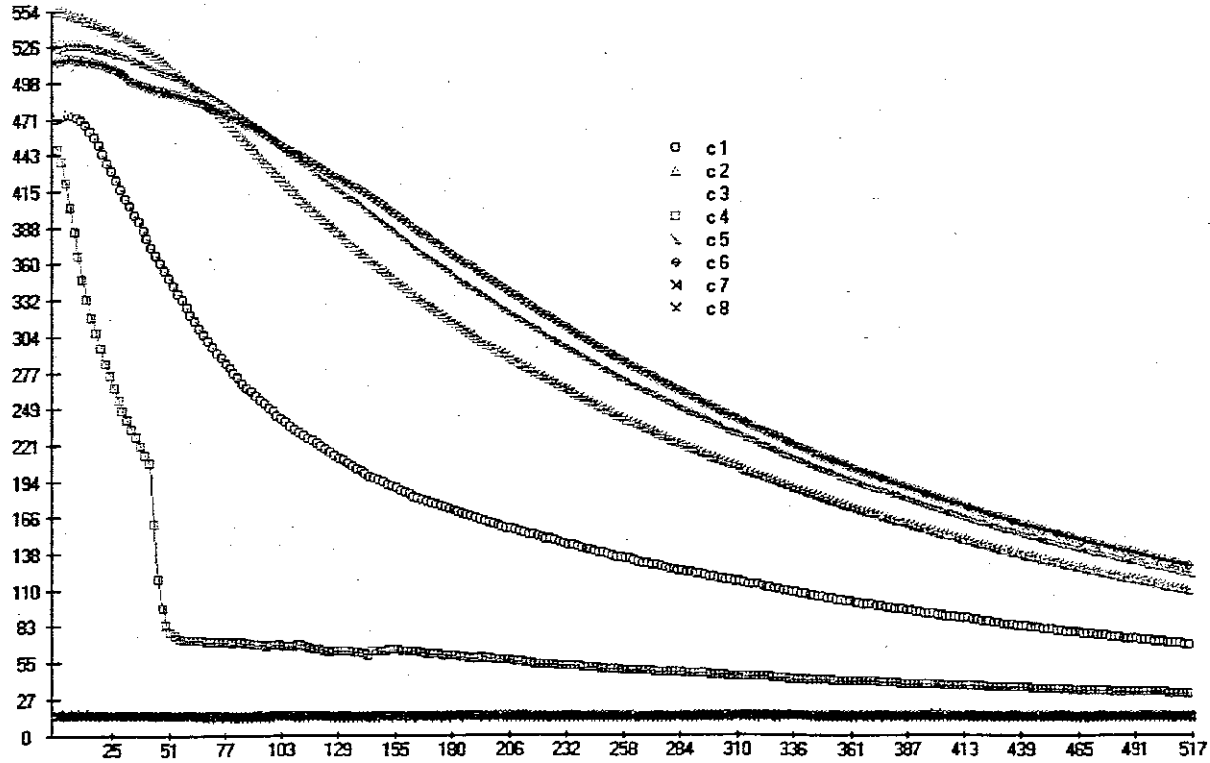

Graph 9.21. Depicting the cooling rates obtained for a water quench

The graph above shows a more gradual cooling as opposed to the previous one. The abrupt change in the slope of curve C4 occurred when the bar was immersed in the water.

Couple Number	Cooling Rate (^{0}C/s)
4	10.7
1	4.3
3	1.9
2	1.4
5	0.24
6	0.23

Table 9.9. The relative positional cooling rates recorded by the thermocouples for water quench.

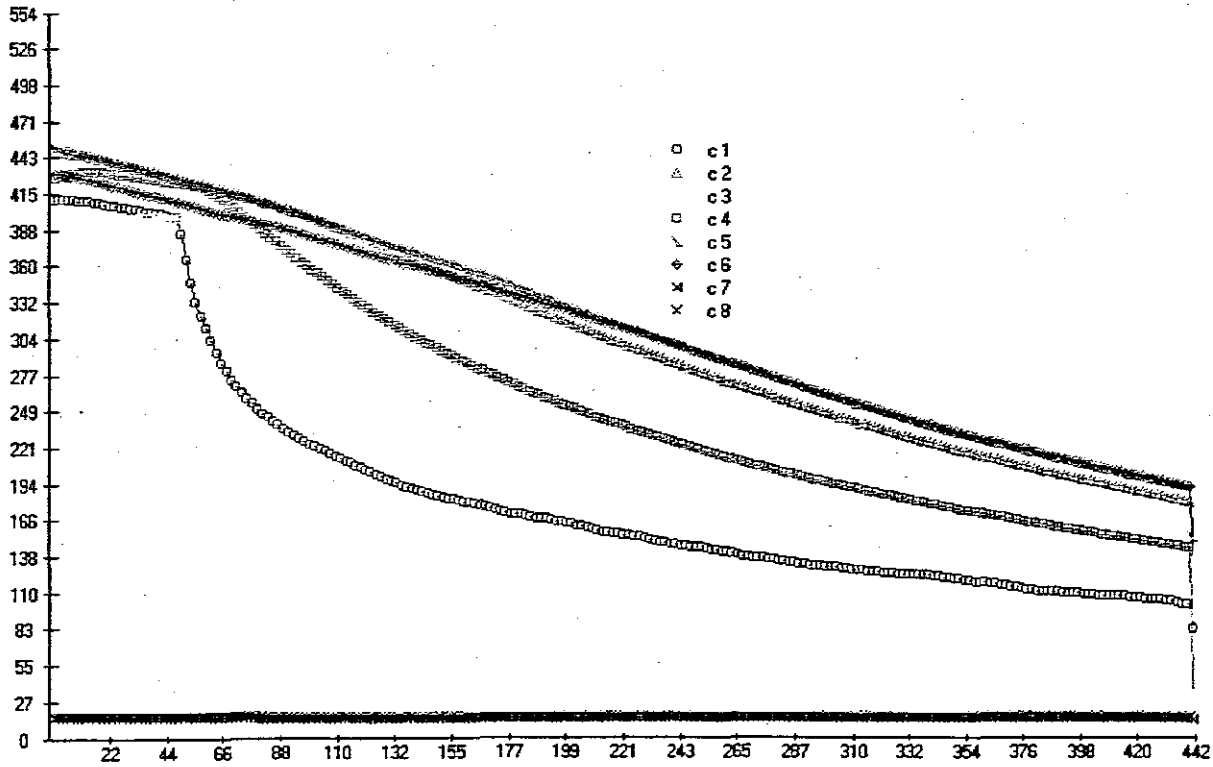

Graph 9.22. Depicting the cooling curves obtained for an oil quench.

The sudden change in the slope of C1 can once again be attributed to the instant the test bar made contact with the oil. The slopes are visibly more gradual when compared to the previous graphs.

Couple Number	Cooling Rate (^{0}C/s)
1	3.5
4	1.2
3	0.71
2	0.71
5	0.71
6	0.47

Table 9.10. The relative positional cooling rates recorded by the thermocouples for oil quench.

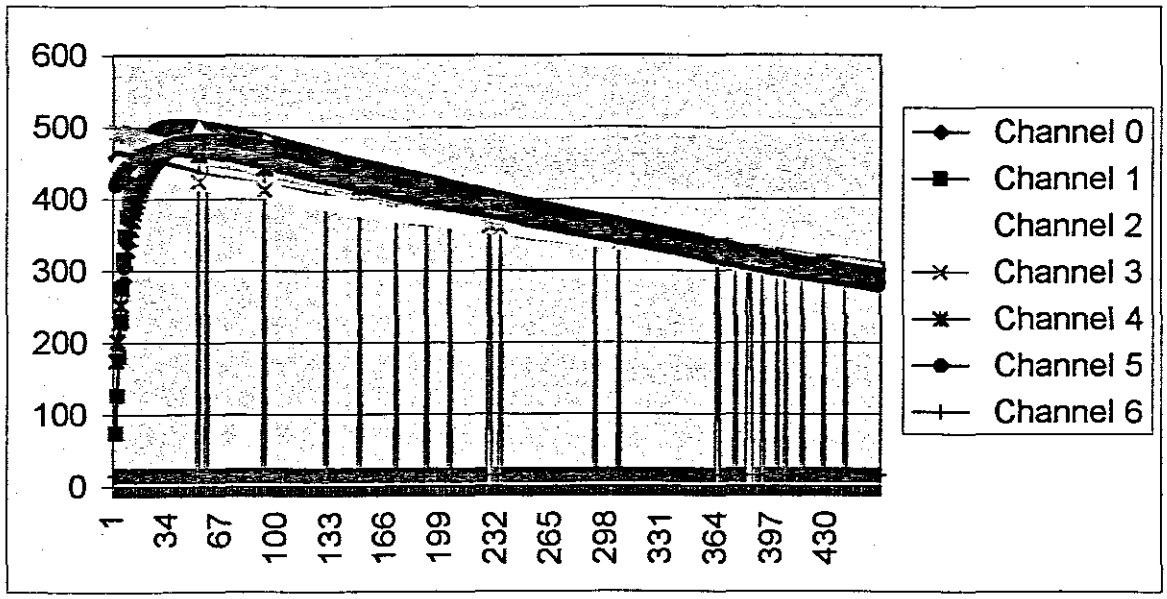

Graph 9.23. Depicting the cooling curves obtained for normalising

This graph had to be created using Excel due to the fact that the C-Builder program experienced difficulty reading the data. The bars were allowed to cool in still air and produced the following cooling rates.

Couple Number	Cooling Rate (^{0}C/s)
0	0.71
1	0.24
2	0.47
3	0.47
4	0.47
5	0.71

Table 9.11. The relative positional cooling rates recorded by the thermocouples for normalising.

The slightly higher cooling rates at couples 0 and5 can be attributed to the additional end surface area of the bar, which is available for radiation heat transfer.

9.12 Hardness Testing

The post-quenched bars were subjected to a Rockwell Hardness test within close proximity of the thermocouple positions along its length. Using a Pyramidal Diamond indentor under a 150kg load, the following hardness curves were obtained. The positions indicated in the tables below may be correlated with those indicated on the standard test bars of figure 9.

Specimen No.	Test Type	Indentor	Load	Position	1	2	3	Readings
5	Rockwell	Pyramidal	150	A	25.5	25.8	25	25.4
	C-Scale	Diamond		B	25.8	25	25.6	25.5
				C	25.8	25.8	25.8	25.8
				D	25.8	25.8	25.8	25.8
				E	26	26	26	26.0
				F	25.8	25.8	25.8	25.8

Table 9.12. Depicting the hardness data obtained for the normalised specimen 5

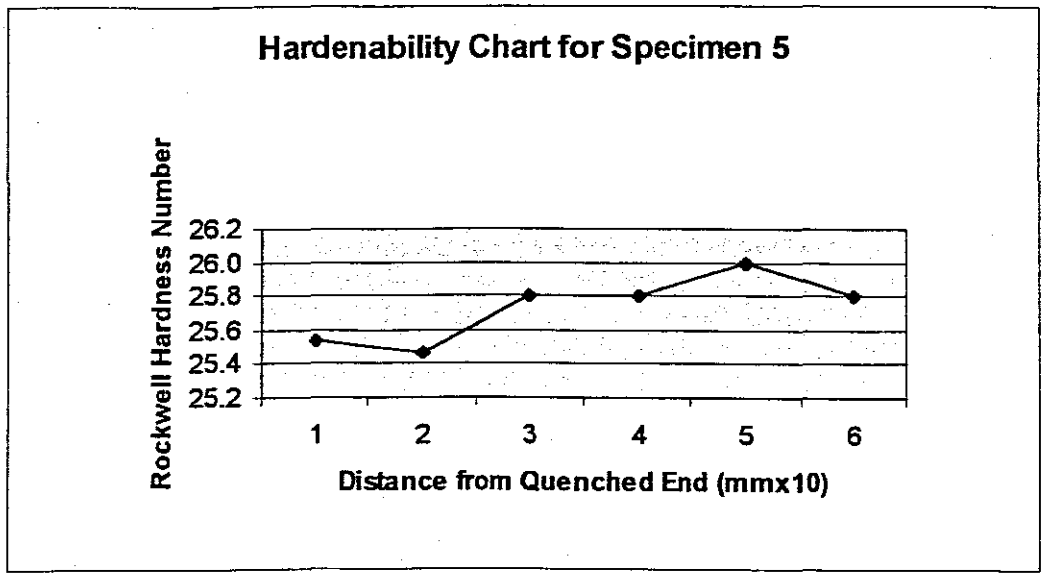

Graph 9.24. Plotting the hardness curve for sample 5.

The Normalised bars were allowed to cool in still air and produced the following hardness curve. As would be expected, the hardness is vitually constant throughout the length of the specimen. The microstructures produced will be discussed in the following section on microstructure.

Specimen No.	Test Type	Indentor	Load	Position	1	2	3	Readings
3	Rockwell	Pyramidal	150	A	32.4	31	31.3	31.6
	C-Scale	Diamond		B	29.9	29.7	29.1	29.6
				C	27.8	29.4	29	28.7
				D	28.6	28.6	28.7	28.6
				E	28.5	28.3	28.7	28.5
				F	27.9	28.2	28.5	28.2

Table 9.13. Depicting the hardness data obtained for oil quenched sample 3.

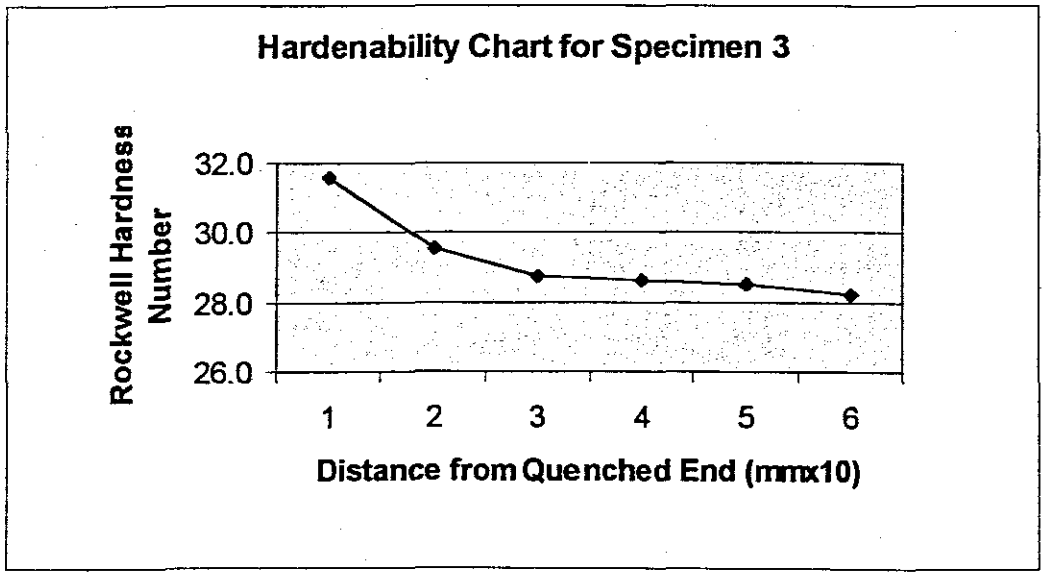

Graph 9.25. Plotting the hardness curve for sample 3

The Oil quenched specimen produced the following hardness curve. It will be noted, that even the furthermost end of the specimen produced a hardness number higher than that of the normalised specimen.

Specimen No.	Test Type	Indentor	Load	Position	1	2	3	Readings
0	Rockwell	Pyramidal	150	A	39.6	40.5	40.2	40.1
	C-Scale	Diamond		B	38.9	38	36.9	37.9
				C	30.8	30.4	30.3	30.5
				D	29.9	29.4	29.7	29.7
				E	29.1	28.8	28.8	28.9
				F	28.7	29	28.2	28.6

Table 9.14. Depicting the hardness data obtained for water quenched sample 0.

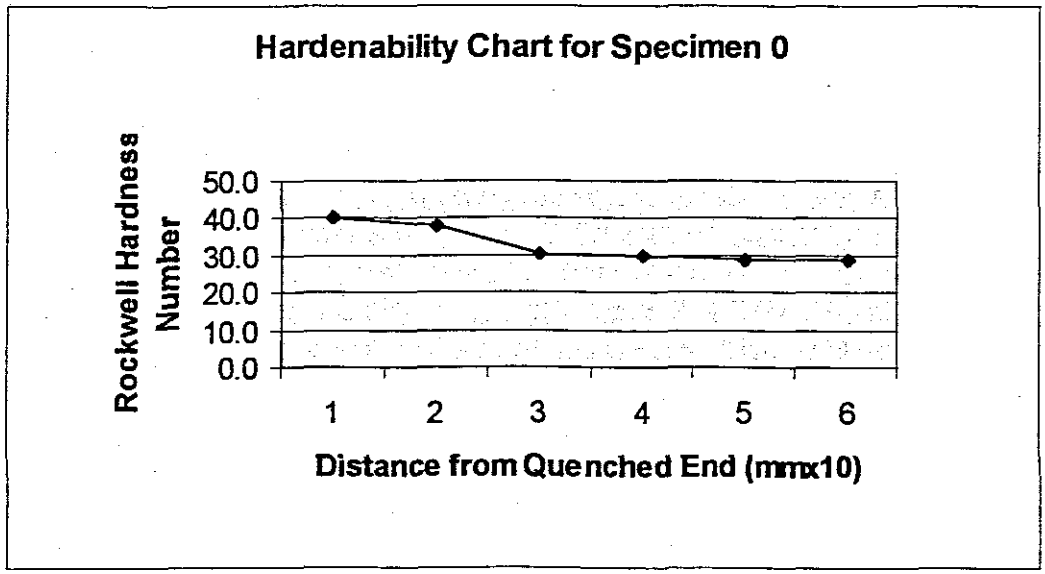

Graph 9.26. Plotting the hardness curve for sample 0.

The Water quench was quite severe, as the results indicate. The furthermost point from the quench medium produced a hardness number of 28.6 on the C-scale.

Specimen No.	Test Type	Indentor	Load	Position	1	2	3	Readings
7	Rockwell	Pyramidal	150	A	50.5	51	50.2	50.6
	C-Scale	Diamond		B	50	50.1	49.8	50.0
				C	49.7	49	49.5	49.4
				D	49.1	49	48.8	49.0
				E	47.8	46.5	47	47.1
				F	46.4	45	44.9	45.4

Table 9.15. Depicting the hardness data obtained for brine quenched sample 7.

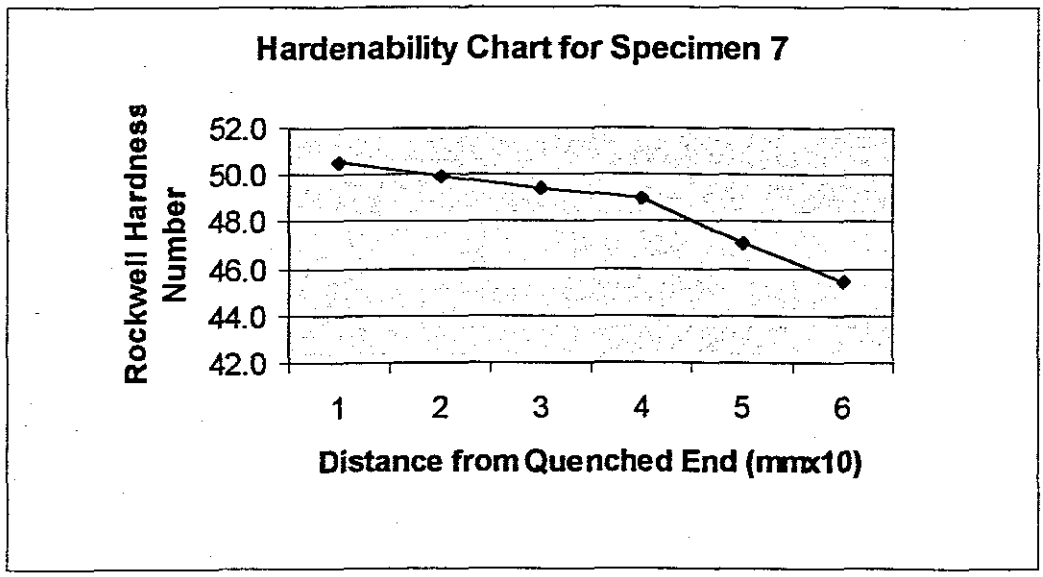

Graph 9.27. Plotting the hardness curve for sample 7.

The Brine quenched specimen produced the following data. The hardness of the specimen was once again changed over its entire length, with the end in contact with the quench medium producing a hardness of 50.6 RC. and the point furthest away registering a hardness of 45.4 RC.

9.13 Metallurgical Microstructure

The standard quenched bars were subjected to a metallurgical examination by taking samples within close proximity of where the thermocouples were embedded to ascertain the microstructure that evolved as a result of a particular cooling regime. The micrographs obtained for the brine quenched bar is as follows:

Figure 9.32. Depicting the microstructure obtained at the end of the bar that was exposed to the most severe cooling rate.

Figure 9.33. Depicting the microstructure obtained halfway through the bar.

As with the brine-quenched bar, the water quenched bar was analysed at the end that was subjected to the most severe cooling rate, midway along the length of the bar and at its furthest extremity from the quenching medium. The following micrographs were obtained:

Quenched End

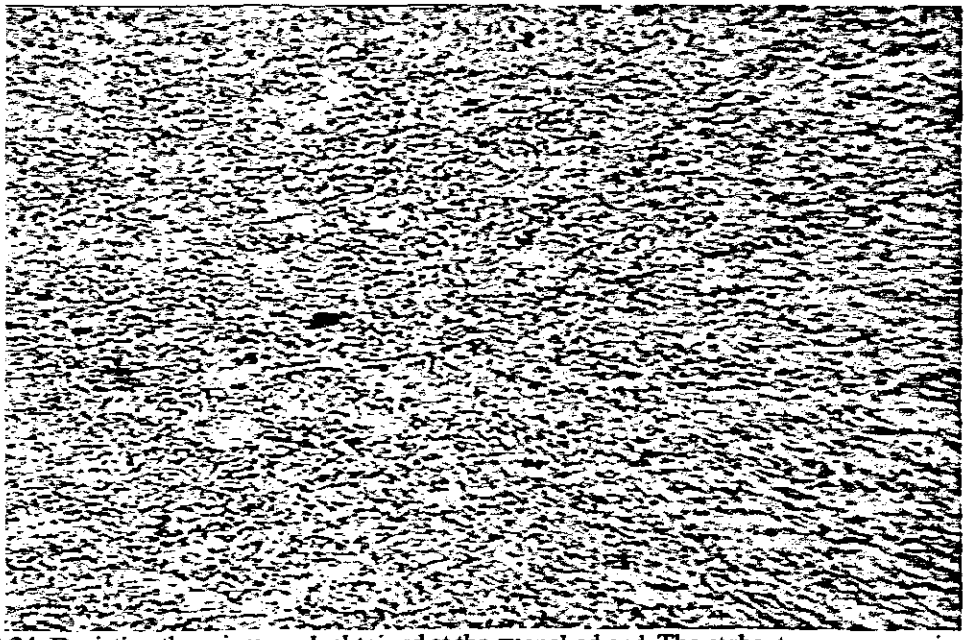

Figure 9.34. Depicting the micrograph obtained at the quenched end. The etchant was once again nital. The colours were obtained by utilising a prism on the microscope. Cooling Rate 10.7°C/s. Hardness 514 Brinell. 100x

Figure 9.35. Depicting the same sample as above magnified 500x. Microstructure formed martensite.

Midway

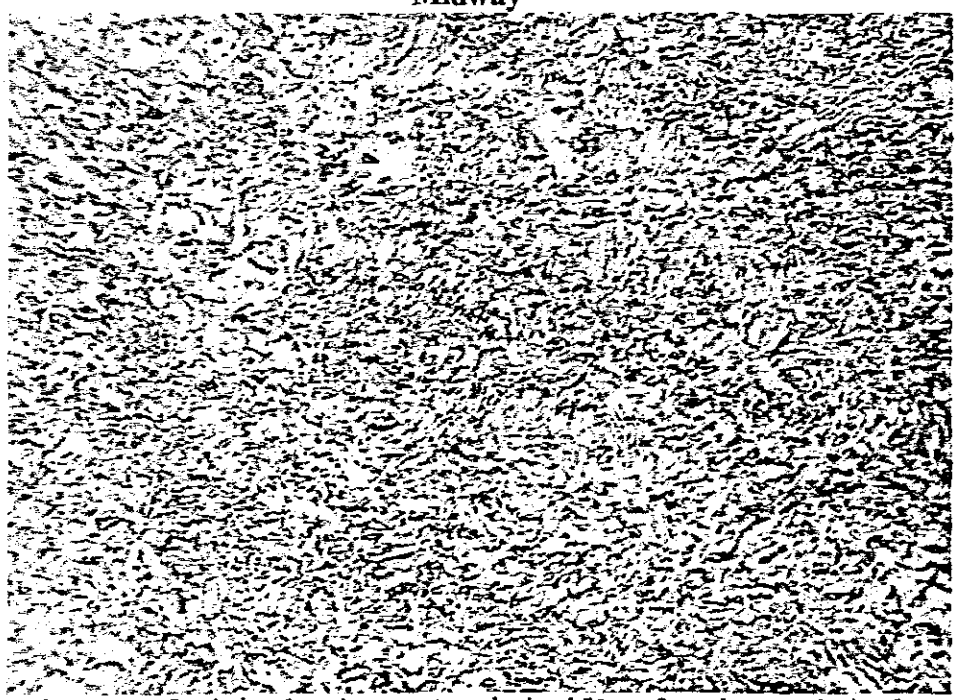

Figure 9.36. Depicting the microstructure obtained 50mm from the quenched end. Cooling Rate 1.9°C/s. Hardness 478 Brinell. 200x.

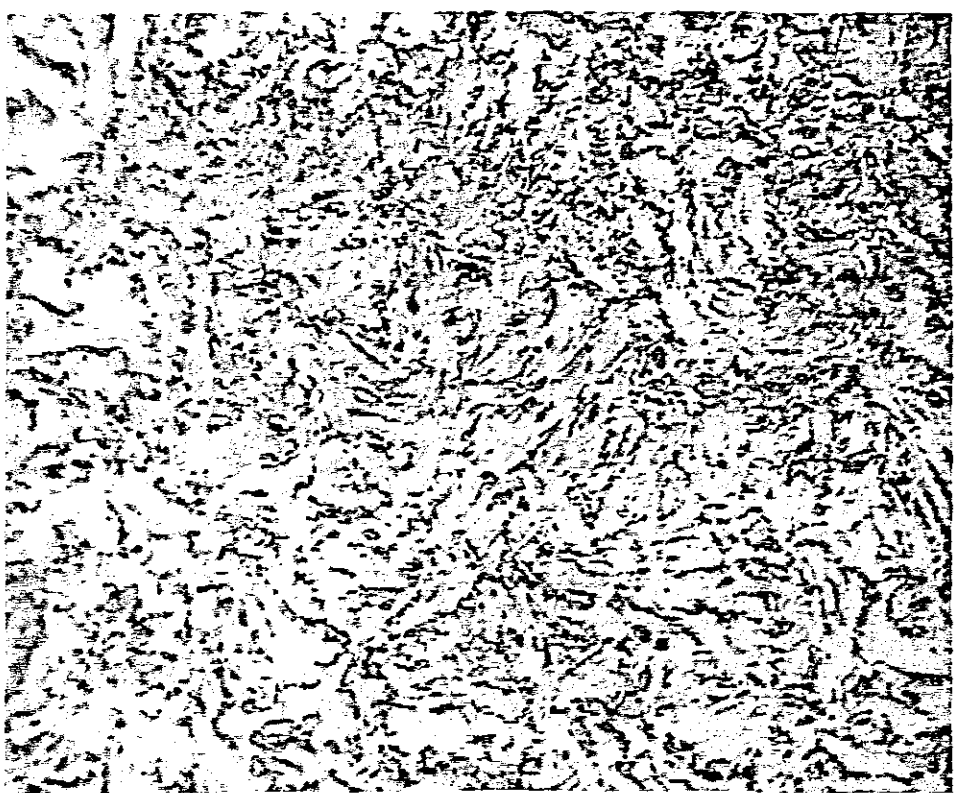

Figure 9.37. Depicting troosto- martensite resulting from the slightly slower cooling rate. 500x

Far End

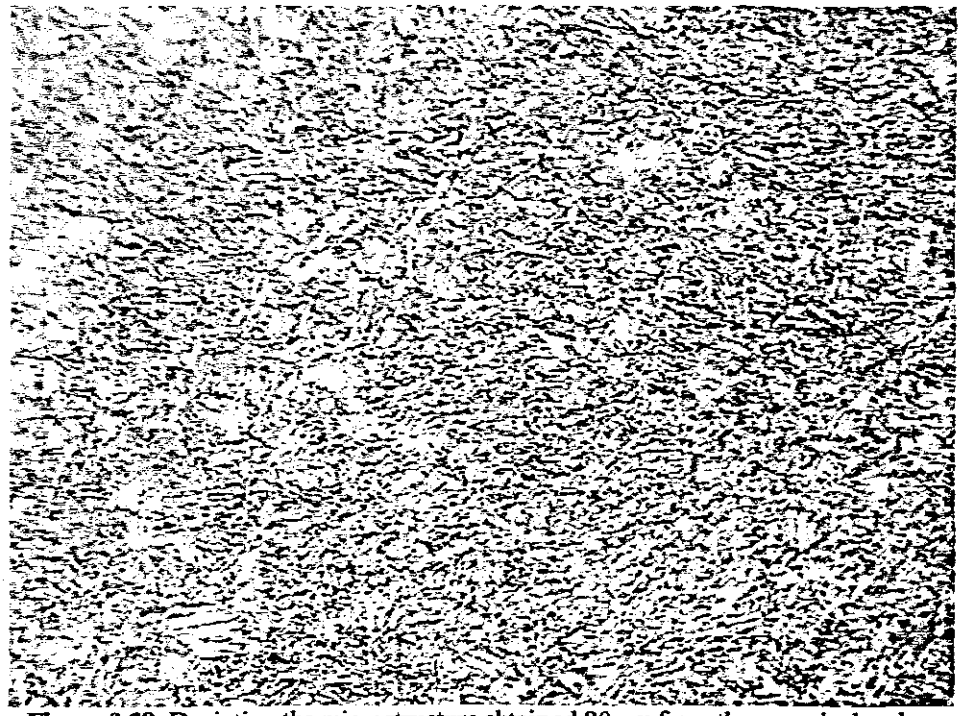

Figure 9.38. Depicting the microstructure obtained 80mm from the quenched end. Cooling Rate 0.23°C/s. Hardness 429 Brinell. 200x.

Figure 9.39. Depicting the separation of pearlite from ferrite. 500x.

The following micrographs were obtained along the length of the oil-quenched bar.

Quenched End

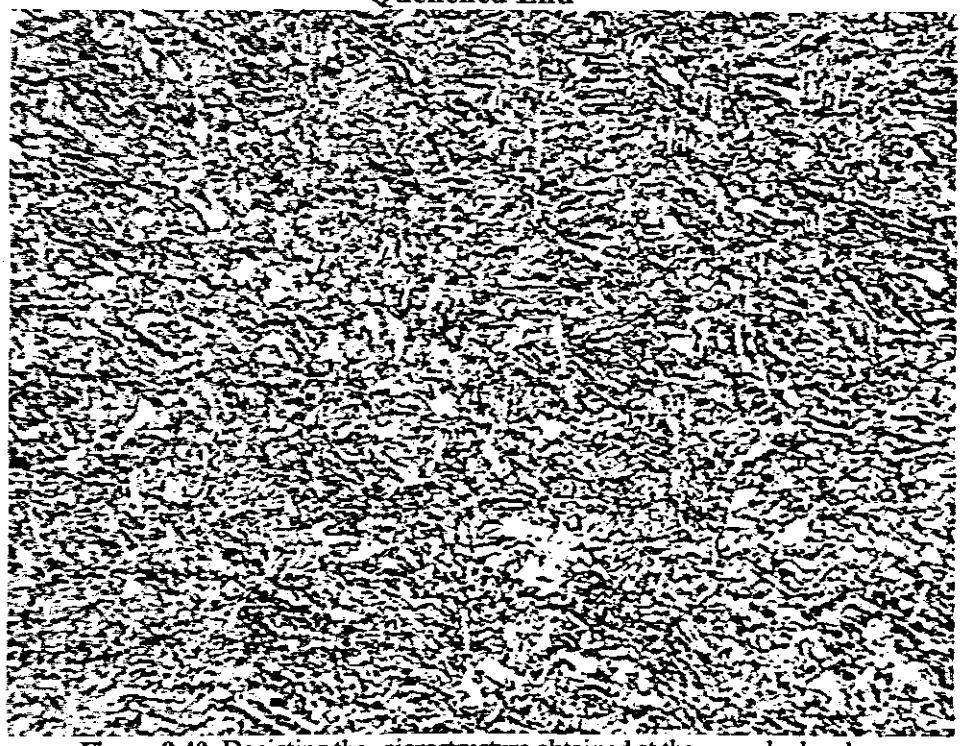

Figure 9.40. Depicting the microstructure obtained at the quenched end. Cooling Rate 3.5°C/s. Hardness 311 Brinell. 100x.

Figure 9.41. Depicting a microstructure of fine martensite retained from the ferrite and carbide of the pearlite, which has passed into solid solution. 500x.

Midway

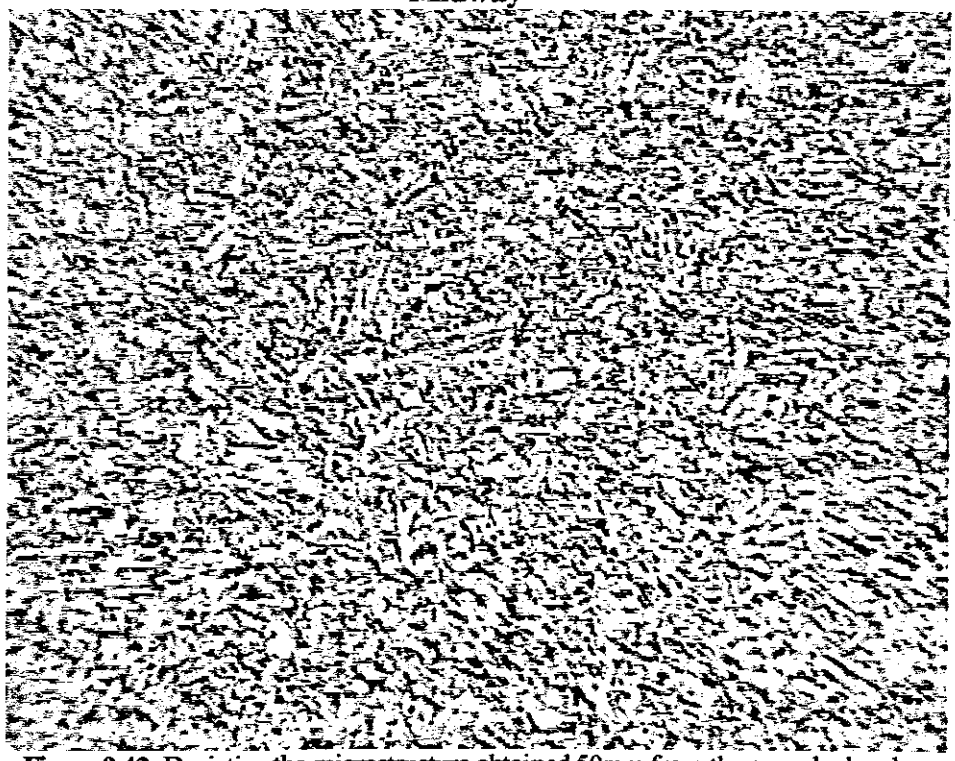

Figure 9.42. Depicting the microstructure obtained 50mm from the quenched end. Cooling Rate 0.71°C/s. Hardness 285 Brinell. 200x.

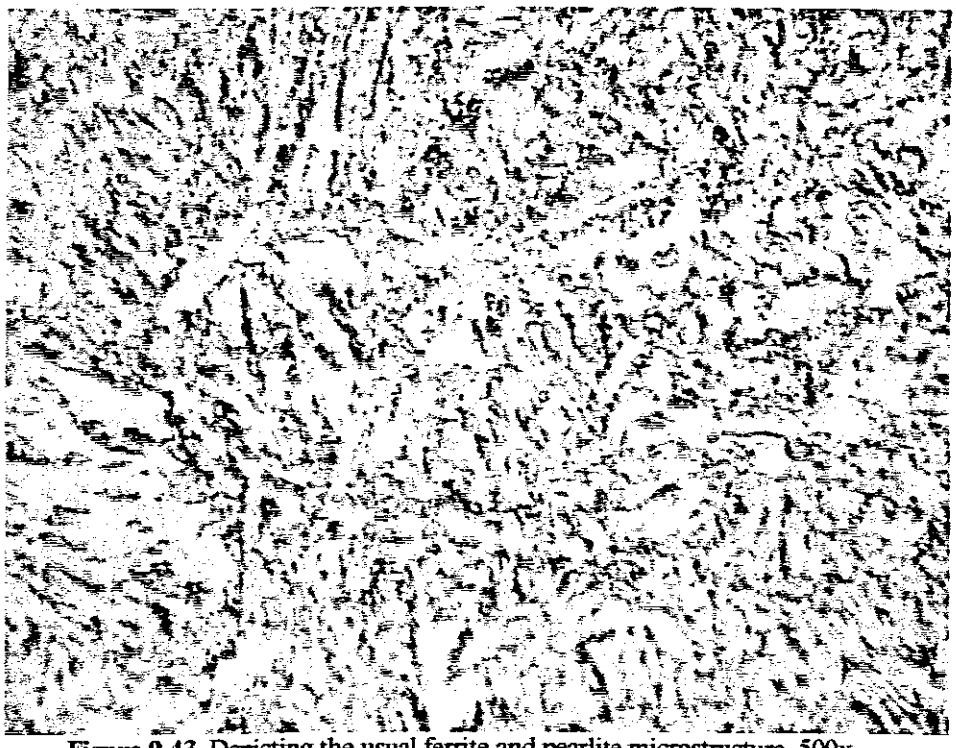

Figure 9.43. Depicting the usual ferrite and pearlite microstructure. 500x.

Far End

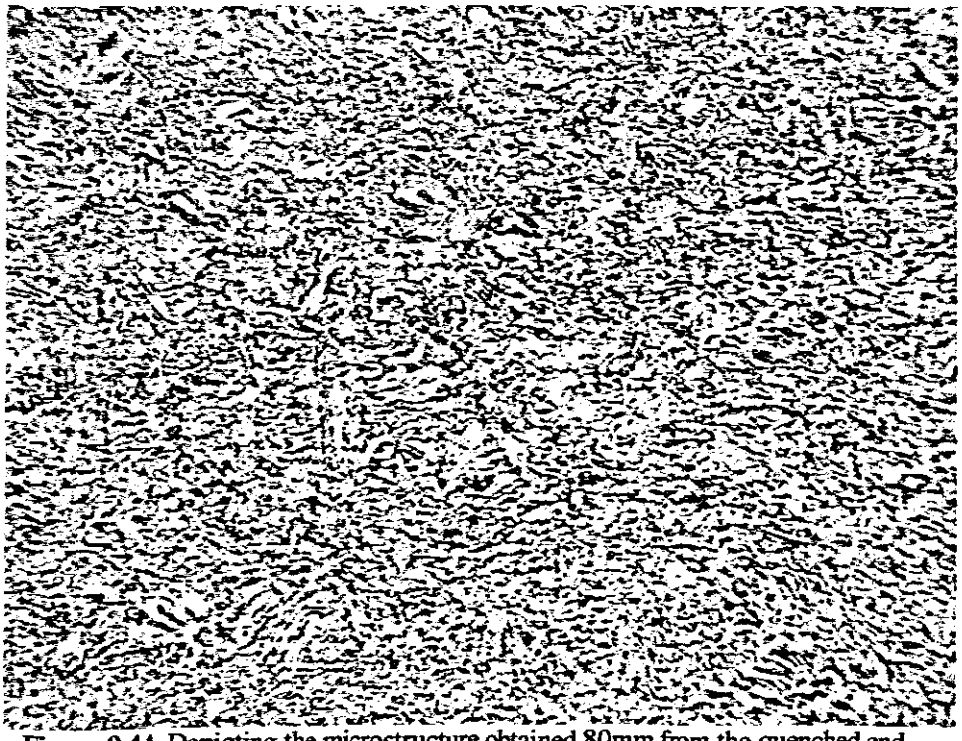

Figure 9.44. Depicting the microstructure obtained 80mm from the quenched end. Cooling Rate 0.47°C/s. Hardness 269 Brinell. 200x.

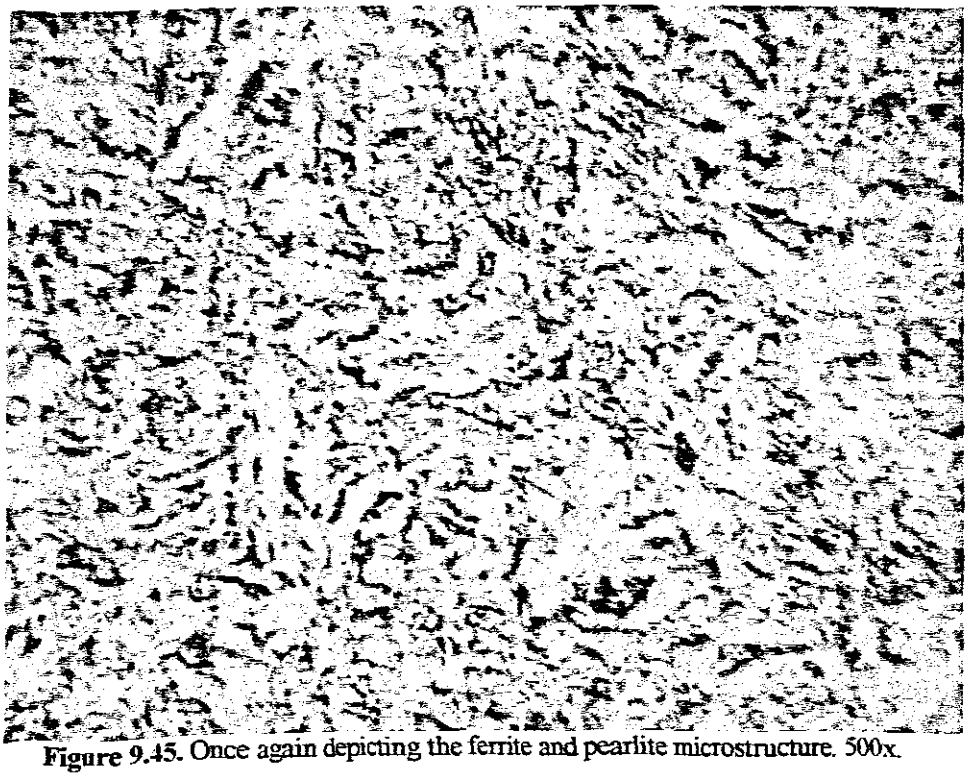

Figure 9.45. Once again depicting the ferrite and pearlite microstructure. 500x.

The normailsed bar was analysed at either end and produced the following micrographs.

End 1.

Figure 9.46. Depicting the microstructure obtained at the one end of the normalised bar. Hardness 262 Brinell. 200x.

Figure 9.47. Depicts the separation of pearlite from ferrite. 500x.

End 2.

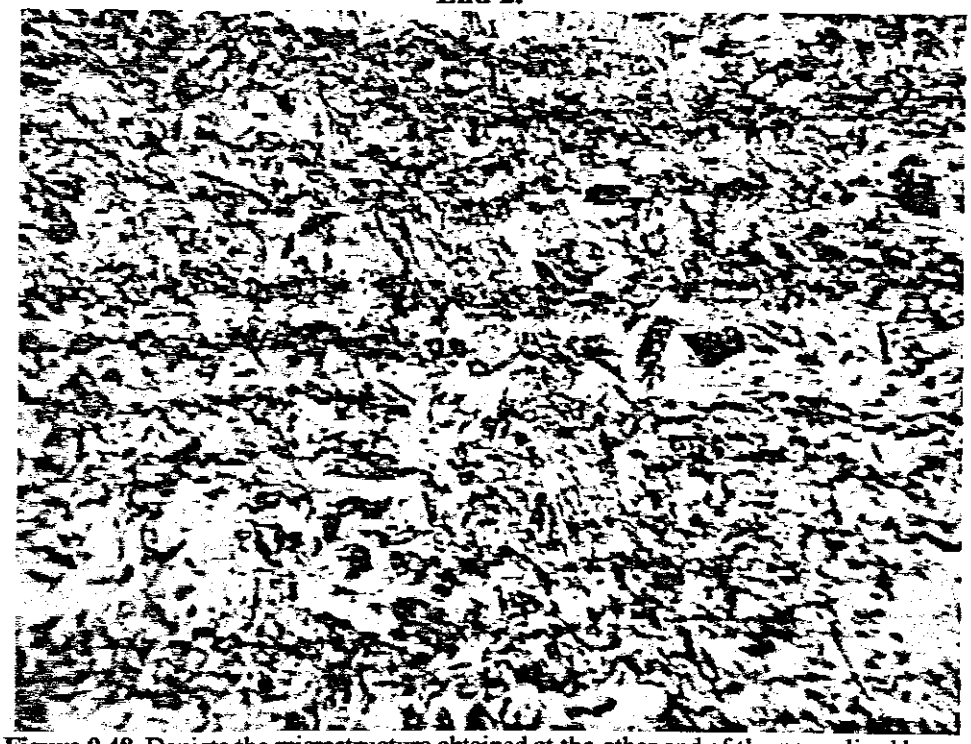

Figure 9.48. Depicts the microstructure obtained at the other end of the normalised bar. Hardness 262 Brinell. 200x.

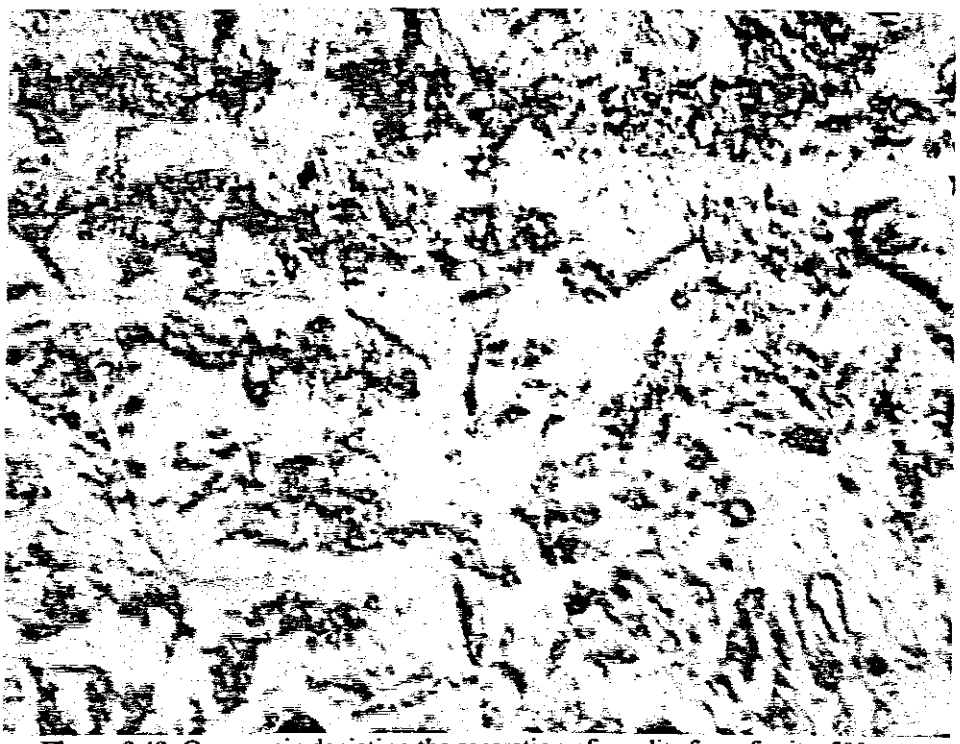

Figure 9.49. Once again depicting the separation of pearlite from ferrite. 500x.

9.14 Statistical Formulae

It has long been established fact, that there is a relationship between the microstructure of a steel and its mechanical properties. With the use of statistical formulae and the chemical compositions of the plates and welding electrodes, the correlation, if any, between the measured mechanical properties and those predicted will be analysed. For the purpose of convenience, the chemical composition and material properties of the plate and electrodes under analysis will be reproduced here.

Chemical composition % (ladle analysis)										
Grade	**Max thickness**	**C**	**Mn**	**Si**	**S (max)**	**P (max)**	**Mo**	**Ni**	**Cr**	**B**
ROQ-tuf AD690	32mm	0.12/ 0.21	0.45/ 0.70	0.20/ 0.35	0.040	0.035	0.50/ 0.65	-	-	0.001/ 0.005

Table 1.2. Depicting chemical composition of ROQ-tuf AD690 (courtesy ISCOR product manuals)

Chemical Composition of Transarc 118.	
% Carbon	0.06-0.10
% Manganese	1.30-1.80
% Silicon	0.50 max
% Sulphur	0.025 max
% Phosphorus	0.025 max
% Nickel	1.70-2.50
% Molybdenum	0.30-0.50

Table 9.16. Depicting the chemical composition of the Transarc 118 electrode (courtesy Transarc Welding Consumable Catologue)

Mechanical Properties to AWS A5.5 in as welded condition	
0.2% Proof Stress	680-760 MPa
Tensile Strength	760 MPa min
% Elongation on 50mm	20 min
Charpy V-notch at 51^{0}C	45J min

Table 9.17. Depicting the Mechanical Properties of the Transarc 118 electrode (courtesy Transarc Welding Consumable Catologue)

Chemical Composition of Armcord LH.	
% Carbon	0.056
% Manganese	1.32
% Silicon	0.30
% Sulphur	0.027
% Phosphorus	0.017
% Nickel	2.07
% Molybdenum	0.36
% Chrome	0.32

Table 9.5 Depicting the chemical composition of the Armcord LH electrode (courtesy OESA Datasheets)

Mechanical Properties to AWS A5.5-92 in as welded condition	
Yield Strength	≥680 MPa
Tensile Strength	760-860 MPa
% Elongation on 50mm	≥16
Charpy V-notch at 51^{0}C	≥50J

Table 9.6 Depicting the Mechanical Properties of the Armcord LH electrode (courtesy OESA Datasheets)

As can be seen from the previous results on tensile testing, the tensile strength for the welds produced exceeds the minimum values provided by the manufacturers. The statistical verification of various metallurgical and mechanical parameters for the Transarc 118 electrode will now be carried out, followed by similar calculations for the Armcord LH electrode. The statistical formulae of chapter 7 have been reproduced here for convenience.

9.14.1 The critical range on heating between Ac_1 and Ac_3

In this calculation only the chemical composition of ROQ-tuf AD690 will be taken into consideration.

$$A_{C1}\,(^0C) = 723 - 20.7Mn + 16.9Ni + 29.1Si + 16.9Cr - 290As + 6.38W \qquad (7.6)$$
$$= 723 - 20.7\times 1.55 + 16.9\times 0 + 29.1\times 0.275 + 16.9\times 0 - 290\times 0 + 6.38\times 0$$
$$A_{C1}(^0C) = 698.92$$

$$A_{C3}\,(^0C) = 910 - 203\sqrt{C} - 15.2Ni + 44.7Si + 104V + 31.5Mo + 13.1W \qquad (7.7)$$
$$= 910 - 203\sqrt{0.19} - 15.2\times 0 + 44.7\times 0.275 + 104\times 0 + 31.5\times 0.575 + 13.1\times 0$$
$$A_{C3}(^0C) = 851.92$$

9.14.2 The Martensite transformation range

The temperature at which the martensite transformation commences will now be computed. Here however, the chemical composition of the electrode will be added to that of the steel and entered into the equation.

$$M_S\,(^0C) = 539 - 423C - 30.4Mn + 17.7Ni + 12.1Cr + 7.5Mo \qquad (7.8)$$
$$= 539 - 423\times 0.27 - 30.4\times 2.125 + 17.7\times 2.1 + 12.1\times 0 + 7.5\times 0.975$$
$$M_S(^0C) = 404.67$$

This temperature is considerably lower than that of 445.46 ^{0}C, which would have been obtained by taking the chemical composition of the plate only into consideration.

9.14.3 The Bainite transformation range

The temperature at which the bainite transformation commences and finishes will now be computed.

$$B_S(^0C) = 830 - 270C - 90Mn - 37Ni - 70Cr - 83Mo \qquad (7.9)$$
$$= 830 - 270 \times 0.27 - 90 \times 2.125 - 37 \times 2.1 - 70 \times 0 - 83 \times 0.975$$
$$B_S(^0C) = 407.23$$

$$with \quad B_{50} = B_S - 60^0C \qquad (7.10)$$
$$B_{50} = 407.23 - 60$$
$$B_{50} = 347.23$$

$$and \quad B_f = B_S - 120^0C \qquad (7.11)$$
$$B_f = 407.23 - 120$$
$$B_f = 287.23\ ^0C$$

The above result once again confirms the fact that the transformation temperatures are suppressed by the addition of other elements, such as those contained in the electrodes.

9.14.4 The ferrite-pearlite transformation range

The start of the ferrite transformation is given by the following equation.

$$10mm\,bar\,diameter\ F_S(^0C) = 878 - 295C - 78Mn \qquad (7.12)$$
$$= 878 - 295 \times 0.27 - 78 \times 2.125$$
$$F_S(^0C) = 632.6$$

The start of the pearlite transformation on air-cooling is given by the following equation.

$$P_S(^0C) = 700 - 60Mn \qquad (7.13)$$
$$= 700 - 60 \times 2.125$$
$$P_S(^0C) = 572.5$$

The above equation may successfully be applied to diameters 10 to 1000mm.

9.14.5 The critical cooling velocity and other significant cooling rates

The critical cooling velocity (CCV.) for the martensite transformation will now be computed. As was stated previously, it is that cooling velocity which must be equaled or exceeded in order to obtain a martensitic transformation. The CCV for martensite formation in seconds, is given by the following expression:

$$\log V_1 = 7.42 - 3.13C - 0.71Mn - 0.37Ni - 0.34Cr - 0.45Mo \qquad (7.15)$$
$$= 7.42 - 3.13\times 0.27 - 0.71\times 2.125 - 0.37\times 2.1 - 0.34\times 0 - 0.45\times 0.975$$
$$\log V_1 = 3.8504$$
$$\therefore\ V_1 = 7085.98\,Kh^{-1}$$
$$\Rightarrow V_1 = 1.892\ ^0C/s$$

The limited rate of cooling (LRC.) for the bainite transformation will now be computed. The LRC is defined as that rate of cooling which just suppresses the transformation to ferrite-pearlite, resulting in bainite formation. The LRC cooling time is given by the following expression:

$$\log V_2 = 6.33 - 2.31C - 0.73Mn - 0.41Cr - 1.37Mo - 0.53Ni \qquad (7.16)$$
$$= 6.33 - 2.31\times 0.27 - 0.73\times 2.125 - 0.41\times 0 - 1.37\times 0.975 - 0.53\times 2.1$$
$$\log V_2 = 1.7063$$
$$\therefore\ V_2 = 86.767\,Kh^{-1}$$
$$\Rightarrow V_2 = -0.052\ ^0C/s$$

The negative sign obtained in the answer to this calculation would imply that the formation of bainite is very unlikely for the given chemical composition

The cooling rate for the formation of ferrite is given by the following equation. CP is defined as the rate of cooling which just suppresses the formation of pearlite. This will result in the formation of ferrite-bainite or ferrite-martensite.

$$\log V_3 = 3.95 - 0.15Mn - 0.11Cr - 0.17Mo - 0.61Ni - 2\sqrt{(Mo)} \qquad (7.17)$$
$$= 3.95 - 0.15\times 2.125 - 0.11\times 0 - 0.17\times 0.975 - 0.61\times 2.1 - 2\sqrt{0.975}$$
$$\log V_3 = 0.2096$$
$$\therefore\ V_3 = 1.621\,Kh^{-1}$$
$$\Rightarrow V_3 = -0.075\ ^0C/s$$

9.14.6 The relationship between hardness and tensile properties

The following regression equations relating hardness and tensile properties will now be applied to ascertain the mechanical properties of the various microstructures occurring in the weld tempered zone.

9.14.7 Tempered Martensite Hardness

$$Hv_M = -75 - 434C - 368Si - 15Mn + 17Cr + 37Ni - 335Mo - 2235V$$
$$+1000/P_r(260 + 616C + 321Si - 21Mn - 35Ni - 11Cr + 352Mo + 2345V) \quad (7.18)$$
$$= -75 - 434 \times 0.27 - 368 \times 0.5 - 15 \times 2.125 + 17 \times 0 + 37 \times 2.1 - 335 \times 0.975 - 2235 \times 0$$
$$+ \frac{1000}{2092.03}(260 + 616 \times 0.27 + 321 \times 0.5 - 21 \times 2.125 - 35 \times 2.1 - 11 \times 0 + 352 \times 0.975$$
$$+ 2345 \times 0$$
$$Hv_M = -268.89$$

where: P_r is a temper parameter which has to be determined as follows:

$$10^3/P_c = 1.365 - 0.205C - 0.233Mo - 0.135V$$
$$10^3/P_c = 1.365 - 0.205 \times 0.27 - 0.233 \times 0.975 - 0.135 \times 0$$
$$\therefore \quad P_c = 923.81$$

This result in turn is used to determine β%, the weld tempered zone percentage.

$$\beta\% = 117.6 - 0.254P_c$$
$$= 117.6 - 0.254 \times 923.81$$
$$\beta\% = -117.05$$

We now determine the mean weld hardness after tempering, P_{rm}.

$$P_{rm} = 0.0298(\beta\%)^2 - 5.141(\beta\%) + 1082$$
$$= 0.0298 \times (-117.05)^2 - 5.141 \times (-117.05) + 1082$$
$$P_{rm} = 2092.03$$

This result is now used to determine the hardness in the weld tempered zones

9.14.8 Tempered Bainite Hardness

$$Hv_B = 262 + 163C - 349Si - 64Mn - 7Ni - 187Cr - 458Mo - 857V$$
$$+ {}^{10^3}\!/_{P_r}(-149 + 43C + 336Si + 79Mn + 16Ni + 196Cr + 352Mo + 1095V) \quad (7.19)$$
$$= 262 + 163 \times 0.27 - 349 \times 0.5 - 64 \times 2.125 - 7 \times 2.1 - 187 \times 0 - 458 \times 0.975 - 857 \times 0$$
$$+ \frac{1000}{2092.03}(-149 + 43 \times 0.27 + 336 \times 0.5 + 79 \times 2.125 + 16 \times 2.1 + 196 \times 0 + 352 \times 0.975$$
$$+ 1095 \times 0$$
$$Hv_B = -190.75$$

9.14.9 Pearlite Ferrite Hardness

$$Hv_F = 152 - 493C - 10Mn - 19Mo + {}^{10^3}\!/_{P_r}(-37 + 726C + 14Mn + 17Mo) \quad (7.20)$$
$$= 152 - 493 \times 0.27 - 10 \times 2.125 - 19 \times 0.975 + \frac{1000}{2092.03}(-37 + 726 \times 0.27 + 14 \times 2.125$$
$$+ 17 \times 0.975)$$
$$Hv_F = 77.27$$

9.14.10 Ultimate Tensile Strength

$$U.T.S.(MPa) = 19.13.10^{-4} HV^2 + 1.89HV + 181.5 \quad (7.21)$$

9.14.11 0.2% Yield Strength

$$Y.S.0.2(MPa) = -266.8 + U.T.S. + 30.41 \log VR + 51.01 \quad (7.22)$$

9.14.12 % Rigidity

$$EI\%(5d) = (-1.38 + 18.2 \times 10^3)/U.T.S. \quad (7.23)$$

The same calculation will now be repeated for the Armcord LH electrode.

9.15.1 The Martensite transformation range

The temperature at which the martensite transformation commences will now be computed. Here however, the chemical composition of the electrode will be added to that of the steel and entered into the equation.

$$M_S\,(^0C) = 539 - 423C - 30.4Mn + 17.7Ni + 12.1Cr + 7.5Mo \qquad (7.8)$$
$$= 539 - 423\times 0.221 - 30.4\times 1.895 + 17.7\times 2.07 + 12.1\times 0.32 + 7.5\times 0.935$$
$$M_S(^0C) = 435.43$$

This temperature is considerably higher than that obtained for the Transarc 118 electrode calculation, largely due to the contribution of the chromium content in the equation.

9.15.2 The Bainite transformation range

The temperature at which the bainite transformation commences and finishes will now be computed.

$$B_S(^0C) = 830 - 270C - 90Mn - 37Ni - 70Cr - 83Mo \qquad (7.9)$$
$$= 830 - 270\times 0.221 - 90\times 1.895 - 37\times 2.07 - 70\times 0.32 - 83\times 0.935$$
$$B_S(^0C) = 423.46$$

with $B_{50} = B_S - 60^0C$ (7.10)

$$B_{50} = 423.46 - 60$$
$$B_{50} = 363.46$$

and $B_f = B_S - 120^0C$ (7.11)

$$B_f = 423.46 - 120$$
$$B_f = 303.46\,^0C$$

The above result is once again higher than the preceding electrode calculation, largely due to the contribution of chromium to the equation.

9.15.3 The ferrite-pearlite transformation range

The start of the ferrite transformation is given by the following equation.

$$10mm\,bar\,diameter\ F_S\,(^0C) = 878 - 295C - 78Mn \qquad (7.12)$$
$$= 878 - 295\times 0.221 - 78\times 1.895$$
$$F_S(^0C) = 664.99$$

The start of the pearlite transformation on air-cooling is given by the following equation.

$$P_S\,(^0C) = 700 - 60Mn \qquad (7.13)$$
$$= 700 - 60\times 1.895$$
$$P_S(^0C) = 586.3$$

The above equation may successfully be applied to diameters 10 to 1000mm.

9.15.4 The critical cooling velocity and other significant cooling rates

The critical cooling velocity (CCV.) for the martensite transformation will now once again be computed using Armcord LH data. CCV for martensite formation in seconds, is given by the following expression:

$$\log V_1 = 7.42 - 3.13C - 0.71Mn - 0.37Ni - 0.34Cr - 0.45Mo \qquad (7.15)$$
$$= 7.42 - 3.13\times 0.221 - 0.71\times 1.895 - 0.37\times 2.07 - 0.34\times 0.32 - 0.45\times 0.935$$
$$\log V_1 = 4.087$$
$$\therefore\ V_1 = 12217.99\,Kh^{-1}$$
$$\Rightarrow V_1 = 3.32\,^0C/s$$

The limited rate of cooling (LRC.) for the bainite transformation will now be computed. The LRC is defined as that rate of cooling which just suppresses the transformation to ferrite-pearlite, resulting in bainite formation. The LRC cooling time is given by the following expression:

$$\log V_2 = 6.33 - 2.31C - 0.73Mn - 0.41Cr - 1.37Mo - 0.53Ni \qquad (7.16)$$
$$= 6.33 - 2.31\times 0.221 - 0.73\times 1.895 - 0.41\times 0.32 - 1.37\times 0.935 - 0.53\times 2.07$$
$$\log V_2 = 1.927$$
$$\therefore\ V_2 = 84.51\,Kh^{-1}$$
$$\Rightarrow V_2 = -0.052\,^0C/s$$

The negative sign obtained in the answer to this calculation would imply that the formation of bainite is very unlikely for the given chemical composition

The cooling rate for the formation of ferrite is given by the following equation. CP is defined as the rate of cooling which just suppresses the formation of pearlite. This will result in the formation of ferrite-bainite or ferrite-martensite.

$$\log V_3 = 3.95 - 0.15Mn - 0.11Cr - 0.17Mo - 0.61Ni - 2\sqrt{(Mo)} \quad (7.17)$$

$$= 3.95 - 0.15\times 1.895 - 0.11\times 0.32 - 0.17\times 0.935 - 0.61\times 2.07 - 2\sqrt{0.935}$$

$$\log V_3 = 0.275$$

$$\therefore \; V_3 = 1.884\, Kh^{-1}$$

$$\Rightarrow V_3 = -0.075\, ^0C/s$$

9.15.5 The relationship between hardness and tensile properties

The following regression equations relating hardness and tensile properties will now be applied to ascertain the mechanical properties of the various microstructures occurring in the weld tempered zone.

9.15.5.1 Tempered Martensite Hardness

$$Hv_M = -75 - 434C - 368Si - 15Mn + 17Cr + 37Ni - 335Mo - 2235V$$

$$+1000/P_r(260 + 616C + 321Si - 21Mn - 35Ni - 11Cr + 352Mo + 2345V) \quad (7.18)$$

$$= -75 - 434\times 0.221 - 368\times 0.575 - 15\times 1.895 + 17\times 0.32 + 37\times 2.07 - 335\times 0.935$$

$$- 2235\times 0 + \frac{1000}{2042.52}(260 + 616\times 0.221 + 321\times 0.575 - 21\times 1.895 - 35\times 2.07$$

$$- 11\times 0.32 + 352\times 0.935 + 2345\times 0)$$

$$Hv_M = -253.37$$

where: P_r is a temper parameter which has to be determined as follows:

$$10^3/P_c = 1.365 - 0.205C - 0.233Mo - 0.135V$$

$$10^3/P_c = 1.365 - 0.205\times 0.221 - 0.233\times 0.935 - 0.135\times 0$$

$$\therefore \; P_c = 907.57$$

This result in turn is used to determine β%, the weld tempered zone percentage.

$$\beta\% = 117.6 - 0.254P_c$$

$$= 117.6 - 0.254\times 907.57$$

$$\beta\% = -112.92$$

We now determine the mean weld hardness after tempering, P_{rm}

$$P_{rm} = 0.0298(\beta\%)^2 - 5.141(\beta\%) + 1082$$
$$= 0.0298 \times (-112.92)^2 - 5.141 \times (-112.92) + 1082$$
$$P_{rm} = 2042.52$$

This result is now used to determine the hardnes in the weld tempered zones

9.15.5.2 Tempered Bainite Hardness

$$Hv_B = 262 + 163C - 349Si - 64Mn - 7Ni - 187Cr - 458Mo - 857V$$
$$+ {}^{10^3}/_{P_r}(-149 + 43C + 336Si + 79Mn + 16Ni + 196Cr + 352Mo + 1095V) \quad (7.19)$$
$$= 262 + 163 \times 0.221 - 349 \times 0.575 - 64 \times 1.895 - 7 \times 2.07 - 187 \times 0.32 - 458 \times 0.935$$
$$- 857 \times 0 + \frac{1000}{2042.52}(-149 + 43 \times 0.221 + 336 \times 0.575 + 79 \times 1.895 + 16 \times 2.07$$
$$+ 196 \times 0.32 + 352 \times 0.935 + 1095 \times 0)$$
$$Hv_B = -218.84$$

9.15.5.3 Pearlite Ferrite Hardness

$$Hv_F = 152 - 493C - 10Mn - 19Mo + {}^{10^3}/_{P_r}(-37 + 726C + 14Mn + 17Mo) \quad (7.20)$$
$$= 152 - 493 \times 0.221 - 10 \times 1.895 - 19 \times 0.935 + \frac{1000}{2042.52}(-37 + 726 \times 0.221$$
$$+ 14 \times 1.895 + 17 \times 0.935)$$
$$Hv_F = 87.54$$

9.15.5.4 Ultimate Tensile Strength

$$U.T.S.(MPa) = 19.13.10^{-4} HV^2 + 1.89HV + 181.5 \quad (7.21)$$

9.15.5.5 0.2% Yield Strength

$$Y.S.0.2(MPa) = -266.8 + U.T.S. + 30.41 \log VR + 51.01 \quad (7.22)$$

9.15.5.6 % Rigidity

$$EI\%(5d) = (-1.38 + 18.2 \times 10^3)/U.T.S. \quad (7.23)$$

Chapter 10 – FINITE ELEMENT NUMERICAL RESULTS

10.1 Finite Element Numerical Simulation Results

The Finite Element Method described in chapter 8 was applied to the problem of simulating the metallurgical phase changes associated with MMA welding of ROQ-tuf AD690. The finite element meshed used is shown below

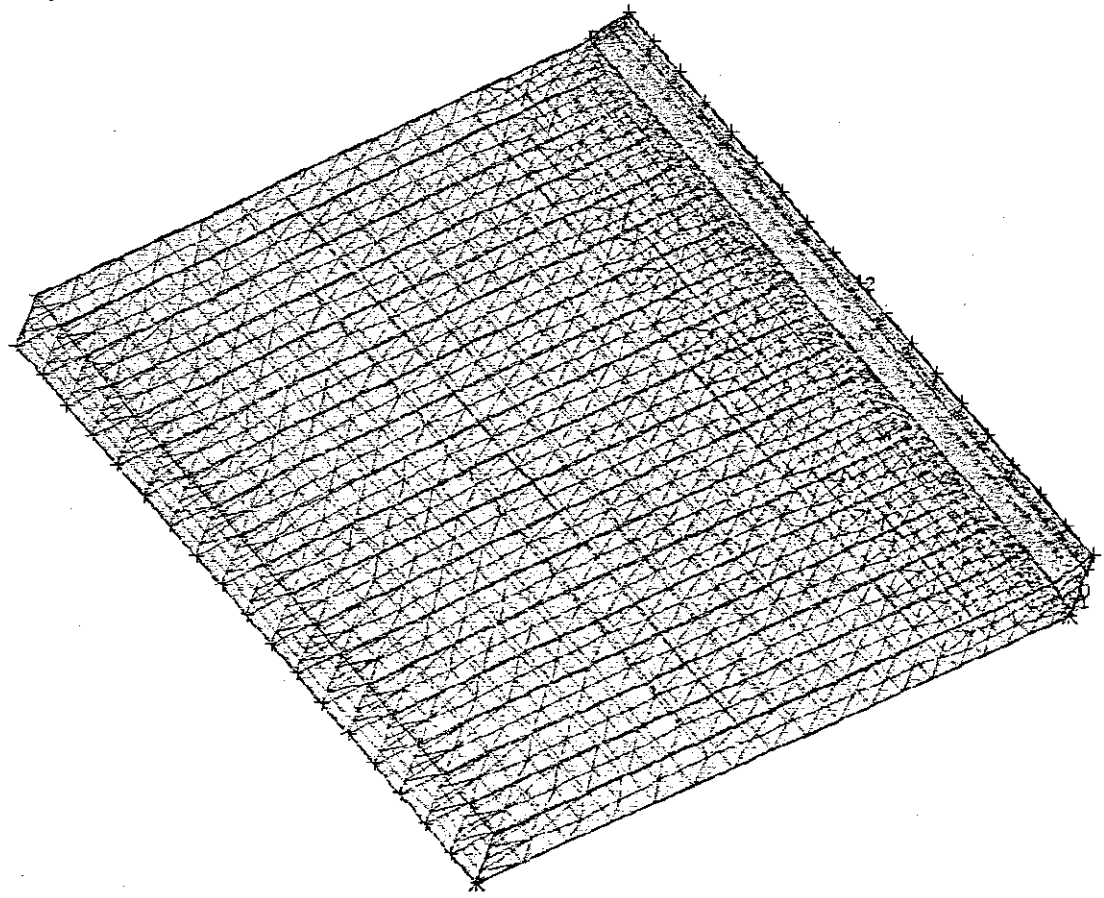

Figure 10. 1. The meshed used for FE simulations.

The result of the modeling of the heat source and cooling conditions is shown below as temperature contours:

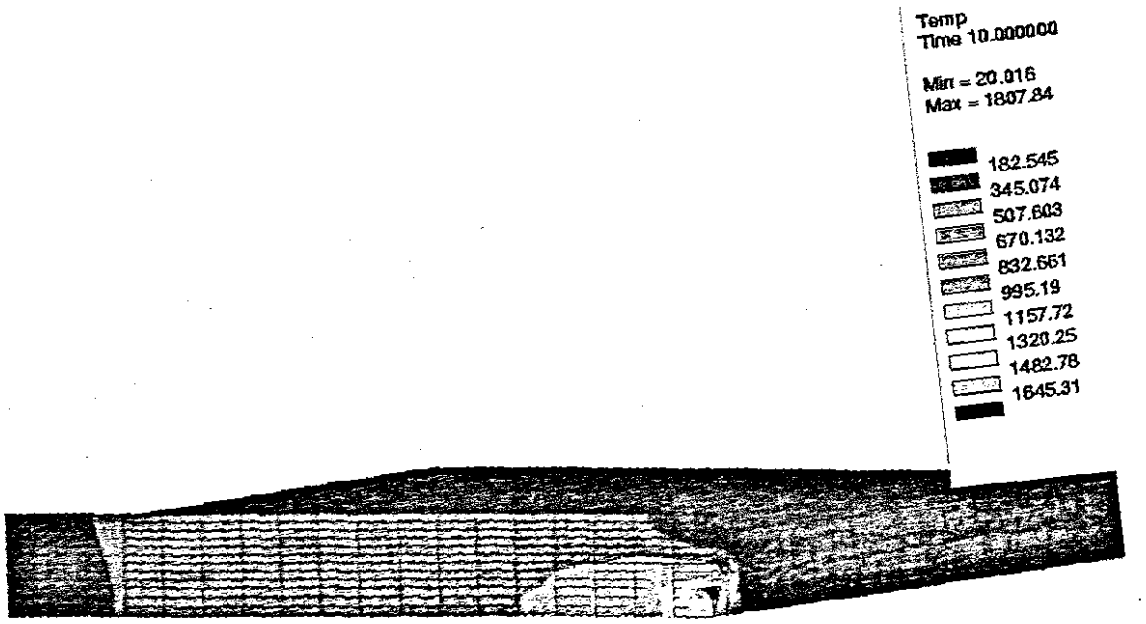

Figure 10.2. The temperature distribution during the first welding pass.

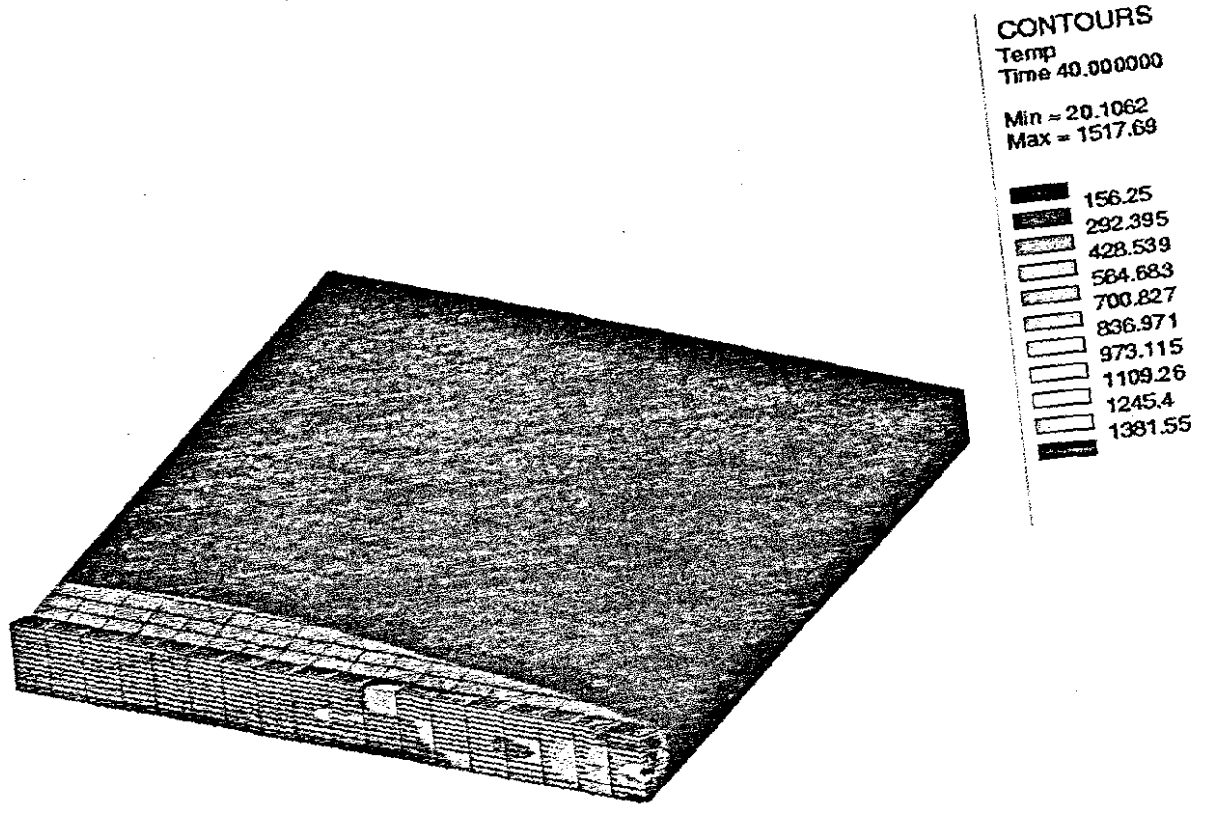

Figure 10.3. The temperature distribution during the second welding pass.

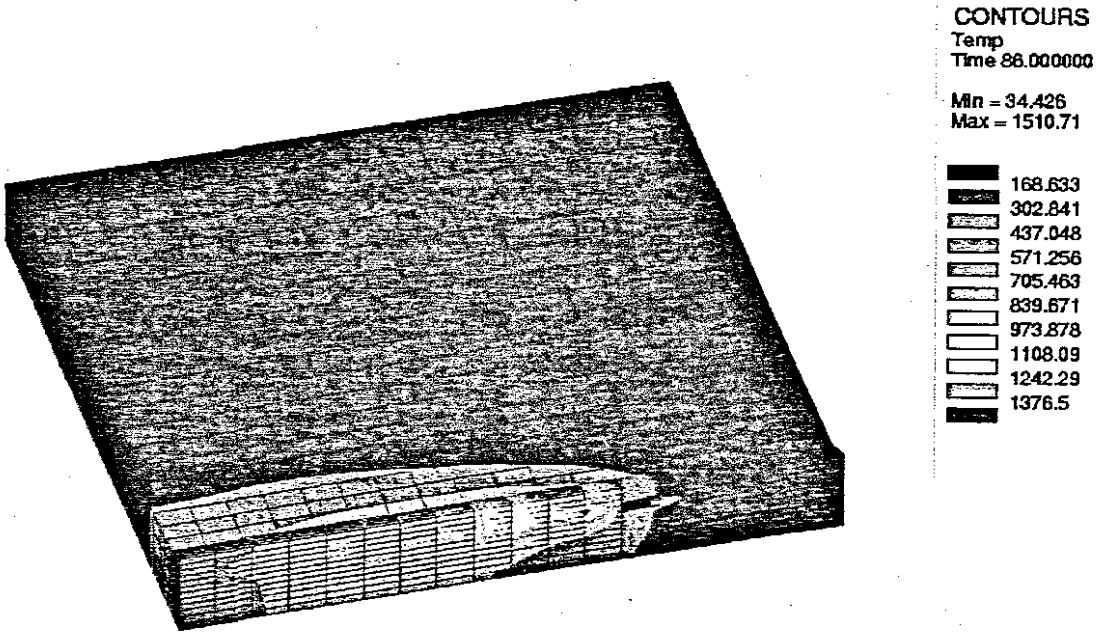

Figure 10.4. The temperature distribution during the third welding pass.

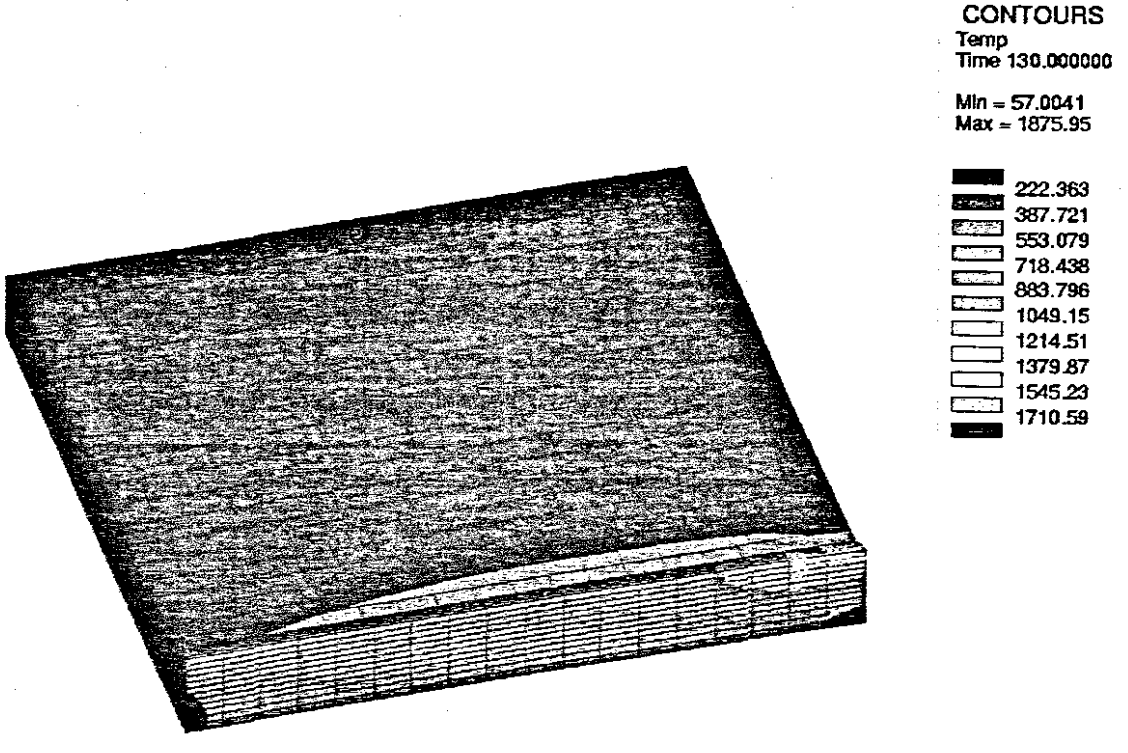

Figure 10.5. The temperature distribution during the fourth welding pass.

The temperature is relatively stable after the start where the root run has a lower temperature and the temperature is higher for the final pass or cap. The stability of the temperature is in some part due to the inclusion of interpass cooling during the simulation. The weld is allowed to cool after each welding pass as shown in the figure below:

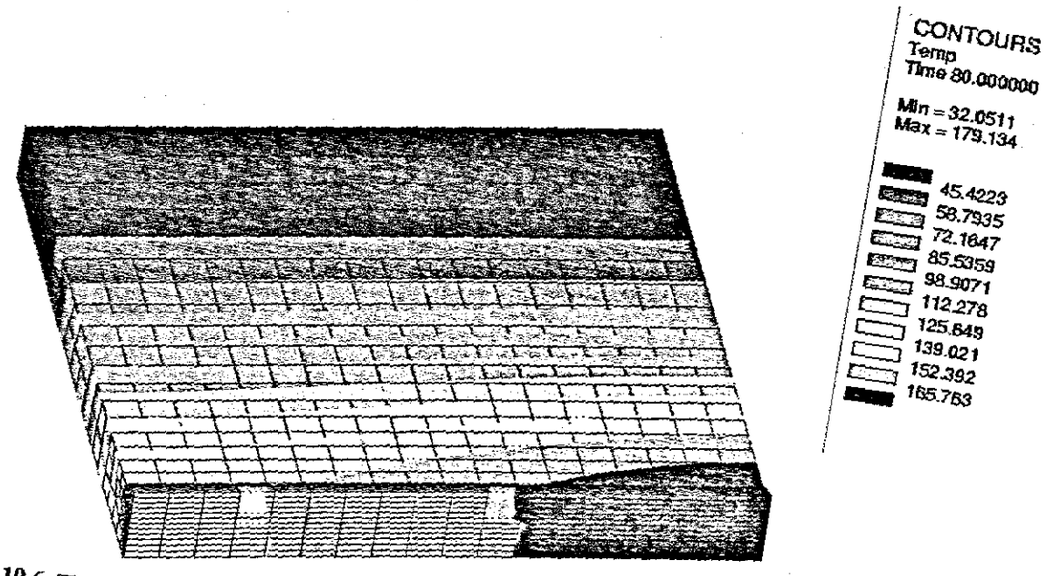

Figure 10.6. The temperature distribution after the second pass during inter-pass cooling.

The weld is finally allowed to cool down after the fourth pass:

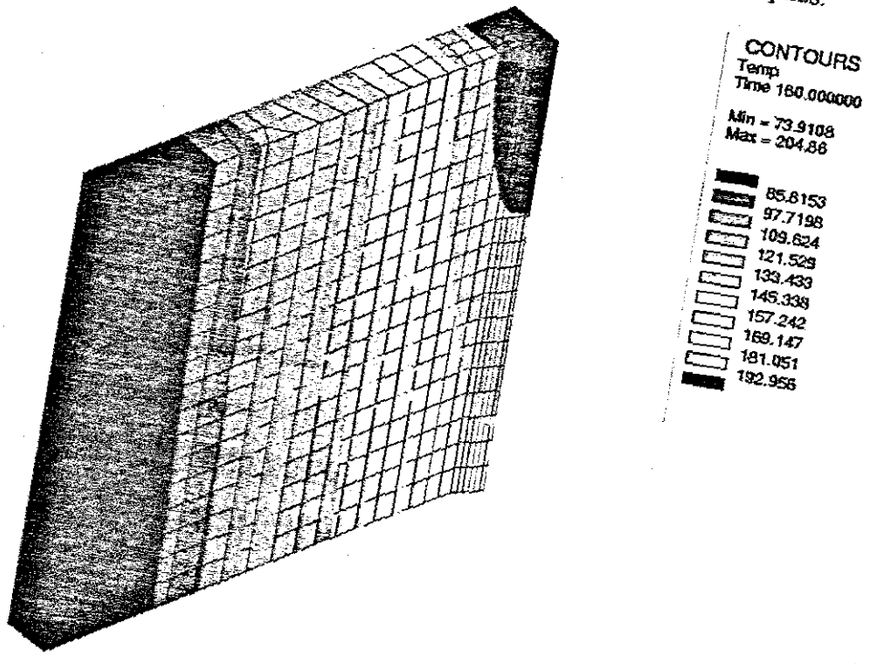

Figure 10.7. The temperature distribution during final cooling

The plate is initially assumed to consist of austempered martensite. For the purpose of simulation the austempered martensite is taken to be a different phase from the martensite produced from the re-austenized HAZ. The tempered martensite is transformed to austenite as a result of heating by the welding arc. The result of re-austenization of the plate and cooling back to martensite is shown in the plots of metallurgical phase fractions shown below:

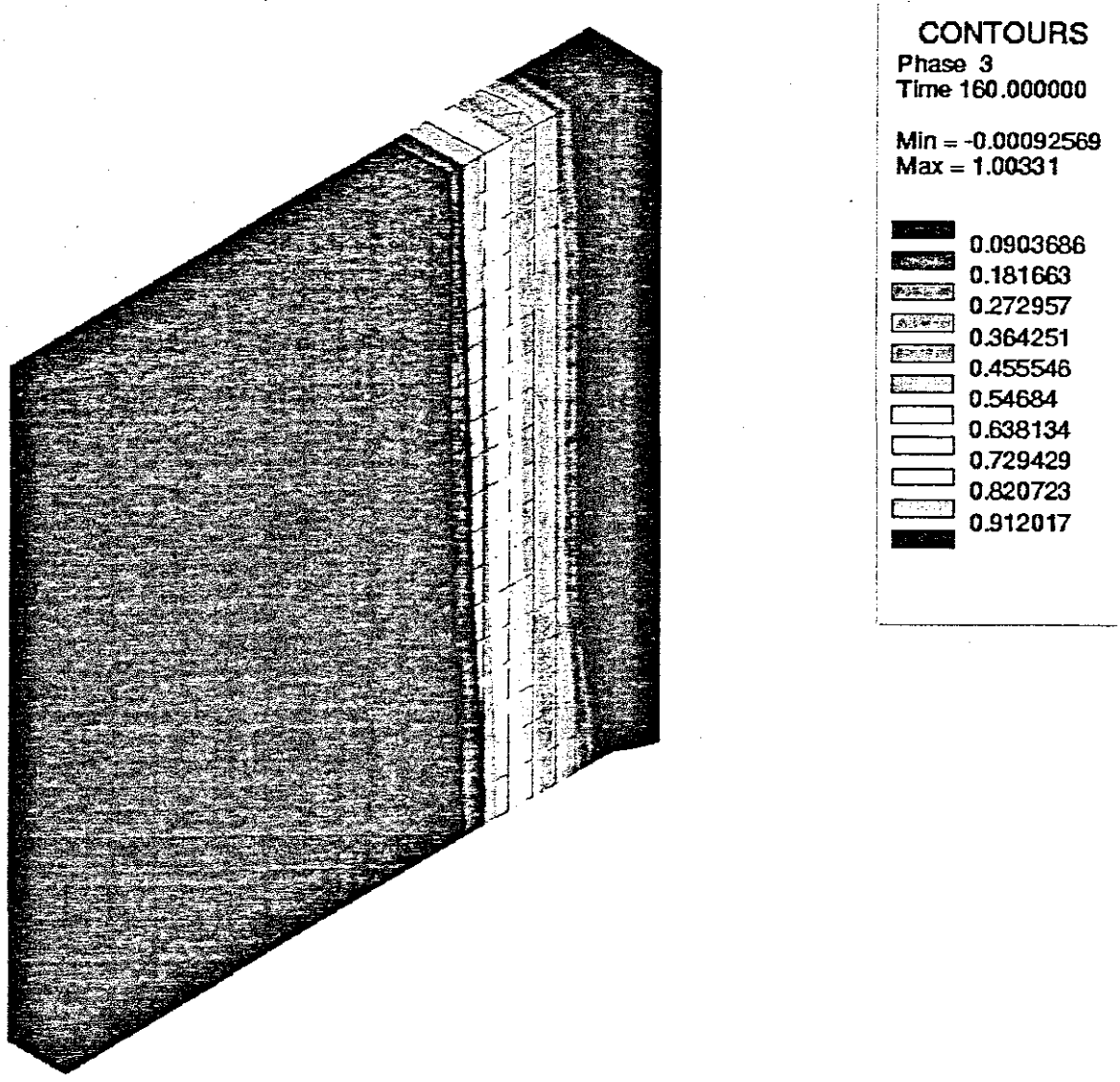

Figure 10.8. The austenite fraction at the end of the simulation.

The blue area in the left of the above plot represents the remaining austempered martensite which was not re-austenized during the heating due to welding. The right blue area represents the area transformed from austenite back to martensite. This martensite region is not tempered and would therefore be a potential zone for brittle fraction as shown in the next figure.

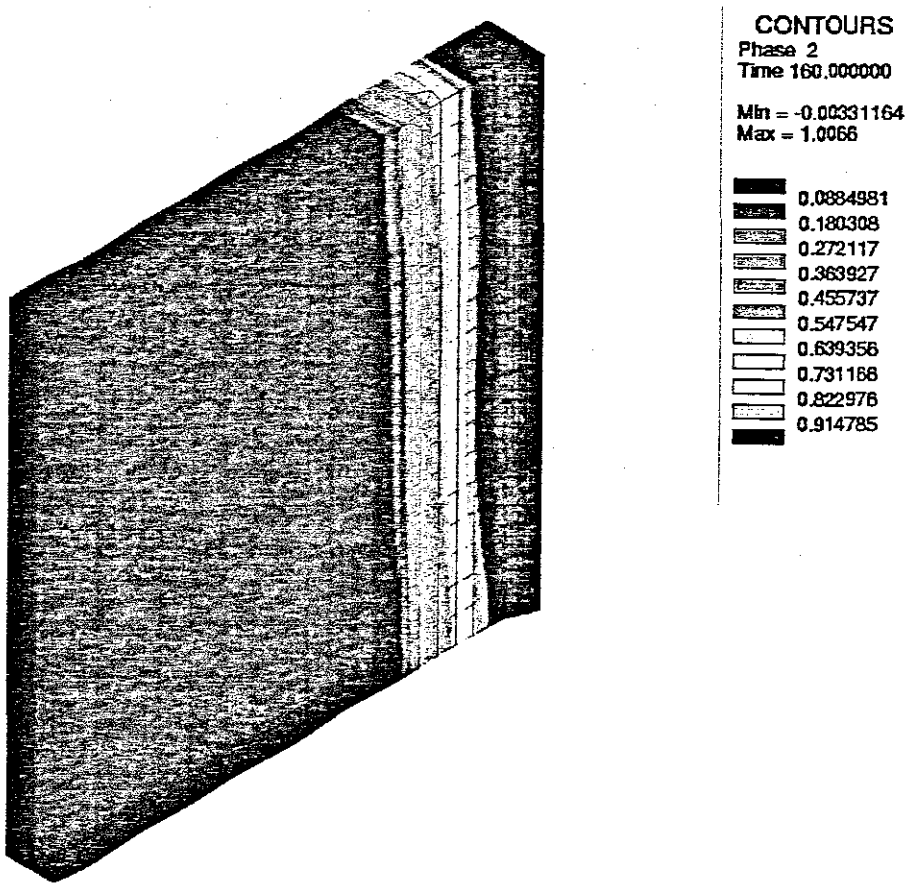

Figure 10.9. The new martensite fraction formed after cooling of the re-austenized HAZ.

The red region in the above plot represents the area of new martensite formation.

Chapter 11 – CONCLUSIONS.

11.1 Conclusions

The aim of this research was to catalogue the metallurgical changes taking place in the tempered martensitic steel, ROQ-tuf AD690, when subjected to the MMA welding process. The preceding literature survey covered all the possible scientific procedures that could have been used to attain this goal. The section on experimental results reflected the procedures followed and the results obtained.

ROQ-tuf AD690 plates of dimension 100x100mm were subjected to a heat treatment regime as depicted in table 9.7. The base stresses in the plates were ultrasonically measured using the Debro-30 and are given in graph 9.1 and table 9.8. Welds were then carried out on the plates using the Transarc 118 and Armcord LH electrodes. The post weld stresses were again measured using the Debro-30 and are also given in graph 9.1 and table 9.8. From the results it can be deduced that irrespective of the thickness of the material or the electrode used the stresses produced in a single butt weld will be highly compressive.

The plates of dimensions 100x100mm had holes machined into them on either side of the single butt V to accommodate thermocouples, as is indicated in figures 9.2 and 9.3. These thermocouples linked to a computer were used to generate the heating and cooling curves generated by the two electrodes. Graph 9.2 depicts the comparative temperature profiles for the root run on plates 3 and 4, both 10mm plates. It can be seen that the heat input by the Transarc 118 electrode is considerably higher than that for the Armcord LH electrode, due to the fact that the input current for optimal welding, is 10 Amps higher in the case of the former. Conversely, the cooling rate for the Transarc 118 electrode is higher than that for the Armcord LH electrode. A similar trend can be seen in graphs 9.3 and 9.4. Both electrodes produced fairly spatter free welds, although it must be said that the weld produced using the Transarc 118 electrode was the cleaner of the two. The weld penetration produced by both electrodes was good and will be further discussed when analyzing the results of the tensile tests.

A similar trend of higher heat input for the Transarc 118 electrode, due to its higher current setting, than the Armcord LH electrode is followed during the welding of the 16mm plates. It should be stated, however, that the welding of a 16mm plate required only 10 passes by the Transarc 118 electrode as opposed to 12 passes by the Armcord LH electrode. This could be interpreted as a 17% higher material deposition rate for the Transarc 118 electrode as opposed to the Armcord LH elctrode and would nullify the initial higher energy consumption for the former.

The welded plates were then sectioned and metallurgical samples prepared, producing the micrographs depicted in section 9.6. The microstructures occurring along the centre line of the 10-pass weld produced by the Transarc 118 electrode is fairly soft and ductile, being primarily ferrite and sorbitic pearlite interspersed with some cementite. This is largely due to the higher temperatures generated in the center and the more gradual cooling rates, allowing for a longer period of metallurgical transformation. Left of the centre line the microstructures produced were martensite, near the cap, due to the higher cooling rate and the ferrite and sorbitic pearlite further down. To the right of the centre line the microstructures produced were ferrite and pearlite.

The Armcord LH electrode produced a 12-pass weld having the following microstructures on the centre line. The center of the cap produced martensite followed by ferrite and sorbitic pearlite lower down. To the left of the center line the microstructures were pearlite, cementite and martensite. To the right of the centre line the microstructures produced were sorbitic pearlite, cementite and martensite. The microstructures produced by the Armcord LH electrode are generally harder and more brittle than that produced by the Transarc 118 electrode and will be further discussed when the mechanical integrity of the weld is analysed in the section on tensile testing.

Tensile specimens were prepared from the post welded plates having the weld bead on the center of the specimen as is depicted in 9.31 and 9.32. These specimens were then subjected to a uni-axial tensile test utilising the computerized tensile tester available, producing the following results. Figure 9.34 depicts the stress versus strain curve for specimen 6.2, which was machined from the 16mm plate and welded with an Armcord LH electrode. The resulting UTS for the weld is 877.69MPa, which correlates well with manufacturers data. Young's Modulus of elasticity for the specimen is calculated at 230.15GPa.

Specimen 8.2 was prepared from a 10mm plate welded with a Transarc 118 electrode. The UTS was calculated at 815.33MPa, which is still well within manufactures specifications. Young's Modulus was calculated at 257.9GPa.

In the section on metallurgical samples it was seen that the microstructures produced in the weld by the Armcord LH electrode were harder and more brittle than those produced in the weld by the Transarc 118 electrode. This point is reinforced by the values of the Young's Modulus calculated from the stress strain curves generated during the tensile tests. The UTS for the Armcord LH weld is, however, much higher than that for the Transarc 118 weld. This can be largely attributed to the mechanism of failure in materials. During failure of a material, atoms will slide over one another until barrier occurs to prevent the sliding. Such a barrier occurs at a dislocation or phase transformation, which is quite severe in the case of the weld produced using the Armcord LH electrode. Atom movement is arrested until the force propagating this sliding is high enough to overcome the barrier, after which the sliding will continue, until the next barrier, or dislocation is reached. This would explain the higher tensile strength produced by the Armcord LH electrode, as opposed to those produced by the Transarc 118 electrode.

The test bars that were quenched in brine, water or oil, or normalized in still air, had thermocouples embedded in them, from which cooling curves were once again generated. From these cooling curves, cooling rates were determined. It stands to reason that the most severe cooling rates will occur at the bar ends in contact with the quench medium, as is evident from graph 9.20. For the brine quench the cooling rates varied from 33.8°C/s for the end in contact with the quenchant, to 0.47°C/s, as is evident from table 9.8.

The cooling rates generated during the water quench was less severe than that for a brine quench and ranged from 10.7°C/s to 0.23°C/s.

Similarly, the cooling rates for the oil quench was less than those for a water or brine quench, ranging from 3.5°C/s to 0.47°C/s.

The normalised bar experienced moderate cooling rates ranging from 0.71°C/s to 0.24°C/s.

When looking at the cooling rates and the relative thermocouple positions, the following deductions can be made, namely, that the first 35mm of the brine and water quenched bars will be transformed to martensite. Similarly, the first 10mm of the oil quenched bar will be transformed to martensite. This can be said because the cooling rates are much higher than the critical cooling rate for transformation to martensite, calculated at 1.892°C/s as will be seen in the section on Statistical Formulae. The remaining sections of the bar will be transformed to softer microstructures such as ferrite, pearlite and cementite in varying proportions.

From the hardness data, it can be deduced that distinct changes in material hardness should be evident where a phase transformation has occurred. After quenching in the various media the bars were surface ground to remove any scale, whilst at the same time making sure that the heat input into the specimens is kept at a minimum to prevent any phase transformations. The hardnesses of the specimens were then measured using the hardness tester available. The hardness measurements together with the metallurgical sections produced were used to indicate the zones of transformation within the HAZ.

In the preceding section on cooling curves it was stated that the first 30mm of both the brine and water quenched bars will be transformed to martensite, due to the severity of the cooling rate. This, however, is not very evident from the hardness readings and curves generated. It must, however, be said that distinct changes in hardness has occurred at approximately these positions along the bars and this might have been further verified by carrying out a microhardness examination of the specimens in question, had the facilities and time been available.

The quenched bars sectioned and metallurgical specimens were produced yielding the following micrographs.

The brine quenched bar had transformed to martensite over 80% of its length.

The micrographs for all other specimens were taken using the new microscope. The water quenched bar transformed to martensite 60% of its length. The remaining length was transformed to pearlite and ferrite in varying proportions.

The first 20% of the oil quenched bar was transformed to fine martensite, as was predicted. In the remaining section of the bar the microstructure had transformed to ferrite and pearlite.

For the normalised bar the microstructure transformed to ferrite and pearlite along 100% of its length.

Empirical formulae were used to predict mechanical properties such as the UTS of the material to give an indication of the strength of the weld for a given welding regime. The microstructures and resulting hardness values obtained from the quenched bars were applied to the microstructures occurring in the HAZ. The mean of these hardness values were computed and used in an empirical formula to predicting the UTS of the weld. From the results obtained it can be seen that the values predicted by the empirical formulae exceed actual measured results by a fair margin. Applying a weighted mean value to the microstructures present in the HAZ and then recalculating could possibly have narrowed the results.

Finite element calculations were done to simulate the MMA welding process applied to ROQ-tuf AD690 following the formulation of Ronda and Oliver [21]. The heat source was modelled with a travelling Gaussian distribution as described in section 8.3. This was matched, to some extent, to experimentally measured temperatures. One difficulty with the thermal measurements was taking measurements close enough to the weld line which meant that only the lower temperatures from about 500 degrees could be measured for comparison with FE contours.

The finite element calculations show that it is possible to model the Phase Transformations induced by MMA welding in ROQ-tuf AD690. The accuracy of the modelling is, however, dependent on the use of appropriate parameters for the phase evolution equations. It was not possible to obtain the exact CCT diagram for the steel in question so some approximation was done using a steel with the closest chemical composition available for which such data was available. A lot of work still needs to be done in this area such as improved modelling of the transformation of the austempered martensite structure during heating prior to the formation of product phases during cooling. Such work, however, falls out of the scope of this thesis and is left to future research as a possible doctoral thesis.

Appendix A

Preheat Temperature for ROQ-tuff AD690

The cracking factor must first be determined using the following expression:

$$P_C = C + \frac{Si}{30} + \frac{Mn}{20} + \frac{Cu}{20} + \frac{Ni}{60} + \frac{Cr}{20} + \frac{Mo}{15} + \frac{V}{10} + 5B + \frac{t}{600} + \frac{H}{60} \quad (1.4)$$

$$= 0.27 + \frac{0.5}{30} + \frac{2.125}{20} + \frac{0}{20} + \frac{2.1}{60} + \frac{0}{20} + \frac{0.975}{15} + \frac{0}{10} + 5 \times 0 + \frac{0.01}{600} + \frac{0}{60}$$

$$= 0.493$$

The preheat temperature will now be calculated:

$$T_o = 1440 P_C - 392 \quad (1.3)$$

$$= 1440 \times 0.493 - 392$$

$$= 317.92^{\circ}C$$

This value of preheat is quite high for a 16mm plate.

Appendix B

Determination of the Specific Heat Capacity

The specific heat capacity of ROQ-tuff AD690 was determined from equation 1.8.

$$cp_{ROQ} = \frac{V \times I \times \eta}{\Delta T} \quad (KJ/kgK) \qquad (1.8)$$

$$= \frac{V \times I \times \eta}{(T_2 - T_1)}$$

$$= \frac{22.4 \times 130 \times 0.7}{200 - 22}$$

$$= 11.45\ KJ/kgK$$

The welding machine settings for the Transarc 118 electrode was used for this calculation, since it required the higher current setting and hence, produced the higher temperature difference.

Appendix C

BS 18.

Table 3.1 Round bar tensile test-pieces. Table of standard dimensions

S_0 (mm^2)	d (*mm*)	L_0 (*mm*)	L_c (*mm*)	r *wrought materials* (*mm*)	r *cast materials* (*mm*)
200	15.96	80	88	15	30
150	13.82	69	76	13	26
100	11.28	50	62	10	20
50	7.98	40	44	8	16
25	5.64	28	31	5	10
12.5	3.99	20	21	4	8

d = Diameter of test-piece, L_0 = gauge length, L_c = parallel length.
S_0 = original cross-sectional area, r = radius at shoulder (refer to Fig. 3.9(a)).
For proportional test-pieces $L_0 = 5.65\ S_0$, $L_0 \simeq 5\ d$.

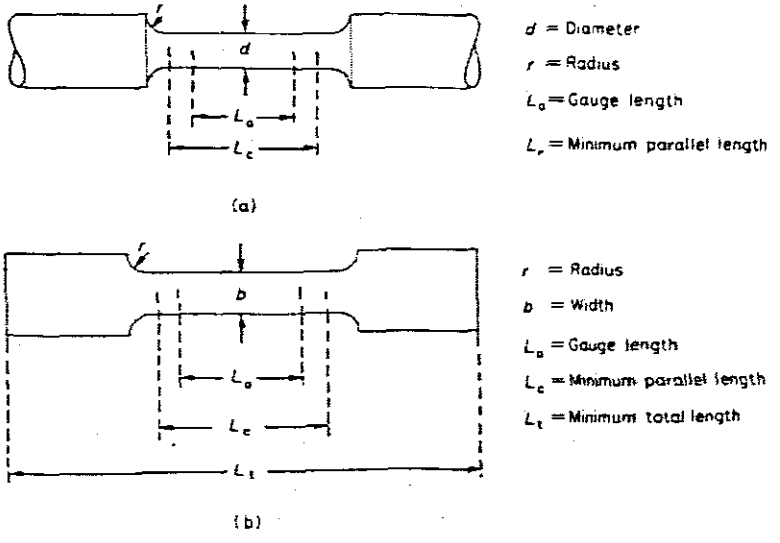

Figure 3.9 Types of tensile test piece: (a) round test-pieces; (b) flat test-pieces.

APPENDIX D.

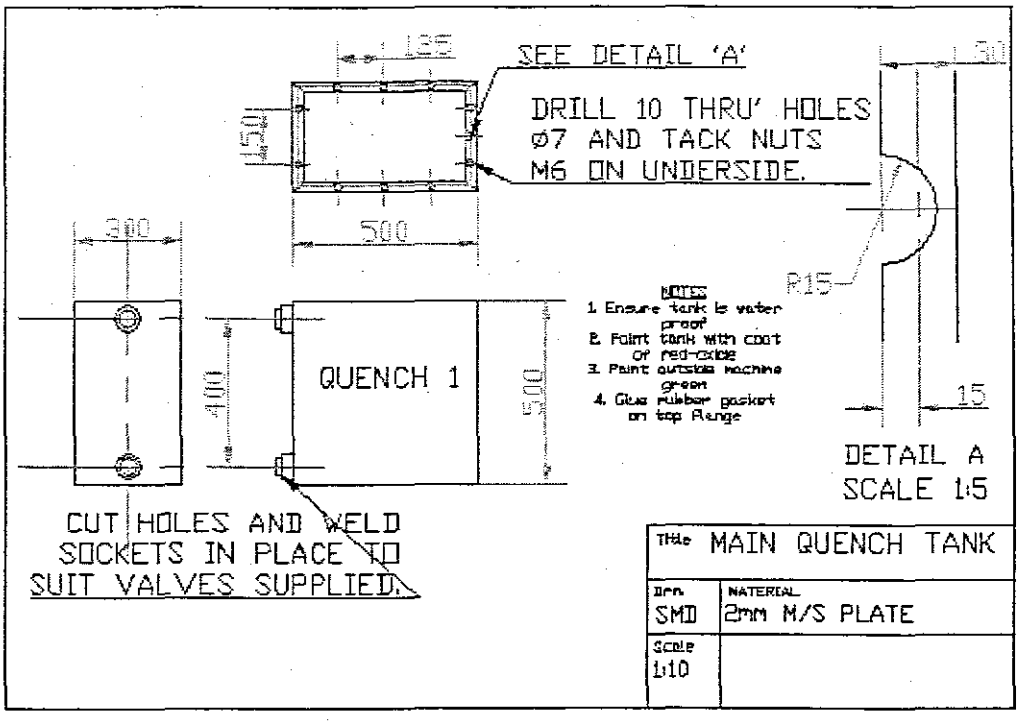

Detail drawing of Quench Tank indicating inlet and outlet socket locations.

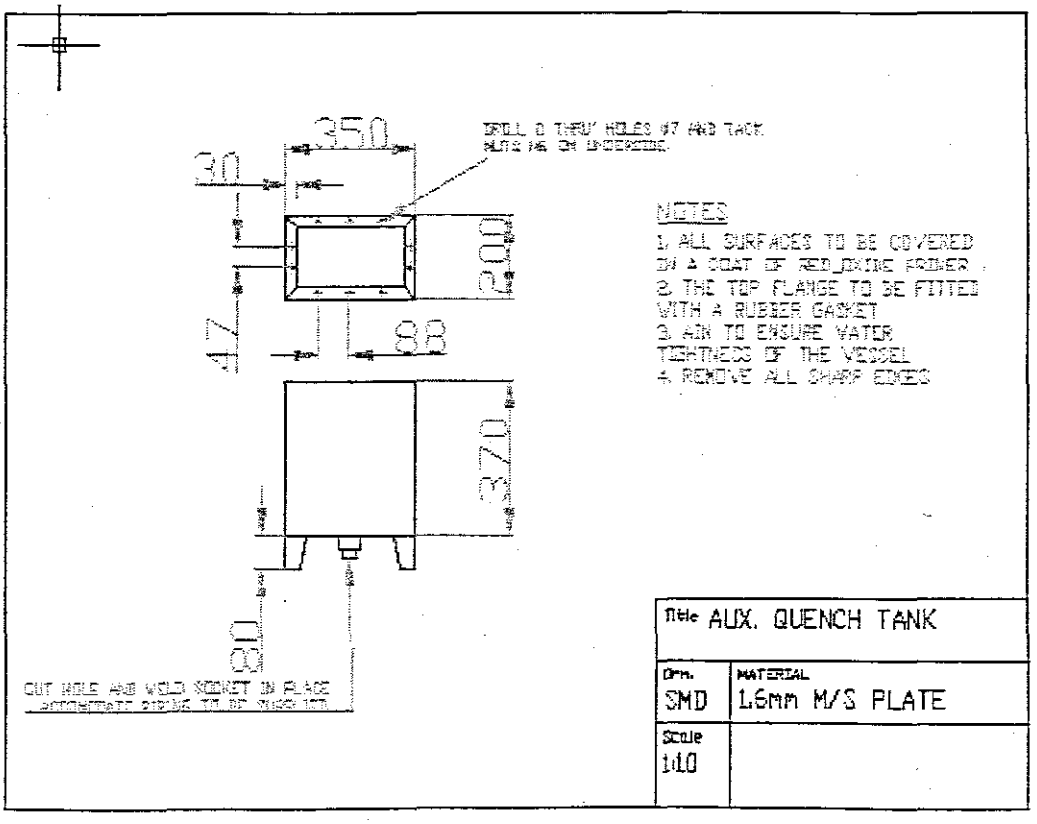

Detail drawing of the Auxilliary tank, which was used as an insert in the main tank to give the required flow pattern.

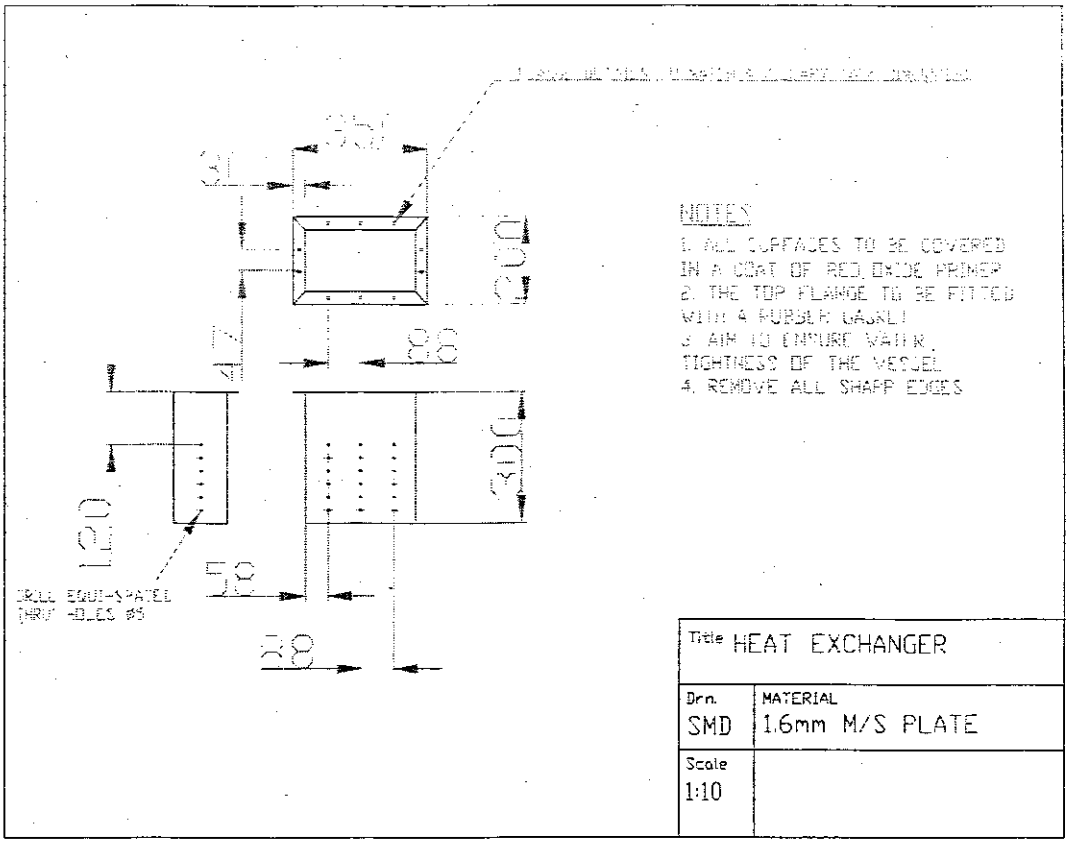

Detail drawing of another insert , which was placed in the main quench tank.

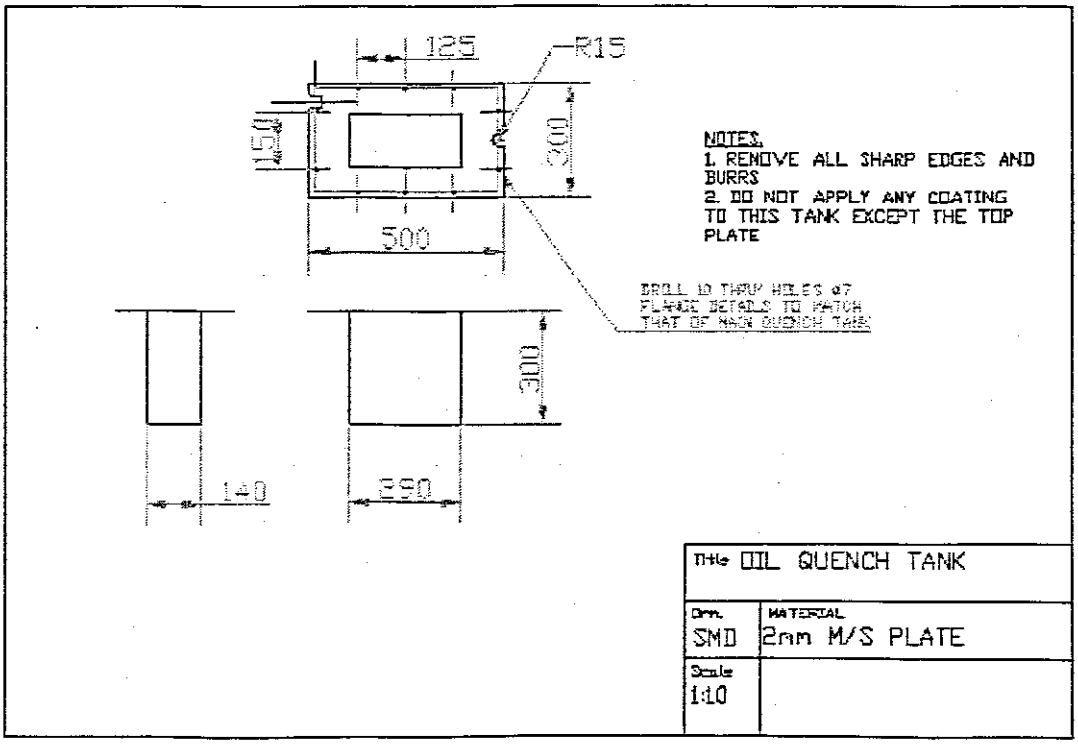

Detail drawing of the insert used for the oil quench. This insert was placed inside the main quench tank, whilst water was flowing through it for optimal heat exchange.

Appendix E

Tensile Test Results

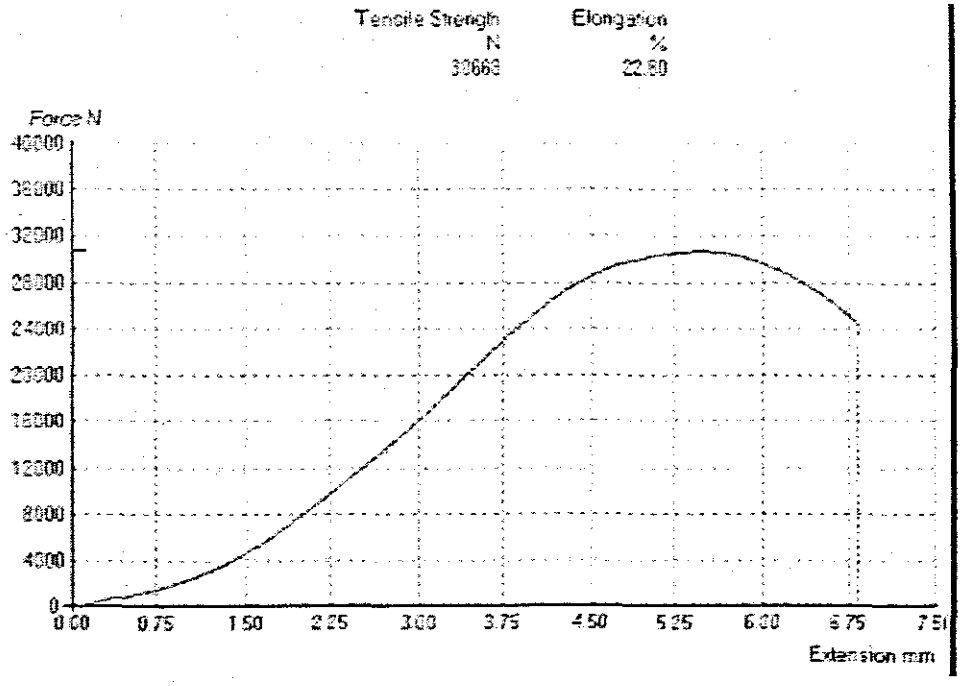

Tensile Test of specimen 7, which was machined from a 16mm plate that was welded with an Armcord LH electrode. UTS. 30.67kN.

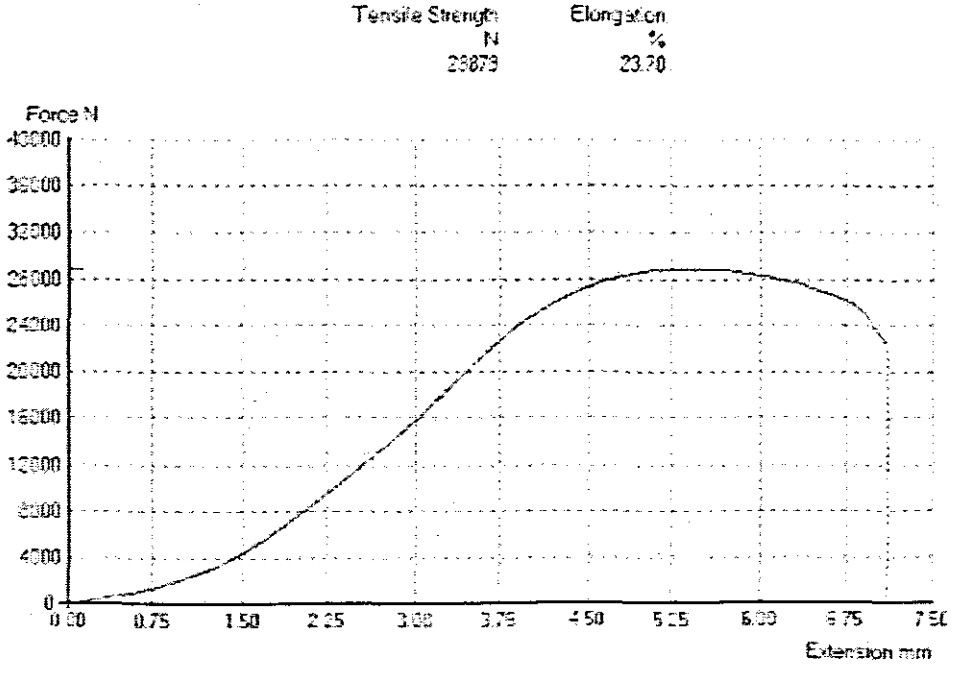

Tensile Test of Specimen 8.1, which was machined from a 10mm plate and welded with a Transarc 118 electrode. UTS. 28.88kN.

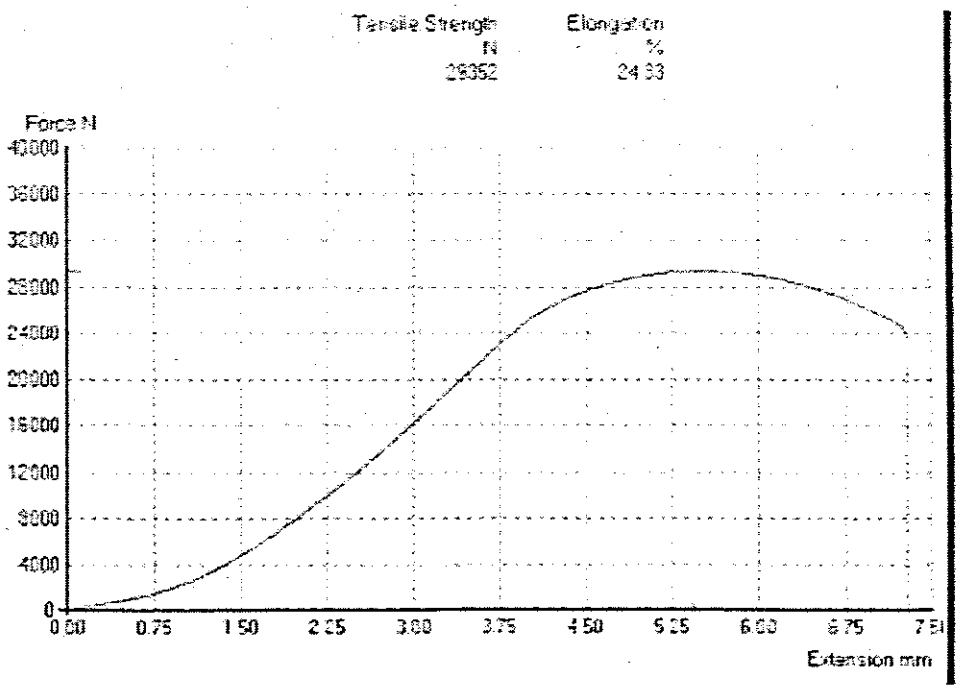

Tensile Test of Specimen 8.2 is the pair of 8.1 discussed previously. UTS. 29.35kN.

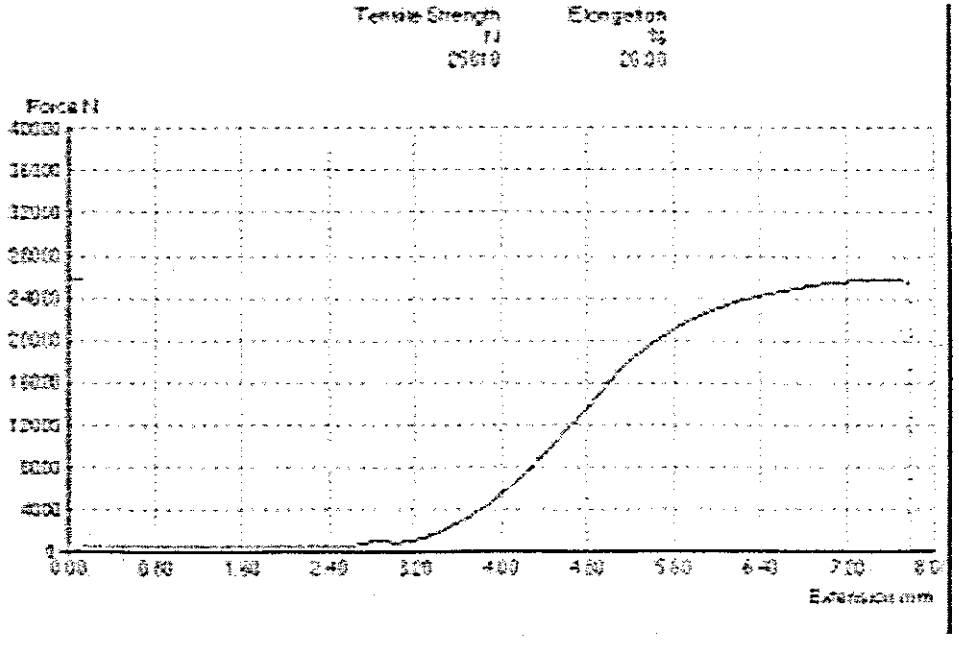

Tensile Test of Specimen 2.2, which was machined from a 16mm plate and welded with a Transarc 118 electrode. Note, a fair amount of slip occurred at the grips. UTS. 25.81kN.

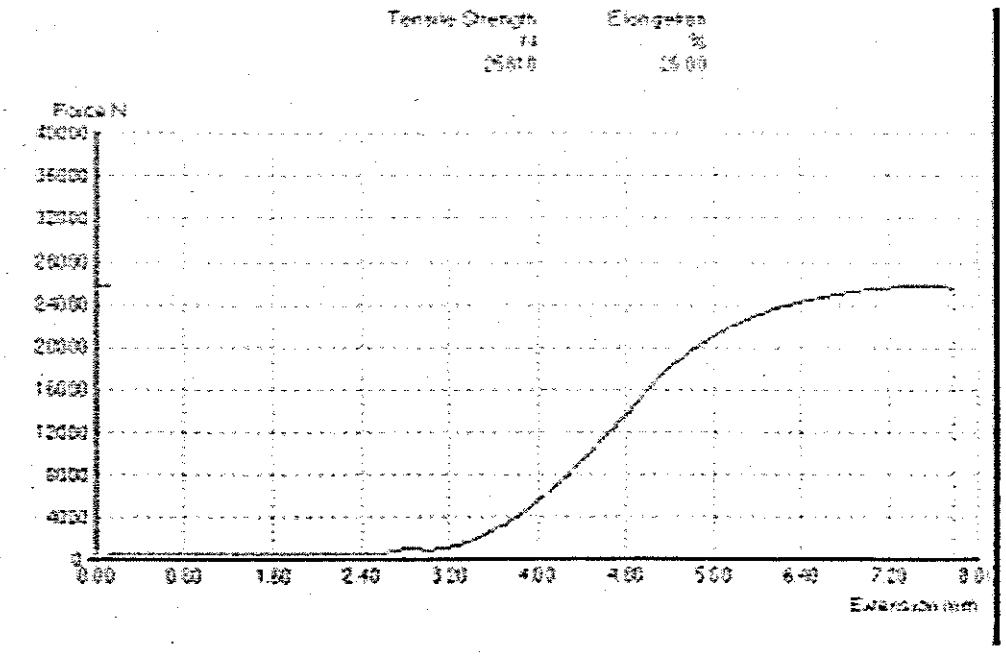

Tensile Test of Specimen 2.1, which is the pair of 2.2, discussed previously. Once again a fair amount of slip has occurred at the grips. UTS. 25.81kN.

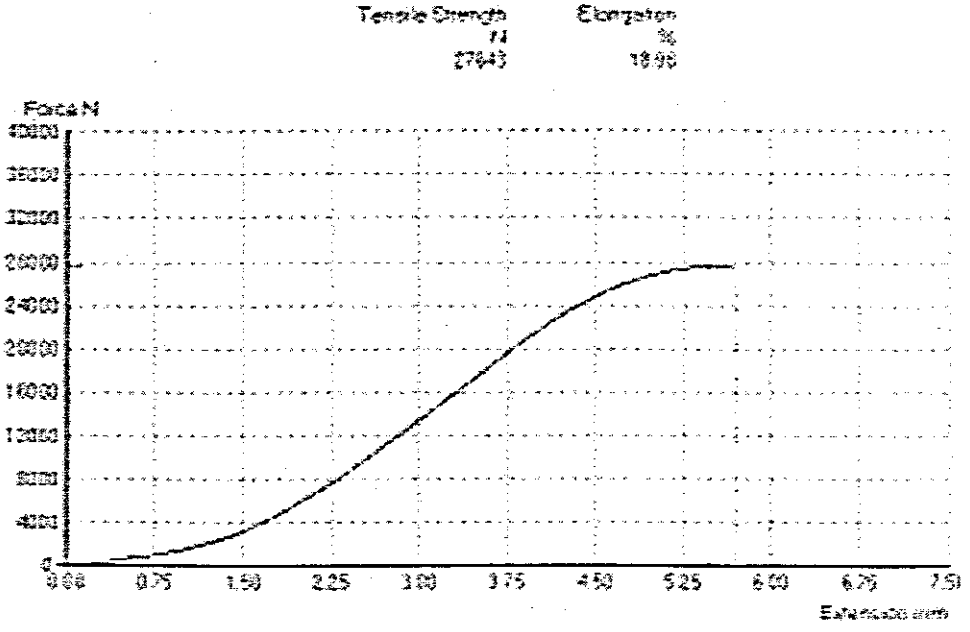

Tensile Test of Specimen 5, which was machined from a 16mm plate and welded with an Armcord LH electrode. UTS. 27.64kN.

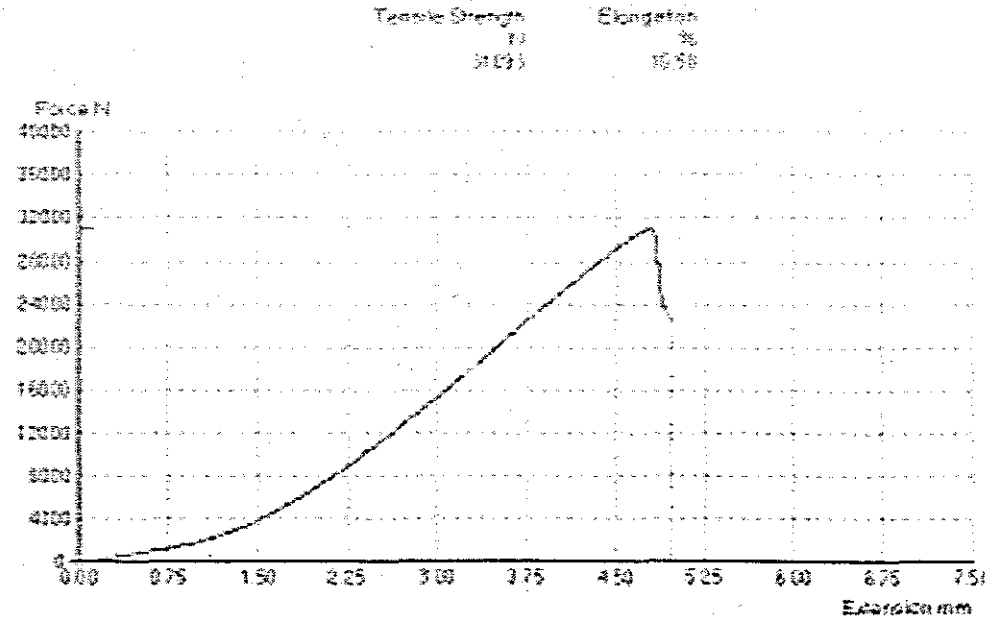

Tensile Test of Specimen 6.1, which was machined from a 16mm plate and welded with an Armcord LH electrode. Note a fairly brittle fracture. UTS. 31.09kN.

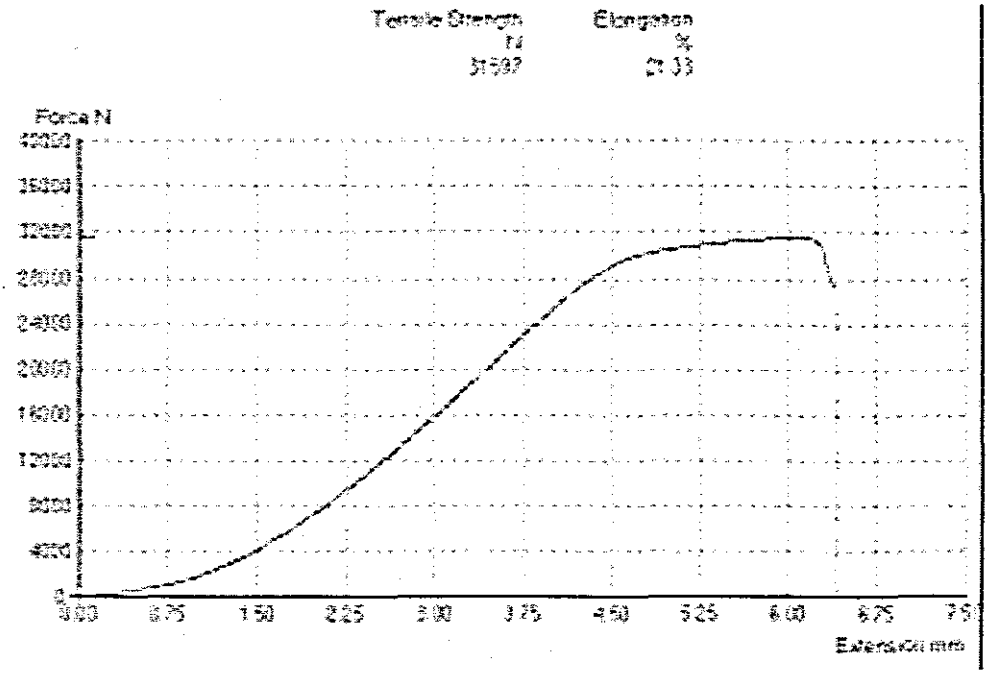

Tensile Test of Specimen 6.2, which was machined from a 16mm plate and welded with an Armcord LH electrode. UTS. 31.6kN.

References

1. Lockspear Sir. B., The Welding of Austenitic Corrosion and Heat Resisting Steels, British Research Association, London, 1953.

2. Afrox Welding Consumables Catalogue, 1998.

3. Iscor Product Manuals, 1996.

4. Little Richard. L., Welding and Welding Technology, McGraw Hill, New York, 1973.

5. Porter D.A. et al., Phase Transformations in Metals and Alloys, 2nd Edition, Chapman Hall, London, 1996.

6. Van Vlack L.H., Elements of Material Science, 2nd Edition, Addison Wesley, Massachusetts, 1970.

7. Hosford William. F. et al., Tensile Testing, 2nd Edition, ASM International, Michigan, 1993.

8. Gray T.G.F. et al., Rational Welding Design, 2nd Edition, Butterworths, London, 1975.

9. Petzow G., Metallographic Etching, 5th Edition, American Society for Metals, Ohio, 1978.

10. Shewmon Paul. G., Transformations in Metals, McGraw Hill, New York, 1969.

11. Askeland Donald, R., The Science and Engineering of Material Science, 3rd Edition, Chapman Hall, London, 1996.

12. Hart P.H.M., Some Aspects of HAZ and Weld Metal Toughness, Proceedings of Metallurgical and Welding Advances in HSLA Steels, 1994.

13. Osberg Eric. et al., Machinery's Handbook, 23rd Edition, Industrial Press Inc., New York, 1989.

14. Hull J.B. et al., Non-Destructive Testing, McMillan Press, London, 1988.

15. Debro-30: Ultrasonic Stress Measurements, Institute of Fundamental Technological Research, Polish Academy of Science, Poland.

16. Cerjak H. & Easterling K.E., Mathematical Modelling of Weld Phenomena, Oxford, 1998.

17. Jeffrey Alan., Linear Algebra and Ordinary Differential Equations, Blackwell Scientific Publications, London, 1990.

18. Borelli Robert. L., Differential Equations, A Modeling Perspective, John Wiley & Sons Inc., New York, 1998.

19. Logan Daryl. L., A First Course in the Finite Element Method, 2nd Edition, PWS Publishing Company, Boston, 1993.

20. Poulikakos D., Conduction Heat Transfer, Prentice Hall, New Jersey, 1994.

21. Ronda J, Oliver G.J., Computational Methods in Applied Mechanics and Engineering, 189 (2000) 361-417, Elsevier, 2000.